LANDSLIDE HAZARD IN A CHANGING ENVIRONMENT

EDITED BY: Davide Tiranti and Roberto Cremonini
PUBLISHED IN: Frontiers in Earth Science

frontiers Research Topics

ISSN 1664-8714
ISBN 978-2-88945-793-9
DOI 10.3389/978-2-88945-793-9

About Frontiers

Frontiers is more than just an open-access publisher of scholarly articles: it is a pioneering approach to the world of academia, radically improving the way scholarly research is managed. The grand vision of Frontiers is a world where all people have an equal opportunity to seek, share and generate knowledge. Frontiers provides immediate and permanent online open access to all its publications, but this alone is not enough to realize our grand goals.

Frontiers Journal Series

The Frontiers Journal Series is a multi-tier and interdisciplinary set of open-access, online journals, promising a paradigm shift from the current review, selection and dissemination processes in academic publishing. All Frontiers journals are driven by researchers for researchers; therefore, they constitute a service to the scholarly community. At the same time, the Frontiers Journal Series operates on a revolutionary invention, the tiered publishing system, initially addressing specific communities of scholars, and gradually climbing up to broader public understanding, thus serving the interests of the lay society, too.

Dedication to Quality

Each Frontiers article is a landmark of the highest quality, thanks to genuinely collaborative interactions between authors and review editors, who include some of the world's best academicians. Research must be certified by peers before entering a stream of knowledge that may eventually reach the public - and shape society; therefore, Frontiers only applies the most rigorous and unbiased reviews.
Frontiers revolutionizes research publishing by freely delivering the most outstanding research, evaluated with no bias from both the academic and social point of view. By applying the most advanced information technologies, Frontiers is catapulting scholarly publishing into a new generation.

What are Frontiers Research Topics?

Frontiers Research Topics are very popular trademarks of the Frontiers Journals Series: they are collections of at least ten articles, all centered on a particular subject. With their unique mix of varied contributions from Original Research to Review Articles, Frontiers Research Topics unify the most influential researchers, the latest key findings and historical advances in a hot research area! Find out more on how to host your own Frontiers Research Topic or contribute to one as an author by contacting the Frontiers Editorial Office: researchtopics@frontiersin.org

LANDSLIDE HAZARD IN A CHANGING ENVIRONMENT

Topic Editors:
Davide Tiranti, Regional Agency for Environmental Protection of Piemonte (Arpa Piemonte), Italy
Roberto Cremonini, Regional Agency for Environmental Protection of Piemonte (Arpa Piemonte), Italy

Image: Thomas Dekiere/Shutterstock.com

Landslides are one of the most dangerous geomorphological processes, responsible for losses of human lives and damages to structures, infrastructures, cultural and natural heritage. During the Anthropocene, impacts of human activity on the environment, including recent climate changes, have caused deep alterations to the natural evolution of surficial geologic processes, causing a progressive increase in the occurrence of landslides.

The goal of this Research Topic is to provide an updated overview of the progress in the field of landslide research, covering all the aspects related to the landslide events: geomorphological characterization and understanding of triggering and predisposing factors, new technologies applied to the study of evolution of slope phenomena, new methodologies to foresee and mitigate landslide hazard.

Citation: Tiranti, D., Cremonini, R., eds. (2019). Landslide Hazard in a Changing Environment. Lausanne: Frontiers Media. doi: 10.3389/978-2-88945-793-9

Table of Contents

04 ***Editorial: Landslide Hazard in a Changing Environment***
Davide Tiranti and Roberto Cremonini

SECTION I
IMPACTS OF CLIMATE CHANGES ON LANDSLIDES

07 ***Economic Losses for Rural Land Value Due to Landslides***
Veronica Zumpano, Luca Pisano, Žiga Malek, Mihai Micu, Pietro P. C. Aucelli, Carmen M. Rosskopf, Dan Balteanu and Mario Parise

20 ***Analysis of Increasing Flash Flood Frequency in the Densely Urbanized Coastline of the Campi Flegrei Volcanic Area, Italy***
Giuseppe Esposito, Fabio Matano and Germana Scepi

SECTION II
LANDSLIDE HAZARD/RISK MODELING

37 ***The Debris Flow Occurred at Ru Secco Creek, Venetian Dolomites, on 4 August 2015: Analysis of the Phenomenon, Its Characteristics and Reproduction by Models***
Carlo Gregoretti, Massimo Degetto, Martino Bernard and Mauro Boreggio

57 ***Evaluating the Differences of Gridding Techniques for Digital Elevation Models Generation and Their Influence on the Modeling of Stony Debris Flows Routing: A Case Study From Rovina di Cancia Basin (North-Eastern Italian Alps)***
Mauro Boreggio, Martino Bernard and Carlo Gregoretti

SECTION III
LANDSLIDE HAZARD ASSESSMENT

83 ***An Integrated Study to Evaluate Debris Flow Hazard in Alpine Environment***
Davide Tiranti, Stefano Crema, Marco Cavalli and Chiara Deangeli

97 ***Multi-Source Glacial Lake Outburst Flood Hazard Assessment and Mapping for Huaraz, Cordillera Blanca, Peru***
Holger Frey, Christian Huggel, Rachel E. Chisolm, Patrick Baer, Brian McArdell, Alejo Cochachin and César Portocarrero

SECTION IV
LANDSLIDE EARLY WARNING SYSTEM

113 ***Combination of Rainfall Thresholds and Susceptibility Maps for Dynamic Landslide Hazard Assessment at Regional Scale***
Samuele Segoni, Veronica Tofani, Ascanio Rosi, Filippo Catani and Nicola Casagli

124 ***The Weather Radar Observations Applied to Shallow Landslides Prediction: A Case Study From North-Western Italy***
Roberto Cremonini and Davide Tiranti

frontiers in Earth Science

EDITORIAL
published: 29 January 2019
doi: 10.3389/feart.2019.00003

Editorial: Landslide Hazard in a Changing Environment

Davide Tiranti and Roberto Cremonini*

Department of Natural and Environmental Risks, Regional Agency for Environmental Protection of Piemonte, Turin, Italy

Keywords: climate change impacts, landslide early warning system, landslide modeling, landslide hazard assessment, debris flow, flash flood, glacial lake overbust flood

Editorial on the Research Topic

Landslide Hazard in a Changing Environment

Landslides are one of the most common natural disasters in the world causing large economic losses and casualties. Their impacts are increasing globally due to rapid development, deforestation and urbanization. According to the Emergency Events Database at Université Catholique de Louvain (UCL)—CRED, from 2008 to 2017 (OFDA/CRED, 2018), landslides has been responsible for 10,338 deaths worldwide, with more than 3 million citizens affected and more than US$ 2.7 billion economic losses. Even in the absence of fatalities, landslides and floods have significant socio-economic impacts. These include the severance of access to and from relatively remote communities for services and markets for goods; employment, health and educational opportunities; and social activities. Recently, a series of debris flows occurred in southern California, US, on January 2018 causing 21 deaths and economic losses for more than US$ 207 million, and landslides caused by heavy rain killed 32 people in Ethiopia in May 2018.

Cruden and Varnes (1996) define landslides as movements of a mass of rock, debris or earth down the slope. Hungr et al. (2014) classified landslides based on failure mechanisms and involved material. Other relevant landslide classifications are related to landslide velocity (Cruden and Varnes, 1996) and size (Fell, 1994) as expression of phenomenal magnitude or related to the triggering factors, like earthquakes or rainfall (Rodríguez et al., 1999; Katsura et al., 2008; Baum and Godt, 2010; Havenith et al., 2016; Calvello, 2017).

During the last decades, climate change has affected the stability of natural and engineered slopes at different temporal and geographical scales (Seneviratne et al., 2012). Several studies demonstrated the impact of climate change on landslide occurrence and investigated future scenarios according to climate model projections (Stoffel et al., 2014, Gariano and Guzzetti, 2016). The type, extent, magnitude and direction of the changes in the stability conditions, and on the location, abundance, activity and frequency of landslides as a consequence of the projected climate changes is under debate (Gariano and Guzzetti, 2016).

In this research topic, Zumpano et al. present two case studies in low-density populated areas in the southern Apennine (Italy) and Romania. In these areas, the main productive activities are based on agricultural and pastoral resources, evaluating the potential economic loss trends in rural areas, according to future scenarios by 2050. Esposito et al. show an interesting analysis of increasing flash flood frequency linked to climate changes in urbanized coastline in southern Italy, during 1970–2014.

Developing landslide hazard/risk modeling applications is a complex task that involves geomorphology, hydrology, geoengineering and statistics (Hungr et al., 1984; Glade, 2005; Fuchs et al., 2008; Bhatt et al., 2013). To properly define hazard/risk scenarios, it is mandatory to characterize and to model the triggering causes and the propagational and deposition pattern of mobilized material. In this research topic, Gregoretti et al. describe the back analysis of the

OPEN ACCESS

Edited and reviewed by:
Steven L. Forman,
Baylor University, United States

****Correspondence:***
Davide Tiranti
davide.tiranti@arpa.piemonte.it

Specialty section:
This article was submitted to Quaternary Science, Geomorphology and Paleoenvironment, a section of the journal Frontiers in Earth Science

Received: *07 November 2018*
Accepted: *07 January 2019*
Published: *29 January 2019*

Citation:
Tiranti D and Cremonini R (2019) Editorial: Landslide Hazard in a Changing Environment. Front. Earth Sci. 7:3. doi: 10.3389/feart.2019.00003

debris flow that occurred in 2015 at Rio Secco Creek (north-eastern Italy), demonstrating that the proposed rainfall-runoff model can reconstruct the triggering factors and the process evolution (propagation and deposition). Boreggio et al. show that the most relevant input in simulations of debris flow routing is the Digital Terrain Model (DEM) with appropriate resolution: several interpolation methods to derive DEM in complex orography are investigated by a GIS framework. Effects of different gridding techniques are also evaluated on modeling of debris flow routing.

Landslide hazard assessment is a relevant step toward landslide hazard and risk management. Pardeshi et al. (2013) provide a comprehensive overview of current techniques in this field of research. In this research topic, Tiranti et al. propose an integrated approach in an Alpine environment (north-western Italy), demonstrating that the comprehensive hazard scenario is evaluated by incorporating the source areas' distribution and characteristics, the actual connection to main channel, estimated by the Connectivity Index, propagation and deposition modeling operated by a 3D Cellular Automata algorithm. Frey et al. describe a study on Quillcay catchment in the Cordillera Blanca, Perú, presenting a scenario-based multi-source glacial lake over burst flood. Beside technical aspects, the study gives special attention to approval and dissemination of hazards information given the complex institutional context.

In 2009, the United Nations Office for Disaster Risk Reduction (UNISDR, 2009) defined an early warning system (EWS) as "a set of capacities needed to generate and disseminate timely and meaningful warning information to enable individual, communities and organizations threatened by a hazard to act appropriately and in sufficient time to reduce the possibility of harm or loss". There are many operational EWSs currently implemented for various types of natural hazards, including landslides. Overview and classification of existing landslide EWSs are presented in Thiebes et al. (2012), Bazin (2012), Stähli et al. (2015), Devoli et al. (2018), and Segoni et al. (2018). In this research topic, a methodology to couple rainfall thresholds and susceptibility maps for hazard assessment at a regional scale is presented by Segoni et al.: this new approach has been tested in northern Tuscany (central Italy) where an appropriate calibration and validation of the hazard matrix has been implemented to meet stakeholder requirements. The availability of quantitative precipitation estimates (QPEs) based on weather radars with high spatial and temporal resolution provides new chances for automatic EWSs: Cremonini and Tiranti illustrate a successful application of an operational EWS in northern Italy. On November 2016, heavy rain hit Piemonte (north-western Italy), causing diffuse landslides and floods: the operational landslide EWS successfully detected the conditions for rainfall-induced landslides.

This Research Topic presents some original research papers on scientific studies representing an updated overview of recent achievements in slope processes research. The presented researches advance our understanding of landslide related hazards and the necessary mitigation actions. These papers also address the possible impacts of climate change on this significant natural hazard.

AUTHOR CONTRIBUTIONS

DT and RC present a sintesys of the state of the art about landslide hazard in the world and introduce the contributions collected in the Research Topic. Both authors listed have made substantial, direct and intellectual contribution to the work, and approved it for publication.

REFERENCES

Baum, R. L., and Godt, J. W. (2010). Early warning of rainfall-induced shallow landslides and debris flows in the USA. *Landslides* 7, 259–272. doi: 10.1007/s10346-009-0177-0

Bazin, S. (2012). *Guidelines for landslide monitoring and early warning systems in Europe – Design and required technology, Project SafeLand "Living With Landslide Risk in Europe: Assessment, Effects of Global Change, and Risk Management Strategies"*. Deliverable 4.8, 153 pp. Available online at: https://www.ngi.no/eng/Projects/SafeLand (Accessed May 7, 2018).

Bhatt, B. P., Awasthi, K. D., Heyojoo, B. P., Silwal, T., and Kafle, G. (2013). Using geographic information system and analytical hierarchy process in landslide hazard zonation. *Appl. Ecol. Environ. Sci.* 1, 14–22. doi: 10.12691/aees-1-2-1

Calvello, M. (2017). Early warning strategies to cope with landslide risk. *Rivista Ital. Geotec.* 2, 63–91, doi: 10.19199/2017.2.0557-1405.063

Cruden, D. M., and Varnes, D. J. (1996). *Landslide types and processes. Landslides: Investigation and Mitigation*. Special Report 247, Transportation Research Board, Washington, 36–75.

Devoli, G., Tiranti, D., Cremonini, R., Sund, M., and Bøje, S. (2018). Comparison of landslide forecasting services in Piemonte (Italy) and in Norway, illustrated by events in late spring 2013. *Nat. Hazards Earth Syst. Sci.* 18, 1351–1372. doi: 10.5194/nhess-18-1351-2018

Fell, R. (1994). Landslide risk assessment and acceptable risk. *Can. Geotech. J.* 31, 261–272. doi: 10.1139/t94-031

Fuchs, S., Kaitna, R., Scheidl, C., and Hübl, J. (2008). *The Application of the Risk Concept to Debris Flow Hazards. Geomechanics and Tunnelling*. Vol. 1; Berlin: Ernst & Sohn Verlag für Architektur und technische Wissenschaften GmbH & Co. KG, 120–129.

Gariano, S. L., and Guzzetti, F. (2016). Landslides in a changing climate. *Earth Sci. Rev.* 162, 227–252. doi: 10.1016/j.earscirev.2016.08.011

Glade, T. (2005). Linking debris-flow hazard assessment with geomorphology. *Geomorphology* 66, 189–213. doi: 10.1016/j.geomorph.2004.09.023

Havenith, H. B., Torgoev, A., Braun, A., Schlögel, R., and Micu, M. (2016). A new classification of earthquake-induced landslide event sizes based on seismotectonic, topographic, climatic and geologic factors. *Geoenviron. Disasters* 3, 1–24. doi: 10.1186/s40677-016-0041-1

Hungr, O., Leroueil, S., and Picarelli, L. (2014). The Varnes classification of landslide types, an update. *Landslides* 11, 167–194. doi: 10.1007/s10346-013-0436-y

Hungr, O., Morgan, G. C., and Kellerhals, R. (1984). Quantitative analysis of debris torrent hazard for design of remedial measures. *Can. Geotech. J.* 21, 663–677. doi: 10.1139/t84-073

Katsura, S., Kosugi, K., Mizutani, T., Okunaka, S., and Mizuyama, T. (2008). Effects of bedrock groundwater on spatial and temporal variations in soil mantle groundwater in a steep granitic headwater catchment. *Water Resour. Res.* 44:W09430. doi: 10.1029/2007WR006610

OFDA/CRED (2018). *International Disaster Database*. Brussels: Université Catholique de Louvain. Available online at: www.emdat.be (Accessed August 9, 2018).

Pardeshi, S. D., Autade, S. E., and Pardeshi, S. S. (2013). Landslide hazard assessment: recent trends and techniques. *Springerplus* 2:523. doi: 10.1186/2193-1801-2-523

Rodríguez, C. E., Bommer, J. J., and Chandler, R. J. (1999). Earthquake induced landslides: 1980–1997. *Soil Dyn. Earthq. Eng.* 18, 325–346. doi: 10.1016/S0267-7261(99)00012-3

Segoni, S., Piciullo, L., and Gariano, S. L. (2018). A review of the recent literature on rainfall thresholds for landslide occurrence. *Landslides* 15, 1483–1501. doi: 10.1007/s10346-018-0966-4

Seneviratne, S. I., Nicholls, N., Easterling, D., Goodess, C. M., Kanae, S., Kossin, J., et al. (2012). "Changes in climate extremes and their impacts on the natural physical environment," in *Managing the Risks of Extreme Events and Disasters to Advance Climate Change Adaptation. A Special Report of Working Groups I and II of the Intergovernmental Panel on Climate Change (IPCC)*, eds C. B. Field, V. Barros, T. F. Stocker, D. Qin, D. J. Dokken, K. L. Ebi, M. D. Mastrandrea, K. J. Mach, G.-K. Plattner, S. K. Allen, M. Tignor, and P. M. Midgley (Cambridge; New York, NY: Cambridge University Press), 109–230.

Stähli, M., Sättele, M., Huggel, C., McArdell, B. W., Lehmann, P., Van Herwijnen, A., et al. (2015). Monitoring and prediction in early warning systems for rapid mass movements. *Nat. Hazards Earth Syst. Sci.* 15, 905–917. doi: 10.5194/nhess-15-905-2015

Stoffel, M., Tiranti, D., and Huggel, C. (2014). Climate change impacts on mass movements – case studies from the European Alps. *Sci. Total Environ.* 493, 1255–1266. doi: 10.1016/j.scitotenv.2014.02.102

Thiebes, B., Glade, T., and Bell, R. (2012). "Landslide analysis and integrative early warning-local and regional case studies," in *Proceeding 11th International Symposium on Landslides* (Banff, AB: CRC Press), 1915–1921.

UNISDR (2009). *UNISDR – ISDR: Terminology*. Available online at: http://www.unisdr.org/eng/library/lib-terminology-enghome.htm (Accessed August 8, 2018).

Conflict of Interest Statement: The authors declare that the research was conducted in the absence of any commercial or financial relationships that could be construed as a potential conflict of interest.

frontiers in Earth Science

ORIGINAL RESEARCH
published: 25 July 2018
doi: 10.3389/feart.2018.00097

Economic Losses for Rural Land Value Due to Landslides

Veronica Zumpano[1,2], Luca Pisano[1,3], Žiga Malek[4], Mihai Micu[2], Pietro P. C. Aucelli[5], Carmen M. Rosskopf[3], Dan Balteanu[2] and Mario Parise[1,6]*

[1] Research Institute for Geo-Hydrological Protection, Consiglio Nazionale Delle Ricerche, Bari, Italy, [2] Institute of Geography, Romanian Academy, Bucharest, Romania, [3] Department of Biosciences and Territory, University of Molise, Isernia, Italy, [4] Environmental Geography Group, Institute for Environmental Studies (IVM), VU University Amsterdam, Amsterdam, Netherlands, [5] Department of Environmental Science, University of Naples Parthenope, Naples, Italy, [6] Department of Earth and Environmental Sciences, University Aldo Moro, Bari, Italy

A high dynamic environment is typically interested by changes affecting the natural processes and their related consequences. Landslides do not only alter the landscape, but substantially affect human activities. When it comes to natural hazards, landslides have been acknowledged as one of the main causes of human casualties or damage to assets. Furthermore, economic losses to rural lands are also significant, despite often being underrated, especially in rural areas. In not densely populated territories, the main productive activities are in fact often based on the agricultural and pastoral resources. We intend to propose a methodology that helps to investigate the potential loss of value (expressed in €) of lands usually exploited for economical profit in rural areas. We test the method on two case studies, belonging to different European Countries with very different economical assets and geological, geomorphological, and environmental conditions. The first study area is located in the Southern Italian Apennines, in the Molise region, while the second area is located in Buzau County, a region belonging to the Romanian Curvature Carpathians and Subcarpathians. Our analysis is focused not only on the actual situation, represented by the past and present landslides, but also on potential future scenarios for 2050. The scenarios foresee future similar socio-economical and technological activities, with no major changes expected. The loss estimation is based on the presence of landslides affecting the rural lands, but it also considers both a present and future landslide susceptibility scenario. This procedure allowed the estimation of the economic losses in the two case-study areas, highlighting how the same natural processes might result in different economical consequences. Following our approach, the results highlight that for the Italian case study there is a loss of 10.4% for 2007 and 9.9% for 2050 of the total land value as concerns landslides susceptibility. In the Romanian case study, on the other hand, the loss corresponds to 29.6 and 29.8% for 2010 and 2050, respectively. In addition, the proposed procedure could be considered a valuable methodological approach to assess landslide-induced economic losses, and be effectively used during spatial planning activities, aimed at supporting decision makers for a more sustainable land management.

Keywords: landslides, land cover changes, economic loss, susceptibility, future scenario

OPEN ACCESS

Edited by:
Davide Tiranti,
Agenzia Regionale per la Protezione Ambientale (ARPA), Italy

Reviewed by:
José Darrozes,
UMR5563 Géosciences Environnement Toulouse (GET), France
Claudia Meisina,
University of Pavia, Italy

***Correspondence:**
Luca Pisano
l.pisano@ba.irpi.cnr.it

Specialty section:
This article was submitted to Quaternary Science, Geomorphology and Paleoenvironment, a section of the journal Frontiers in Earth Science

Received: *28 February 2018*
Accepted: *29 June 2018*
Published: *25 July 2018*

Citation:
Zumpano V, Pisano L, Malek Ž, Micu M, Aucelli PPC, Rosskopf CM, Balteanu D and Parise M (2018) Economic Losses for Rural Land Value Due to Landslides. Front. Earth Sci. 6:97. doi: 10.3389/feart.2018.00097

INTRODUCTION

Natural hazards, including landslides, cause severe damage to a large variety of assets (meaning structural, infrastructural, and social goods), determining losses on population activities, natural, and human environment all over the world (Zêzere et al., 2008; Petley, 2012; Promper and Glade, 2016; Salvati et al., 2018).

There is an increasing interest on studying how anthropogenic pressure on the ecosystems can determine changes in the spatial distribution of landslides (Reichenbach et al., 2014; Malek et al., 2015; Schmaltz et al., 2017; Gariano et al., 2018). It is also important to underline that changes in the socio-economical structure are going to affect also the number and the type of assets exposed to natural hazards and risks, including landslides (Pisano et al., 2017a). The interactions among exposed assets, landslides, and economic analysis of the occurred damage have therefore become object of several studies since a few decades (i.e., Schuster, 1996; Godt et al., 2000).

Estimating consequences of landslides in terms of direct and indirect damage (Fleming and Taylor, 1980; Schuster and Fleming, 1986) is imperative in the framework of reliable risk assessment and management strategies.

When dealing with natural disasters, direct and indirect losses have to be distinguished. According to the United Nations Office for Disaster Risk Reduction (UNISDR): *"Direct losses refer to damage to human lives, buildings, infrastructure, and natural resources. Indirect disaster losses are declines in output or revenue, as a consequence of direct losses or owing to impacts on a supply chain"* (GAR, 2015). Other types of costs are intangible costs, business interruption costs, and risk mitigation costs, as defined in Kreibich et al. (2014). The damage observed, and the related costs, may be also very different to quantify depending upon the type of natural hazards (Parise et al., 2013; Vennari et al., 2015, 2016; Salvati et al., 2018).

Furthermore, there are generally two ways to assess costs of natural hazards, namely *"ex-post"* are those estimates after the event, meanwhile with "*ex-ante*" can be named those estimated taking into account the likely future hazard occurrence. Following Donnini et al. (2017) the first is the approach most commonly addressed in the scientific literature, because it provides information relevant to the stakeholders or planners related to the compensation and economic support.

When a natural hazard occurs, there can be a great variety of elements at risk affected, but commonly the focus is on buildings and public infrastructure such as roads, railroads, and other communication routes (Alexander, 1986; Chiocchio et al., 1997; Iovine and Parise, 2002; Calcaterra et al., 2008; Calò et al., 2012; Del Soldato et al., 2017). However, when it comes to rural areas the main economic resources are strictly tied to the exploitation of agricultural, pastoral, and natural resources, therefore land damage represents a serious threat to the socio-economic development. In this case, the landslide direct damage can be identified as the partial or complete loss of agricultural production and of soil productivity in time, and/or the reduction in land value.

Indirect damages caused by landslides, on the other hand, are related to the reduction of functions derived by rural activities normally taking place in the affected land (for example harvesting, plowing, pasture), determining also the reduction in the normally produced public services.

It is quite common that the losses to rural land, caused by activity of slope movements, tend to be underrated, due to the fact that they do not constitute a practical risk to personal safety. For instance, at present there is quite relevant scientific literature available concerning loss or damage of rural lands due to natural hazards such as drought (IPCC, 2012; WMO, 2014; Lesk et al., 2016) or floods (Ward et al., 2013; Tanoue et al., 2016), but almost anything about landslides to the best of our knowledge.

Economic damage produced by soil erosion and landslide phenomena in rural environments, together with the lack of methodological approaches to assess landslide-induced damage, makes difficult to take decisions concerning land management, or to plan and develop actions to prevent and mitigate such damage. This amplifies the need to develop methods potentially contributing to a more precise and rapid evaluation of the likely economic consequences.

In this work we propose a methodology that helps to determine the loss of value suffered by those land parcel types which are exploited for economical profit in rural areas. The method is a multi-disciplinary approach, based on the integration of GIS applications, effective and easy to use because it does not require a large amount of data. To test its robustness we applied it to two different case studies, characterized by different socio-economical environments, geological and geomorphological settings, and data availability and resolution as well.

In addition, considering that future damage is often considered the essential basis of risk reduction strategies and preparedness planning in any risk analysis (Van Westen et al., 2006; Vranken et al., 2013), we further analyse the expected losses for both case studies, according to a possible Business As Usual (BAU) scenario for year 2050.

STUDY AREAS

The study is focused on two areas located in different European Countries. The first one is the Rivo catchment in the Molise region of the Italian Southern Apennine, while the second is placed in the Curvature sector of the Romanian Carpathians and corresponds to the upper sector of the Bălăneasa catchment. Selection of these two areas lies in the fact that they are representative for the rural environment in the respective countries. In addition, they were selected also on account of the fact that we wanted to apply the methodology in two quite distinct settings from both the environmental and the socio-economical standpoints.

Rivo Catchment

The Rivo catchment study area covers an area of 82 km^2 and is located along the Adriatic flank of Molise region (Southern Italy). It is a small hilly to low mountainous basin which is part of the larger valley system of the Trigno River, one of the major water courses in the region. The area is characterized by altitudes ranging from ca. 230 to 980 m above sea level. From a geological standpoint the outcropping geological formations consist mainly

of marly-arenaceous and clayey deposits (from Upper Oligocene to Middle Miocene), with subordinate limestone and Middle-Lower Miocene bio-calcilutites, as reported in the sheet 393 "Trivento" of the geological map (Sgrosso and Naso, 2012).

Slope modeling processes, such as landslides and deep gully erosion, take place extensively on steep slopes modeled on clayey lithologies (mainly varicolored scaly clays; Aucelli et al., 2010).

Landslides belong to the categories of earthflows and complex earthslide-earthflows, and are primarily triggered by rainfall (Rosskopf and Aucelli, 2007; Borgomeo et al., 2014). Most of the phenomena are dormant and relatively superficial (depth $\leq$4 m); they are typically found along fluvial slopes directly bordered by stream incisions, and thus severely affected by river undercutting (Aucelli et al., 2001, 2004).

The area lies within a prevalently rural context with low population density. The prevailing land use is represented by crops (55.4%), forest lands (32.87%), and pasture (4.7%). The most common population sustenance methods are agricultural, pastoral, and crafting activities, and small enterprises.

Bălăneasa Catchment

The second study area is situated in the Curvature sector of the Romanian Carpathians, at the limit between the Buzău Carpathians and Subcarpathians (see **Figure 1**), an area considered representative for the two main morpho-structural units in respect to the landslide typology—land cover categories relationship. Overlaying the upper catchment of Bălăneasa River (main tributary of Buzau), the area extends from 1,100 m to 300 m a.s.l., and can be divided in two almost equal sub-sectors: an upper mountainous zone, and a lower hilly zone. The northern mountainous area (Buzău Carpathians) features low-altitude summits (1,000–800 m a.s.l.) and elongated, NE-SW-oriented, smooth ridges alternating with large valleys carved in Mid-Upper Palaeogene flysch deposits (Eocene schistose sandstone flysch, Oligocene sandstone flysch with schistose intercalations, bitumen and conglomerates). The lithological features, together with the highly folded and faulted structures, constitute the main predisposing factors of the active morphodynamics. The slopes are modeled by large, deep-seated landslides (debris/rock slumps, rock block slides), triggered by snowmelt or long-lasting rains, with a high reactivation potential, especially in the form of shallow and medium-seated earth/debris slides. The southern hilly sector corresponding to the Buzău Subcarpathians consists of an alternation of low-to-high rounded hills with enlarged valleys as a result of differentiated erosion exerted on the different-consistence molasse deposits of Low Neogene age (Miocene schistose clays and schists, alternating with thin sandstone, gypsum or conglomerate layers). Developed between 800 and 300 m a.s.l., the Subcarpathian sector is marked by intense landslide activity, conditioned by the lithology and enhanced by human activity (road cuts). The landslide typology consists of shallow and medium-seated earth/debris slides and numerous earthflows, triggered by early spring showers or torrential summer rains. Throughout both sectors, slope processes are strongly correlated with the river network, both at the level of large valleys and smaller tributaries, so that in numerous cases landslide deposits cause river blockages and temporary landslide dams. The human activities are leaving strong imprints on the landscape. Even if it is a rural area, social, and political-economical frameworks marked changes in the land-cover patterns. Partial collective agriculture until 1990, followed by a transition period and by Romania's EU joining procedures (2007) induced different management procedures, in which recent deforestations, property fragmentation or abandonment strongly influenced the correlation between slope processes (landslides and erosion) and land coverage/usage (Micu, 2008). The broad-leaved forests are covering the majority of the land in the Carpathian sector, being replaced in the Subcarpathians by orchards and hayfields. The settlements are usually clustered along valleys, while seldom households could

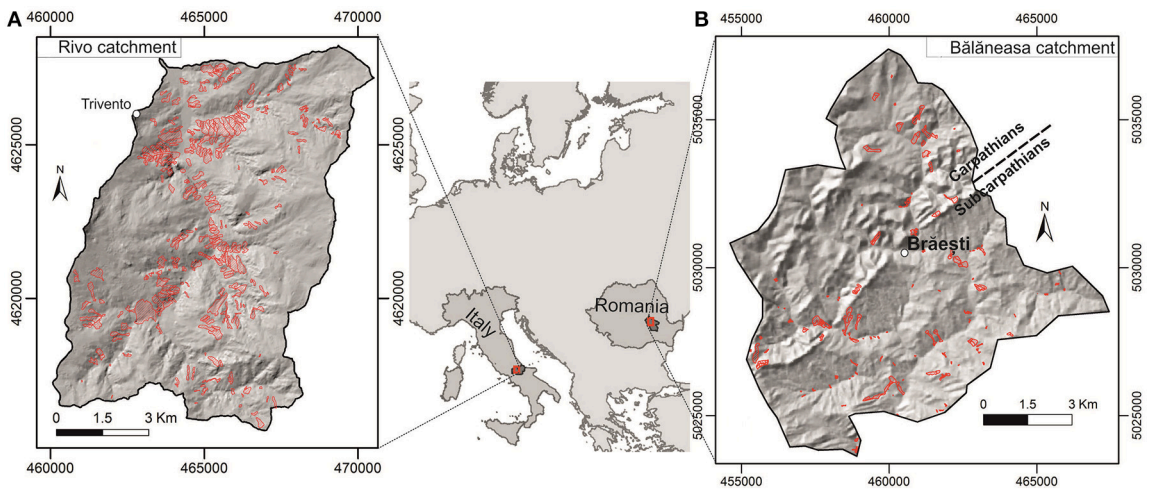

FIGURE 1 | General overview of the study areas locations (in **A** Rivo catchment; in **B** Balaneasa catchment) and landslides bodies (reported in red) used for the analysis.

be encountered scattered across the upper slopes and used mainly during the harvest periods (of both fruits and hay). The subsistence agriculture prevails, while arable lands are limited in extension and used mainly for maize or potato crops.

DATA PREPARATION AND METHODS

Estimation of the damage suffered by rural lands lying on slopes prone to landslides is built through the interaction of two features, namely: (i) land use/cover type and associated economic value, and (ii) landslide susceptibility. These two are overlapped by using GIS software in order to obtain the potential degree of loss suffered by rural and agricultural lands due to different levels of landslides susceptibility. To this aim, we completed the landslide susceptibility analyses for the two case studies, and collected information related to the average land values of forested areas, pastures, cultivated land, bareland, and shrubland for both the case studies. Landslides susceptibility classes and land values were eventually intersected by means of a matrix that, after the application of specific indicators, provided a net land value reduced by the estimated loss, called the "real" value.

This section illustrates the data and the methods used to perform the analysis, whilst land use data and the future 2050 scenario were developed by Pisano et al. (2017b,c). Here the output related to the 2007 land cover, and the so-called 2050 trend scenarios, together with the associated susceptibility, were used as input data in order to calculate the potential loss of economic value of the rural lands due to susceptibility. For the Bălăneasa catchment case study, we performed the land cover scenario and the associated susceptibility (for years 2010 and 2050) by adopting the same methodology used for the Rivo catchment. In the following sections we present data and methods related, in both case studies, to the land cover and landslide susceptibility, the economic value of the rural lands and its loss due to landslide susceptibility, an overall overview of the methodology adopted is given in the flowchart provided as the Supplementary Materials (Supplementary Figure 1).

Land Cover and Land Cover Scenarios

Land cover maps were designed in the framework of a multi-temporal analysis aimed at evaluating land cover changes in a 50 year period (Pisano et al., 2017b,c). The multi-temporal land cover mapping was performed in GIS environment by using ortho-rectified and co-registered aerial photos. The aerial image interpretation was performed using a scale of 1:5,000, organized in the following seven classes: settlements, cultivated area, forested land, pasture, shrubland, wetland, and bareland.

In these works, we considered only those land cover classes exploited as agricultural, pastoral, and natural resources in less populated territories where rural activities are the main source of income. In detail, they are forested areas, pastures, cultivated land, bareland, and shrubland.

For the Bălăneasa case study we used the land cover maps developed by Malek et al. (2014) starting by classifying the forest cover through Landsat images for the years 1989, 2000, and 2010. To map settlements and cropland, we combined the Landsat data with most recent high resolution Google Earth images. More detailed topographic maps and spatial plans obtained from local authorities were also used to help with manual digitization of settlements and cropland. The final land cover map had a 89% overall accuracy. More information on the land cover classification and the underlying data are available in Malek et al. (2014).

Regarding the scenario modeling, we projected future land use changes in both study areas for the year 2050 by simulating future changes based on the observed historical trends, which we assumed to continue in the future. To spatially allocate future land cover change, we developed a model using Dinamica EGO. Dinamica EGO is a GIS, particularly suitable for spatial land cover change simulation on a high spatial and temporal resolution (Soares-Filho et al., 2002).

The demands of future land cover were based on observed trends. In this way, we simulated how the future land cover might look like if socio-economic conditions, current agricultural, and forestry practices, as well as spatial planning will continue with the business as usual (BAU) scenario. In both areas, we however modified the observed trends, to allow the continuation of the most significant processes. For example, forest expansion was observed as the prevailing process in the landscape. To allow the continuation of the forest expansion trends, we therefore had to modify the change rates of other processes, that occurred on a smaller spatial extent. This did not influence the final results, as we only limited cropland and urban expansion change rates to exclude expansion on the account of forests. Moreover, agricultural abandonment and subsequent overgrowth have been identified as a major land use process in European mountain areas (van Vliet et al., 2015), a trend likely to continue.

The trend scenarios were different for the two areas: whereas the Italian area witnessed cropland and urban expansion, that in Romania was characterized by forest expansion and to some extent small scale deforestation, as indicated by forest management trends at the regional level (Malek et al., 2015, 2018).

In future scenarios particular land cover types, such as forest or cropland, are in our study areas more likely to be found near or adjacent to existing forests or croplands. We therefore mostly modeled expansion of particular land cover, instead of forming new isolated patches in a landscape. We still allowed the formation of new patches of specific land cover, based on the observed size and variation of observed past land cover changes. In this way, we aimed to capture more realistic spatial patterns of future land cover change specifically for each of the study areas.

Landslide Susceptibility and Associated Scenario

To quantify the potential loss of value of rural lands due to landslides we considered the landslide susceptibility of the two analyzed case studies, starting from the landslide susceptibility analysis already available for the Rivo catchment (Pisano et al., 2017c). We carried out the susceptibility using the Spatial Multi Criteria Evaluation (SMCE) (Alkema, 2007; Boerboom and Alan, 2012; Pourghasemi et al., 2014) in GIS environment using ILWIS

software (ILWIS™ Academic 3.3, 2012)[1] and taking into account seven predisposing factors (slope angle, slope aspect, altitude, internal relief, land cover, soils, and ancient landslide deposits), for which the frequency ratio (FR) was calculated (Pradhan and Lee, 2010; Yalcin et al., 2011; Persichillo et al., 2017). FR was calculated exploiting the landslide dataset points extracted in the source zone, in order to represent the probability of occurrence from the initiation area. To the variables were assigned weights representing their relative importance; namely, we gave the highest weights to slope declivity and land cover (0.19), followed by slope orientation, large old landslide deposits (0.14), internal relief (0.13), soil (0.11), and altitude (0.09). The dataset was divided in two parts, allowing to have two independent dataset, one of which representing the 10% of the total to be used for validation. This latter was operated applying the receiver operating characteristic (ROC) curve (Pisano et al., 2017c).

In the SMCE the FR was used to relate the factor classes weights to the landslide density standardized using the maximum linear function; meanwhile the factors standardization was performed using the direct method based on expert judgment (Pisano et al., 2017c). The obtained map (**Figure 2**) for 2007 has been re-classified using five intervals from very low to very high, and showed a ROC curve of 0.814 (Pisano et al., 2017c). The map identifies the highest susceptibility in the central areas in correspondence of the most clayey formations, i.e., Varicoloured Scaly Clays, that showed high Frequency Ratio values (Pisano et al., 2017c), and is known to be highly affected by landslides in the Southern Apennines of Italy (Fiorillo et al., 1996; Parise and Wasowski, 1999; Rosskopf and Aucelli, 2007).

Following the same approach, we carried out the susceptibility analysis for the Bălăneasa catchment. Based on a wide knowledge of the geological and geomorphological characters and of the main hydro-geological processes occurring in the area, we prepared the conditional factors maps useful for the SMCE method application. Further, in doing so, several previous studies focusing on landslides occurrence and spatial distribution in proximal areas were considered in the selection of the conditional factors (i.e., Damen et al., 2014; Zumpano et al., 2014; Hussin et al., 2016). Therefore, we sorted out the following parameters: slope declivity, slope aspect, altitude, internal relief, land cover, soil, and ancient landslides deposits.

The geomorphological parameters were derived in GIS environment from a DEM (25 m cell size) extracted from a topographical map produced by the Military Topographic Direction (scale 1:25,000); the soil map (scale 1:100,000) was available from the Institute of Geography Archives, and the land cover map was derived from digital aerial photo interpretation. We decided to take in consideration also old large landslides areas among the conditional factors, due to the fact that in the region very often new landslides develop within old, large, landslide bodies (Micu et al., 2014). Old landslides areas were extracted from archive inventory data from the Institute of Geography of the Romanian Academy, and from previous studies (Damen

[1]ILWIS (2012). *Academic 3.3*. Available online at: http://www.ilwis.org/open_source_gis_ilwis_download.htm

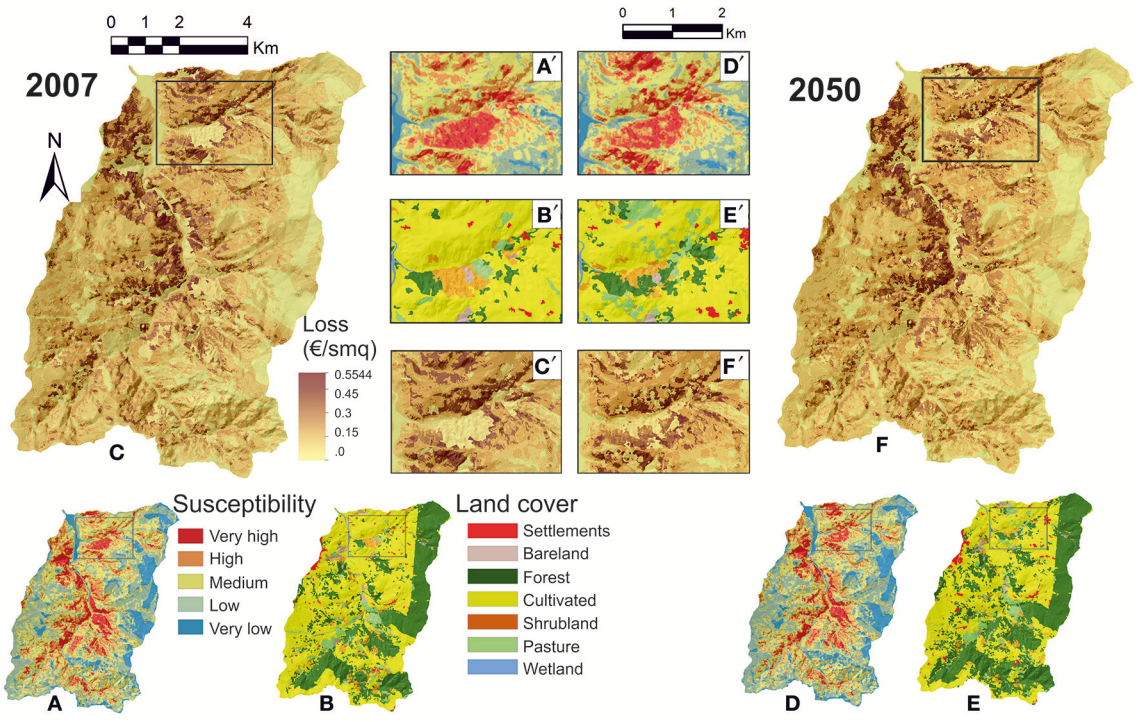

FIGURE 2 | Rivo catchment landslide susceptibility **(A)**, land cover **(B)**, and damage **(C)** maps for 2007 and 2050 (respectively, **D–F**). In the zoomed squares (A′-C′ for 2007 and D′-F′ for 2050) some sectors of the related maps are highlighted.

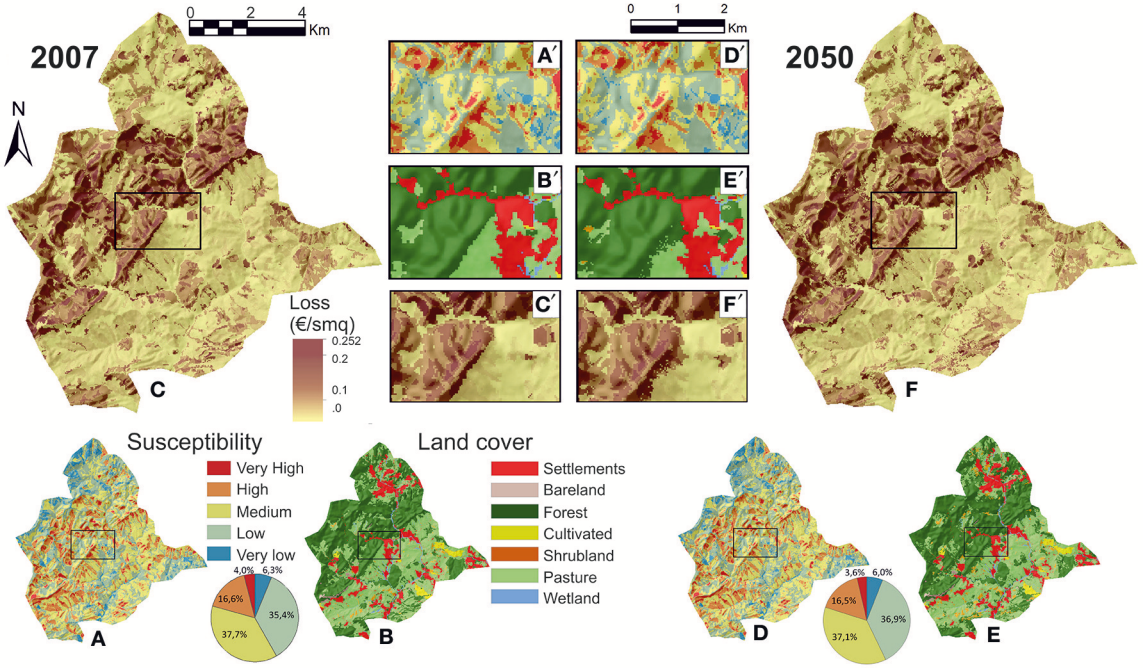

FIGURE 3 | Bălăneasa catchment landslide susceptibility **(A)**, land cover **(B)**, and damage **(C)** maps for 2010 and 2050 (respectively, **D–F**). In the zoomed squares (A′-C′ for 2010, and D′-F′ for 2050) some sectors of the related maps are highlighted. The pie charts represent the percentage area of the susceptibility classes related to the susceptibility maps **(A,D)**.

et al., 2014). For the SMCE, guided by the tool available in ILWIS software, we standardized the factors using the expert judgment and conversely to what was done before for the Rivo catchment, we weighted the factors classes by integrating the FR values with the expert judgment. This was given by the fact that a preliminary analysis carried out using only the FR values turned out in unreliable results, probably because the landslides database is compiled starting from civil protection reports and field activity, resulting in a non-uniform dataset, partially incomplete, across the area.

The validity of the analysis' performance was evaluated by using the ROC curve, which for this map showed a value of 0.811. Finally, we run the susceptibility analysis scenario adopting the land cover 2050 scenario among the input factor replacing the land cover 2010 in both models. We maintained the same factors weights and the same standardization approach, the resulting map being presented in **Figure 3**.

Land Value and Estimated Economic Loss

The second phase of the data preparation focused on the collection of the information related to the economic land values for the two case studies.

The average land values for the Rivo catchment were extracted from the regional dataset available at the Italian Income Revenue Agency of the Ministry of the Economy and Finance website (http://wwwt.agenziaentrate.gov.it/mt/Osservatorio%20immobiliare/valori_agricoli_medi/molise/CB_2007.pdf). The dataset organized for regions provides values in €/ha at the provincial level for all the agricultural land types falling within the province. As reported in the website, the numbers represent the weighted averages of agricultural values within the region based on the indemnity to be paid to the owner of an agricultural land expropriated for public use, according to the actual cultivation practiced. From the database we collected the values for the Campobasso province and correlated them to the Rivo land cover classes, afterward we transformed the values to €/m^2 (**Table 1**).

For the Bălăneasa catchment the data related to the land values were collected through an accurate survey of both the formal legal documents recommending values and procedures of selling/buying land parcels according to the Romanian law (LG 17/2014), but also taking into account informal transactions documents. This duplex approach was demanded by the fact that in terms of land value based on its coverage/usage, there are major differences between informal (suggested benchmarks) and official transaction values. Prices vary a lot when taking into account the relief (morphometry, accessibility) and the economic and social requirements (village location inside different relief units, imposing different requirements for agricultural land). In addition, they depend also on its quality as a reflection of relief units and settlements' presence relationship, but also on the size of the land parcels, since in the study area there are not many properties exceeding 5-10 ha in surface. For this application we decided to take into consideration an average of the prices provided as guides for the real-estate market by the Romanian National

TABLE 1 | Economic values of the selected land cover classes in the Rivo area.

	Pasture	Forest	Shrubland	Bareland	Cultivated
Euro/m^2	0.34	0.45	0.26	0.18	0.77

TABLE 2 | Economic values of the selected land cover classes in the Bălăneasa area.

	Pasture	Forest	Shrubland	Bareland	Cultivated
Euro/m^2	0.09	0.28	0.07	0.06	0.17

Association of Authorized Evaluators (**Table 2**); however, one should take in consideration this ambiguity when looking at the value loss. Finally, values were converted into €/m^2, and correlated to the land cover classes object of interest in this study.

For both case studies we decided to use also the present economic values for the future land cover scenario. This was due to the fact that considering forecasted economic variables to predict future prices for the scenarios would have made the calculation very complex and difficult to manage, in addition producing final outcomes difficult to be compared (Mela et al., 2012).

To establish the economic damage in terms of loss value we decided to set up a rapid and feasible approach based on three parameters, namely the average land value in €/m^2 (LV), the susceptibility class, ranging from very low to very high (S), and a specific land cover damage index (DI), according to the formula:

$$\text{LOSS} = \text{LV x (S x DI)} \quad (1)$$

The first parameter (S) was ranked ascribing, based on expert judgment, proportionally higher values from 0 to 0.9 to the five susceptibility classes (from very low to very high; **Table 3**). We decided not to use 1 for the highest value, given the fact that we are estimating here a probability or proneness, thus not having the certainty of the landslide occurrence. For the DI parameter we have attributed qualitatively a value from 0 to 1 based on a qualitative estimation conceived to represent the resilience of the land parcel to reconstitute its potential use after a landslide event.

We choose to combine the susceptibility classes (S) and the landslide-damage index (DI) by multiplying them in a matrix (**Table 3**) from which we obtained a value that, multiplied to the land value (LV), gives the value loss (LOSS).

Finally we calculated also a net land value that considers the estimated loss, which can be intended as the real economic land value.

The matrix was used for both present and future scenarios, and the final results were compared in order to examine how landslide susceptibility affects, and might affect in the future, the land values.

Further, with our application we investigate the extent of this potential loss considering future land cover changes anticipated by a business as usual (BAU) scenario in the two considered European Countries, highlighting how the same natural process might result in quite different economic consequences.

TABLE 3 | Matrix used to correlate the land cover damage index (DI) and the susceptibility classes indexes (S).

			Land cover damage index (DI)				
			Forest	Cultivated	Shrubland	Bareland	Pastures
			1	0.8	0.3	0.3	0.3
Susceptibility classes (S)	VH	0.9	0.9	0.72	0.27	0.27	0.27
	H	0.7	0.7	0.56	0.21	0.21	0.21
	M	0.4	0.4	0.32	0.12	0.12	0.12
	L	0.2	0.2	0.16	0.06	0.06	0.06
	VL	0	0	0	0	0	0

RESULTS

To quantify the changes in the economic values for the land cover categories considered relevant for the rural economic activity of the study areas, we started to evaluate the variations in the total land value exclusively due to land cover changes for the period 2007–2050 in the Rivo catchment, and 2010–2050 for Balaneasa (section Variations in the Land Values Due to Land Cover Changes and Scenario); afterwards, we present the results obtained for the estimated loss due to susceptibility (section Landslide Susceptibility and Scenario) for the past situation and for the future 2050 scenario. Eventually, we compare the loss in the two case studies considering the respective land cover, the differences in the land prices, the degree of landslide susceptibility and the scenarios.

Variations in the Land Values Due to Land Cover Changes and Scenario

By means of the application of the proposed method implemented in GIS, we observed the changes in the total land values by comparing the actual and the future 2050 extent for each class in the Rivo and the Bălăneasa catchments (**Tables 4**, **5**).

As shown in the tables, there is a difference in the associated values for the classes for both case studies. For the Rivo area some classes such as cultivated, shrub and bareland are decreasing their extent (Pisano et al., 2017c). Due to the fact that cultivated land has the highest value, its variation pays the highest contribution to the value of the total area. This loss is partially balanced primarily by the increase of forest extension (see **Table 4**). As a consequence, there is a decrease in the total rural land value of ∼2 Mln€ (representing 3.6%, with respect to the initial value).

In the Bălăneasa catchment, the forest expansion due to abandonment of cropland and pastures was identified as the prevailing process. In this area the changes are not so straightforward, and forest and shrubland expansion are about 2% of the total area. On the other hand, pasture is the class showing the most significant decrease. The highest forest value with respect to the other classes determines an increase of the

TABLE 4 | Variations in the total land values due to land cover changes in the Rivo case study.

Land cover classes	% of the class respect to total area 2007	Total class value 2007	% of the class with respect to total area 2050	Total class value 2050
Cultivated	55.4	35,536,900.00	48.59	31,151,600.00
Forest	32.87	12,316,100.00	40.3	15,099,200.00
Pasture	4.73	1,309,710.00	5.01	1,417,110.00
Shrubland	4.62	1,000,770.00	3.42	740,246.00
Bareland	1.13	185,868.00	0.83	125,145.00
Wetland	0.23	0	0.23	0
Settlements	1.01	0	1.,63	0
Total		50,349,348,00		48,533,301.00

TABLE 5 | Variations in the total land values due to land cover changes in the Bălăneasa study area.

Land cover classes	% of the class respect to total area 2010	Total class value 2010	% of the class with respect to total area 2050	Total class value 2050
Cultivated	1.68	254,469.00	1.68	254,469.00
Forest	45.68	11,396,200.00	47.57	11,868,900.00
Pasture	39	3,127,500.00	35.26	2,827,460.00
Shrubland	0.99	61,556.30	2.83	176,750.00
Bareland	0.57	30,712.50	0.57	30,712.50
Wetland	1.28	0	1.28	0
Settlements	10.81	0	10.81	0
		14,870,437,80		15,158,291,50

total land value of around 290,000 €, corresponding to 2% of the total land value.

Landslide Susceptibility and Scenario

The values related to each land cover class, presented in the previous section, must be considered as gross values, given that they do not take into any consideration the possible land depreciation given by landslides spatial probability of occurrence that might affect them. For this reason we used the landslide susceptibility organized in five classes, interpolated with the land cover maps to understand the degree of loss that can affect the rural land. This procedure was applied by assigning also a coefficient that considers the resilience of the land according to its use type.

The results carried out for the present and for future scenario are presented in **Figures 2**, **3**.

Landslide susceptibility in the Rivo catchment, as described in Pisano et al. (2017c), shows a decrease in the highest susceptibility classes, primarily linked to the transformation of pasture, bareland, and shrubland into forest and cultivated area. In fact, the highest susceptibility classes vary from 26.8% in 2007 to 25.2% in 2050.

As a first approach, we estimated the loss due to susceptibility in the year 2007. By following the approach described in section Land Value and Estimated Economic Loss and summarized with the matrix (**Table 3**) we obtained the loss of land value for the examined areas, as displayed in **Figures 2**, **4**.

In the Rivo catchment the loss values for 2007 and 2050 have been analyzed. These range from a minimum of 0, where the susceptibility is very low, to a maximum of 0.55 €/m^2. The highest loss is concentrated where the susceptibility is the highest and corresponds to the cultivated land cover class, that is indeed the most valuable. The zoomed areas reported in the figure highlight how the land cover changes according to our method play a major control on the susceptibility spatial distribution and intensity, and consequently the land price.

The results obtained show how the most affected areas are placed in the central-western sector where there is the higher landslide susceptibility. Information related to each land cover class values changes are reported in **Figure 4**. The histograms in **Figures 4**, **5** indicate for both case studies a quantification of the loss of value for land cover types after considering the susceptibility for the present and the scenario (2007/2010 real and 2050 real).

In the tables associated to the histograms (**Figures 4**, **5**) the percentage of loss is calculated as the difference between the standard value and the net land value that considers the estimated loss. The percentage values are calculated based on the total land value (1st and 3rd columns), and on the single class (2nd and 4th columns). These numbers are the results of the product of land value, susceptibility and damage coefficient. In the Rivo catchment the outcome resembles very well the fact that even under similar conditions of susceptibility, the most valuable classes (i.e., cultivated and forest) present higher loss, given by the highest economic values and higher damage index. The total loss for the study area is estimated in about 5 Mln€ for 2007 and 4.8 Mln€ for 2050 (corresponding to 10.45 and 9.90% of the total, respectively).

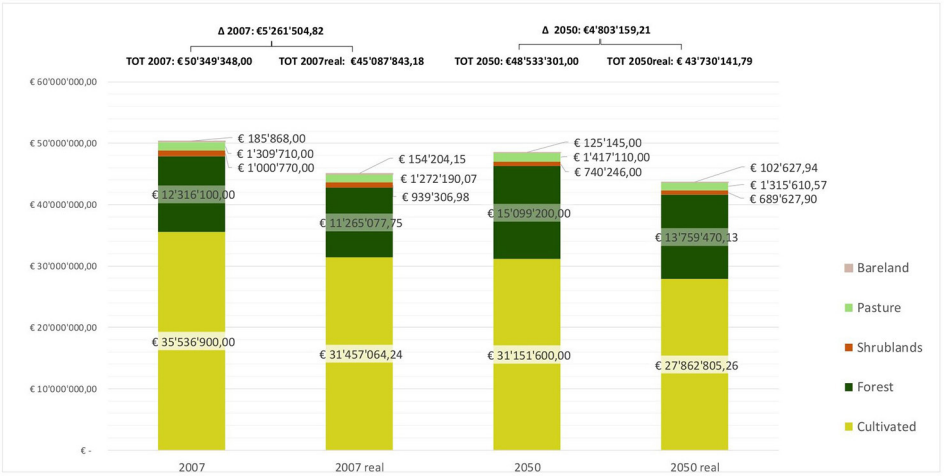

	2007		2050	
	% Loss to total	% Loss to class	% Loss to total	% Loss to class
Bareland	0,06	17,04	0,05	17,99
Pasture	0,07	2,86	0,21	7,16
Shrubland	0,12	6,14	0,10	6,84
Forest	2,09	8,53	2,76	8,87
Cultivated	8,10	11,48	6,78	10,56

FIGURE 4 | Histogram of the Rivo land monetary values for 2007 and 2050, differentiated between the official standard values and those diminished by the interaction with landslide susceptibility (real). In the bottom table the loss percentages with respect to the total area (% Loss to the total), and to the class official value (% Loss to the class) are listed.

Cultivated areas, together with barelands, are the classes giving the highest contribution to the total area land value loss, with the first one being the class with the highest value loss, followed by the forest.

The highest percentage loss for the single class due to landslide susceptibility occurs mainly in the cultivated, bareland, and forest classes. Nevertheless, the economic loss for bareland is substantially low when compared to the cultivated and forest classes. Namely, bareland losses around 30,000 € for 2007 and 20,000 € for 2050, meanwhile forest loses around 1 Mln€ for 2007 and 2050, and cultivated loses 4 Mln€ for 2007 and around 3.3 Mln€ for 2050. This is attributable to the extension of the single class in the area and even more to the initial economic value.

For the Bălăneasa catchment the susceptibility analysis was applied for the first time, even though similar applications have been run in nearby areas (Damen et al., 2014; Zumpano et al., 2014; Hussin et al., 2016; Malek et al., 2018). The resulting maps for 2010 and 2050 are presented in **Figures 3A,D**. For both years, the highest susceptibility is distributed at the contact between the Carpathians and the Subcarpathians, where we find high energy relief, with strong rock heterogeneity and deformation. At a greater detail, the spatial distribution of the most landslide prone areas is mostly controlled by the relief and in particular by slope and aspect. Further, a significant influence seems to be played by the ancient landslides deposits too, in correspondence of which the highest susceptibility classes are reported. The five susceptibility classes from very low to very high cover have, respectively for 2010 and 2050, the following areal percentages: VL 6.3–6%; L 35.4–36.9%; M 37.7–37.1%; H 16.6–16.5%; and VH 4–3.6% (cfr. diagram in **Figure 4A**). The difference in the spatial distribution and in the percentage of classes between 2010 and 2050 is attributable to the estimated changes in the land cover, namely due to the forest enlargement at the expense of cropland and pastures.

Moving to the loss due to susceptibility (**Figures 3C,F**), for both years the highest value corresponding to the highest susceptibility classes is 0.252 €/m^2. This value is concentrated where also the most valuable land cover classes such as forest and, secondarily, cultivated areas meet the highest susceptibility classes.

The histogram in **Figure 5** gives an insight about the loss in each land cover type in the two considered years, also allowing useful comparison. The total loss for year 2010 is 4.3 and 4.5 Mln€ for 2050, that correspond to the 29.6 and 29.81% with respect to the initial value.

The class giving the highest contribution to the total loss is forest (25.57%). Forest and cultivated are also the classes with the highest differences between the standard and the real value, namely 33.37 and 25.63% (highest percentage loss to the class, table in **Figure 5**), corresponding to about 3.8 Mln€ and 400,000 €, respectively.

In addition, given that cultivated areas are not widespread at the site, they contribute poorly to the total loss, contrarily to what happens with forest, even though this latter is not characterized by very high susceptibility.

For the scenario 2050, the total loss is 4.5 Mln€, and similar considerations can be drawn, given that they show similar figures.

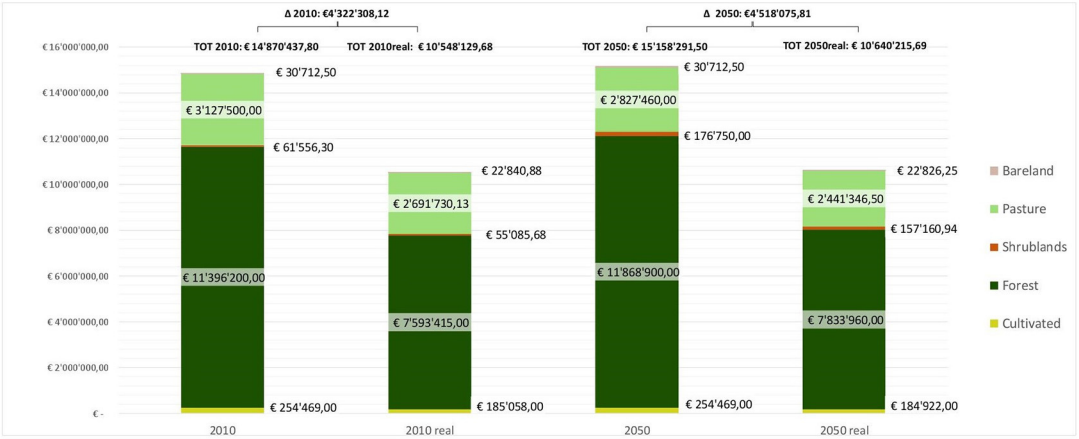

	2010		2050	
	% Loss to the total	% Loss to the class	% Loss to the total	% Loss to the class
Bareland	0,05	25,63	0,05	25,68
Pasture	2,93	13,93	2,55	13,66
Shrublands	0,04	10,51	0,13	11,08
Forest	25,57	33,37	26,62	34,00
Cultivated	0,47	27,28	0,46	27,33

FIGURE 5 | Histogram of the Bălăneasa land monetary values for 2010 and 2050 differentiated between the official standard values and those diminished by the interaction with landslide susceptibility (real). In the bottom table the loss percentages with respect to the total area (% Loss to the total), and to the class official value (% Loss to the class) are listed.

DISCUSSION AND CONCLUSION

In this work we have introduced a semi-quantitative approach applicable at the regional scale to estimate the loss of value suffered by rural lands and, in a local way and to a lesser degree, by agricultural lands due to landslide susceptibility. The approach is mostly expert-based and quantifies the susceptibility and the land resilience through indexes that, once interpolated with the land cover values, allow to estimate the loss.

We produced two sets of landslide susceptibility maps related to two time frames (2007/2010 and 2050), in order to evaluate possible values changes and trends related to land cover variations. It is known, in fact, that landslide susceptibility is influenced by land cover, which changes might determine variations in the spatial distribution of the highest landslide susceptibility classes (Vanacker et al., 2003; Wasowski et al., 2010, 2014; Promper et al., 2014; Reichenbach et al., 2014; Pisano et al., 2017b,c).

We tested our method for the evaluation of the economic loss in two different study areas placed in different countries, with different socio-economic and environmental settings.

The main findings show how land value may suffer changes due land cover variations through time, or due to landslide susceptibility that interferes with the land itself.

In particular for the Rivo catchment we observed a change in the total land value consisting in about 2 Mln€, representing 5% of the entire area land value, that is due mainly to the decrease of cultivated areas according to the modeled scenario. On the contrary, for the susceptibility the loss is estimated to be 5 Mln€ for 2007 and 4.8 Mln€ for 2050, with the highest loss values in the cultivated areas and forest. However the class with the highest percentage loss with respect to the initial class value is bareland, that is the most susceptible class in the area, even though it is the one with the lowest economical value.

In the Bălăneasa area the land cover changes observed in the trend scenario are few, with a slight increase in the economic values (+0.29 Mln€) ascribable mostly to the changes from forest to pasture. As regards the depreciation due to susceptibility there is a loss of 29.6% and 29.81% with respect to the initial total land value for 2010 and 2050, respectively. The class suffering the highest loss is forest, given that it is also the most valuable in the area; in addition, it gives the highest contribution to the total land value, due to the fact it is the main class, covering almost 45%. As for the other classes, bareland and cultivated areas are subject to high losses in 2010 and 2050, being the most susceptible classes in the area; nevertheless, they do not contribute predominantly to the total loss, as a result of their reduced areal extension, and low economic values as regards bareland.

Looking at numbers, it appears that the total losses obtained for the Italian case study are higher. Actually, these outcomes are biased by the initial land values, which are not comparable, and present higher numbers for the Rivo catchment.

The results represent a first example of the estimation of loss values in rural environments, which in the literature are often not taken into any account, since evaluation of the loss typically is focused on buildings and infrastructures. The present work ranks therefore among the very few scientific publications devoted to present a methodology aimed at evaluating this type of loss. Being a first attempt in using such an approach, it might contain some uncertainties, and could certainly be improved in the near future. However, the method has proven to be reasonable and easily applicable. The amount of data needed is acceptable and quite

easy to find, which allows an application even in contexts where the data are incomplete, or when there is the need to run a quick estimate as a pre-analysis before a following, more detailed, study. Furthermore, our approach even if simple takes in consideration both factors influencing the land values, namely the land cover variation and the landslide proneness, besides the fact it allows to estimate the potential loss before the occurrence of the landslide event.

By applying this approach, it is possible to obtain results that could be exploited for land use planning, given that landslides occurrence threatens the productive activities and hence might have a severe impact on the involved communities.

In conclusions, considering the growing attention toward global changes, especially by decision makers increasingly worried about geo-hydrological consequences (Gariano and Guzzetti, 2016), we believe that applying the method exploiting future scenarios could provide useful information for a more sound and reasonable land management in territories with high susceptibility to landslides. Using these information as a hint to plan future land uses, without excluding the possibility of occurrence of landslides, could result in a decrease of the losses of land value and land productivity. At the same time, a conscious land planning, taking into account the distribution and activity of slope movements, could in turn contribute to mitigate the risk associated to occurrence of landslide phenomena.

DATA AVAILABILITY

The raw data supporting the conclusion of this manuscript will be made available by the authors, without undue reservation, to any qualified researcher.

AUTHOR CONTRIBUTIONS

VZ, LP, MP, and PPCA were responsible for the conceptual design of the work. LP and VZ mapped the landslides for Rivo area and LP mapped the land cover for the same area. MM and VZ collected the landslide data for Bălăneasa catchment. ŽM mapped past land cover for Bălăneasa and performed all the analysis for the land cover scenario for both case studies. VZ, LP, and MP carried out calculation and data interpretation. MM and DB provided all the other information regarding the Romanian case study. VZ and LP lead writing and compilation of figures and tables. MP, ŽM, and MM contributed significantly to improve the manuscript. PPCA and CR helped in the conceptualization of the work and final overview.

FUNDING

Part of the data acquisition and elaboration were carried out in the framework of the CHANGES project (Changing Hydro-meteormological Risks—as Analyzed by a New Generation of European Scientists), a Marie Curie Initial Training Network, funded by the European Community's 7th Framework Programme FP7/2007-2013, Grant Agreement No. 263953.

SUPPLEMENTARY MATERIAL

The Supplementary Material for this article can be found online at: https://www.frontiersin.org/articles/10.3389/feart.2018.00097/full#supplementary-material

REFERENCES

Alexander, D. (1986). Landslide damage to buildings. *Environ. Geol. Water Sci.* 8, 147–151. doi: 10.1007/BF02509902

Alkema, D. (2007). *Simulating Floods; on the Application of a 2D-Flood Model for Hazard and Risk Assessment*. Ph.D. thesis, University of Utrecht, Utrecht.

Aucelli, P. P. C., Balteanu, D., Izzo, M., and Rosskopf, C. M. (2004). "Types and mechanism of slope failure due to the rainfall event on January 2003 in Molise region (S. Italy)," in *Geomorphological Environment,* eds H. S. Savindra Singh, Kr. De. Sharma, and Sunil (Kolkata: ACB Publications), 125–142.

Aucelli, P. P. C., Cinque, A., and Rosskopf, C. M. (2001). Geomorphological map of the Trigno basin (Italy): explanatory notes. *Geografia Fisica e Dinamica Quaternaria* 24, 3–12.

Aucelli, P. P. C., Robustelli, G., Rosskopf, C. M., Scarciglia, F., Di Paola, G., and Luc,á, F. (2010). Geomorphological map of the area between Frosolone and Trivento (Molise, Italy). *J. Maps* 6, 423–434. doi: 10.4113/jom.2010.1039

Boerboom, L. G. J., and Alan, Ö. O. (2012). Implementation, challenges and future directions of integrating services from the gis and decision science domains: a case of distributed spatial multi-criteria evaluation. *OSGeo J.* 10, 49–54.

Borgomeo, E., Hebditch, K. V., Whittaker, A. C., and Lonergan, L. (2014). Characterising the spatial distribution, frequency and geomorphic controls on landslide occurrence, Molise, Italy. *Geomorphology* 226, 148–161. doi: 10.1016/j.geomorph.2014.08.004

Calò, F., Calcaterra, D., Iodice, A., Parise, M., and Ramondini, M. (2012). Assessing the activity of a large landslide in southern Italy by ground-monitoring and SAR interferometric techniques. *Int. J. Remote Sens.* 33, 3512–3530. doi: 10.1080/01431161.2011.630331

Calcaterra, D., Ramondini, M., Cal,ò, F., Longobardi, V., Parise, M., and Galzerano, C. M. (2008). "DInSAR techniques for monitoring slow-moving landslides. in Landslides and Engineered Slopes," in *Proceedings of the 10th International Symposium on Landslides,* eds Z. Cheng, J. Zhang, Z. Li, F. Wu, and K. Ho (Xi'an), 1095–1101.

Chiocchio, C., Iovine, G., and Parise, M. (1997). "A proposal for surveying and classifying landslide damage to buildings in urban areas," in *Proceedings of the 10th International Symposium on Engineering Geology and the Environment* (Athens) 23–27.

Damen, M., Micu, M., Zumpano, V., van Westen, C. J., Sijmons, K., and Balteanu, D. (2014). "Landslide mapping and interpretation: implications for landslide susceptibility analysis in discontinuous data environment," in *Proceedings of the International Conference Analysis and Management of Changing Risks for Natural Hazards* (Padua), 18–19.

Del Soldato, M., Bianchini, S., Calcaterra, D., De Vita, P., Di Martire, D., Tomás, R., et al. (2017). A new approach for landslide-induced damage assessment. *Geomat. Nat. Hazards Risk* 8, 1524–1537. doi: 10.1080/19475705.2017.1347896

Donnini, M., Napolitano, E., Salvati, P., Ardizzone, F., Bucci, F., Fiorucci, F., et al. (2017). Impact of event landslides on road networks: a statistical analysis of two Italian case studies. *Landslides* 14, 1521–1535. doi: 10.1007/s10346-017-0829-4

Fiorillo, F., Parise, M., and Wasowski, J. (1996). "Slope instability in the Bisaccia area (Southern Apennines, Italy)," in *Proceedings of the 7th International Symposium on Landslides* (Trondheim), 965–970.

Fleming, R. W., and Taylor, F. A. (1980). *Estimating the Costs of Landslide Damage in the United States*. U.S. Geol. Surv. Circ. 832:21.

Gariano, S. L., and Guzzetti, F. (2016). Landslides in a changing climate. *Earth Sci. Rev.* 162, 227–252. doi: 10.1016/j.earscirev.2016.08.011

Gariano, S. L., Petrucci, O., Rianna, G., Santini, M., and Guzzetti, F. (2018). Impacts of past and future land changes on landslides in southern Italy. *Reg. Environ. Chang.* 18, 437–449. doi: 10.1007/s10113-017-1210-9

Global Assessment Report on Disaster Risk Reduction (GAR) (2015). *United Nations Office for Disaster Risk Reduction* (UNISDR). Available online at: https://www.unisdr.org/we/inform/gar

Godt, J. W., Coe, J. A., and Savage, W. Z. (2000). "Relation between cost of damaging landslides and construction age, El Niño winter storm season, 1997-98," in *Proceedings of the 8th International Symposium on Landslides* (Alameda County, CA), 26–30.

Hussin, H. Y., Zumpano, V., Reichenbach, P., Sterlacchini, S., Micu, M., van Westen, C., et al. (2016). Different landslide sampling strategies in a grid-based bi-variate statistical susceptibility model. *Geomorphology* 253, 508–523. doi: 10.1016/j.geomorph.2015.10.030

Intergovernmental Panel on Climate Change (IPCC) (2012). "Summary for policymakers: managing the risks of extreme events and disasters to advance climate change adaptation," in *A Special Report of Working Groups I and II of the Intergovernmental Panel on Climate Change,* eds C. B. Field, V. Barros, T. F. Stocker, D. Qin, D. J. Dokken, K. L. Ebi, M. D. Mastrandrea, K. J. Mach, G.-K. Plattner, S. K. Allen, M. Tignor, and P. M. Midgley (Cambridge, UK; New York, NY: Cambridge University Press)

Iovine, G., and Parise, M. (2002). Schema classificativo per il rilievo dei danni da frana in aree urbane. *Mem. Soc. Geol. Ital.* 57, 595–603.

Kreibich, H., van den Bergh, J. C. J. M., Bouwer, L. M., Bubeck, P., Ciavola, P., Green, C., et al. (2014). Costing natural hazards. *Nat. Clim. Chang.* 4, 303–306. doi: 10.1038/nclimate2182

Lesk, C., Rowhani, P., and Ramankutty, N. (2016). Influence of extreme weather disasters on global crop production. *Nature* 529, 84–87. doi: 10.1038/nature16467

Malek, Ž., Scolobig, A., and Schröter, D. (2014). Understanding land cover changes in the Italian Alps and Romanian Carpathians combining remote sensing and stakeholder interviews. *Land* 3, 52–73. doi: 10.3390/land3010052

Malek, Ž., Zumpano, V., and Hussin, H. (2018). Forest management and future changes to ecosystem services in the Romanian Carpathians. *Environ. Dev. Sustain.* 20, 1275–1291. doi: 10.1007/s10668-017-9938-4

Malek, Ž., Zumpano, V., Schröter, D., Glade, T., Balteanu, D., and Micu, M. (2015). "Scenarios of land cover change and landslide susceptibility: an example from the Buzau Subcarpathians, Romania," in *Engineering Geology for Society and Territory Vol 5,* eds G. Lollino, A. Manconi, F. Guzzetti, M. Culshaw, P. Bobrowsky, and F. Luino (Switzerland: Springer International Publishing), 743–746.

Mela, G., Longhitano, D., and Povellato, A. (2012). "The evolution of land values in italy. does the influence of agricultural prices really matter ?" in *123rd Eaae Seminar - Price Volatility and Farm Income Stabilisation: Modelling Outcomes and Assessing Market and Policy Based Responses* (Dublin). Available online at: http://purl.umn.edu/122479

Micu, M. (2008). *Landslide Hazard Assessment in the Subcarpathians Between Teleajen and Buzau Rivers*. Ph.D Thesis, Institute of Geography, Bucharest.

Micu, M., Jurchescu, M., Micu, D., Zarea, R., Zumpano, V., and Bălteanu, D. (2014). A morphogenetic insight into a multi-hazard analysis: Bâsca Mare landslide dam. *Landslides* 11, 1131–1139. doi: 10.1007/s10346-014-0519-4

Parise, M., Vennari, C., Guzzetti, F., Marchesini, I., and Salvati, P. (2013). Preliminary outcomes from a catalogue of natural and anthropogenic sinkholes in Italy, and analysis of the related damage. *Rendiconti Online della Società Geologica Italiana* 24, 225–227. doi: 10.1038/504196a

Parise, M., and Wasowski, J. (1999). Landslide activity maps for the evaluation of landslide hazard: three case studies from Southern Italy. *Nat. Hazards* 20, 159–183. doi: 10.1023/A:1008045127240

Persichillo, M. G., Bordoni, M., and Meisina, C. (2017). The role of land use changes in the distribution of shallow landslides. *Sci. Total Environ.* 574, 924–937. doi: 10.1016/j.scitotenv.2016.09.125

Petley, D. (2012). Global patterns of loss of life from landslides. *Geology* 40, 927–930. doi: 10.1130/G33217.1

Pisano, L., Zumpano, V., Dragone, V., and Parise, M. (2017a). "Built-up area exposure to landslides and related social impacts in Molise (Italy) - advancing culture of Living with Landslides," in *Advances in Landslide Science Vol 2*, eds M. Mikos, B. Tiwari, Y. Yin, and K. Sassa (Cham: Springer International Publishing), 837–845.

Pisano, L., Zumpano, V., Malek, Ž., Micu, M., Rosskopf, C. M., and Parise, M. (2017b). "Multi-temporal landslide susceptibility maps and future scenarios for expected land cover changes (Southern Apennines, Italy) - advancing culture of living with landslides: *Vol 5*," in *Landslides in Different Environments,* eds M. Mikoš, V. Vilímek,Y. Yin, and K. Sassa (Cham: Springer International Publishing), 379–387.

Pisano, L., Zumpano, V., Malek, Ž., Rosskopf, C. M., and Parise, M. (2017c). Variations in the susceptibility to landslides, as a consequence of land cover changes: a look to the past, and another towards the future. *Sci. Total Environ.* 601, 1147–1159. doi: 10.1016/j.scitotenv.2017.05.231

Pourghasemi, H. R.,Moradi, H. R., Fatemi Aghda, S. M., Gokceoglu, C., and Pradhan, B. (2014). GIS based landslide susceptibility mapping with probabilistic likelihood ratio and spatial multi-criteria evaluation models (North of Tehran, Iran). *Arab. J. Geosci.* 7, 1857–1878. doi: 10.1007/s12517-012-0825-x

Pradhan, B., and Lee, S. (2010). Delineation of landslide hazard areas on Penang Island, Malaysia, by using frequency ratio, logistic regression, and artificial neural network models. *Environ. Earth Sci.* 60, 1037–1054. doi: 10.1007/s12665-009-0245-8

Promper, C., and Glade, T. (2016). Multilayer-exposure maps as a basis for a regional vulnerability assessment for landslides: applied in Waidhofen/Ybbs, Austria. *Nat. Hazards* 82, 111–127. doi: 10.1007/s11069-016-2311-3

Promper, C., Puissant, A., Malet, J.-P., and Glade, T. (2014). Analysis of land cover changes in the past and the future as contribution to landslide risk scenarios. *Appl. Geogr.* 53, 11–19. doi: 10.1016/j.apgeog.2014.05.020

Reichenbach, P., Busca, C., Mondini, A. C., and Rossi, M. (2014). The influence of land use change on landslide susceptibility zonation: the briga catchment test site (Messina, Italy). *Environ. Manage.* 54, 1372–1384. doi: 10.1007/s00267-014-0357-0

Rosskopf, C. M., and Aucelli, P. P. C. (2007). "Analisi del dissesto da frana in Molise," in *Rapporto Sulle Frane in Italia. Il Progetto IFFI–Metodologia, Risultati e Rapporti Regionali 78*, ed A. Trigila (Rapporti APAT), 493–508.

Salvati, P., Petrucci, O., Rossi, M., Bianchi, C., Pasqua, A. A., and Guzzetti, F. (2018). Gender, age and circumstances analysis of flood and landslide fatalities in Italy. *Sci. Total Environ.* 610–611, 867–879. doi: 10.1016/j.scitotenv.2017.08.064

Schmaltz, E. M., Steger, S., and Glade, T. (2017). The influence of forest cover on landslide occurrence explored with spatio-temporal information. *Geomorphology* 290, 250–264. doi: 10.1016/j.geomorph.2017.04.024

Schuster, R. L. (1996). "Socio-economic significance of landslides," in *Landslides Investigation and Mitigation: Transportation Research Board*, Vol. 247, eds A. K. Turner and R. L. Schuster (Washington, DC: National Academy Press), 12–35.

Schuster, R. L., and Fleming, R. W. (1986). Economic losses and fatalities due to landslides. *Bull. Ass. Eng. Geol.* 23, 11–28. doi: 10.2113/gseegeosci.xxiii.1.11

Sgrosso, I., and Naso, G. (2012). *Note Illustrative del Foglio 393 "Trivento" della Carta Geologica d'Italia alla scala 1:50000*. Roma: ISPRA.

Soares-Filho, B. S., Coutinho Cerqueira, G., and Lopes Pennachin, C. (2002). DINAMICA - a stochastic cellular automata model designed to simulate the landscape dynamics in an Amazonian colonization. *Front. Ecol. Model.* 154, 217–235. doi: 10.1016/S0304-3800(02)00059-5

Tanoue, M., Hirabayashi, Y., and Ikeuchi, H. (2016). Global-scale river flood vulnerability in the last 50 years. *Sci. Rep.* 6:36021. doi: 10.1038/srep36021

Vanacker, V., Vanderschaeghe, M., Govers, G., Willems, E., Poesen, J., Deckers, J., et al. (2003). Linking hydrological, infinite slope stability and land-use change models through GIS for assessing the impact of deforestation on slope stability in high Andean watersheds. *Geomorphology* 52, 299–315. doi: 10.1016/S0169-555X(02)00263-5

van Vliet, J., de Groot, H. L., Rietveld, P., and Verburg, P. H. (2015). Manifestations and underlying drivers of agricultural land use change in Europe. *Landsc. Urban Plan.* 133, 24–36. doi: 10.1016/j.landurbplan.2014.09.001

Van Westen, C. J., Asch, T. W. J., and Soeters, R. (2006). Landslide hazard and risk zonation—why is it still so difficult? *Bull. Eng. Geol. Environ.* 65, 167–184. doi: 10.1007/s10064-005-0023-0

Vennari, C., Santangelo, N., Santo, A., and Parise, M. (2015). A database on flood and debris-flow processes in alluvial fans: a preliminary analysis aimed at evaluation of the damage. *Geophys. Res. Abstracts* 17, 528.

Vennari, C., Santangelo, N., Santo, A., and Parise, M. (2016). A database on flash flood events in Campania, southern Italy, with an evaluation of their

spatial and temporal distribution. *Nat. Hazards Earth Syst. Sci.* 16, 2485–2500. doi: 10.5194/nhess-16-2485-2016

Vranken, L., Van Turnhout, P., Van Den Eeckhaut, M., Vandekerckhove, L., and Poesen, J. (2013). Economic valuation of landslide damage in hilly regions: a case study from Flanders, Belgium. *Sci. Total Environ*. 447, 323–336. doi: 10.1016/j.scitotenv.2013.01.025

Ward, P. J., Jongman, B., Weiland, F. S., Bouwman, A., Van Beek, R., Bierkens, M. F. P., et al. (2013). Assessing flood risk at the global scale: model setup, results, and sensitivity. *Environ. Res. Lett*. 8, 1–10. doi: 10.1088/1748-9326/8/4/044019

Wasowski, J., Lagreca, M. D., and Lamanna, C. (2014). "Land-use change and shallow landsliding: a case history from the Apennine Mountains, Italy," in *Landslide Science for a Safer Geoenvironment, The International Programme on Landslides (IPL) Vol. 1*. eds K. Sassa, P. Canuti, Y. Yin (Cham, Springer International Publishing), 267–272.

Wasowski, J., Lamanna, C., and Casarano, D. (2010). Influence of land-use change and precipitation patterns on landslide activity in the Daunia Apennines, Italy. *Q. J. Eng. Geol. Hydrogeol.* 43, 387–401. doi: 10.1144/1470-9236/08-101

World Meterological Organization (WMO) (2014). *Atlas of Mortality and Economic Losses from Weather, Climate and Water Extremes* (1970–2012). World Meterological Organization.

Yalcin, A., Reis, S., Aydinoglu, A. C., and Yomralioglu, T. (2011). A GIS-based comparative study of frequency ratio, analytical hierarchy process, bivariate statistics and logistics regression methods for landslide susceptibility mapping in Trabzon, NE Turkey. *Catena* 85, 274–287. doi: 10.1016/j.catena.2011.01.014

Zêzere, J. L., Garcia, R. A. C., Oliveira, S. C., and Reis, E. (2008). Probabilistic landslide risk analysis considering direct costs in the area north of Lisbon (Portugal). *Geomorphology* 94, 467–495. doi: 10.1016/j.geomorph.2006.10.040

Zumpano, V., Hussin, H. Y., Reichenbach, P., Balteanu, D., Micu, M., and Sterlacchini, S. (2014). A landslide susceptibility analysis for Buzău County, Romania. *Rom. J. Geogr. Roum. Geogr*. 58, 9–16.

Conflict of Interest Statement: The authors declare that the research was conducted in the absence of any commercial or financial relationships that could be construed as a potential conflict of interest.

frontiers in Earth Science

ORIGINAL RESEARCH
published: 08 June 2018
doi: 10.3389/feart.2018.00063

Analysis of Increasing Flash Flood Frequency in the Densely Urbanized Coastline of the Campi Flegrei Volcanic Area, Italy

Giuseppe Esposito[1], *Fabio Matano*[1]* *and Germana Scepi*[2]

[1] *Consiglio Nazionale delle Ricerche, Istituto Ambiente Marino Costiero, Naples, Italy,* [2] *Dipartimento di Scienze Economiche e Statistiche, Università degli Studi di Napoli Federico II, Naples, Italy*

Climate change is affecting the frequency and severity of extreme meteorological and geo-hydrological events hitting the coastal zone of the Campi Flegrei volcanic district (southern Italy), which is prone to a wide spectrum of natural hazards, including volcanism, earthquakes, ground deformation, flash floods, landslides, and coastal erosion. This study documents the trend of flash floods affecting the town of Pozzuoli, located along the coastline of the Campi Flegrei volcanic area, during the 1970–2014 time period. An archive research together with the collection of data published on news websites and social media allowed understanding of the triggering and evolution mechanisms of flash floods in the area, as well as the most recurrent damages. Rainfall data collected by the rain gauge located within the Pozzuoli watershed were also analyzed. Results of this study show an increased frequency of flash flood events occurred in the study area. The variation in flash flood frequency is likely not related to urbanization changes, as no increase of the urban area occurred after the year 2000. The observed increase of flash flood events in recent years (2000–2014) can be reasonably ascribed to variations in the rainfall regime. Our research provides a contribution for the understanding of flash flood processes in the study area as well as relevant information for hazard and risk assessment.

Keywords: climate change, flash flood, extreme precipitations, Pozzuoli, Italy

OPEN ACCESS

Edited by:
Davide Tiranti,
Agenzia Regionale per la Protezione Ambientale (ARPA), Italy

Reviewed by:
Nadia Solovieva,
University College London, United Kingdom
Manolis G. Grillakis,
Technical University of Crete, Greece

***Correspondence:**
Fabio Matano
fabio.matano@cnr.it

Specialty section:
This article was submitted to Quaternary Science, Geomorphology and Paleoenvironment, a section of the journal Frontiers in Earth Science

Received: *29 January 2018*
Accepted: *11 May 2018*
Published: *08 June 2018*

Citation:
Esposito G, Matano F and Scepi G (2018) Analysis of Increasing Flash Flood Frequency in the Densely Urbanized Coastline of the Campi Flegrei Volcanic Area, Italy. Front. Earth Sci. 6:63. doi: 10.3389/feart.2018.00063

INTRODUCTION

Changes in extreme weather and climate events, including an increase in warm temperature extremes and an increase in the number of heavy precipitation events, have been observed since about 1950 in many regions worldwide (IPCC, 2014). Specifically, changes in precipitation regimes are modifying the magnitude, frequency, and timing of floods at both regional and local scales. Blöschl et al. (2017), for example, evaluated a shift in the timing of river floods in Europe, during the past 50 years, as well as Diakakis (2014) observed in recent decades an increase in flood frequency associated with increases in extreme daily precipitation around Athens (Greece).

Extreme floods and flash floods are the most frequent and among the costliest and deadliest natural disasters worldwide (Gaume et al., 2016). In the Mediterranean area, coastal sectors of the central-western countries (e.g., France, Italy, Spain) result the most exposed to high impact and high magnitude events because of climatic and topographic conditions (Llasat et al., 2010; Tarolli et al., 2012; Gaume et al., 2016). Here, floods result frequently in fatalities and significant economic losses due to the high concentration of urban settlements and population.

The Italian coasts were recurrently affected by flash floods in the last years, especially during the late summer-autumn period. The latest event occurred on September 10, 2017 and hit the urban area of Livorno, a port city located along the Tuscan coastline. Such event was triggered by a quasi-stationary mesoscale convective system (MCS) characterized by a V-shaped plume, which released about 230 mm of rain in 3 h (Regione Toscana, 2017). During this flood, eight people died. Previously, other deadly events affected urban areas widespread along the Italian coasts, such as the major flash floods occurred in 2000 in Calabria (13 deaths—Federico et al., 2003; Montani et al., 2003), 2009 in Siciliy (38 deaths—Aronica et al., 2012), 2011 in Tuscany and Liguria (19 deaths—Cevasco et al., 2012; Silvestro et al., 2012; Faccini et al., 2015). These and other events, also affecting inland areas of Italy, may be correlated with a general tendency toward a decrease in the number of rainy days, and an increase in the frequency of high-intensity precipitation events. According to Brunetti et al. (2004), these trends were observed since the end of the nineteenth century and resulted amplified in the last decades.

Ducrocq et al. (2014) mostly relate the occurrence of heavy precipitation events in the Mediterranean region to the MCSs development. Most of these systems occur in the autumn season (September to November), when the Mediterranean Sea is still relatively warm with high evaporation rates (Mariotti et al., 2002). The warm sea surface temperatures increase air-sea surface heat fluxes, which in turn moisten and destabilize the marine atmospheric boundary layer (Ducrocq et al., 2014). The warm and moist low-level air flows that impact with reliefs surrounding the Mediterranean Sea are then uplifted, initiating a cycle of condensation and convection processes that can be renewed at the same location for hours, as long as the flux of low-level moisture remains intact (Ducrocq et al., 2014). In addition, flash floods can be also triggered by short-lived convective cells with a limited areal extent (typically <100 km^2), or by occasional heavy rainfall developing within large-scale perturbations lasting several days (Gaume et al., 2016).

Location and magnitude of flash floods are influenced by rainfall properties (i.e., spatial extent, duration, intensity), as well as by topography, land use, soil types, and the initial soil moisture content of the affected watersheds (Hapuarachchi et al., 2011). In many regions, natural watersheds underwent massive urbanization associated to strong modification of local drainage patterns. The permeable soils were replaced with impermeable surfaces such as roads, roofs, parking lots, and sidewalks, reducing infiltration of water into the ground and accelerating the runoff rates (Konrad, 2003). These modifications increased both likelihood of flash floods and risk conditions. In spite of this, people living in flood or landslide prone areas are expected to increase in the coming years because of population growth and urban development (United Nations, 2011). On the other side, the globally averaged surface temperature is also projected to rise over the twenty-first century under all assessed emission scenarios (IPCC, 2014). For these reasons, it is very likely that the climate change-related effects, such as extreme floods, flash floods, and rapid-moving landslides (e.g., soil slips, debris flows, rock falls) will occur more often, potentially leading to loss of human life and economic damages.

In this work, we have analyzed the historical frequency of flash flood events affecting the urban area of Pozzuoli, a densely populated town located near Naples in southern Italy (**Figure 1**). In a previous paper (Esposito et al., 2015), we described the flash flood event that hit the Pozzuoli town on November 6, 2011, by analyzing meteorological conditions, rainfall properties, ground effects and results obtained by simulating the flow propagation. The new research presented in this paper is aimed at verifying the eventual increase of flash flood events in the 1970–2014 time interval and related causes, as well as at characterizing the flash flood-triggering rainfall properties. The work wants also give a valuable contribution to the more wide research topic concerning the identification of an increasing trend in the frequency of extreme floods in the central Mediterranean region under the current climate change scenario.

THE POZZUOLI STUDY AREA

Pozzuoli is the most important town of the Campi Flegrei volcanic area, located in the western sector of the wide urban area of Naples (Italy). Very important roman monuments such as amphitheater Flavius and Temple of Serapis are present in the historical town center of Pozzuoli. More than 81,000 people inhabit this territory, with a population density of about 1,800 inhabitants per square kilometer. The town center is located along the coastline, and spreads out over the surface of four volcanic edifices formed during the past explosive activity of the still active Campi Flegrei caldera (e.g., Di Vito et al., 1999): Astroni, Cigliano, Gauro, and Solfatara (**Figure 1**). These cones extend from the sea level to an altitude of 325 m a.s.l. Since historical times, slope instability processes including shallow landslides and rock falls involved the volcanic slopes, as well as sediment-laden flows (hyperconcentrated flows and streamflows - Pierson and Costa, 1987), affected the drainage network near the coastline. Nevertheless, only a few studies related to geo-hydrological events in the whole Campi Flegrei area have been made in relatively recent years (e.g., Beneduce et al., 1988; Calcaterra et al., 2003; Di Martire et al., 2012), given that the scientific community dedicated more interest toward volcanic and seismic processes.

The flash flood hazard in the urban area of Pozzuoli have been analyzed in a previous work (Esposito et al., 2015). Authors evaluated in 360 ha the extent of the partially-urbanized watershed involved by flash floods, and in 18.6° its average slope angle, reaching values of about 70° within the drainage channels located in its central zone. The geological framework is characterized by welded pyroclastic rocks like tuff and

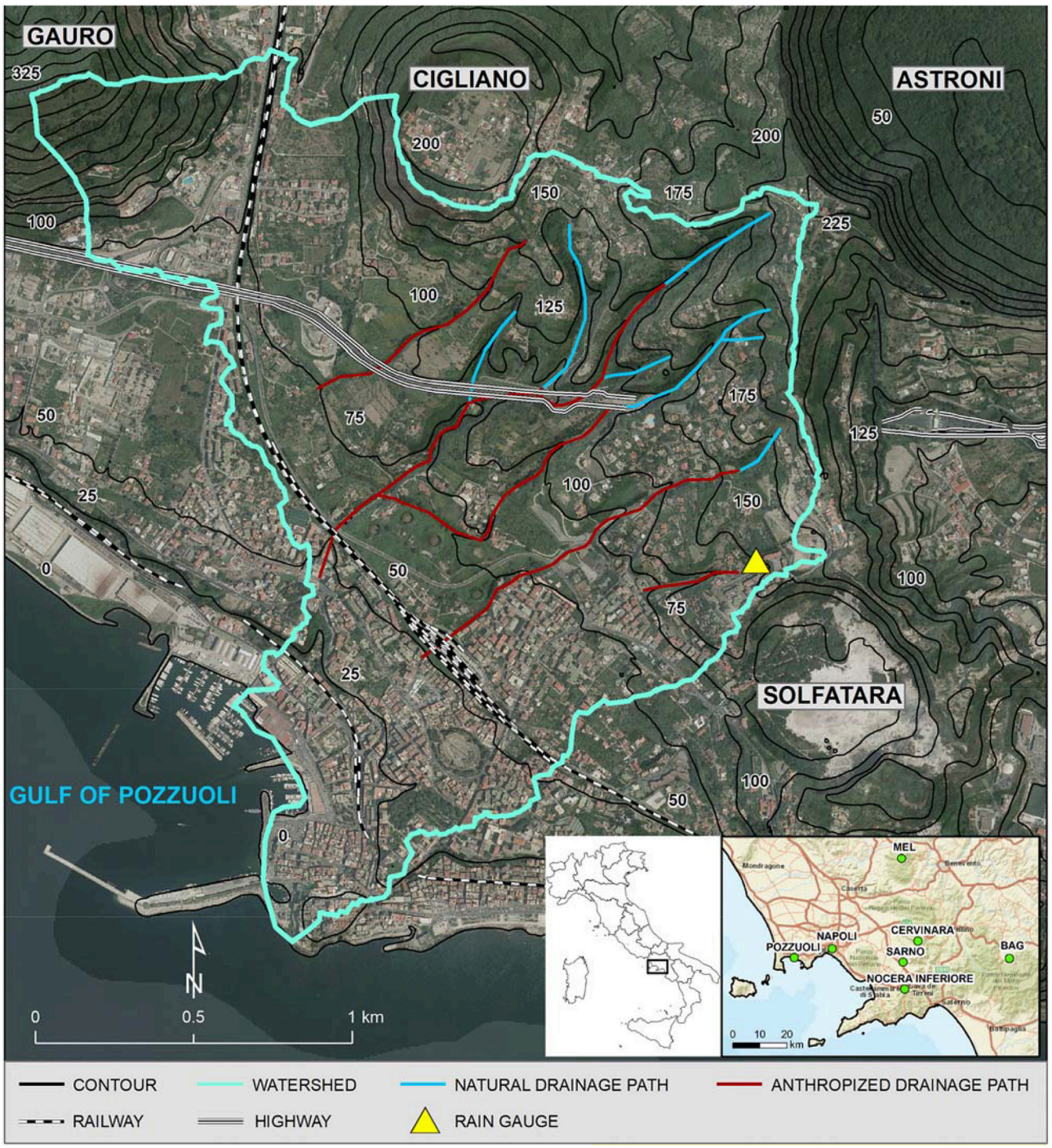

FIGURE 1 | Aerial view and location of the Pozzuoli town within the Campania Region, southern Italy. The most important infrastructures and position of the rain gauge are also indicated. The contour interval is 25 m.

ignimbrite, and locally by lava domes/flows. Such lithologies are often mantled by incoherent primary volcaniclastic deposits constituted by ashes, scoria, and pumices, and by reworked pyroclastics and colluvial soils, together with alluvial deposits derived from the water-driven surface erosion of the slopes. The climatic setting is of Mediterranean type, with hot, dry summers and moderately cool rainy winters. Mean annual temperatures are in the order of 16°C and the mean annual rainfall is of ca. 875 mm. The most intense rainy period is between October and December, when heavy rainfall occur (**Figure 2**).

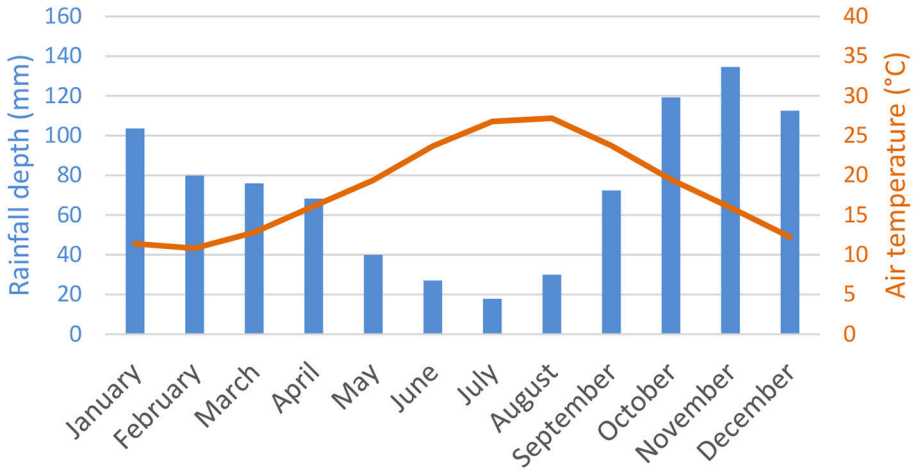

FIGURE 2 | Average monthly rainfalls and temperatures related to the Pozzuoli area for the 1970–2014 time period.

The rain regime in this part of Italy is characterized by typical rainfall patterns, among frontal rainfalls, hurricane-like rainfalls or isolated convective storms (De Luca et al., 2010). The seasonal effects of rainfall on shallow deposits and unsaturated pyroclastic soils have been studied in Cascini et al. (2014). A typical trend of soil suction is characterized by very high values (>30 kPa) from June to August due to the intense sun radiation, high values from September to October (20–30 kPa), intermediate value (10–20 kPa) in November and December, and the lowest values of soil suction (<10 kPa) from January to May (Cascini et al., 2014). No direct measurements of soil moisture were available for the pyroclastic soils outcropping in the study area. Some relative soil moisture data for a 5 cm layer in pyroclastic soils, measured at Bagnoli and Melizzano sites (see BAG and MEL in the inset of **Figure 1**), show high values during winter to spring rainy periods and very low values during summer dry periods (Brocca et al., 2011; Dorigo et al., 2011). Relationships between soil suction data and soil volumetric water content have been studied in several sites characterized by unsaturated pyroclastic soils in Campania region, such as the slopes near Cervinara (Greco et al., 2013), Nocera Inferiore (De Chiara et al., 2016), and Sarno (De Vita et al., 2013; Napolitano et al., 2016) (inset in **Figure 1**), showing opposite trends. Generally, such soils can be affected by erosion phenomena at the end of the dry season (August to October), during intense rainstorms, with a consequent triggering of flash flood events dominated by hyperconcentrated flows (Cascini et al., 2014; Vennari et al., 2016).

MATERIALS AND METHODS

In order to characterize the flash flood-triggering rainfalls and precipitation regime, in this study we have analyzed the rainfall data collected by a rain gauge located within the Pozzuoli watershed (**Figure 1**). Given its location, this was able to capture representative flash flood-triggering rainfall data reported in the Results section. Since 1970 and up to 1999, this rain gauge was included in the national network of the Italian Hydrographical Service, regularly reporting only daily rainfall values. In the year 2000, the rain gauge was included in the real-time hydrological monitoring network of the Campania Regional Agency of Civil Protection, and was set for collecting rain data every 10 min. For this reason, the rainfall dataset used in this study consists of two subsets. The first subset includes daily rainfalls related to the 1970–1999 time interval, that were extracted from Hydrological Annals—Part I, available on the Institute for environmental Protection and Research (ISPRA) website (http://www.acq.isprambiente.it/annalipdf/). The second dataset includes rainfall data collected in the 2000–2014 time interval with a temporal resolution of 10 min, which were supplied by the Campania Regional Agency of Civil Protection (http://centrofunzionale.regione.campania.it/). Analysis of the frequency distribution of daily rainfall values with respect to different thresholds allowed characterizing the rainfall regime of the study area, as well as addressing identification of the occurred flash flood events.

A first list of flash flood events hitting the Pozzuoli urban center, obtained from previous scientific studies and inventories, such as AVI (Aree Vulnerate in Italia) (Guzzetti et al., 1994) and SICI (Sistema Informativo Catastrofi Idrogeologiche) databases (http://sici.irpi.cnr.it/gndci.htm), as well as from local news websites, was presented in the previous work of Esposito et al. (2015). In order to obtain an updated and complete list of flash flood events occurred in the 1970–2014 time interval, it was performed an archive research at the National Library of Naples. Here, information related to flash flood events (rainfall qualitative data, description of damages, photos, etc.) were collected from the most relevant local newspaper (namely "Il Mattino"), edited in Naples since 1892.

In order to address the archive research by avoiding time wasting efforts, we selected an arbitrary daily rainfall threshold of 40 mm that allowed us to identify rainy days with high probability of flash flood occurrence. This kind of threshold corresponded to the lowest value of daily rainfall measured in a day for a flash

flood event occurred in 2009, as reported in Esposito et al. (2015). Our assumption was hence that all events of the first subset should be occurred in days characterized by cumulated rainfall amounts equal or higher than 40 mm. At the same time, we verified if such amount was reached or exceeded at the turn of two consecutive days, also to include potential rainstorms occurred between midnights. In this way, we selected a series of dates that were investigated through the historical archive research. With the aim of identifying all the occurred flood events, we addressed the archive research by visually checking also the newspaper editions related to a brief period (2–3 days) after the day characterized by high probability of flash flood occurrence. After this, in order to avoid data gaps and verify effectiveness of the adopted threshold, we expanded the archive research by checking days characterized by cumulated rainfall amounts higher than 30 mm. An accuracy analysis aimed at validating the used threshold and at verifying relationships between a series of other thresholds and occurrence of flash flood events was then performed.

Supplementary data for the more recent events were collected from web sources, including news websites and social networks. It is worth noting that, in order to avoid an information bias toward the last decade when reports from web sources were widespread, identification of the flash flood events was primarily obtained by means of the archive research, and supplementary materials were only used for better characterizing the magnitude of processes, affected zones, and consequent damages from a qualitative point of view. After the identification of flash flood events, the effective daily rainfall and, when available, other properties, such as maximum 1-h rainfall and 10-min peak storm intensity, were collected. Both flash flood and rainfall data were finally elaborated and represented by means of specific plots, aimed at highlighting related behaviors.

A comparison performed in GIS environment between the 1:10,000 topographic map of the study watershed, dated 1965 and available on the Città Metropolitana di Napoli website (http://sit.cittametropolitana.na.it/), and orthophotos related to the years 2000 and 2012, available on the National Geospatial archive of the Italian Ministry for the Environment (www.pcn.minambiente.it/mattm/), allowed quantifying the urban growth occurred through the considered time spans.

RESULTS

Daily Rainfall Regime

The rainfall dataset analyzed in this study is related to the period between January 1970 and December 2014, and includes 13,078 daily rainfall measurements. The first subset (1970–1999, 30 years) encompasses 7,891 days of measurements, while the second subset (2000–2014, 15 years) encompasses 5,187 days. Data related to some years (i.e., years 1972–1974, 1991–1996, 2000) were not included in the analysis because daily rainfall measurements were discontinuous.

The cumulated annual rain time series shows a clear variability around an average value of 875 mm/year (**Figure 3**), and stronger oscillations can be observed during the 1970–1990 period.

The daily rain time series (**Figure 4**) does not show a particular statistical trend, but it is characterized by both seasonal and monthly fluctuations, as well as by several daily peaks also higher than 100 mm. Specifically, it can be noted that daily peaks are more frequent but less severe during the 1970–1999 time interval, and are less frequent but more severe during the 2000–2014 (**Figure 4**).

Analysis of the frequency distribution of daily rainfall values is represented with respect to classes defined according to different rain thresholds (**Table 1**), by using a bi-logarithmic diagram (**Figure 5**). The two analyzed datasets do not show important

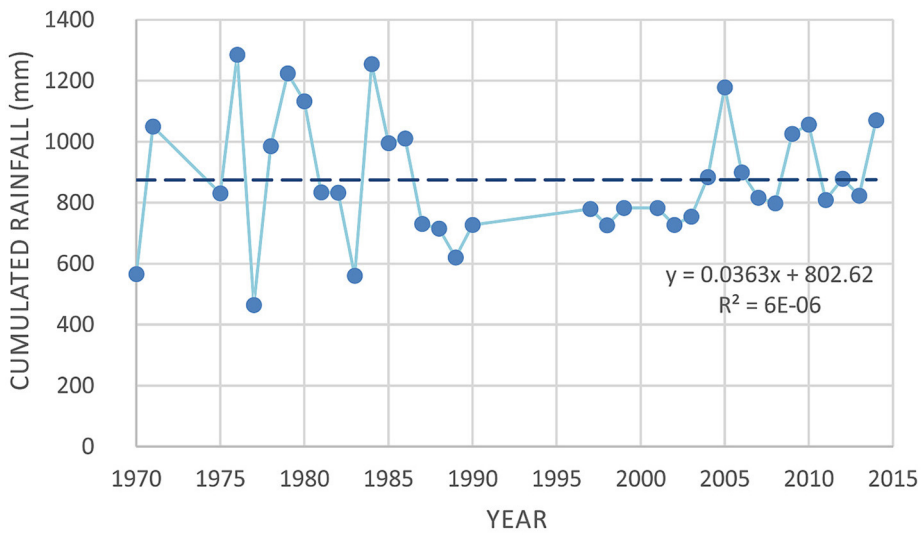

FIGURE 3 | Cumulated annual rain at the Pozzuoli rain gauge.

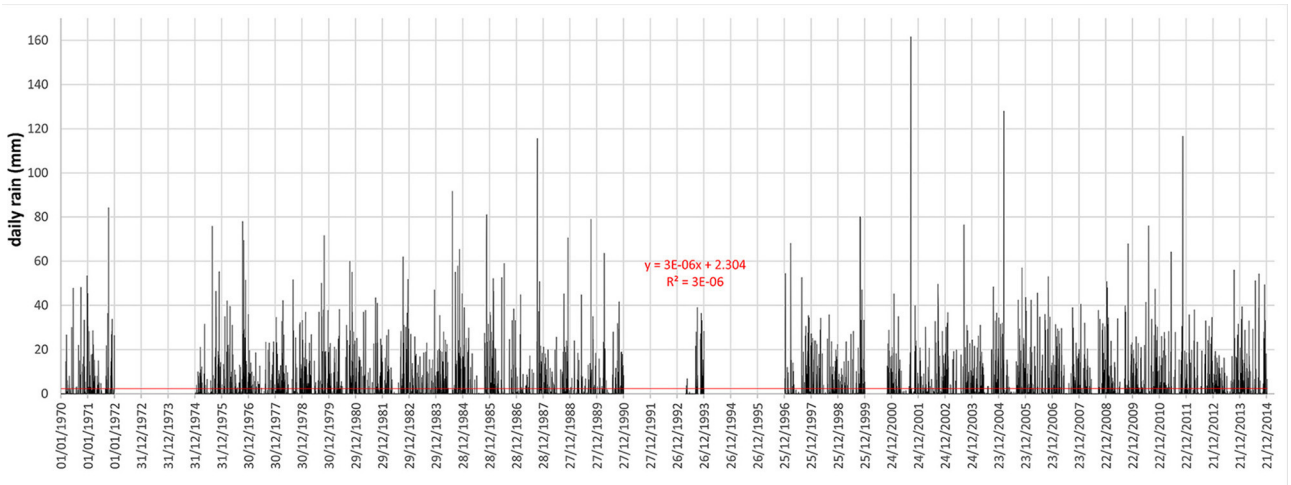

FIGURE 4 | Daily rain time series measured by the Pozzuoli rain gauge.

TABLE 1 | Distribution of daily measurements for different daily rainfall classes.

Class	Daily rain threshold (mm)	Cumulate number (1970–2014)	Cumulated frequency (1970–2014)	Relative frequency (1970–2014)	Cumulate number (1970–1999)	Cumulated frequency (1970–1999)	Cumulate number (2000–2014)	Cumulated frequency (2000–2014)
$P > 0$	0.001	13078	100.00	71.13	7891	100.00	5187	100.00
$P > 0.1$	0.2	3775	28.87	6.68	2153	27.28	1622	31.27
$P > 1$	1	2902	22.19	13.95	1687	21.38	1215	23.42
$P > 10$	10	1077	8.24	4.95	631	8.00	446	8.60
$P > 20$	20	430	3.29	1.86	260	3.29	170	3.28
$P > 30$	30	187	1.43	0.83	112	1.42	75	1.45
$P > 40$	40	78	0.60	0.23	51	0.65	26	0.50
$P > 50$	50	48	0.37	0.18	34	0.43	13	0.25
$P > 60$	60	25	0.19	0.07	18	0.23	7	0.13
$P > 70$	70	16	0.12	0.05	11	0.14	5	0.10
$P > 80$	80	9	0.07	0.04	6	0.08	3	0.06
$P > 100$	100	4	0.03	0.03	1	0.01	3	0.06

differences in frequency distribution. Taking as reference daily thresholds of 40 and 75 mm, the frequency of days with relatively higher cumulated amounts is similar for the two studied periods: 51 days with rain >40 mm (0.65% of total daily measurements) and 9 days with rain >75 mm (0.11%) during the 1970–1999, 26 days with rain >40 mm (0.50%), and 5 days with rain >75 mm (0.10%) during the 2000–2014 (**Table 1**).

However, by considering the full series, a clear change in the threshold/frequency relationship occurs around thresholds between 10 and 20 mm, as represented by the two different power-laws in **Figure 5**. At the high frequencies ($f = 10$–100), corresponding to daily rainfalls lower than 10 mm, the curve is very steep indicating a very rapid decrease in frequency for an increase of daily rain. At the low to very low frequencies ($f = 0.01$–10), corresponding to daily rainfalls higher than 20 mm, the curve flattens and shows a slight linear increasing behavior since the 30 mm threshold.

Monthly distribution of the relatively most rainy days (rain >40 mm/day) occurred within the entire 1970–2014 time period shows a strong seasonality (**Figure 6**), concentrating mostly in the autumn season. However, some differences can be observed between the two analyzed periods, such as a strong peak recorded in October only during the 1970–1999 period.

Inventory of Flash Flood Events

The most dramatic flood event of the last century occurred on October 25, 1918 (AVI database; Guzzetti et al., 1994), causing the collapse of a building and 13 fatalities in the urban center of Pozzuoli. For this event, no rain data is available and the archive research gave us only a qualitative description of the event: "*an extreme rainstorm with torrential rain and strong winds caused the collapse of a two-floor building located in San Leonardo street, in the town center, at 5 a.m.*" (source: "Il Mattino," issue dated 26–27 October 1918). Beside this

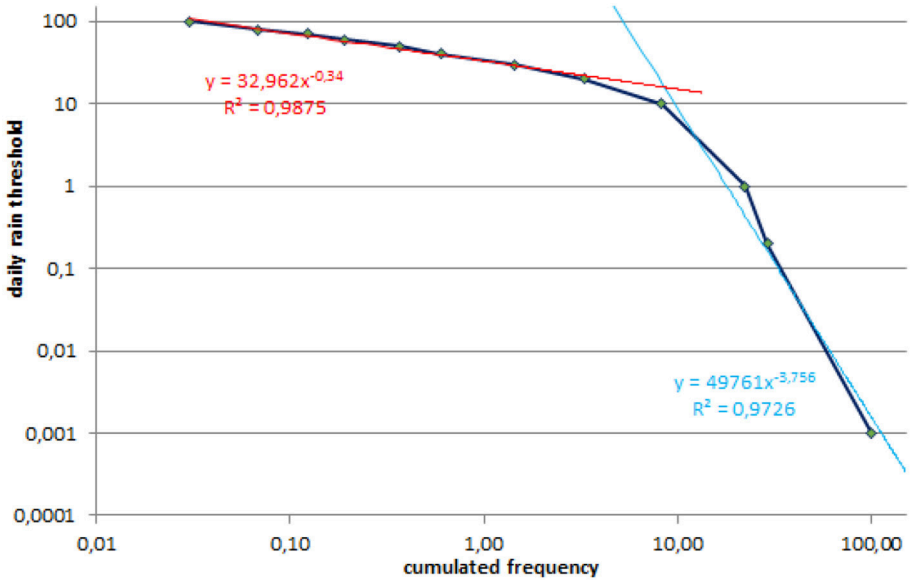

FIGURE 5 | Bi-logarithmic diagram of threshold classes and cumulated frequency of daily rain data.

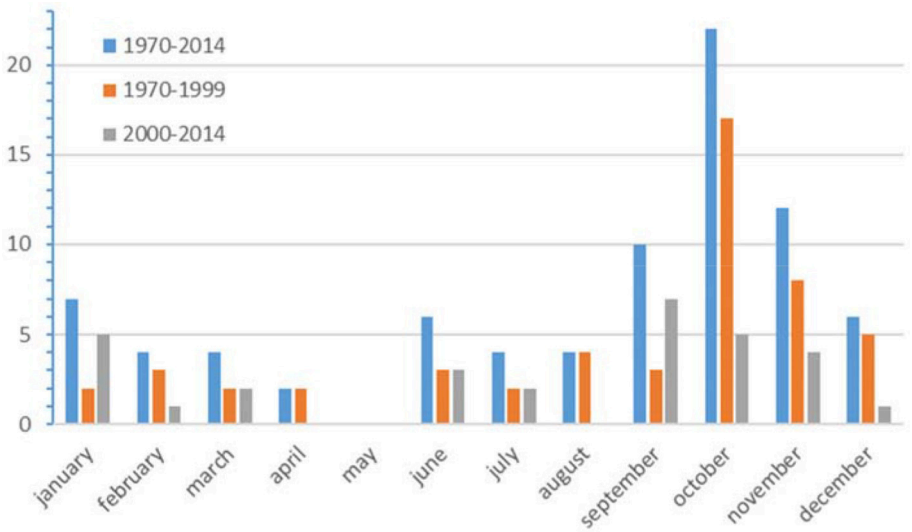

FIGURE 6 | Monthly frequency of days characterized by rain amounts major than 40 mm for the 1970–1999 and 2000–2014 time spans, as well as for the entire period.

main event, and probably other minor events occurred in the first half of the last century, the results of the archive research revealed that in the 1970–2014 time interval nine flash flood events hit the Pozzuoli town (**Table 2**). Among these, four events occurred in the 1970–1999 (i.e., 30 years) and five events in the 2000–2014 (i.e., 15 years) time spans. Analysis of the record showed that events mostly occurred in the late summer-autumn period (78%), whereas in the spring (11%), and summer seasons (11%) they were less frequent. No event has been recorded in the winter season. This seasonal distribution is coherent with the average monthly distribution of the most severe rainfalls occurred in the 1970–2014 time period (**Figure 6**).

Analysis of information related to the most recent events (e.g., 2011 event; Esposito et al., 2015) supplied a clear explanation of the flash flood dynamic in the study area. Specifically, enhanced runoff processes initiate during heavy rainstorms along the volcanic hillslopes, eroding pyroclastic soils and supplying sediment-laden flows downstream. In the upper part of the watershed, these flows pour down along hollows and natural channels (**Figure 7**), where soil slips can also affect hilly slopes and channel sides. Downstream, the sediment-laden flows

TABLE 2 | Flash flood events occurred in the Pozzuoli area in the 1970–2014 time interval and related daily rainfalls.

Flash flood event	Daily rainfall (mm)	% of annual precipitation	2 days rainfall (mm)
15/10/1971	84.2	9	88.8
26/08/1975	76	9	101.6
18/11/1985	81	8	148.2
10/10/1987	115.6	15	122
15/09/2001	161.6	20	163.2
04/03/2005	128	11	133
14/09/2009	40	4	74.8
30/07/2010	76.4	7	76.4
06/11/2011	116.6	14	117.2

The "2-days rainfall" column reports the overall rainfall amounts measured in both the flash flood-related day and in the previous day.

have been reported along the road network connecting the neighborhoods located up in the watershed with the littoral zone (**Figure 7**). In many cases, flows were able to drag motorcycles and cars together with people. The documented rapid flows induced heavy damages to the railway crossing the urban center and to the buildings realized close to the coastline, or in proximity of the flooded roads (Esposito et al., 2015). Deposits of mud reported in the littoral zone reached up to one meter in thickness, whereas other amounts of sediments flowed into the sea. No fatalities have been recorded during the recognized events.

The accuracy analysis revealed that the adopted threshold of 40 mm was suitable to identify flash flood events occurred in the study area by means of the performed archive analysis. This emerged after testing further thresholds by means of several accuracy statistics commonly used for assessing models of weather forecasting, landslide susceptibility and other (Frattini et al., 2010), such as the False Positive rate (FP), True Positive rate (TP), True skill statistic score (Peirce, 1884; Hanssen and Kuipers, 1965), Efficiency (Finley, 1884), and the Odd ratio skill score (Yule, 1900). Such statistics allowed assessing the model performance by comparing observed data (occurrence or absence of a flash flood response after a daily rain exceeding a given threshold) with the model (i.e., selected thresholds) by means of a contingency table (**Table 3**). Results of the accuracy analysis are shown in **Table 4**, with reference to thresholds ranging from 30 to 80 mm.

Generally, FP and TP give an insufficient performance statistics, because they ignore false negatives and false positives, respectively (Frattini et al., 2010). In this study, however, the 30 and 40 mm thresholds gave a full sensitivity. The same result was given by the odd ratio skill score that conveniently ranges between −1 and 1 and takes prior probabilities into account (Frattini et al., 2010), resulting in better scores for rare events like the analyzed flash floods. The True skill statistic score, that uses all elements of contingency table and does not depend on event frequency, showed better results for the 40 mm threshold (**Table 4**). The Efficiency measured the percentage of events that were correctly classified by the used model (threshold), but all the scores resulted very high because were heavily influenced by the most common class (true negative). It was therefore not evenhanded.

Properties of the Flash Flood-Triggering Rainfalls

Properties of rainfalls related to the four flash floods occurred in the first analyzed time interval are reported in **Table 5** (gray rows). Daily amounts range from a minimum of 76 mm recorded on August 26, 1975 to a maximum of 115.6 mm recorded on October 10, 1987. The 1-h rainfall amount is available for the 1971 and 1987 events only, resulting in 30 and 40 mm respectively. The 10-min peak storm intensity was recorded for the 1971 event only and resulted in 60 mm h^{-1}. These four flash floods were recognized within a selection of 51 days characterized by daily rainfall amounts equal or >40 mm (**Figure 8**), 47 of which did not correspond therefore to any event on checked newspapers.

Properties of rainfalls related to the five flash floods occurred in the second analyzed time interval (subset 2000–2014) are also reported in **Table 5** (orange rows). Daily amounts range from a minimum of 40 mm recorded on September 14, 2009 to a maximum of 161.6 mm recorded on September 15, 2001. The 1-h amounts range from a minimum of 34.4 mm recorded on September 14, 2009 to a maximum of 80 mm recorded on September 15, 2001. The 10-min peak storm intensities range from a minimum of 54 mm h^{-1} recorded on March 4, 2005 to a maximum of 140.4 mm h^{-1} recorded on September 15, 2001. These five flash floods were recognized within a selection of 26 days characterized by daily rainfall amounts equal or >40 mm (**Figure 9**), 21 of which did not correspond therefore to any event. With reference to these 26 days, a torrential character of precipitations is generally recorded, as highlighted in **Figure 9**, where daily rains, 1-h maximum amounts and peak intensities recorded in 10 min are compared. These observations were obtained thanks to the availability of rain gauge measurements characterized by a high temporal resolution (i.e., 10 min), since the year 2000. For this latter time interval, we have observed that, in the study area, the flash flood triggering rainfalls consist of two types. The type 1 includes abundant rainfall persisting on the same area for several hours, with variable intensities that can reach peaks in 10 min up to 100 mm h^{-1}; the type 2 includes short-duration, high-intensity rainstorms able to release significant amounts of rain in <1 h. Examples of both types are shown in **Figure 10**.

A general analysis of rainfall data related to flash floods (**Table 5**) revealed that the 1-h rainfall amount and the 10-min intensity exceeded the 30 mm and 54 mm/h, respectively, as well as daily rainfall usually showed values higher than 76 mm, except for the 2009 event (40 mm).

Land Use Changes

Processes described in the previous section were favored by a severe modification of the natural drainage pattern together with an increased urbanization of the watershed that occurred through the second half of the XX century.

FIGURE 7 | Photographs of the different sectors of the studied watershed: **(A)** hilly sector with hollows and partly-natural channels, and soil slips along the slopes; **(B)** intermediate sector with a tunnel passing under the highway, and a drainage channel transformed in a road for connecting the urban center; the dashed line highlights the scar of a shallow landslide triggered by intense rainfalls; **(C)** lower and fully urbanized sector.

Drainage channels, in fact, were deeply modified and many of them were transformed in roads or were buried by means of culverts, compromising their capability of drain flood discharges. The hydrographic network is partly natural in the hilly sectors of the watershed, on the upstream side of the highway, and became completely anthropized downstream, where roads (**Figures 1**, **7**, and **11**) have replaced natural channels. For this reason, in all the recent inventoried events, we found that the channelized flows leaved their natural path to overwhelm the urban center with high energy downstream.

TABLE 3 | Contingency table used for flash flood model evaluation (modified after Frattini et al., 2010).

Observed	Predicted	
	class 0 (–) daily rain under threshold	class 1 (+) daily rain exceeding threshold
class 0 (–)absence of FF	(– –) true negative (tn)/absence of FF in a day with daily rain under threshold	(+ –) false positive (fp)/absence of FF in a day with daily rain exceeding threshold
class 1 (+)occurrence of FF	(– +) false negative (fn)/occurrence of FF in a day with daily rain under threshold	(+ +) true positive (tn)/occurrence of FF in a day with daily rain exceeding threshold

TABLE 4 | Classification of rainy days with different thresholds combined with flash flood events and results of related accuracy statistics (the best scores are in bold letters).

Rain threshold (mm)	True positive	False positive	False negative	True negative	False positive rate (*1*-specificity)	True positive rate *(sensisivity)*	True skill statistics (Pierce's skill score)	Efficiency	Odds ratio skill score
	tp	*fp*	*fn*	*tn*	*FP = fp/(fp + tn)*	*TP = tp/(tp + fn)*	*TP – FP*	*(tp + tn)/T*	*(tp*tn) – (fp*fn)/(tp*tn) + (fp*fn)*
30	9	174	0	12,895	0.01331	**1**	0.98669	0.96241	**1**
40	9	73	0	12,996	0.00559	**1**	**0.99441**	0.96994	**1**
50	8	42	1	13,027	0.00321	0.88889	0.88568	0.97218	0.99919
60	8	18	1	13,051	0.00138	0.88889	0.88751	0.97397	0.99966
70	8	8	1	13,061	0.00061	0.88889	0.88828	**0.97717**	0.99985
80	6	3	3	13,066	0.00023	0.66667	0.66644	0.97494	0.99977

TABLE 5 | Rainfall properties related to the flash flood events occurred in the Pozzuoli area.

Flash flood event	Daily rainfall (mm)	1-h rainfall (mm)	10-min peak storm intensity (mm h^{-1})
15/10/1971	84.2	30	60
26/08/1975	76	–	–
18/11/1985	81	–	–
10/10/1987	115.6	40	–
15/09/2001	161.6	80	140.4
04/03/2005	128	37	54
14/09/2009	40	34.4	57.6
30/07/2010	76.4	40.6	126
06/11/2011	116.6	44.2	67.2

Gray rows refer to the 1970–1999 subset, orange rows to the 2000–2014 subset.

According to Pesaresi and Marta (2014), the main part of an urban sprawl occurred over the last decades of the XX century (1970–2000). Later, a strong decrease in the growth of artificial surfaces took place. The quantitative GIS analysis performed in this study revealed that the urbanized surface of the Pozzuoli watershed (area 3,615,454 m^2) raised of 31.2% in the 1965–2000 time interval, and of only 0.7% in the 2000–2012 time span (**Table 6**). **Figure 11** shows the areas involved by such urban developments.

DISCUSSION AND CONCLUSIONS

In the Pozzuoli area, the oldest and most severe (13 fatalities) flash flood event occurred in 1918 (for location see **Figure 11**), but no rain data is available for that time. After this, 9 events have been recognized between 1970 and 2014; all of them caused several damages to roads, buildings and the railway in the town center with a comparable level of severity. Data presented in this research highlight as the frequency of flash flood events varied in the Pozzuoli area throughout the 1970–2014 time interval. The most relevant finding is that the frequency increased in the 2000–2014 time span (5 events in 15 years; 0.33 ev./yr) respect to the 1970–1999 time span, when 4 events occurred in 30 years (0.13 ev./yr). Cumulated frequency of days with rainfall amounts equal or higher than 40 mm (threshold selected for the archive research) shows a constant trend through the analyzed time interval (1970–2014), without significant variations (**Figure 12**). Conversely, cumulated frequency of flash flood events highlights an increasing trend since the year 2000, while the urbanization of the area increased only before the year 2000 (**Figure 12**).

The lower occurrence of flash floods in the first period cannot be related to a lack of historical data. In fact, information related to the occurrence of all the inventoried flash floods were reported by the same authoritative source for both the analyzed time periods. Such newspaper had always been careful to report any local incident that had an impact on society, such as fatalities and injuries, road diversions, rail delays, flooding

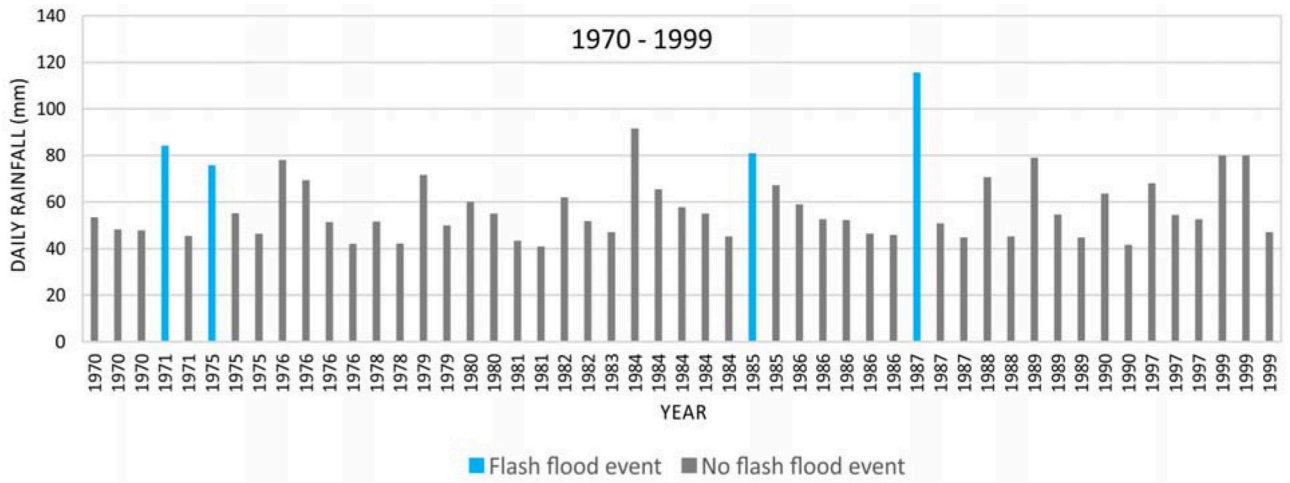

FIGURE 8 | Daily cumulative rainfall recorded in selected dates of the 1970–1999 time interval. Rainfall data associated to flash floods are highlighted in blue.

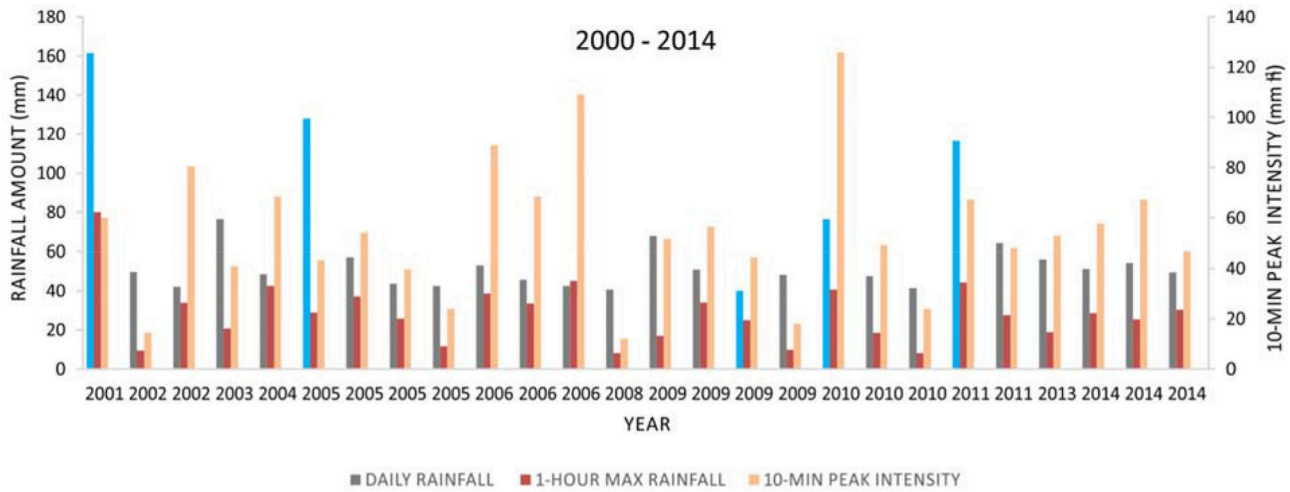

FIGURE 9 | Daily cumulative rainfall, 1-h max rainfall amount and 10-min peak intensity related to selected dates of the 2000–2014 time interval. Daily rainfall data associated to flash floods are highlighted in blue.

and other damages typical of flash floods, as testified by the example of the oldest event noticed to (i.e., the 1918 one). However, the greater amount of data supplied by web sources for events occurred in the last decade, resulted very useful for better understanding the triggering and evolution mechanisms of flows, the affected areas and types of damages. Specifically, as reported by Esposito et al. (2015) for the 2011 event, video footages captured with smartphones by people living in different areas of the Pozzuoli watershed gave us relevant information about flow types, their paths, and the variable depths reached within the urban center. Many studies emphasized the valuable use of web sources, especially social media for flood mapping (Brouwer et al., 2017 and references therein), streamflow estimation (Restrepo-Estrada et al., 2018), and damage assessment (e.g., Diakakis et al., 2016). According to Pennington et al. (2015), the use of social media enables to acquire detailed information about the impacts, remediation and triggers at the time of the event, many of which could be otherwise unknown.

The strategy of determining a daily rainfall threshold for addressing the archive research and extending inventory of flash floods occurred in the study area demonstrated to be very effective in terms of time optimization and accuracy of results. The adopted threshold of 40 mm resulted in fact very accurate from a statistical point of view, as reported in **Table 4**. Moreover, taking into account overall results of the accuracy analysis, as well as properties of rainfalls triggering the identified flash floods (**Table 5**), higher daily thresholds of 60 or 70 mm would have led to less valuable results. In referring to this consideration, however, it is worth underlining that application of such method requires a preliminary set of events, which is essential to take

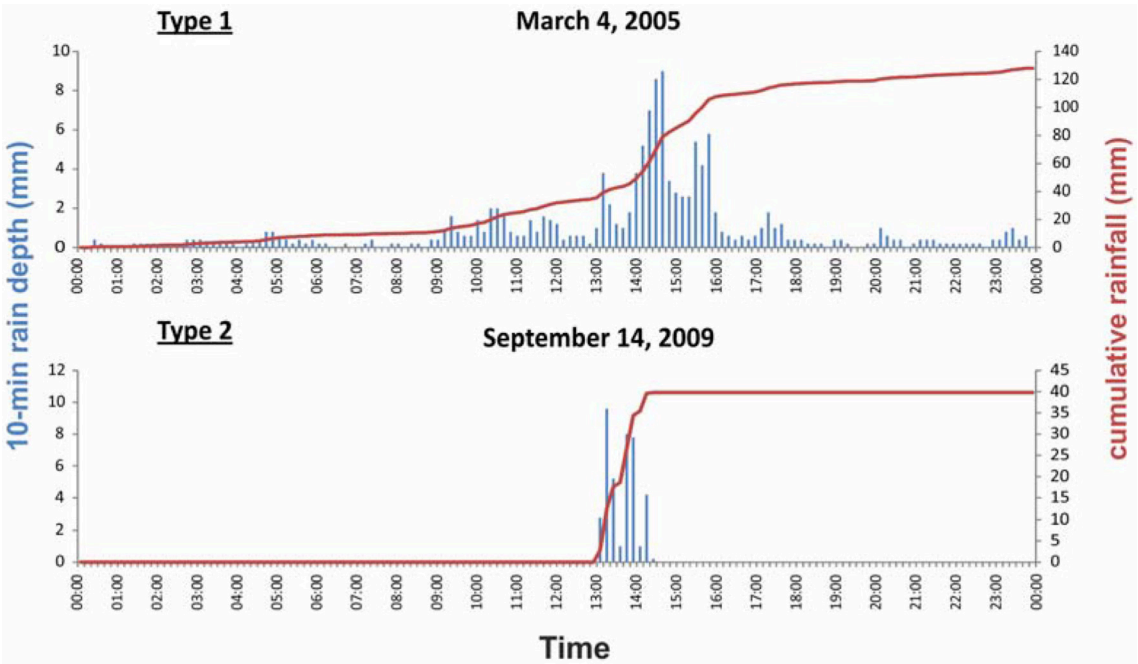

FIGURE 10 | Examples of the two types of rainfall recorded during flash flood events.

adequate decisions about the daily rainfall threshold that should be used. The only analysis of daily rainfall data series is not wholly sufficient.

In order to address causes of the increased flash flood trend, it was assessed the urbanization progress occurred in the studied watershed throughout the 1965–2012 time interval. The analysis of topographic maps and orthophotos of the Pozzuoli area documented the high level of urbanization, representing a complex and critical factor for risk management in the area. Our GIS analysis allowed assessing that urbanized surface of the Pozzuoli watershed raised from 24 to 55% in the 1965–2000 time interval. A strong decrease in the growth of artificial surfaces took place instead during the 2000–2012 time span, when the urbanization has increased only for 0.7% of the watershed area (**Figure 11**). In the light of this, the frequency of flash floods and the rate of urbanization followed opposite behaviors, since 2000 (**Figure 12**), indicating that the temporal distribution of events is ostensibly controlled by different factors. The initial soil moisture content may also have a marginal role, given that in this period is relatively low in the whole region and that the flood-triggering rainfalls are often characterized by high rain rates exceeding the soil's infiltration capacity. In the volcanic and peri-volcanic areas of the Campania Region, moreover, this behavior is enhanced within hillslopes that during the summer season are hit by wildfires generating soil water repellency conditions (e.g., Esposito et al., 2017). In small and highly urbanized watersheds like that of Pozzuoli, the hydrological response to high-intensity rainstorms is very rapid and almost all the rain supplies overland flows characterized by discharges that are often not able to be drained by artificial channels and culverts. Unfortunately, the studied watershed is not gauged with instruments for flow discharge measurements, so that we have not accurate data about this. Analysis of the collected multimedia data also highlighted that flow discharges were increased by a relevant concentration of fine sediments, mostly derived from surface erosion of volcanic soils and pyroclastic units outcropping in the hilly sector of the study area.

Taking into account the findings described previously, the observed increase in the flash flood trend can be reasonably ascribed to some variations in the rainfall regime.

The frequency of days with most abundant cumulated rainfall (i.e., $\geq$40 mm) is very similar for the two analyzed periods, and a generally constant trend can be observed since 1970 (**Figure 12**). The factor that has probably played the major control on the increase of flash flood events in the study area has been a change in the rainfall intensity. However, intensity data are fully available only for the 2000–2014 dataset, and are therefore not sufficient to definitively confirm this hypothesis. As consequence, the use of future 10-min registrations would help to define appropriate rain intensity trends.

In the Eastern Mediterranean, a significant rise in the flood frequency, partially related to the increased rainfall intensity (Philandras et al., 2010), has been documented by Diakakis (2014) in the metropolitan area of Athens (Greece). According to this Author, such increment mostly occurred in recent decades (i.e., from 1970 to 2010), with a concentration of events in the autumn season, as in the current case history. In Athens too, heaviest damages occurred in specific locations mostly near the city's natural drainage network, parts of which have been

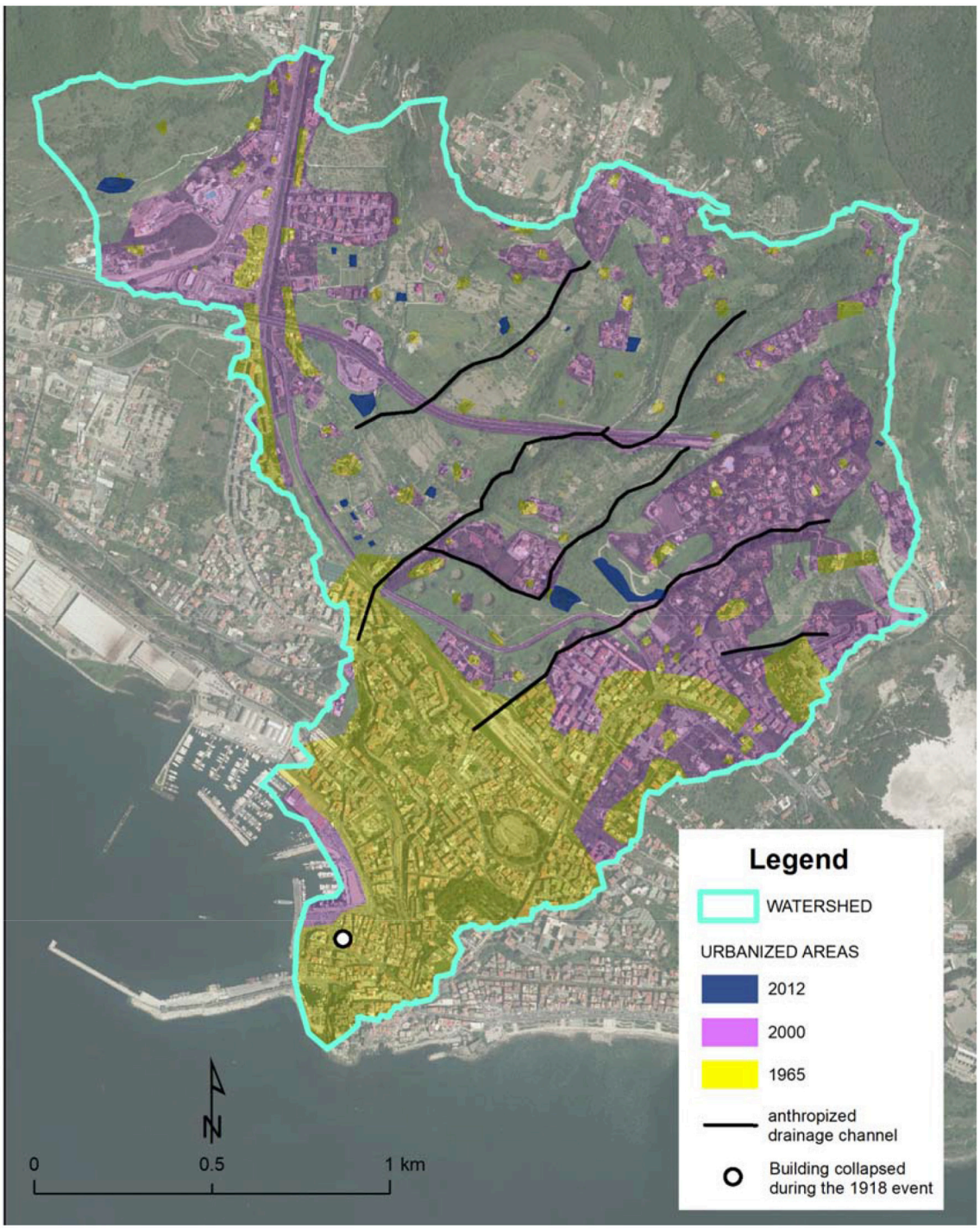

FIGURE 11 | Map showing the urban expansion of the Pozzuoli town in the years 1965, 2000, and 2012.

converted to culverts or streets and were derelict for decades (Diakakis et al., 2016).

Even though it was not possible to calculate significant intensity trends in this study, a torrential character of sub-hourly precipitations recorded since the year 2000 (e.g., **Figures 9**, **10**) is evident. The 1-h amounts range from 30 to 80 mm, while the 10-min peak storm intensities range from 54 to 140.4 mm h^{-1}. According to Tranfaglia et al. (2016), for example, the meteorological event that hit the cities of Naples and Pozzuoli on September 15, 2001 was undoubtedly one

of the most intense events ever recorded on such territory. This event, as well as those triggering the other flash floods, were rather restricted on the most urbanized areas of the Campi Flegrei coastline. This circumstance may be explained by considering these areas as Urban Heat Islands (UHI) that release high amount of suspended particles together with sensible heat in the atmosphere, contributing to increase its mechanical turbulence and to create favorable conditions for severe convective rainstorms (Chandler, 1965). At this effect should be associated the contribution of the rugged topography of the volcanic hillslopes that, also in other parts of the Campi Flegrei (e.g., Santo et al., 2012), influenced both the development of convective cells and triggering of flash floods. According to Marchi et al. (2010), orography plays an important role in regulating atmospheric inflow to the storm and in controlling storm motion and evolution, as well as topographic relief is

TABLE 6 | Quantitative urbanization changes in the Pozzuoli watershed during the 1965–2012 time span.

year	Urbanized area (m^2)	Urbanized area (% watershed)	Increase (m^2)	Increase (%)
1965	878,506	24.3		
2000	2,008,033	55.5	+1,129,527	+31.2
2012	2,032,568	56.2	+24,535	+0.7

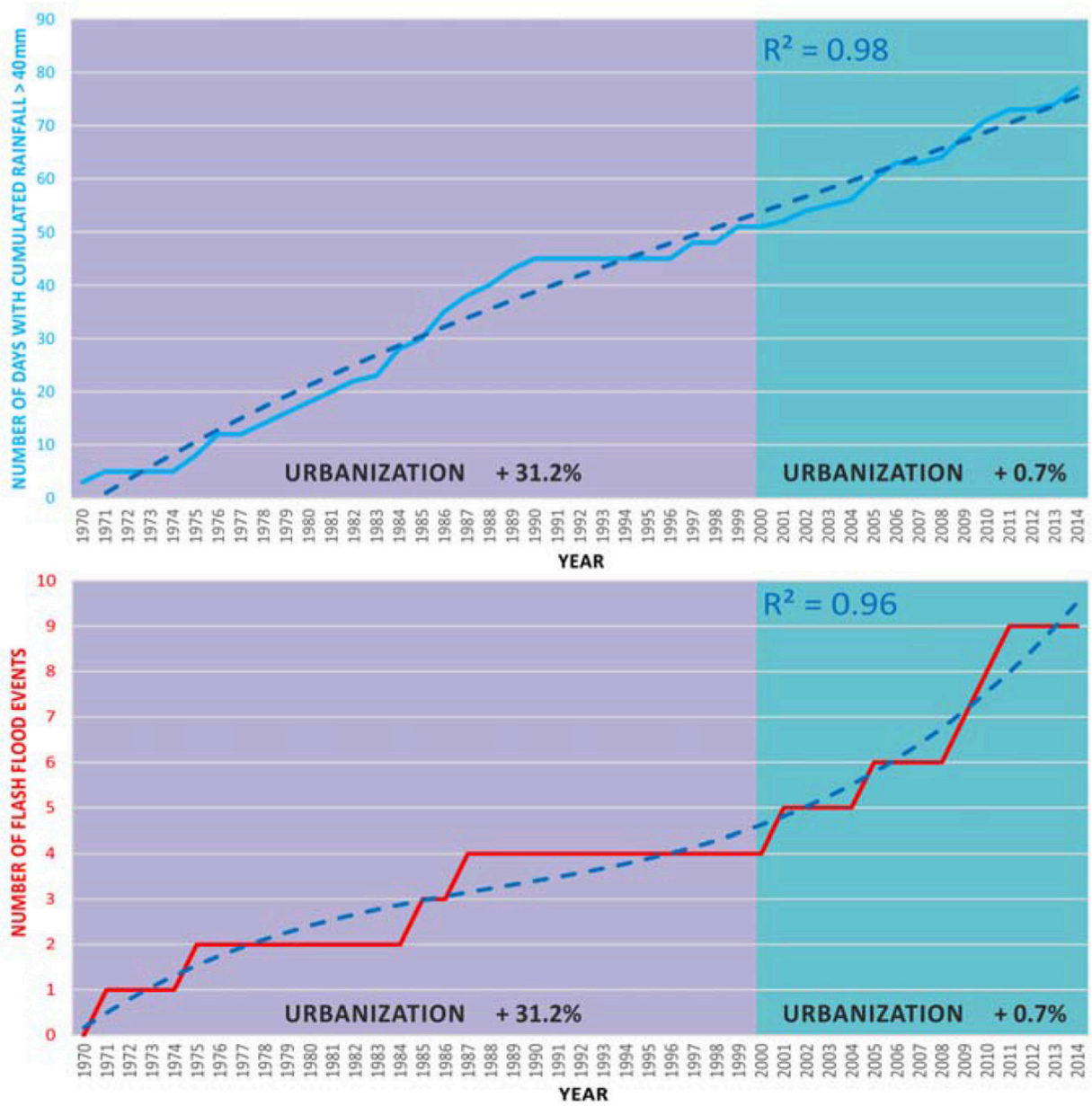

FIGURE 12 | Trend of days characterized by a cumulative rainfall depth ≥40 mm (above) and trend of flash flood events (below) related to the 1970–2014 time interval. Urbanization rates are also reported for comparison

necessary for promoting flow concentration along drainage ways, which result in high unit discharges and relevant geomorphic effects.

The increased frequency of flash floods here described seems to do not follow the trends recognized at larger scales in the Mediterranean region, probably due to the limitations of the available datasets and some complex overlapping signals (e.g., decadal and inter-decadal variability). In fact, Madsen et al. (2014) indicate that there is some evidence of a general increase in observed extreme precipitation, whereas there are no clear indications of significant increasing trends at regional or national levels of observed extreme streamflow in Europe. Gaume et al. (2016) also detected no significant trends in the frequency and magnitude of extreme floods for the Mediterranean area. According to Llasat et al. (2016), the lack of a common or significant trend is a general result found in the majority of works dealing with flood time series analysis, as pointed out by the IPCC, both in their reports on Extremes (IPCC, 2012) and in the Fifth Report (IPCC, 2014).

In spite of this, some increments were clearly identified at local scales. For example, other than findings of Diakakis (2014) discussed previously, Llasat et al. (2013) calculated positive trends for extraordinary floods (0.13 floods yr^{-1}) occurred between 1981 and 2010 in north-east Spain, south-east France and south-west Italy. Petrow and Merz (2009) detected increasing trends in flood frequency in some parts of Germany, and correlated them with temporal changes in atmospheric circulation patterns. Wilhelm et al. (2012) identified flash flood events that affected an alpine watershed in the NW French Alps, during the 1740–2007 time span, and discovered that most of the extreme flood events took place since the beginning of the twenty-first century, with the strongest occurring in 2005. These authors also related the occurrence of high magnitude torrential flood events in high-altitude watersheds to the climate warming. An increment of flash floods in the 1986–2015 time span was also found by Vennari et al. (2016) for other parts of the Campania region.

Taking into account this framework, it seems that local conditions in terms of atmospheric circulation, topography and vulnerability are prevailing on factors acting at larger scales. This requires more efforts to the scientific community engaged in the evaluation of climate change-related effects, also to predict future social consequences.

In summary, results presented in this contribution highlight as urbanization of the Pozzuoli watershed has become relatively stable since the year 2000, whereas frequency of flash floods has increased. This supports the hypothesis of local changes in the extreme precipitations. Information provided by archive chronicles and web sources demonstrate as the current urban setting plays a fundamental role in making the Pozzuoli area prone to future flash flood events that, probably, will be increasingly favored by the occurrence of more extreme rainstorms, as already forecasted for rainfall-induced landslides in other parts of southern Italy (Gariano et al., 2017).

AUTHOR CONTRIBUTIONS

GE performed the archive research. GS and FM performed the statistical analysis; GE, GS and FM processed rainfall and flash flood data; GE and FM wrote the paper.

FUNDING

Financial support was provided by the Research Project PON-MONICA (contract no. PON01_01525) (2012-2016) and by the Research Project ABBACO (2017-2018).

ACKNOWLEDGMENTS

The authors are grateful to the Civil Protection Agency of Campania Region for allowing us access to rainfall data on the study area, and to editor and reviewers for the useful comments that helped us to improve the manuscript.

REFERENCES

Aronica, G. T., Brigandí, G., and Morey, N. (2012). Flash floods and debris flow in the city area of Messina, north-east part of Sicily, Italy in October 2009: the case of the Giampilieri catchment. *Nat. Hazards Earth Syst. Sci.* 12, 1295–1309. doi: 10.5194/nhess-12-1295-2012

Beneduce, P., D'Elia, G., and Guida, M. (1988). Morfodinamica dei versanti dell'area flegrea (Campania): erosione in massa ed erosione lineare. *Mem. Soc. Geol. It.* 41, 949–961.

Blöschl, G., Hall, J., Parajka, J., Perdigão, R. A. P., Merz, B., Arheimer, B., et al. (2017). Changing climate shifts timing of European floods. *Science* 357, 588–590. doi: 10.1126/science.aan2506

Brocca, L., Hasenauer, S., Lacava, T., Melone, F., Moramarco, T., Wagner, W., et al. (2011). Soil moisture estimation through ASCAT and AMSR-E sensors: an intercoparison and validation study across Europe. *Remote Sens. Envir.* 115, 3390–3408. doi: 10.1016/j.rse.2011.08.003

Brouwer, T., Eilander, D., van Loenen, A., Booij, M. J., Wijnberg, K. M., Verkade, J. S., et al. (2017). Probabilistic flood extent estimates from social media flood observations. *Nat. Hazards Earth Syst. Sci.* 17, 735–747. doi: 10.5194/nhess-17-735-2017

Brunetti, M., Maugeri, M., Monti, F., and Nanni, T. (2004). Changes in daily precipitation frequency and distribution in Italy over the last 120 years. *J. Geophys. Res.* 109:D05102. doi: 10.1029/2003JD004296

Calcaterra, D., Del Prete, S., and Mele, R. (2003). "The influence of landslides on the coastal settlements of the Phlegrean district (Campania region, Italy)," in *Proceedings of the International Conference CITTAM 2003, The Requalification of Mediterranean Coasts Among Tradition, Development and Sustainability* (Naples: Arte Tipografica Editrice), 524–534.

Cascini, L., Sorbino, G., Cuomo, S., and Ferlisi, S. (2014). Seasonal effects of rainfall on the shallow pyroclastic deposits of the Campania region (southern Italy). *Landslides* 11, 779–792. doi: 10.1007/s10346-013-0395-3

Cevasco, A., Pepe, G., and Brandolini, P. (2012). Shallow landslides induced by heavy rainfall on terraced slopes: the case study of the October, 25, 2011 event in the Vernazza catchment (Cinque Terre, NW Italy). *Rend. Online Soc. Geol. It.* 21, 384–386. Available Online at: https://rendiconti.socgeol.it/297/article-874/shallow-landslides-induced-by-heavy-rainfall-on-terraced-slopes-the-case-study-of-the-october-25-2011-event-in-the-vernazza-catchment-cinque-terre-nw-italy.html

Chandler, T. J. (1965). *The Climate of London*. Cambridge: W. Heffer and Sons.

De Chiara, G., Ferlisi, S., Cascini, L., and Matano, F. (2016). "Rainfall-induced slope instabilities in pyroclastic soils: the case study of Mount Albino

(Campania region, Southern Italy)," in *Volcanic Rocks and Soils*, eds T. Rotonda, M. Cecconi, F. Silvestri and P. Tommasi (London: Taylor & Francis Group), 327–333.

De Luca, C., Furcolo, P., Rossi, F., Villani, P., and Vitolo, C. (2010). Extreme rainfall in the Mediterranean," in *Proceedings of the International Workshop on Advances in Statistical Hydrology* (Taormina: University of Catania - IAHS - STAHY), 1–11. Available Online at: http://www.risorseidriche.dica.unict.it/Sito_STAHY2010_web/proceedings.htm

De Vita, P., Napolitano, E., Godt, J. W., and Baum, R. L. (2013). Deterministic estimation of hydrological thresholds for shallow landslide initiation and slope stability models: case study from the Somma-Vesuvius area of southern Italy. *Landslides* 10, 713–728. doi: 10.1007/s10346-012-0348-2

Diakakis, M. (2014). An inventory of flood events in Athens, Greece, during the last 130 years. seasonality spatial distribution. *J. Flood Risk Manag.* 7, 332–343. doi: 10.1111/jfr3.12053

Diakakis, M., Deligiannakis, G., Katsetsiadou, K., Lekkas, E., Melaki, M., and Antoniadis, Z. (2016). Mapping and classification of direct effects of the flood of october 2014 in Athens. *Bull. Geol. Soc. Gr.* 50, 681–690. doi: 10.12681/bgsg.11774

Di Martire, D., De Rosa, M., Pesce, V., Santangelo, M. A., and Calcaterra, D. (2012). Landslide hazard and land management in high-density urban areas of Campania region, Italy. *Nat. Hazards Earth Syst. Sci.* 12, 905–926. doi: 10.5194/nhess-12-905-2012

Di Vito, M. A., Isaia, R., Orsi, G., Southon, J., de Vita, S., D'Antonio, M., et al. (1999). Volcanism and deformation since 12.000 years at the Campi Flegrei caldera (Italy). *J. Volcanol. Geotherm. Res.* 91, 221–246.

Dorigo, W. A., Wagner, W., Hohensinn, R., Hahn, S., Paulik, C., Drusch, M., et al. (2011). The international soil moisture network: a data hosting facility for global *in situ* soil moisture measurements. *Hydrol. Earth Syst. Sci.* 15, 1675–1698. doi: 10.5194/hess-15-1675-2011

Ducrocq, V., Braud, I., Davolio, S., Ferretti, R., Flamant, C., Jansa, A., et al. (2014). HyMeX-SOP1, the field campaign dedicated to heavy precipitation and flash flooding in the northwestern Mediterranean. *Bull. Amer. Meteor. Soc.* 95, 1083–1100. doi: 10.1175/BAMS-D-12-00244.1

Esposito, G., Fortelli, A., Grimaldi, G. M., Matano, F., and Sacchi, M. (2015). I fenomeni di flash flood nell'area costiera di Pozzuoli (Napoli, Italia): risultati preliminari sull'analisi dell'evento del 6 novembre 2011. *Rend. Online Soc. Geol. It.* 34, 74–85. doi: 10.3301/IJG.2015.41

Esposito, G., Matano, F., Molisso, F., Ruoppolo, G., Di Benedetto, A., and Sacchi, M. (2017). Post-fire erosion response in a watershed mantled by volcaniclastic deposits, Sarno Mountains, Southern Italy. *Catena* 152, 227–241. doi: 10.1016/j.catena.2017.01.009

Faccini, F., Luino, F., Sacchini, A., Turconi, L., and De Graff, J. V. (2015). Geohydrological hazards and urban development in the Mediterranean area: an example from Genoa (Liguria, Italy). *Nat. Hazards Earth Syst. Sci.* 15, 2631–2652. doi: 10.5194/nhess-15-2631-2015

Federico, S., Bellecci, C., and Colacino, M. (2003). Quantitative precipitation of the Soverato flood: the role of orography and surface fluxes. *Il Nuovo Cimento* 26C, 7–22. Available Online at: https://www.sif.it/riviste/sif/ncc/econtents/2003/026/01

Finley, J. P. (1884). Tornado predictions. *Am. Meteorologic. J.* 1, 85–88.

Frattini, P., Crosta, G., and Carrara, A. (2010). Techniques for evaluating the performance of landslide susceptibility models. *Eng. Geol.* 111, 62–72. doi: 10.1016/j.enggeo.2009.12.004

Gariano, S. L., Rianna, G., Petrucci, O., and Guzzetti, F. (2017). Assessing future changes in the occurrence of rainfall-induced landslides at a regional scale. *Sci. Tot. Envir.* 596–597, 417–426. doi: 10.1016/j.scitotenv.2017.03.103

Gaume, E., Borga, M., Llasat, M. C., Maouche, S., Lang, M., and Diakakis, M. (2016). "Mediterranean extreme floods and flash floods," in Hydro-meteorological extremes, chapter 3, *The Mediterranean Region under Climate Change, A Scientific Update*, ed Allenvi (Marseille: Coll. Synthèses, IRD Editions), 133–144. Available Online at: http://www.editions.ird.fr/produit/433/9782709922210/The%20Mediterranean%20Region%20under%20Climate%20Change

Greco, R., Comegna, L., Damiano, E., Guida, A., Olivares, L., and Picarelli, L. (2013). Hydrological modelling of a slope covered with shallow pyroclastic deposits from field monitoring data. *Hydrol. Earth Syst. Sci.* 17, 4001–4013. doi: 10.5194/hess-17-4001-2013

Guzzetti, F., Cardinali, M., and Reichenbach, P. (1994). The AVI Project: a bibliographical and archive inventory of landslides and floods in Italy. *Environ. Manag.* 18, 623–633. doi: 10.1007/BF02400865

Hanssen, A. W., and Kuipers, W. J. A. (1965). On the relationship between the frequency of rain and various meteorological parameters. *Mededelingenen Verhandelingen* 81, 2–15.

Hapuarachchi, H. A. P., Wang, Q. J., and Pagano, T. C. (2011). A review of advances in flash flood forecasting. *Hydrol. Processes* 25, 2771–2784. doi: 10.1002/hyp.8040

IPCC (2012). *Managing the Risks of Extreme Events and Disasters to Advance Climate Change Adaption (SREX)*. Cambridge: Intergovernmental Panel on Climate Change; Cambridge University Press.

IPCC (2014). *Climate Change 2014: Impacts, Adaptation, and Vulnerability*. IPCC Working Group II Contribution to the Fifth Assessment Report of the Intergovernmental panel on climate change. Available online at: http://www.ipcc.ch/report/ar5/wg2/

Konrad, C. P. (2003). *Effects of urban Development on Floods*. U.S. Geological Survey Fact Sheet FS-076-03. Available online at: https://pubs.usgs.gov/fs/fs07603/

Llasat, M. C., Llasat-Botija, M., Petrucci, O., Pasqua, A. A., Rosselló, J., Vinet, F., et al. (2013). Towards a database on societal impact of Mediterranean floods in the framework of the HYMEX project. *Nat. Hazards Earth Syst. Sci.* 13, 1–14. doi: 10.5194/nhess-13-1337-2013

Llasat, M. C., Llasat-Botija, M., Prat, M. A., Porcù, F., Price, C., Mugnai, A., et al. (2010). High-impact floods and flash floods in Mediterranean countries: the flash preliminary database. *Adv. Geosci.* 23, 1–9. doi: 10.5194/adgeo-23-47-2010

Llasat, M. C., Marcos, R., Turco, M., Gilabert, J., and Llasat-Botija, M. (2016). Trends in flash flood events versus convective precipitation in the Mediterranean region: the case of Catalonia. *J. Hydrol.* 541, 24–37. doi: 10.1016/j.jhydrol.2016.05.040

Madsen, H., Lawrence, D., Lang, M., Martinkova, M., and Kjeldsen, T. (2014). Review of trend analysis and climate change projections of extreme precipitation and floods in Europe. *J. Hydrol.* 519, 3634–3650. doi: 10.1016/j.jhydrol.2014.11.003

Marchi, L., Borga, M., Preciso, E., and Gaume, E. (2010). Characterisation of selected extreme flash floods in Europe and implications for flood risk management. *J. Hydrol.* 394, 118–133. doi: 10.1016/j.jhydrol.2010.07.017

Mariotti, A., Struglia, M. V., Zeng, N., and Lau, K. M. (2002). The hydrological cycle in the Mediterranean region and implications for the water budget of the Mediterranean Sea. *J. Climate* 15, 1674–1690. doi: 10.1175/1520-0442(2002)015<1674:THCITM>2.0.CO;2

Montani, A., Marsigli, C., Nerozzi, F., Paccagnella, T., Tibaldi, S., and Buizza, R. (2003). The soverato flood in Southern Italy: performance of global and limited-area ensemble forecasts. *Nonlin. Proc. Geophys.* 10, 261–274. doi: 10.5194/npg-10-261-2003

Napolitano, E., Fusco, F., Baum, R. L., Godt, J. W., and De Vita, P. (2016). Effect of antecedent-hydrological conditions on rainfall triggering of debris flows in ash-fall pyroclastic mantled slopes of Campania (southern Italy). *Landslides* 13, 967–983. doi: 10.1007/s10346-015-0647-5

Peirce, C. S. (1884). The numerical measure of the success of predictions. *Science* 4, 453–454. doi: 10.1126/science.ns-4.93.453-a

Pennington, C., Freeborough, K., Dashwood, C., Dijkstra, T., and Lawrie, K. (2015). The national landslide database of great britain: acquisition, communication and the role of social media. *Geomorphology* 249, 44–51. doi: 10.1016/j.geomorph.2015.03.013

Pesaresi, C., and Marta, M. (2014). Applicazioni GIS per l'analisi dell'urbanizzazione nella provincia di Napoli. Un'analisi multitemporale in aree esposte a elevato rischio vulcanico. *Boll Assoc Ital. Cartogr.* 150, 34–53. Available Online at: https://www.openstarts.units.it/handle/10077/11318

Petrow, T., and Merz, B. (2009). Trends in flood magnitude, frequency and seasonality in Germany in the period 1951 - 2002. *J. Hydrol.* 371, 129–141. doi: 10.1016/j.jhydrol.2009.03.024

Philandras, C. M., Nastos, P. T., Paliatsos, A. G., and Repapis, C. C. (2010). Study of the rain intensity in Athens and Thessaloniki Greece. *Adv. Geosci.* 23, 37–45. doi: 10.5194/adgeo-23-37-2010

Pierson, T. C., and Costa, J. E. (1987). "A rheologic classification of subaerial sediment-water flows," in *Debris Flows/Avalanches: Process, Recognition, and*

Mitigation, eds J. E. Costa, G. F. Wieczorek (Boulder, CO: Geological Society of America, Reviews in Engineering Geology) 7, 1–12.

Regione Toscana (2017). *Report Evento Meteo-Idrologico dei Giorni 9 e 10 Settembre 2017*. Centro Funzionale Della Regione Toscana. Available online at: http://www.cfr.toscana.it/supports/download/eventi/report_evento_9-10_settembre_2017.pdf

Restrepo-Estrada, C., de Andrade, S. C., Abe, N., Fava, M. C., Mendiondo, E. M., and de Albuquerque, J. P. (2018). Geo-social media as a proxy for hydrometeorological data for streamflow estimation and to improve flood monitoring. *Comput. Geosci*. 111, 148–158. doi: 10.1016/j.cageo.2017.10.010

Santo, A., Di Crescenzo, G., Del Prete, S., and Di Iorio, L. (2012). The Ischia island flash flood of November 2009 (Italy): phenomenon analysis and flood hazard. *Phys. Chem. Earth* 49, 3–17. doi: 10.1016/j.pce.2011.12.004

Silvestro, F., Gabellani, S., Giannoni, F., Parodi, A., Rebora, N., Rudari, R., et al. (2012). A hydrological analysis of the 4th November 2011 event in Genoa. *Nat. Hazards Earth Syst. Sci*. 12, 2743–2752. doi: 10.5194/nhess-12-2743-2012

Tarolli, P., Borga, M., Morin, E., and Delrieu, G. (2012). Analysis of flash flood regimes in the North-Western and South-Eastern Mediterranean regions. *Nat. Hazards Earth Syst. Sci*. 12, 1255–1265. doi: 10.5194/nhess-12-1255-2012

Tranfaglia, G., Braca, G., Monacelli, G., Biafore, M., Porfido, S., and Mazzarella, A. (2016). Real time monitoring for diagnosis and prevention of extreme rainfall events: an application to intense rainfalls on the coastal city of naples, italy. *J. Geogr. Nat. Disast*. 6:180. doi: 10.4172/2167-0587.1000180

United Nations (2011). *World Urbanization Prospects: The 2011 Revision*. United Nations, Department of Economic and Social Affairs (DESA), Population Division, Population Estimates and Projections Section, New York, NY.

Vennari, C., Parise, M., Santangelo, N., and Santo, A. (2016). A database on flash flood events in Campania, southern Italy, with an evaluation of their spatial and temporal distribution. *Nat. Hazards Earth Syst. Sci*. 16, 2485–2500. doi: 10.5194/nhess-16-2485-2016

Wilhelm, B., Arnaud, F., Enters, D., Allignol, F., Legaz, A., Magand, O., et al. (2012). 35 Does global warming favour the occurrence of extreme floods in European Alps? First evidences from a NW Alps proglacial lake sediment record. *Climatic Change* 113, 563–581. doi: 10.1007/s10584-011-0376-2

Yule, G. U. (1900). On the association of attributes in statistics. *Philosophic. Transact. Royal Soc. Lond*. 194A, 257–319. doi: 10.1098/rsta.1900.0019

Conflict of Interest Statement: The authors declare that the research was conducted in the absence of any commercial or financial relationships that could be construed as a potential conflict of interest.

frontiers in Earth Science

ORIGINAL RESEARCH
published: 13 November 2018
doi: 10.3389/feart.2018.00080

The Debris Flow Occurred at Ru Secco Creek, Venetian Dolomites, on 4 August 2015: Analysis of the Phenomenon, Its Characteristics and Reproduction by Models

Carlo Gregoretti, Massimo Degetto, Martino Bernard and Mauro Boreggio*

Department Land Environment Agriculture and Forestry, University of Padova, Legnaro, Italy

On 4 August 2015, a very high intensity storm, 31.5 mm in 20 min (94.5 mm/h), hit the massif of Mount Antelao on the Venetian Dolomites triggering three stony debris flows characterized by high magnitude. Two of them occurred in the historical sites of Rovina di Cancia and Rudan Creek and were stopped by the retaining works upstream the inhabited areas, while the third routed along the Ru Secco Creek and progressively reached the resort area and the village of San Vito di Cadore, causing fatalities and damages. The main triggering factor of the Ru Secco debris flow was a large rock collapse on the northern cliffs of Mount Antelao occurred the previous autumn. The fallen debris material deposited on the Vallon d'Antrimoia inclined plateau at the base of the collapsed cliffs and, below it, on the Ru Salvela Creek, covering it from the head to the confluence with the Ru Secco Creek. The abundant runoff, caused by the high intensity rainfall on 4 August 2015, entrained about 52,500 m^3 of the debris material laying on the Vallon d'Antrimoia forming a debris flow surge that hit and eroded the debris deposit covering the downstream Ru Salvela Creek, increasing its volume, about 110,000 m^3 of mobilized sediments. This debris flow routed downstream the confluence, flooding the parking of a resort area where three people died, and reached the village downstream damaging some buildings. A geomorphological analysis was initially carried out after surveying the whole basin. All liquid and solid-liquid contributions to the phenomenon were recognized together with the areas subjected to erosion and deposition. The elaboration of pre and post-event topographical surveys provided the map of deposition-erosion depths. Using the rainfall estimated by weather radar and corrected by the nearest rain gauge, about 0.8 km far, we estimated runoff by using a rainfall-runoff model designed for the headwater rocky basins of Dolomites. A triggering model provided the debris flow hydrographs in the initiation areas, after using the simulated runoff. The initial solid-liquid surge hydrographs were, then, routed downstream by means of a cell model. The comparison between the simulated and estimated deposition-erosion pattern resulted satisfactory. The results of the simulation captured, in fact, the main features of the occurred phenomenon.

Keywords: survey, multi-temporal topographical data, runoff, debris flow, initiation area, routing, damages

OPEN ACCESS

Edited by:
Davide Tiranti,
Agenzia Regionale per la Protezione Ambientale (ARPA), Italy

Reviewed by:
Chiara Deangeli,
Politecnico di Torino, Italy
Fabio Matano,
Consiglio Nazionale Delle Ricerche (CNR), Italy

****Correspondence:***
Carlo Gregoretti
carlo.gregoretti@unipd.it

Specialty section:
This article was submitted to Quaternary Science, Geomorphology and Paleoenvironment, a section of the journal Frontiers in Earth Science

Received: *28 February 2018*
Accepted: *28 May 2018*
Published: *13 November 2018*

Citation:
Gregoretti C, Degetto M, Bernard M and Boreggio M (2018) The Debris Flow Occurred at Ru Secco Creek, Venetian Dolomites, on 4 August 2015: Analysis of the Phenomenon, Its Characteristics and Reproduction by Models. Front. Earth Sci. 6:80. doi: 10.3389/feart.2018.00080

1. INTRODUCTION

The Boite Valley in Venetian Dolomites (Northestern Italian Alps) was affected by several runoff generated debris flows during the summer of 2015 (Baglioni and De Marco, 2015). The evening of 4 August a high intensity storm hit the top area of the Monte Antelao massif and caused three stony debris flows of high magnitudo on the sites, South to North of Rio Rudan Creek, Rovina di Cancia channel and Ru Secco Creek (**Figure 1**). The first two sites are periodically affected by debris flows (Gregoretti and Dalla Fontana, 2008) and are defended by a check dam and some retaining basins respectively that reduced and stopped the solid part of the solid-liquid waves. Ru Secco Creek just experienced its first debris flow since 1950s and was without any defense. Consequently, the debris flow flooded from it causing three deaths in the parking of a resort area and partially damaging some buildings of the village of San Vito di Cadore downstream. The runoff generated debris flows are very common in the Boite Valley (Berti and Simoni, 2005; Gregoretti and Dalla Fontana, 2008) as elsewhere on Alps (Theule et al., 2012; Navratil et al., 2013; Tiranti and Deangeli, 2015; Destro et al., 2018) and worldwide (Imaizumi et al., 2006; Cannon et al., 2008; Coe et al., 2008; Okano et al., 2012; Kean et al., 2013; Hurlimann et al., 2014; Hu et al., 2016). These phenomena, increased in number due to the climate change, are among the most dangerous natural hazards for human settlements in the Boite Valley since the last two centuries. According to Mattea et al. (2016), Thiene et al. (2017) and Stancanelli et al. (2017), they could have a strong socio-economic impact. The aim of the present research is the study of this debris flow event by means of pre and post-event topographical data, post-event direct surveys and its reproduction by modeling the physical processes associated to its occurrence. Multi-temporal topographical data and direct post-event surveys are important for identifying the phenomenon and its characteristics. The phenomenon reconstruction through models is also important, because it shows the evolution of the event. In addition, it is a reliability test of the models. Models, in fact, can play a crucial role in hazard assessment and in risk analysis, and, only the use of models satisfactorily tested against field data can provide reliable results. Consequently, we propose the use of a methodology for simulating the cascade of the physical processes that origin a debris flow phenomenon by models. After the debris flow occurrence, all the areas surrounding the Ru Secco Creek were carefully surveyed with the scope of identifying the development of the phenomenon and its characteristics. This field survey gave the general view of all the single phenomena that contributed to the formation and routing of the solid-liquid surge along the Ru Secco Creek. All

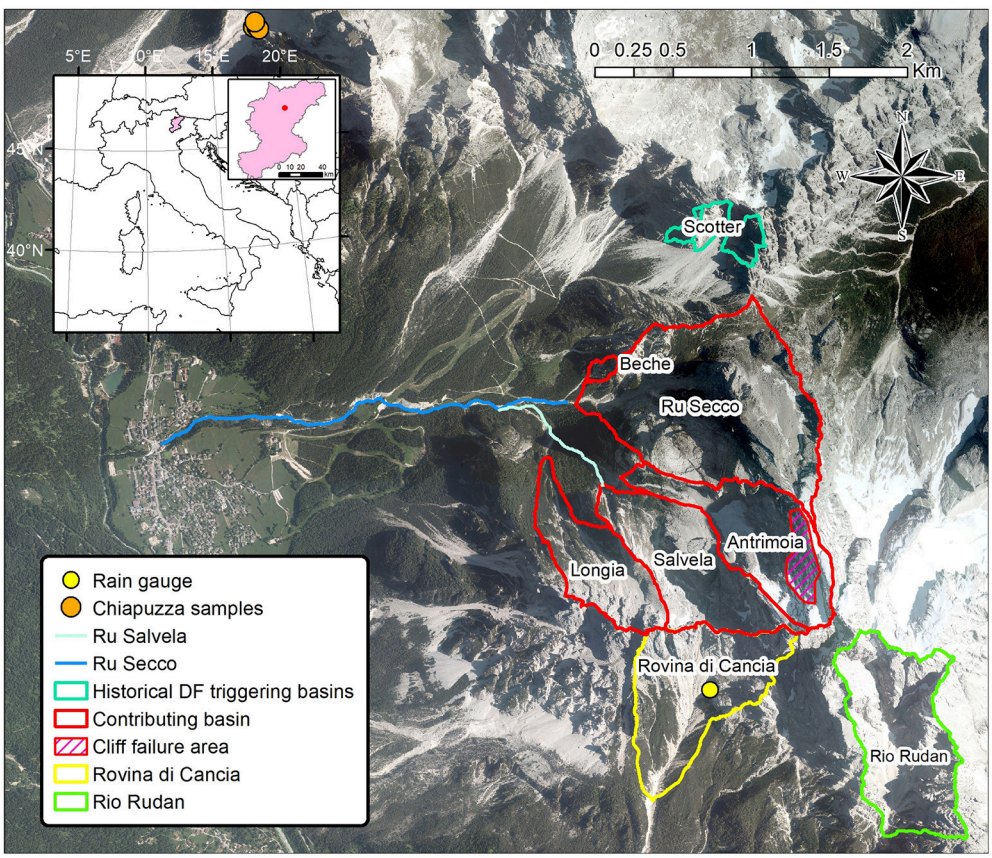

FIGURE 1 | Aerial view of whole area with the contributing hydrological basins and the basins of Rovina di Cancia and Rudan.

the areas that provided solid-liquid or liquid flows were identified with the corresponding watersheds. These results were used for identifying the watersheds where modeling runoff and solid-liquid hydrographs as well the debris flow routing. After building the DEMs of all the contributing watersheds, needed for the hydrological simulations, pre and post-event topographical data were used for building the pre and post-event DEMs of the area affected by the occurred debris flow. The difference between the pre and post-event DEMs provided the map of the deposition-erosion depths and the total sediment volume mobilized during the event. The result of field surveys and analysis of this map showed the main features of the occurred phenomenon. Rainfalls on the contributing watershed were obtained through radar estimates corrected by rainfall depths measurements given by a rain gauge placed at the base of the southern rock walls of Mount Antelao, in the contiguous basin of Rovina di Cancia at an altitude of about 2,150 m a.s.l. (**Figure 1**). Runoff hydrographs were, then, modeled by the rainfall-runoff model proposed by Gregoretti et al. (2016a) for headwater rocky basins while the solid-liquid hydrographs were modeled extending the method proposed by Gregoretti et al. (2016b). Finally, we used an updated version of the GIS-based cell model of Gregoretti et al. (2016b) that ensures a fully bi-phase routing for modeling the debris flow propagation downstream the initiation areas. This updated version, proposed by Gregoretti et al. (2018), allows a better simulation of the entrainment processes that have a crucial role in the estimation of the sediment volume transported by a debris flow that is needed for an efficient hazard assessment. The transported sediment volume, in fact, influences the extension and height of the inundation (Iverson et al., 1998; Rickenmann, 1999; Santi et al., 2008; Reid et al., 2016), that are decisive to evaluate the impact of debris flow. The comparison between the simulation results with the deposition-erosion depth map accounts for the reliability of the phenomenon reconstruction, that is the capturing of its main features.

The remainder of this paper is organized as follows. Section 2 describes the materials and methods, divided in four sub-sections concerning: the study site of Ru Secco Creek with the big rock fall occurred on November 2014, the topographical data and the set up of pre and post-event DEMs, the correction of the radar rainfalls estimates and the models used for the simulations. The field surveys and the geomorphical analysis of the occurred phenomena are presented in section 3, while section 4 shows the reconstruction of the phenomenon by models. Section 5 discusses the results and, finally, section 6 reports the conclusions.

FIGURE 2 | Frontal view of the upper basins that contributed to the phenomenon. The blue arrows show the runoff routing, the red arrows the debris flow starting locations and its routing, and the black arrows the path of the debris flow on the right slope, that did not contribute significatively to solid-liquid wave routing along Ru Secco (flight of 5 August 2015).

2. MATERIALS AND METHODS

2.1. The Study Site and the Rock Fall Occurred on 14 November 2014

The storm event of the 4 August 2015 hit all the areas contributing to Ru Secco Creek. **Figure 1** shows the plan view of the sub-basins that provided runoff and the routing paths. **Figure 2** shows a frontal view of the upper part of the study area, where the arrows point the path of the liquid and solid-liquid contributions to the whole phenomenon. Ru Secco Creek origins downstream Forcella Piccola Fork and following a quasi straight route reaches the bottom of the Boite Valley where it crosses the village of San Vito di Cadore and flows into the Boite river. It initially flows between two rocky walls and after a drop, it runs on the bottom of the valley between the northern rocky slopes of Mount Antelao, where Ru Salvela Creek origins (**Figure 1**), and the slopes starting at the feet of the rocky massif between Bel Pra and Scotter tops along Northwest-Southeast direction. Along its route, downstream the drop, Ru Beche and Ru Salvela Creeks join it on the right and left side (**Figure 3a**) respectively. About 800 m downstream the second confluences, the Ru Secco Creek is culverted to allow the joining of a slope ski on the right side with a chairlift located on the left side of the creek (**Figure 3b**). In the reach from a location about 300 m upstream the culvert to the inhabitated of San Vito di Cadore, the bed of the Ru Secco creek is protected by a series of check dams. At the entrance of the inhabitated of San Vito di Cadore the Ru Secco is again culverted, and after the exit, it flows into the Boite river. This area, located in the Venetian Dolomites, is dominated by carbonatic Platform formations. The rocky massifs are formed of a thick succession of the calcareous "'Dolomia Principale" Formation with overlaying

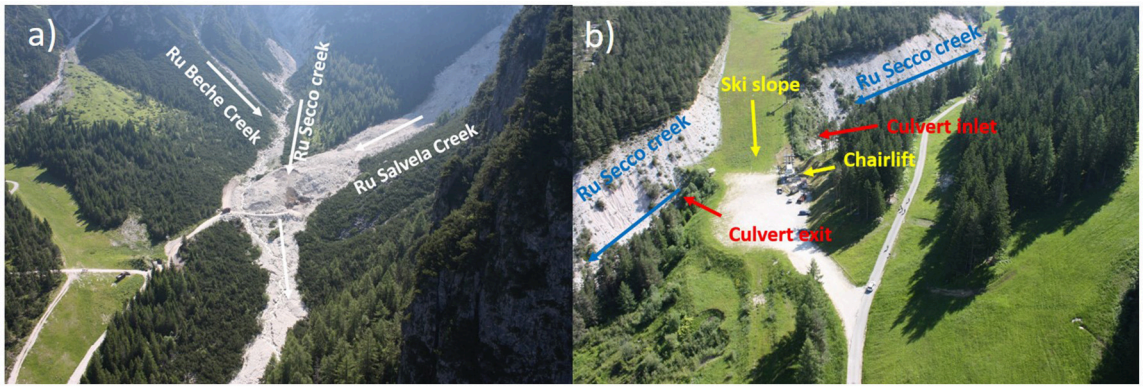

FIGURE 3 | Pre-event images: view of the large debris deposits covering the Ru Salvela and Ru Secco creeks during their removal (flight of 1 July 2015) **(a)** and the culverting of the Ru Secco in correspondence with the ski resort area **(b)**.

limestones of the "Calcari Grigi" Formation. The night of 12 November 2014 a cliff failure on the northern side of Mount Antelao (**Figures 1**, **4**) caused a large rock fall that part deposited on the rocky sloping surface of Vallon d'Antrimoia at the base of the collapsed cliffs and part traveled downstream along the Ru Salvela Creek. It reached the confluence with the Ru Secco Creek and stopped just a hundred meters downstream. All the Ru Salvela Creek, and the Ru Secco Creek from the confluence to a hundred meters downstream, were covered by a thick layer of debris material. In **Figures 3a, 4** the debris thick layer covering the Ru Salvela and Ru Secco Creeks (about 175,000 m^3 according to the computations of section 3). Starting from the Ru Secco Creek, debris material began to be removed: **Figure 3a** shows the situation about 1 month before the occurrence of the debris flow event with the works for reducing the large debris deposits on the Ru Salvela Creek.

About the characteristics of sediments forming the debris deposits that were eroded by runoff and debris flows, we can refer to the grain size analysis carried out through the frequency-by-weight method, on five samples taken on the channelized initiation area of Chiapuzza debris flow (about 1 km north) located on the scree of Cadino dei Ross formed by the rocks collapsed from the overhanging rocky walls of Punta Ross Top. Both the debris deposits on the sites of Vallon d'Antrimoia-Ru Salvela Creek and Cadin dei Ross formed for the collapse of the overhanging rocky cliffs with the same geological Formations. For these reasons, the properties and the characteristics of the debris material are assumed to be quite the same. The five samples of material have a composition ranging in the following intervals for each type of soil: 4% silt ($0.002 \leq d < 0.063$ mm), 33–50% sand ($0.063 \leq d < 2$ mm), 48–58% gravel ($2 \leq d < 63$ mm), and 1–3% cobbles ($63 \leq d < 200$ mm), with a mean density of 2.62 kg/m^3 and a solid volumetric concentration of 0.73. The static friction angle, 39°, was also estimated through triaxial tests.

2.2. Topographical Data

Topographical data are given by two LiDARs flights held on November 2011 and 2015, the photogrammetric restitution of photos of the large debris deposit taken 1 month before the event, a drone photogrammetric flight held 2 days after the event and direct GPS survey held about 2 months after the event. **Figure 5** gives a schematic view of the cover provided by the different topographical data. The pre-event Digital Elevation Model (DEM) is built by using the LiDAR 2011 for all the areas but the debris deposit covering the Ru Salvela Creek till the confluence with Ru Secco Creek where photogrammetric points provided by photos elaboration, are used. The post-event DEM is built using the GPS points, the drone photogrammetric points and for the areas uncovered by this flight the LiDAR 2015. GPS points corresponding to the check dams are also used for the pre-event DEM because they remained substantially

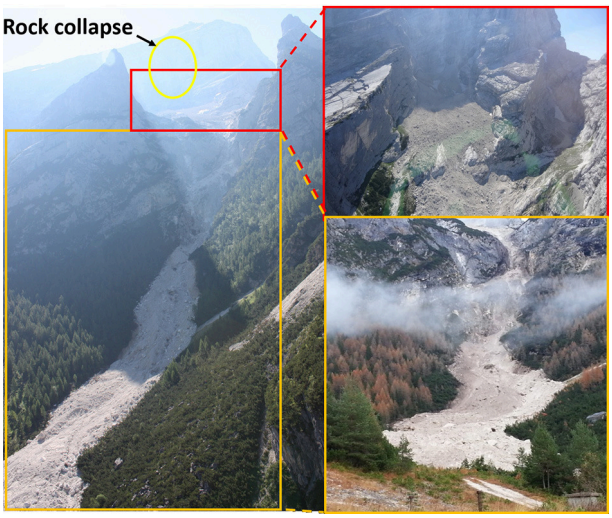

FIGURE 4 | View of the collapsed cliff on the northwestern side of the Mount Antelao (flight of 1 July 2015) and the deposits of debris material from the base of the collapsed cliff to just upstream the confluence with Ru Secco creek. Top right insert shows the debris material covering the Vallon d'Antermoia rocky surface at the base of the collapsed cliff (flight of 1 July 2015). Bottom right insert shows the Ru Salvela creek covered by debris material till the confluence with Ru Secco creek that was obstructed (picture taken on November 2014).

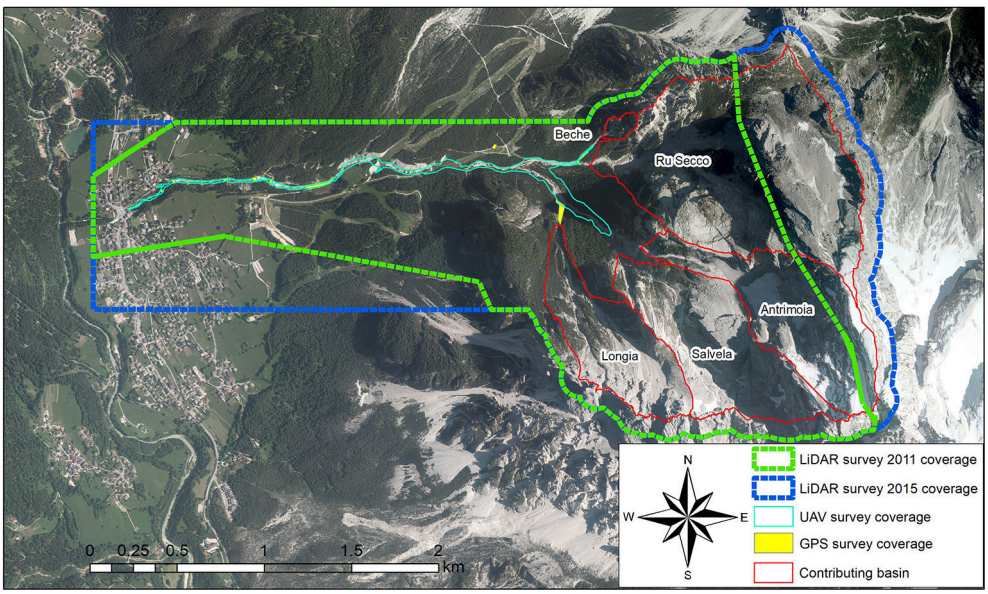

FIGURE 5 | Schematic view of the cover of the topographical data.

unchanged. The DEMs for the hydrological simulations of the basins depicted in **Figure 1** were built by using the LiDAR 2015. LiDAR 2011, in fact, does not cover the upper part of the basins that in part changed after the cliff failure of November 2014, and, the DEMs derived by points along the contour lines of the Regional Techinical Map are characterized by a poor accuracy that could cause a noticeable underestimation of the simulated peak discharge (Degetto et al., 2015). Therefore, as only a part of the surface of the Vallon d'Antrimoia changed after the event due to the erosion, with no significative influence on the hydrological simulation, we used the LiDAR 2015. Density points of the LiDAR 2011 survey is about 1.2 pts/m^2 while that of LiDAR 2015 is about 1.5 pts/m^2. Points provided by the drone flight have a larger density, about 30 pts/m^2. The photogrammetric restitution through the photos relative to the Ru Salvela Creek after the rock fall of November 2014 and before the debris flow event (one is that shown in **Figure 3a**), was carried out by using the software 3DF Zephyr (Lo Brutto and Meli, 2013).

Usually, the accuracy assessment of DEMs is carried out through independent topographic survey points called checkpoints, which should be at least three times more accurate than the DEM elevations being evaluated (Höhle and Höhle, 2009). Unfortunately, an unchanged and significative area, where independent ground control points could be taken, was not available because of the restoration works. This hampered the possibility to perform an extensive vertical accuracy assessment of each employed topographic dataset in a common area. About LiDAR2015 an extensive vertical accuracy assessment was performed using independent Real Time Kinematic GPS measurements, acquired according to a cross-sections morphological-guided spatial sampling scheme along the upper part of the Rovina di Cancia channel on November 2015 (Boreggio et al., 2018). The median of the errors was equal to 0.020 m, and it represents the systematic vertical shift between LiDAR point cloud and the GPS validation data. Conversely, the robust standard deviation of the errors (i.e., the Normalized Median of Absolute Errors) was equal to 0.237 m, which corresponds to the random error component of the LiDAR dataset. More details are in Boreggio et al. (2018). About "photogrammetric points" and "drone points," on some small areas of the Ru Salvela Creek that remained unchanged during the debris flow event we compared the two points data sets. It resulted a nearly good agreement with average differences of about 0.1 m and the largest of 0.4 m.

2.3. The Precipitation

The rainfall on the five basins depicted in **Figure 1** that mainly contributed to the event was obtained after the correction of weather radar estimates with the data of the rain gauge of the monitoring and alarm system installed on the Rovina di Cancia channel by the Province of Belluno. This rain gauge is located at the base of the southeastern cliffs of the Monte Antelao group, at an altitude of 2,150 m a.s.l. and is about 0.8 km far from the centroids of the Salvela and Antrimoia hydrological basins (**Figure 1**). **Figure 6** shows the rainfall depths sampled at 5 min by the rain gauge with those of the corrected radar estimates for each of the five considered hydrological basins. On average the observed rainfall depths are just a slightly smaller than those given by the radar corrected estimates. The core of the precipitation that caused the larger quantity of runoff lasted 20 min and ranged in a 31.5–36.2 mm interval for all the five basins. The corresponding mean intensity values ranged between 94.5 and 108.6 mm/h, while the largest intensity values corresponding to the depth in 5 min, between 118.8 and 159.6 mm/h. This very high intensity and short duration rainfall is a typical precipitation causing the runoff generated debris

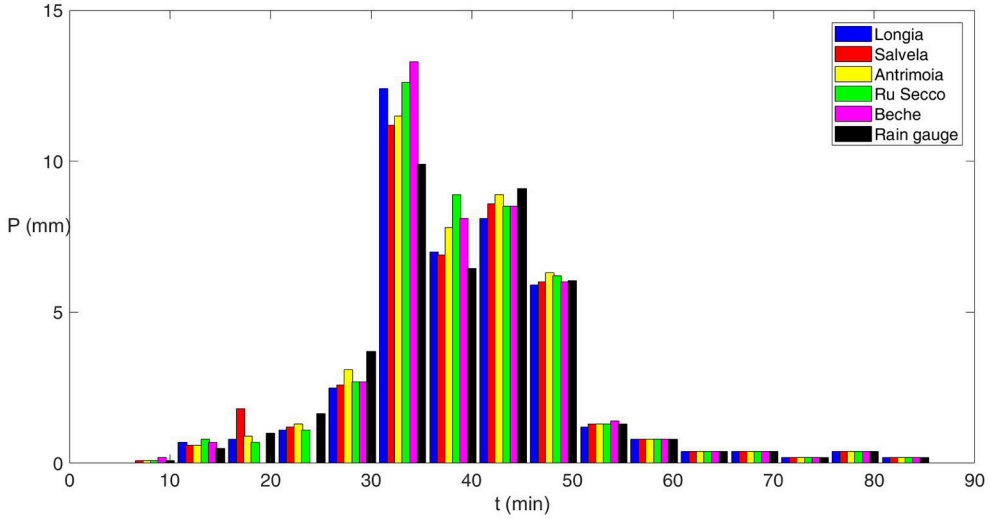

FIGURE 6 | Hyetograph of the rainfall depths from the rain gauge and the corrected radar estimates.

flows that occur along the Boite valley (Bacchini and Zannoni, 2003; Berti and Simoni, 2005; Gregoretti and Dalla Fontana, 2007).

2.4. The Models

In this section, the models used for modeling rainfall-runoff and debris flow routing are presented.

2.4.1. Hydrological Modeling

The hydrological model used in the present study was proposed for headwater rocky catchments by Gregoretti et al. (2016a), after directly testing it by runoff discharge measurements at the outlet of a rocky channel incised on the cliffs of the Dimai Peak (14 km far from Ru Secco Creek), and also indirectly by the debris flow/runoff transit in the initiation area of two other dolomitic catchments, the Acquabona and Rovina di Cancia basins according to Rengers et al. (2016). The centroids of these basins are 8 and 1 km far from the Antrimoia hydrological basin centroid respectively. All these catchments belong to the same geological context and have very similar morphological features.

The excess rainfall P_e contributing to the runoff discharge is computed by coupling the SCS-CN method with a simplified Horton equation that assumes a constant infiltration rate f_c. At each time step t, P_e is given by:

$$P_e(t) = \begin{cases} 0 & t \le t_{I_a} \\ \dfrac{\left(P(t) - I_a\right)^2}{P(t) - I_a + S} & t > t_{I_a}, I < f_c \\ P_e(t) = P_e(t - \Delta t) & \\ +P(t) - P(t - \Delta t) - f_c \Delta t & t > t_{I_a}, I > f_c, P_e < P_{eSCS} \end{cases} \quad (1)$$

where I_a is the initial abstraction, t_{I_a} is the time within I_a occurs, $I_a = 0.2S$, S is the potential maximum retention ($S = 1000/CN - 10$), I is the mean rainfall intensity during the time step Δt, and P_{eSCS} is the excess rainfall of the total precipitation determined through the SCN-CN method. The empirical parameter CN depends on the type, use, and antecedent moisture condition (AMC) of the terrain. Three AMCs are assumed: I, dry condition; AMC II, standard condition; AMC III, wet condition. Following Gregoretti et al. (2016a) for mountain watersheds $I_a = 0.1S$ while Bernard (2018), after examining a larger number of runoff events, diminishes to 2 days the previous rainfall depth for determining the antecedent moisture conditions (AMC). Excess rainfall is conveyed to the channel network along the steepest direction, with a constant value of runoff velocity U, that varies with the terrain typology. The contributes to the channel network are routed to the outlet of the basin using the matched diffusivity kinematic-wave model proposed by Orlandini and Rosso (1996), providing the liquid hydrograph.

2.4.2. The GIS-Based Cell Model

The routing model here introduced is the bi-phase version of the GIS-based cell model proposed by Gregoretti et al. (2016b) that provides a better simulation of the entrainment process (Gregoretti et al., 2018). The governing flow equations are those of mass and momentum conservation coupled with the Exner equation and a modified version of the empirical law of Egashira and Ashida (1987) to express the rate of change of the bed elevations. The mass conservation is stated by means of the continuity equations of the mixture and of the solid phase, while the momentum conservation by means of simplified motion equations of the mixture after assuming equal velocities for both the solid and liquid phases according to Rosatti and Begnudelli (2013). The flow pattern is discretized by the square cells of the DEM. At the cell scale, the continuity equations read:

$$A \frac{d\,(h + z)}{dt} + \sum_{k=1}^{8} Q_k = 0 \quad (2)$$

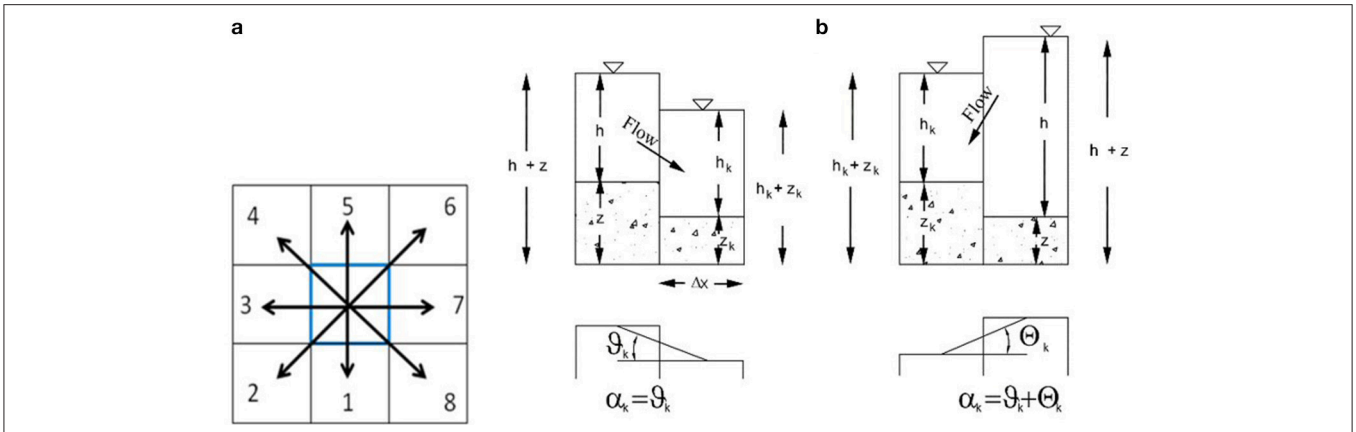

FIGURE 7 | The eight possible flow directions **(a)** and the two possible flow conditions of the routing model **(b)**; partial redrawing of the **Figures 1** and **2** of Gregoretti et al. (2016b).

$$A\,\frac{d(c\,h + c_*\,z)}{dt} + \sum_{k\,=\,1}^{8} Q_k \;=\; 0 \tag{3}$$

where A is the area of the cell, t is time, z is the bottom elevation, h is the flow depth, c is the sediment volumetric concentration of the mixture, c_* is the solid volumetric concentration of the dry bed, and Q_k is the discharge exchanged with the surrounding cells along the $k - th$ direction (**Figure 7a**), assumed to be positive if outflowing and negative otherwise. Following the kinematic wave approach, a uniform flow equation is locally applied if the flow occurs along positive slopes while a broad-crested weir equation is considered if the flow occurs along adverse slopes (**Figure 7b**). The discharges are expressed by the following relationships:

$$\begin{aligned} Q_k \;&=\; \Delta x\,C\,h\,w_k\,\sqrt{g\,h\,\sin\theta_k},\, w_k = \frac{\sin\theta_k}{\sum_{k\,=\,1}^{n}\sin\theta_k},\\ &\theta_k = tan^{-1}\frac{z - z_k}{\Delta x} \end{aligned} \tag{4}$$

$$\begin{aligned} Q_k \;&=\; \Delta x\,C_q\,s_k\,\sqrt{2g}(h - z_k)^{1.5}, s_k = \frac{h - z_k}{\sum_{k\,=\,1}^{m}(h - z_k)},\\ &\Theta_k = tan^{-1}\frac{h + z - h_k - z_k}{\Delta x} \end{aligned} \tag{5}$$

where Δx is the cell size ($= A^{0.5}$), θ_k is the angle formed with the horizontal by the line joining the center of the considered cell with that of the $k - th$ adjacent cell, C is the conductance coefficient (Tsubaki, 1972), and C_q is a discharge coefficient, assumed equal to that of the water (0.385) because of the missing of experimental observations. The two weighting functions w_k and s_k are introduced for partitioning the flow along the eight ($n + m \leq 8$) different directions issuing from a given cell to the adjacent cells, provided that the corresponding bed (θ_k) and flow surface ($h - z_k$) drops are positive.

The choice of the kinematic approach, also used by Lenzi et al. (2003), is justified by the analysis of Arattano and Savage (1994), and Di Cristo et al. (2014) for which a kinematic model can provide reliable simulations of debris flow propagation along sloping channels. The uniform flow Equation (4) can be straightforwardly derived by integrating along the flow depth the dispersive normal stress given by Bagnold (1954), typical of a grain-collision dominated rheology that rules the stony debris flows dynamics (Takahashi, 2007). The use of such a law (i.e., the assumption of grain-inertial rheology) is here justified by the absence of clay and the poor percentages of silt in the material sampled in the initiation areas of the neighboring areas of Chiapuzza (see section 2.1) and Rovina di Cancia (Gregoretti et al., 2018), that have nearly the same characteristics of that eroded on Vallon d'Antrimoia and Ru Salvela Creek. Takahashi (2007) provided also an expression for the conductance coefficient C, depending on an empirical constant that can vary on a large interval, and consequently C up to ten times (Gregoretti, 2000; Takahashi, 2007; Armanini et al., 2009). Therefore, it should be calibrated against field measurements. The Exner equation:

$$\frac{dz}{dt} = D - E \tag{6}$$

provides the rate of change of the cell elevation by the difference between the deposition *(D)* and erosion *(E)* rates. This difference is modeled modifying the empirical relationship of Egashira and Ashida (1987) (see also Brufau et al., 2000; Egashira et al., 2001):

$$E - D = K[(\sin\alpha_k - \sin\theta_{LIM})\,V_{max}] \tag{7}$$

where K is an empirical constant, ranging between 0 and 1, $\alpha_k = \theta_k$ in the case of the uniform flow described by Equation (4), and $\alpha_k = \Theta_k + \theta_k$ in the case of the weir flow associated with Equation (5), with Θ_k the angle that the horizontal forms with the line joining the center of the flow surface of the considered cells along which the flow is directed (**Figure 7b**). Erosion and deposition are computed along the steepest direction, where the maximum value V_{max} of the mean velocities contributing to the discharges Q_k is attained. In particular, deposition occurs if $V_{max} < V_{LIM}$ and $\alpha_k < \theta_{LIM}$, while erosion requires that

$V_{max} > V_{LIM}$ and $\alpha_k > \theta_{LIM}$. The limiting values V_{LIM} and θ_{LIM} are different for deposition (V_{LIM-D}, θ_{LIM-D}) and erosion (V_{LIM-E}, θ_{LIM-E}). Note that, considering a generic direction transversal to the steepest direction could lead to unrealistically large depositions. Furthermore, a cell could be subjected to both erosion and deposition at the same time.

In addition three more conditions descending from the debris flow physics are imposed. Erosion is computed only if $dh/dt > 0$ because according to the field observations of Berger et al. (2011) erosion generally occurs during the passage of the debris flow front, and starts before the maximum value of the flow depth is reached. Moreover, erosion cannot indefinitely occur (i.e., sediment concentration tending to unity) and is allowed within a given cell if $c < 0.9c_*$, maximum transport concentration value according to Takahashi (2007). Likewise deposition can take place if $c > c_D$.

The limiting concentration for deposition, $c_D = 0.05$, is introduced to prevent c from becoming negative if large deposition rates occur, even though no substantial quantitative differences have been observed by setting $c_D = 0$.

The original law of Egashira and Ashida (1987) was adapted after eliminating the reasons for the equilibrium angle because it can lead to uncorrect results. In Gregoretti et al. (2016b) more details about it with its physical justification. Please note that also Hussin et al. (2012) use, even if more simplified, a similar approach to estimate the bed deposition/entrainment rate.

An explicit scheme is used to solve numerically the model equations with the time step computed according to the Courant-Friedrichs-Lewy stability condition. Flow discharges and the rate of change bed elevation are computed for each cell by Equations (4–7) and used in Equation (2) to provide the flow depth. Finally Equation (3) provides the sediment concentration. The reader is referred to Gregoretti et al. (2016b) for more details and explanations about the numerical integration.

3. THE DEBRIS FLOW EVENT: GEOMORPHOLOGICAL ANALYSIS

The geomorphological analysis is essential for understanding whichever gravitative mass movement on earth, and allowing its reliable reproduction by models. It also provides information about its occurrence and behavior to be used in future studies as recommendations for countermeasures. All the basin was carefully surveyed to identify all the contributions, liquid or solid-liquid, to the debris flow that routed along Ru Secco. The entrained and deposited sediment volumes were estimated through the deposition-erosion depths map (**Figures 8a**, **9**) that was obtained differencing the pre and post-event DEMs. The deposition and erosion depths are grouped into classes of 2 m size, about twenty and five times larger the average and maximum error (that of photogrammetric points) respectively. The map of **Figure 9** allows the computation of the sediment volumes deposited and entrained: 108,700 and 57,165 m^3, respectively. Their difference 51,535 m^3 is the sediment volume that runoff entrained on the Vallon d'Antrimoia sloping plateau, upstream the Ru Salvela head. This volume is increased to 52,535 m^3 to consider the sediment volume that reached the Boite River, so that the total mobilized sediment volume raises up to about 110,000 m^3. Therefore, the debris flow event was triggered upstream the Ru Salvela Creek. Abundant runoff descending the northern cliffs of Mount Antelao corresponding to the basins of Antrimoia and Salvela in **Figure 1**, hit the debris deposits laying on the Vallon d'Antrimoia inclined plateau (upper blue arrows in **Figure 2**) and entrained enough sediment to generate a solid-liquid surge. This surge descended along the rock chutes linking the Vallon d'Antrimoia with the Ru Salvela head (upper red arrows in **Figure 2**) and propagated over the debris deposit covering the Ru Salvela Creek. This deposit (**Figures 3a**, **4**) has a volume of 175,000 m^3 obtained differencing the pre-event DEM with that before the rock collapse on November 2014, obtained through the LiDAR 2011 points. During the propagation over the rock fall deposits on Ru Salvela Creek, it entrained the debris material and meanwhile received the liquid contribution from Ru Longia (blue arrow on the right in **Figure 2**), that increased its erosive power. At the confluence with Ru Secco Creek, the well formed debris flow was supplied with the stream flow descending along Ru Secco Creek and the solid-liquid contribution from the debris flow triggered along the Ru Beche. These contributions increased its solid-liquid volume. The large runoff amount and the entrained sediments deriving from cliffs collapse in absence of clay and low percentage of silt, point out to a debris flow of stony type (Takahashi, 2007). The deposition-erosion map of **Figure 8a** clearly shows the erosion occurred along the middle part, in longitudinal sense, of the debris deposit covering the Ru Salvela Creek where the solid-liquid surge, descending from the Vallon d'Antrimoia inclined plateau, excavated a channel (bottom middle insert of **Figure 8a**). Both the sides of this channel are characterized by small debris deposits, i.e., the typical lateral levee that debris flow creates during its routing. These deposits usually occur on debris flow sides when the relative flow depth is small and terrain roughness is able to stop the flowing material. Upstream the confluence, debris flow began also to deposit significative quantities of sediments anticipating that occurred in larger size on the right side of Ru Secco Creek just before and in correspondence of the confluence. **Figure S1** shows the bottom longitudinal profile of the channel excavated by debris flow on the debris deposit covering Ru Salvela Creek with some cross-sections. It can be observed that in the upstream part, debris flow entrained most of the debris material of deposit from the rock collapse while in the downstream part it did not. Debris flow, then, channelized along Ru Secco mainly depositing sediments on the sides and eroding the bed in the middle. About 380 m upstream the first culvert inlet, debris flow began to deposits. This reach is in fact protected by check dams and the bed slope diminishes. The debris flow front reached the inlet culvert where it stopped. Photos taken during the sediment removal operations and located in the Supplemental Material (**Figure S2**) show some big rocks obstructing inlet, i.e., the debris flow front that stopped, while the culvert is not clogged of sediments. In the same **Figure S2**, the exit of the culvert just after the event appears mainly free. The stoppage of the front imposed the deposition of the solid part of the current flowing behind it, that extended both in depth and upstream (up to 380

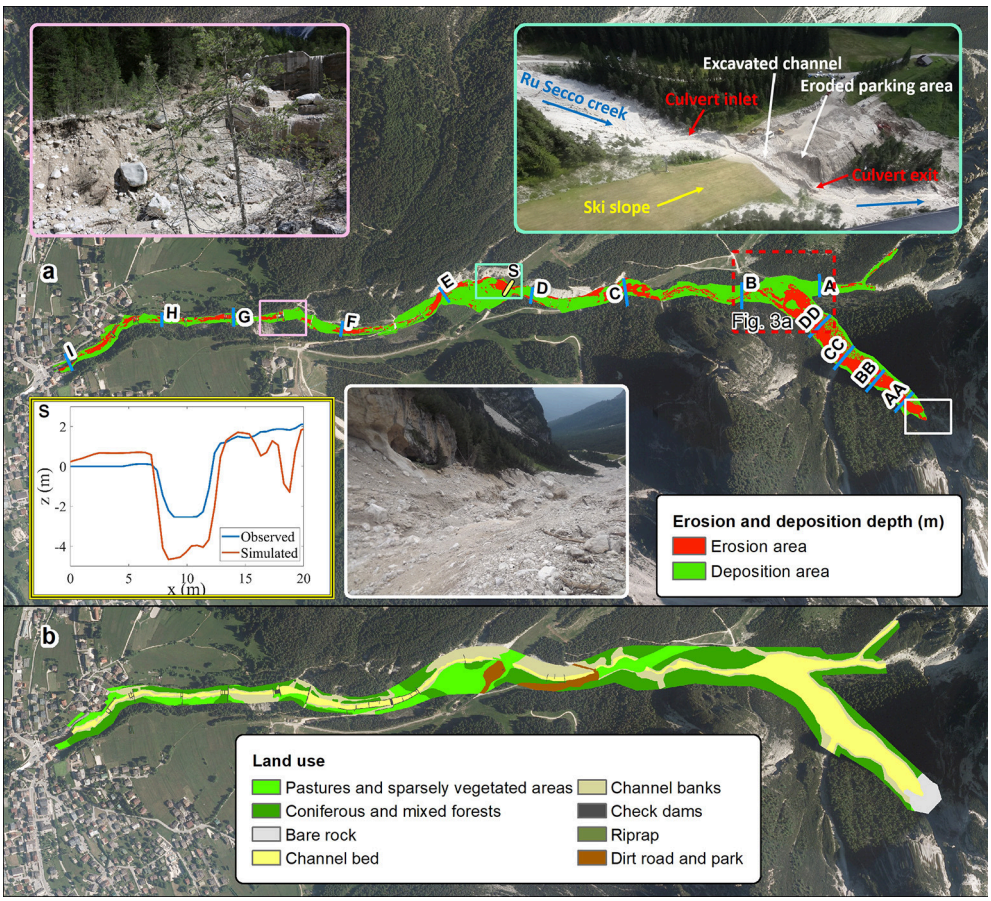

FIGURE 8 | View of the area subjected to deposition or erosion and land use. The upper image **(a)** is the general view of the areas routed by debris flows and subjected to deposition or erosion. The top right insert is the post-event view of the area depicted in **Figure 3b** while the other three inserts show the downstream view of debris flow route incising the debris material covering the Ru Salvela creek (bottom middle), the observed and simulated cross-section of the channel excavated by debris flow above the culvert (bottom left) and a particular of a bank erosion after the upper culvert (top left). The position of the cross-sections that are shown in the **Supplemental Materials** is also indicated. The lower image **(b)** is the landuse of terrain for the routing simulation.

m), interesting all the creek cross-section and only the liquid part flowed downstream. **Figure S3** of the Supplemental Material shows the pre and post-event bottom longitudinal profiles along Ru Secco Creek from the confluence to the village with nine cross-sections (A–I). Upstream the culvert, the bottom is in general raised up respect to the pre-event situation. Nevertheless, the rear part of the solid-liquid current, flowing over this large deposit, reached the culvert and flooded all the area surrounding it. This overflow caused sediments deposition on the main part of the parking and flow returned to the Ru Secco Creek after eroding all the border area of the parking on the creek side (top right insert of **Figure 8a**). The overflow on the terrain above the culvert eroded it creating an erosion channel. Top right and bottom left inserts of **Figure 8a** shows the downstream view of this channel and its cross section respectively. The re-channalized flow routed downstream causing erosion on some bends and mainly downstream the check dams (top left insert of **Figure 8a**) because of the large drop (see also sections E and F of **Figure S3**). The distribution of the volumes of deposited and eroded sediments is analyzed after dividing the flow pattern in five significative areas. **Figure 9** shows the areas with a table listing the corresponding entrained and deposited sediment volumes: most of erosion downstream the Vallon d'Antrimoia inclined plateau, occurred on the debris deposit covering the Ru Salvela Creek (35,400 m^3, about 63% of the total), while most of deposition occurred along Ru Secco between the confluence with the Ru Salvela Creek and the culvert inlet (62,700 m^3, about 55% of the total). The values of the volumes of the deposited and eroded sediments downstream the culvert, about 29,581 and 12,721 m^3 respectively, show that debris flow transformed in an hyperconcentrated flow. This occurred for two main reasons: (1) the large deposition occurred upstream the culvert that stopped the anterior part of debris flow that is usually richer of sediments; (2) the bed slope, that in this reach decreases from 11 and 2°, is not able to guarantee the transport of large quantities of sediments. The view of the cross-sections E–I, downstream the culvert with the pre and post-event bottom longitudinal profiles of the Ru Secco Creek (**Figure S3**) shows that some reaches were subjected to deposition (the larger part), while other subjected to erosion. In **Figure 2** it can be also observed a small debris flow

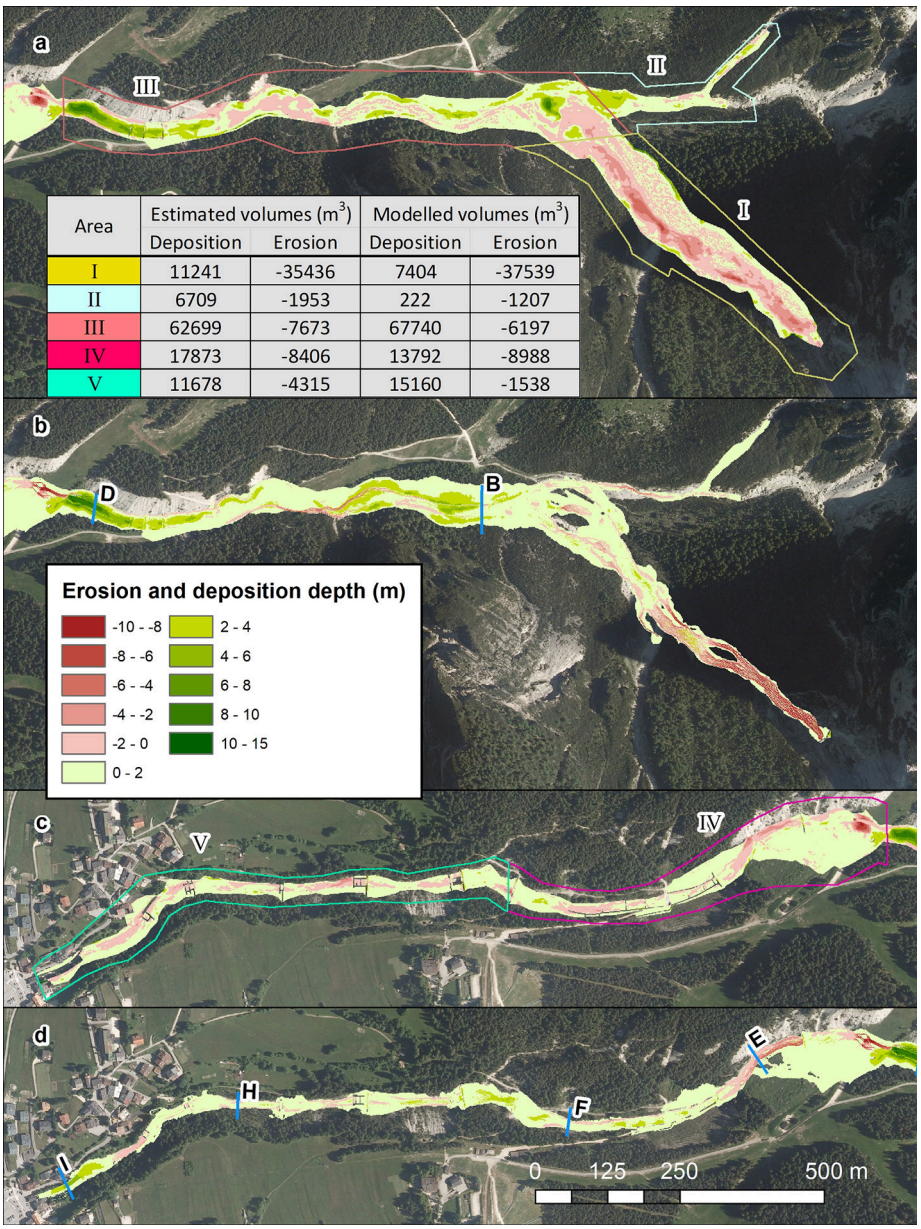

Area	Estimated volumes (m^3)		Modelled volumes (m^3)	
	Deposition	Erosion	Deposition	Erosion
I	11241	-35436	7404	-37539
II	6709	-1953	222	-1207
III	62699	-7673	67740	-6197
IV	17873	-8406	13792	-8988
V	11678	-4315	15160	-1538

FIGURE 9 | Deposition and erosion depths map for the two groups of reaches. Upper image **(a)** is the map of estimated deposition and erosion for the reaches I-III, while the image below **(b)** is that simulated. Images **(c,d)** are the corresponding of **(a,b)** for the reaches IV-V respectively. The position of the six sections (B, D, E, F, H, and I) is also shown.

channel joining the Ru Secco on its right side. Direct field survey showed that its contribution was negligible and for this reason it was not considered in the routing simulations. Until late '50s the slopes on the right side were routed by debris flow providing the main solid-liquid contributions to Ru Secco (**Figures S4**, **S5**). The works for transforming this area in a touristic resort area stopped them. About 200 m downstream the base of the overhanging rocky cliffs, the slope was reshaped, and, where needed, some protection works (walls and pottings) were built. The small debris flow routed a new path on the reshaped slope, avoiding, the protection works.

4. THE PHENOMENON REPRODUCTION BY MODELS

This section concerns the reproduction of the entire phenomenon by models. It is divided in three subsections relative to the hydrological modeling, the solid-liquid hydrographs determination and the debris flow routing. The hydrological modeling provides runoff hydrographs that directly contributed to the phenomenon or entrained the debris material forming the solid-liquid hydrographs of the initial surges. Both runoff and solid liquid hydrographs are the input for the routing modeling.

TABLE 1 | Parameters adopted in the hydrological model.

Coefficient	Rocky surface	Mountain pine slopes	Scree slopes
CN	91.4	61.0	65–70
U (m/s)	0.70	0.05	0.10
f_C (cm/h)	3.5	5.5	10.8

Symbols are defined as follows: CN, Curve Number for computing the excess rainfall; U, runoff velocity; f_c infiltration rate.

4.1. Hydrological Simulations

The rainfall-runoff modeling for the five basins depicted in **Figure 1** was carried out by the model of Gregoretti et al. (2016a). The model computes the excess rainfall for each cell of the basin and routes it through the steepest path to the channel network. The routing to the channel network occurs with constant velocity while that along the channel network to the outlet is ruled by means of a matched-diffusivity kinematic wave model. Parameters for the excess rainfall computation and slope routing are CN, the infiltration rate f_C and slope velocity U which assume different values for each soil typology covering the basin. The values of these parameters are shown in **Table 1** with those of CN and f_C for rocky soil updated by Bernard (2018). Parameters for channel network routing are the roughness coefficient $k_S = 9\mathrm{m}^{1/3}/\mathrm{s}$, the channel width at the outlet, b_0, and a morphological exponent, $b_1 = 0.26$. The values of b_0 were measured in the case of the basins of Ru Longia, Ru Secco and Ru Beche, while for the Salvela and Antrimoia basins, they were obtained by LiDAR 2015 data. These values are shown in **Table 2**. The event occurred in AMC I conditions, because it did not rain in the previous 2 days (Bernard, 2018). The flow path from each cell of the basin to the channel network is obtained through the DEM (see Gregoretti et al., 2016a for details). The channel network cannot be provided by cells with a drainage area larger than 0.005 km^2 as proposed by McGlynn and Seibert (2003) and McGuire et al. (2005). This threshold value was successfully tested by Gregoretti et al. (2016a) in the head water rocky basin of Dimai that has the same morphological features of those investigated here and about 10 km far but, unfortunately, it cannot be applied to the Ru Beche basin. Its area is too small (about 0.022 km^2) and that threshold does not work because too large. For this reason, we investigated the transition from slope to channel routing by using two different methodologies: (1) the convergence of the upslope drainage area values after using different techniques (Wilson and Gallant, 2000); (2) the slope scaling method (Ijjasz-Vasquez and Bras, 1995). The first method examines the convergence of values of the upslope drainage area computed following the $D8$ and $D\infty$ methods (Tarboton, 1997). The value where the values of drainage areas converge, is the area threshold value for determining the channel network. The second method explores the behavior of the drainage area vs. its mean slope. The drainage area values, where there is a discontinuity, correspond to the transition from slope routing to channel routing. The two methods provide the same results supporting the reliability of the obtained threshold value for the determining the channel network. **Figure S6** shows the results of the two methods. These values together those of the morphometric characteristics of the basins are shown in **Table 2**. Simulations were carried out using both the radar estimates and the observed rainfall depths. Results are shown in **Figure 10**. Simulations corresponding to the corrected radar estimates provide runoff hydrographs slightly larger except that of the Ru Secco basin whose peak value is about 25% larger.

TABLE 2 | Morphometric characteristics of the basins: A_B, basin area; A_T, threshold area for channel network; z_O, basin outlet altitude; z_M, mean basin altitude; z_{MAX}, maximum basin altitude; SL_{MEAN}, mean slope; SL_{MAX}, maximum slope; b_0, outlet width.

	Ru Longia	Salvela	Antrimoia	Ru Secco	Ru Beche
A_B (km^2)	0.4	0.57	0.57	1.25	0.022
A_T (km^2)	0.0096	0.0095	0.0098	0.0096	0.00071
z_O (m a.s.l.)	1,537	1,698	1,873	1,477	1,578
z_M (m a.s.l.)	2,112	2,303	2,584	2,143	1,727
z_{MAX} (m a.s.l.)	2,557	3,142	3,218	2,900	1,889
SL_{MEAN} (%)	113	145	2,584	119	175
SL_{MAX} (%)	2,759	6,044	3,218	5,362	1,684
b_0 (m)	2.5	3	3	3	1.5

4.2. The Solid-Liquid Hydrographs

The sites on the Vallon Antrimoia sloping plateau where the solid-liquid surges formed after the impact of runoff with the debris deposits could not be surveyed because of their inacessibility. Therefore, we determineted the solid-liquid hydrographs at the middle of the rock chute following the methodology proposed by Gregoretti et al. (2018). We adopted a triangular shape of the solid-liquid hydrograph with an abrupt raise to peak and a less rapid decreasing because downstream the triggering area, the debris flow surge tends to assume such a shape. The solid-liquid volume is given by the sum of the solid volume with the volumes of runoff contributing to debris flow and of the interstitial water of the entrained sediments as also proposed by Gregoretti et al. (2012, 2016a). Because of the high intensity precipitation and the quite high permeabilty of the debris, deposits are assumed to be nearly in saturated conditions. The solid volume can be obtained by the volume of sediments entrained on the Vallon d'Antrimoia that is provided by the difference between the computed deposited and eroded sediment volumes downstream it: $108{,}700 - 57{,}165 = 51{,}535$ m^3. This volume is increased to 52,535 m^3 to consider the sediment volume that reached the Boite River (see the previous section). The solid volume is the entrained sediments volume multiplied by c_*. The runoff contributing to debris flow is the part of runoff hydrograph where the runoff discharge is larger than the triggering discharge (see also Gregoretti et al., 2016b and Han et al., 2017). In the present case, the inaccessibility of the triggering site prevented direct measurements, and the unit width triggering discharge was estimated as 0.05 m^2/s through the relationship proposed by Gregoretti and Dalla Fontana (2008) after assuming reasonable values of sediments mean size (0.1 m) and bed slope angle (30°). The interstitial water volume is given by the difference between the entrained sediments volume and the just computed solid volume. The solid-liquid hydrograph is

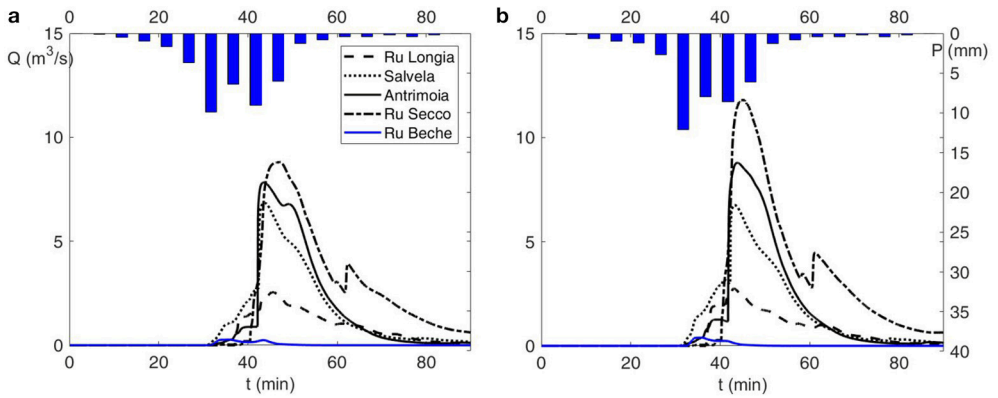

FIGURE 10 | Modeled runoff hydrographs for the five basins corresponding to the measures **(a)** and corrected radar estimates **(b)** of rainfall depth.

TABLE 3 | Values of the parameters used in the routing simulations for the different terrains.

Terrain	C	θ_{LIM-D} (°)	V_{LIM-D} (m/s)	θ_{LIM-E} (°)	V_{LIM-E} (m/s)
Debris flow channel	5	14	1	16	1.8
Debris flow channel banks	3	8	0.5	9	0.9
Channel downstream culvert - upper reach	6	5	0.8	9	1.3
Banks downstream culvert - upper reach	4	4	0.5	7	0.8
Channel downstream culvert - lower reach	6	2.5	0.8	5	1.3
Banks downstream culvert - lower reach	4	2	0.5	4	0.8
Wood	1	12	0.8	20	3
Grass	3	14	1	20	2
Parking	5	8	0.8	12	1

the triangle with the height equal to the peak discharge value and the base equal to the ratio between the double of the solid-liquid volume and the peak value. The peak solid-liquid discharge, Q_P, is computed following the relationship provided by Lanzoni et al. (2017):

$$\frac{Q_P}{Q_0} = 0.75 \frac{c_*}{c_* - c_F} \tag{8}$$

where c_F is the solid volumetric concentration of the debris flow front, and, Q_0 is the runoff peak discharge. The value for c_* is assumed equal to 0.62 (value proposed by Gregoretti et al., 2016b for unchannelized debris deposits that are not subjected to compaction) and that for c_F equal to $0.9c_*$ (0.558) according to Takahashi (2007). The two solid-liquid hydrographs are computed by using the runoff hydrograph of the two basins of Antrimoia and Salvela after partioning the sediments volume (52,535 m^3) in 38,035 and 14,500 m^3, respectively. The Antrimoia basin, in fact, occupies the larger part of the Vallon Antrimoia sloping plateau where debris deposits lie. The resulting solid-liquid hydrographs are shown in **Figure S7**.

4.3. Routing Simulations

Parameters of debris flow routing simulation depend on the terrain (channel, scree, grass, wood) and slope because flow resistance and deposition-entrainment processes vary with them. **Figure 8b** shows the land use of the terrain interested by the phenomenon. The values of parameters used for the routing simulation are shown in **Table 3**. This set of parameters, until the culvert, is that used by Gregoretti et al. (2016b, 2018) for reproducing two occurred debris flows after a sensitivity analysis based on the comparison between simulations and observations of deposition/erosion depths. Only the conductance coefficient, C, respect to Gregoretti et al., 2016b, was increased from 3 to 5 where the flow is channelized. Gregoretti et al. (2016b) in fact simulated the dispersion in several directions on a fan of a debris flow of high magnitude while in present case the flow is channelized. In the case of channelized flow, estimates of C, from field data of stony debris flows with a magnitude much lower than that here studied (Gregoretti, 2000; Hurlimann et al., 2003; Okano et al., 2012), mostly range in the interval 1–3. Flume experiments of Tognacca (1999) and Lanzoni et al. (2017) on stony debris flows show that the velocity increases with the triggering discharge much more than the flow depth, and consequently also the conductance coefficient C increases with it. **Figure S8** shows, in fact, the growth of the experimental values of C with the triggering discharge. This means that the debris flow discharge, and thus the magnitude of the debris flow, increases with the amount of the runoff generating the event, while the flow resistance decreases. Therefore, the value of the conductance coefficient was raised to 5 because this

event, characterized by a magnitude higher than that of the observed and above referenced debris flows, was triggered by a larger runoff amount. Downstream the culvert, debris flow transforms to hyperconcentrated flow because most of solid material deposited upstream and bed slope decreases from 11° to 2° along the flow direction. This means an increase of the conductance coefficient and a decrease of the limit values of angle and velocity both for deposition and entrainment because the transported solid concentration decreases (Armanini, 2015). The values of parameters downstream the culvert were assigned after calibration. For all the channelized flows, different values of parameters were adopted for the banks where, due to the low submergence, flow resistance is larger and for the wooded and grass areas. The value of the parameter relevant for erosion, θ_{lim-E}, was assumed equal to 16°, inferior angle associated to the occurrence of mature channalized stony debris flows according to the experiments of Lanzoni et al. (2017). This value was also confirmed by the field observations of Jordan (1994). According to Gregoretti et al. (2018), we also adopted values of K equal to 0.1 and 0.5 for deposition and entrainment respectively.

The simulated deposition and erosion depths are shown together those estimated in **Figure 9**. The flow pattern, for a better comparison between simulation and estimate of the deposited and eroded sediments volume, has been divided in five reaches: the Ru Salvela Creek (I), the Ru Beche (II), the Ru Secco Creek upstream the culvert (III), the Ru Secco Creek downstream the culvert with a mean bed slope of 8° (IV) and the ending reach with a mean bed slope of 4.5° (V). In particular both the simulated and estimated deposition and erosion depths are shown in two groups of reaches, I–III and IV–V respectively, allowing a more detailed analysis together with a table the values of the simulated and estimated sediment volumes, that were eroded and deposited for each reach. The comparison of simulation results with the observations (**Figure 9**) shows that the main features of the deposition-erosion pattern are captured by the simulation except at the confluence of Ru Salvela with Ru Secco Creek and in the downstream part of the ending reach where the bed sloping angle decreases to a value of about 2°. The simulated volumes of deposited and eroded sediments are 104,318 and 55,469 m^3, respectively. Both of them underestimate those observed of 4 and 3% respectively. This overall satisfactorily agreement between observations and simulations, obtained using the same parameters for reproducing two other debris flows in the Dolomites, points to a validation of the routing model here used for simulating solid-liquid flows in the grain-inertial range. The examination of the results reach by reach allows a better understanding of the model capability to simulate the occurred phenomenon. In reach I (that of Ru Salvela creek), the simulated eroded sediment volume quasi coincides with that estimated but it is more concentrated in the upstream part of Ru Salvela. This could be due to an imperfect reproduction of the pre-event DEM at the head of the Ru Salvela. This zone is just under the cliffs and some three dimensional shapes of debris deposits could be not detectable by the photos by which the pre-event DEM has been built. For this reason, in the upstream part, the simulated debris flow front mainly concentrated in a narrow path that was highly eroded. Resulting debris surge was too concentrated and, therefore, eroded a smaller amount of sediments in the downstream part. About deposition, the large deposits at the confluence were not satisfactory reproduced due to missed local bed reproduction of the terrain in the pre-event DEM. The deposits on this area were subjected to excavation during the restoration works in the month between the photo time and the event. Therefore, some path and the flat area built by the excavators, that we could not to reproduce, could have significatively conditioned the flow routing. Sediment volume that did not deposited there during simulation, in fact, deposited just downstream the confluence (beginning of reach III). In fact simulated deposition depths, there, are on average larger than those estimated. Routing along Ru Beche (reach II) was satisfactory simulated but not that along the Ru Secco Creek between the two confluences with Ru Beche and Ru Salvela Creeks. This could be a result of the missed deposition of flow arriving from the Ru Salvela Creek, explained above. There is a quite good agreement between simulation results and observations along reach III: nearly coincidence of areas subjected to the main deposition and erosion phenomena combined with the nearly coincidence of the simulated and estimated sediments volumes that were depositated and entrained (the percentage of simulated deposited sediments volume is 8% higher than that observed due to the missing of simulated deposits at the confluence). The flooding of the park and the erosion of it, together the excavation of a channel in the terrain overlaying the culvert, is also nealry satisfactory simulated. The bottom left insert of **Figure 8a** shows the comparison between the surveyed and simulated cross section of the excavated channel. The simulation of the excavation appears fairly satisfactorily, even if larger. For the reach IV visual inspection of **Figures 9c,d** shows that erosion and deposition pattern is well reproduced and the simulated eroded sediments volume nearly coincides with that estimated. Only the deposition volume is underestimated. For the reach V, the agreement is not so satisfactory both for the volumes and the areas. In fact the erosion on its downstream part is not captured, while conversely deposition is overestimated. **Figure 11** shows the simulated solid-liquid and solid discharge, Q (left) and Q_S (right) respectively, for the six sections shown in **Figure 9**. The solid-liquid discharge reaches its maximum after the confluence and then it begins to decrease. The solid discharge is consistent until section F (**Figure 9**) due to the large erosion occurred upstream. After that, it decreases to negligible values, characteristics of bed-load sediment transport.

5. DISCUSSION OF RESULTS

The direct post-event field survey and the analysis of the pre-event morphology during time allowed the geomorphological analysis of the event. It consisted in the recognition of the phenomenon occurrence and of its main features. The analysis of the pre-event morphology between '50s and nowadays also showed that slopes on the right side of Ru Secco Creek were

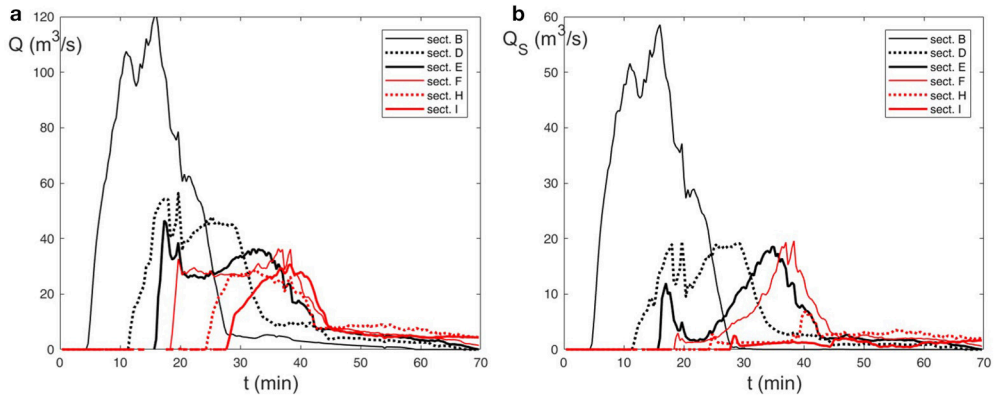

FIGURE 11 | Simulated hydrographs of solid-liquid **(a)** and solid discharge **(b)**, Q and Q_S respectively, corresponding to the the traces of the six sections of **Figure 9**.

routed by debris flows before their transformation in a ski resorting area while the left side was not subjected to debris flow phenomena (**Figures S4**, **S5**). In the present case study, the environmental changes due to man works can stop or reduce debris flow activity in areas prone to debris flow susceptibility, while those due to natural causes, as the formation of debris deposits caused by local terrain instabilities, if connected to the channel network (Cavalli et al., 2013; Tiranti et al., 2016, 2018), allow the conditions for debris flow occurrence, where it never did. Both the historical basins where debris flows formed until '50s and the new one of Ru Salvela are debris flow dominated according to the geomorphic indexes: the ruggedness number of Melton close or larger than 1 [0.75 is the inferior threshold value according to DeScally and Owens (2004)] and local slope larger than 0.6 m/m in the schematic diagram between local slope and drainage area proposed by Montgomery and Foufoula-Georgiou (1993) for the hillslope to valley transition also used by Tarolli and Dalla Fontana (2009). Therefore, even if the basins are prone to debris flow activity according to the geomorphic indexes above, debris flow occurrence is determined by sediment availability as the concentration of abundant runoff on it. Finally, the geomorphological analysis, providing a reliable description of the occurred phenomenon, is at the base of simulation of the phenomenon by models. The reproduction of the occurred phenomenon was the results of two phases: a careful survey of all the sub-basins supplying solid-liquid and liquid flows both the debris deposits covering Ru Salvela Creek and the Ru Secco Creek, allowed the identification of all the significative solid-liquid and liquid contributions (1); simulation by models of the formation and routing of these contributions and their impact on debris deposits (2). Reliable models results were allowed by trustworthy rainfall estimates that provided the input to the hydrological model and by topographical data that provided the base for running and testing them. The pre-event topographical data provided the DEM for running the routing simulations. The post-event topographical data were used for determining the post-event DEM of the area routed by debris flow that, subtracted to the pre-event DEM, provided the deposition-erosion depths map, essential for understanding the phenomenon and testing the modeling. For this reason, the availability of pre and post-event data becomes fundamental for a reliable understanding of the phenomenon, as for its reproduction by models. Unfortunately, the simultaneous availability of pre and post-event data is not frequent but rare because in many cases the pre event terrain topography is usually unknown: previous occurred debris flow phenomena, also of small magnitude, and local instability phenomena (rock falls from upstream cliff and/or channel bank failures) can significatively change the flow path morphology, and consequently, debris flow routing could not be captured by simulations.

The reproduction of the occurred phenomenon, shown in the previous section, appears, in general, satisfactory. The deposition and erosion pattern, in fact, is quite well reproduced both in terms of areas and volumes apart some parts of the Ru Salvela Creek and of the ending reach. The simulation in the upstream reaches of Ru Salvela and Ru Secco Creeks is conditioned by pre-event local topographical data that are partially inaccurate and missing respectively. In the first case, the exact shape of pre-event debris deposit at the head of the Salvela Creek was not captured, while in the second case, due to the restoration work, the topography of some areas close to the confluence of Ru Salvela Creek with Ru Secco Creek changed. The presence of excavator tracks and flat areas due to the debris deposits reworking could have significatively conditioned the local routing simulation. As a consequence the deposition at the confluence was understimated. The simulation downstream these reaches provides quite good results: the areas subjected to large phenomena of deposition and erosion are captured. Only the deposition depths upstream the culvert slightly overstimate those observed because of the missed deposition at the confluence of Ru Salvela Creek with Ru Secco Creek, and some areas subjected to erosion in the ending reach are missed. Moreover, the shape of the channel excavated by the debris flow after the culvert occlusion is nearly approximated (bottom left insert of **Figure 8a**). The analysis of the solid-liquid and solid discharges (**Figure 11**) allows a better understanding of the occurred phenomenon. After the confluence of Ru Salvela with Ru Secco the debris flow discharge peak has the maximum value and that of solid discharge is

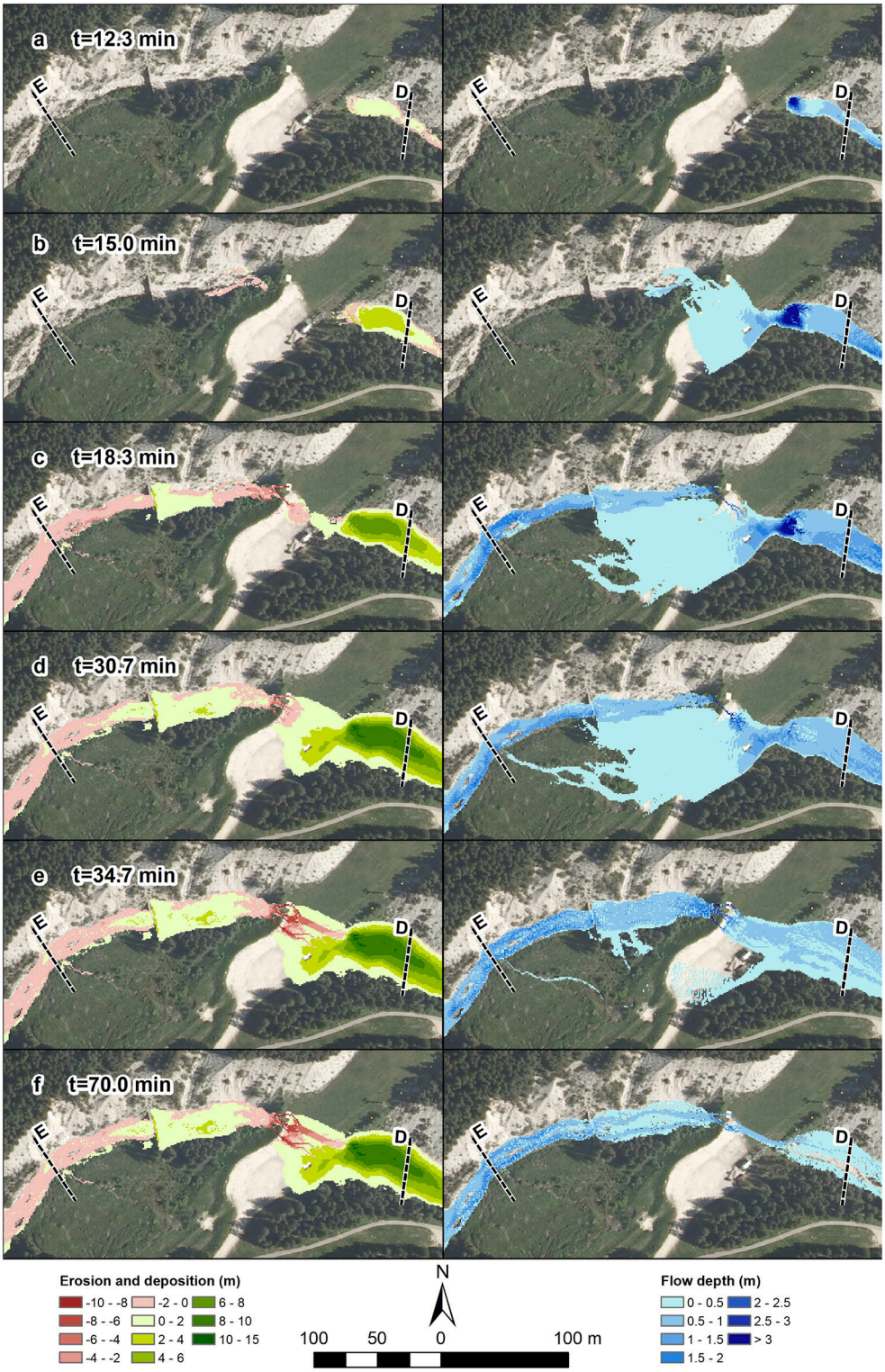

FIGURE 12 | The deposition and erosion depths (Left) and flow depths (Right) maps at different times [**(a)** t = 12.3 min, **(b)** t = 15.0 min, **(c)** 18.3 min, **(d)** t = 30.7 min, **(e)** t = 34.7 min, **(f)** t = 70.0 min] from the beginning of the simulation of the area close to the culvert and parking.

nearly the half (cross-section B). Just upstream the culvert (cross-section D) the solid-liquid discharge peak is reduced to less than 50% while that of solid one to about 30% due to the large deposition phenomena mostly due to the culvert occlusion. In the reach upstream the culvert solid-liquid and liquid discharge are in phase while in the downstream reach, it does not occur. In the cross-section E, downstream the culvert, the discharge in the first ten minutes is mostly liquid because the occlusion at the culvert inlet causes the deposition of most of solid phase. Solid discharge, in fact after an initial but moderate increase, decreases to a neglegible value and then increases again to a value nearly the half of the total discharge. This behavior is the consequence of the initial erosion on the bend downstream the culvert followed by that of the parking on the Ru Secco side and on the terrain overlaying the culvert. **Figure 12** shows the time evolution of the simulated deposition and erosion pattern with the flow depth in correspondence of the culvert: at the beginning there is only a mainly liquid flow over the terrain downstream the culvert inlet that reaches the Ru Secco and causes the erosion on its right side as shown by **Figures 12a–c**. This is coherent with the initial moderate solid discharge peak in cross-section E (**Figure 11**). In the following 20 min the deposition and erosion on parking become consistent with the excavation of the channel just over the culvert (**Figures 12d–f**) that is responsible of the second solid discharge peak in cross–section E (**Figure 11b**). In cross-section F the behavior is analogous but for the absence of the initial moderate peak of solid discharge, reasonably due to an upstream deposition. Along cross-sections H and I solid-liquid peak discharge remains unchanged while flow volumes diminish because of the deposition. The solid discharge, in fact, decreases to negligible values, typical of bed load sediment transport. This could be the main reason for the not satisfactory simulation of the end part of the last reach V. In fact the hyperconcentrated flow transforms to a flow with low concentration values that on bed sloping angles of about 4.5° the cell model could be not able to simulate with efficacy.

The in general satisfactory and reliable reproduction of the occurred phenomenon provides a confirm of the methodology here followed for simulating a runoff generated debris flow when information on the triggering site are scarce: simulation of runoff, determination of the solid-liquid hydrograph in the initiation area and simulation of its downstream routing. Concerning the debris flow initiation, McGuire et al. (2017) proposed a more general and refined mathematical modeling, here not usable due to lack of information on the triggering area that resulted inaccessible. However, the simple and direct determination of the solid-liquid hydrograph, here proposed, proved to be reasonable and reliable. For debris flow routing, only models that consider deposition and entrainment should (Chen et al., 2006; Medina et al., 2008; Armanini et al., 2009; Hussin et al., 2012; Frank et al., 2015; Cuomo et al., 2016) should be used, provided their capability to simulate these processes. Finally, present work of back analysis of the phenomenon is also important, because it provides the framework and data needed for testing other models.

6. CONCLUSIONS

The 4th of August 2015, a high intensity storm concentrated on a square of about two kilometers and triggered some in-channel debris flows on Venetian Dolomites. The debris flow occurred on Ru Secco Creek was of large magnitude with about 100,000 m^3 entrained sediments. Ru Secco Creek was not routed by debris flows since late 50s after works for transforming its right side generally affected by debris flows, into a ski resort area. The debris flow of August 2015 started, in fact, on the opposite side because of the presence of very large debris deposits at the base of northeastern cliffs of Mount Antelao after a rock collapse occurred on November 2014. Direct field surveys and the analysis of pre and post-event topography allowed the recognition of liquid and solid-liquid contributions to the occurred phenomenon and its main features, as well as the map of deposition and erosion depths. Finally the phenomenon was modeled from rainfall-runoff transformation to deposition-erosion processes with satisfactory results: most of entrainment and deposition processes were captured except where initial topography data were partially inaccurate or missing or when solid discharge decreased to values typical of bed load. For the part strictly concerning the routing, these results were mainly due to the cell model of Gregoretti et al. (2018) that allows a better simulation of the entrainment process.

Based on these analysis and modeling results, the main conclusions of this work can be summarized as follows. One of the main triggering factor for runoff generated debris flows is the sediment availability. The presence of debris deposits, due to local terrain instability phenomena, lead to the occurrence of a debris flow where it never occurred before. Furthermore, the satisfactorily results obtained in the reproduction of the phenomenon suggest that a reliable reproduction of an occurred debris flow should be based on four factors:

1. an accurate geomorphic analysis showing the main processes that caused it and occurred during its evolution. This analysis provides a guide for the implementation of the models simulating the physical processes concurrent to its development as well as the initial conditions;
2. a sufficiently accurate topographic base for the generation of DEMs on which models should run. Inaccuracy of topographical data or their missing can lead to unexpected and unreliable results;
3. a models cascade simulating all the physical processes associated to the debris flow occurrence;
4. the capability of the used models of capturing the main features of the phenomena associated to debris flow occurrence as the impulsive response of runoff to rainfall at the base of rocky cliffs and the entrainment and deposition processes occurring during the debris flow routing.

The in general satisfactory reproduction of the phenomenon by models proved the reliability of both the used methodology and single models. It should be stressed that the values of parameters used for running the models are mostly those resulting from the comparison between observations and simulations of other events. This is a good outcome because it shows the predictability

characteristics of the models here used. Reliability of models is very important because a trustworthy prediction of debris flow routing (discharge hydrograph, deposition and erosion depths as the inundated area) is essential in any analysis of hazard assessment and countermeasures planning. At this purpose, the capability of the routing model to adequately simulate the entrainment process has a crucial role because the solid-liquid discharge peak and the transported sediments volume mainly depend on it. At least the updated cell model used here for the routing simulation proved to give reliable results also for hyperconcentrated flow and bed slopes larger than 8°.

AUTHOR CONTRIBUTIONS

CG carried out the surveys, determined the solid-liquid hydrographs, provided the cell routing model and run the routing simulations. MD carried out the surveys, analyzed the topografical data, built the pre and post-event DEMs, studied the hydrological groups of terrain and its morphology preparing most data for running the hydrological model. MBe helped in the pre and post-event DEM building, provided the hydrological model and run the hydrological simulation, contributed to the solid-liquid hydrographs determination prepared the file data for running the routing simulations, helped in run the routing simulations, analyzed the results, made figures. MBo helped in the pre and post-event DEM building, run the occurrence model, prepared the file data for running the routing simulations, helped in run the routing simulations, analyzed the results, made figures.

ACKNOWLEDGMENTS

This work was supported by the municipality of San Vito di Cadore that is thanked by the authors. Authors wish also to thank the Regional Civil Work Agency of Veneto for the LiDAR 2015, the drone flight, the photos of the helicopter flights of 1 July and 5 August 2015 and the documentation relative to the occurred debris flow; the Regional Environment Protection Agency of Veneto and the Department of Soil Defence of the Province of Belluno for the meteorological data; the Department Land Defence and Civil Protection of the Province of Belluno for the LiDAR 2011, the Meteorological Service of the Province of Bolzano for the weather radar observations. Finally, the authors wish to thanks the reviewers for their criticisms and suggestions that helped to improve significantly the manuscript. Data are available under request to the corresponding author.

SUPPLEMENTARY MATERIAL

The Supplementary Material for this article can be found online at: https://www.frontiersin.org/articles/10.3389/feart.2018.00080/full#supplementary-material

REFERENCES

Arattano, M., and Savage, W. (1994). Modelling debris flows as kinematic waves. *Bull. Int. Assoc. Eng. Geol.* 49, 3–13. doi: 10.1007/BF02594995

Armanini, A. (2015). Closure relations for mobile bed debris flows in a wide range of slopes and concentrations. *Adv. Water Resour.* 81, 75–83. doi: 10.1016/j.advwatres.2014.11.003

Armanini, A., Fraccarollo, L., and Rosatti, G. (2009). Two-dimensional simulation of debris flows in erodible channels. *Comput. Geosci.* 35, 993–1006. doi: 10.1016/j.cageo.2007.11.008

Bacchini, M., and Zannoni, A. (2003). Relation between rainfall and triggering of debris flow: case stydu of cancia (dolomites, northeastern italy). *Nat. Hazards Earth Syst. Sci.* 3, 71–79. doi: 10.5194/nhess-3-71-2003

Baglioni, A., and De Marco, P. (2015). *Fenomeni di colata detritica ed inondazione verificatosi nel bacino del Ru Secco (San Vito di Cadore) il 4/8/2015. Osservazioni geologiche preliminari*. Technical Report - Regional Civil Work Agency of Veneto Region.

Bagnold, R. A. (1954). Experiments on a gravity-free dispersion of large solid spheres in a newtonian fluid under shear. *Proc. R. Soc. Lond. Ser. A* 225, 45–63. doi: 10.1098/rspa.1954.0186

Berger, C., McArdell, B., and Schlunegger, F. (2011). Direct measurement of channel erosion by debris flows, illgraben, switzerland. *J. Geophys. Res.* 116:F01002. doi: 10.1029/2010JF001722

Bernard, M. (2018). *Analysis of Rainfalls Triggering Debris Flows and Modelling of Corresponding Runoff*. PhD. Thesis - Università degli Studi di Padova.

Berti, M., and Simoni, A. (2005). Experimental evidences and numerical modelling of debris flow initiated by channel runoff. *Landslide* 2, 171–182. doi: 10.1007/s10346-005-0062-4

Boreggio, M., Bernard, M., and Gregoretti, C. (2018). Evaluating the influence of gridding techniques for digital elevation models generation on debris flow routing modelling: a case study From Rovina di Cancia basin (North-Eastern Italian Alps). *Front. Earth. Sci.* 6:89. doi: 10.3389/feart.2018.00089

Brufau, P., Garcia-Navarro, P., Ghilardi, P., Natale, L., and Savi, F. (2000). 1-d mathematical modelling of debris flow. *J. Hydraul. Res.* 38, 435–446. doi: 10.1080/00221680009498297

Cannon, S., Gartner, J. E., Wilson, R. C., Bowers, J. C., and Laber, J. L. (2008). Storm rainfall conditions for floods and debris flows from recently burned areas in southwestern colorado and southern california. *Geomorphology* 96, 250–269. doi: 10.1016/j.geomorph.2007.03.019

Cavalli, M., Trevisano, M., Comiti, F., Bowers, J. C., and Marchi, L. (2013). Geomorphometric assessment of spatial sediment connectivity in small alpine catchments. *Geomorphology* 188, 31–41. doi: 10.1016/j.geomorph.2012.05.007

Chen, H., Crosta, G., and Lee, C. (2006). Erosional effect on run-out of fast landslide, debris flows and avalanches: a numerical investigation. *Geotechnique* 56, 305–322. doi: 10.1680/geot.2006.56.5.305

Coe, J. A., Kinner, D. A., and Godt, J. W. (2008). Initiation conditions for debris flows generated by runoff at Chalk Cliffs, Central Colorado. *Geomorphology* 96, 270–297. doi: 10.1016/j.geomorph.2007.03.017

Cuomo, S., Pastor, M., Capobianco, V., and Cascini, L. (2016). Modelling the space- time bed entrainment for flow-like landslide). *Eng. Geol.* 212, 10–20. doi: 10.1016/j.enggeo.2016.07.011

Degetto, M., Gregoretti, C., and Bernard, M. (2015). Comparative analysis of the differences between using lidar contour-based dems for hydrological modeling of runoff generating debris flows in the dolomites. *Front. Earth Sci.* 3:21. doi: 10.3389/feart.2015.00021

DeScally, F., and Owens, I. (2004). Morphometric controls and geomorphic responses on fans in the southern alps, new zealand. *Earth Surf. Process. Landforms* 29, 311–322. doi: 10.1002/esp.1022

Destro, E., Amponsah, W., Nikolopoulos, E., Marchi, L., Marra, F., Zoccatelli, D., et al. (2018). Coupled prediction of flash flood response and debris flow occurrence: application on an alpine extreme flood event. *J. Hydrol.* 558, 225–237. doi: 10.1016/j.jhydrol.2018.01.021

Di Cristo, C., Iervolino, M., and Vacca, A. (2014). Applicability of kinematic, diffusion and quasi-steady dynamic wave models to shallow mud flows. *J. Hydrol. Eng.* 19, 956–965. doi: 10.1061/(ASCE)HE.1943-5584.0000881

Egashira, S., and Ashida, K. (1987). "Sediment transport in steep slope flumes," in *Proceedings of the RoC Japan Joint Seminar on Water Resources*.

Egashira, S., Honda, N., and Itoh, T. (2001). Experimental study on the entrainment of bed material into debris? *ow. Phys. Chem. Earth (C)* 26, 645–650.

Frank, F., McArdell, B., Huggel, C., and Vieli, A. (2015). The importance of entrainment and bulking on debris flow runout modeling: examples from the swiss alps. *Nat. Hazards Earth Syst. Sci.* 15, 2569–2583. doi: 10.5194/nhess-15-2569-2015

Gregoretti, C. (2000). "Estimation of the maximum velocity of a surge of debris flow propagating along an open channel," in *International Symposium Interpraevent 2000 Villach 26-30 June*, 99–108.

Gregoretti, C., Adams, M., Hagen, K., Laigle, D., Liebault, F., Degetto, M., et al. (2012). "Forecast system guidelines debris flows. guidelines for the implementation of forecast system against debris flow hazard (wp6)," in *Project PARAmount imProved Accessibility: Reliability and Security of Alpine Transport Infrastructure Related to Mountainous Hazards in a Changing Climate, Alpine Space, European Regional Development Fund (ERDF)* (Brussels).

Gregoretti, C., and Dalla Fontana, G. (2007). "Rainfall threshold for the initiation of debris flows by channel bed failure of the dolomites," in *Proceedings of the Fourth International Conference on Debris Flow Hazards Mitigation*, eds C. L. Chen and J. J. Major (Chengdu: Balkema), 11–21.

Gregoretti, C., and Dalla Fontana, G. (2008). The triggering of debris flow due to channel-bed failure in some alpine headwater basins of the dolomites: analyses of critical runoff. *Hydrol. Process.* 22, 2248–2263. doi: 10.1002/hyp.6821

Gregoretti, C., Degetto, M., Bernard, M., Crucil, G., Pimazzoni, A., De Vido, G., et al. (2016a). Runoff of small rocky headwater catchments: field observations and hydrological modeling. *Water Resour. Res.* 52, 8138–8158. doi: 10.1002/2016WR018675

Gregoretti, C., Degetto, M., and Boreggio, A. (2016b). Gis-based cell model for simulating debris flow runout on a fan. *J. Hydrol.* 534, 326–340. doi: 10.1016/j.jhydrol.2015.12.054

Gregoretti, C., Stancanelli, L. M., Bernard, M., Boreggio, M., Degetto, M., and Lanzoni, S. (2018). Relevance of erosion processes when modelling in-channel gravel debris flows for efficient hazard assessment. doi: 10.1016/j.jhydrol.2018.10.001

Han, X., Chen, J., Xu, P., and Zhan, J. (2017). A well-balanced numerical scheme for debris flows run-out predictions in the xiaojia gully considering different hydrologic designs. *Landslide* 14, 2105–2114. doi: 10.1007/s10346-017-0850-7

Höhle, J., and Höhle, M. (2009). Accuracy assessment of digital elevation models by means of robust statistical methods. *ISPRS J. Photogrammet. Remote Sens.* 64, 398–406. doi: 10.1016/j.isprsjprs.2009.02.003

Hu, W., Dong, X. J., Wang, G. H., van Asch, T. W. J., and Hicher, P. Y. (2016). Initiation processes for run-off generated debris flows in the wenchuan earthquake area of china. *Geomorphology* 253, 468–477. doi: 10.1016/j.geomorph.2015.10.024

Hurlimann, M., Abanco, C., Moya, J., and Villalosana, I. (2014). Results and experiences gathered at the rebaixader debris-flow monitoring site, central pyrenees, spain. *Landslide* 2, 161–175. doi: 10.1007/s10346-013-0452-y

Hurlimann, M., Rickenmann, D., and Graf C. (2003) Field and monitoring data debris-flow events in the Swiss Alps. *Can. Geotech. J.* 40, 161–175. doi: 10.1139/T02-087

Hussin, H., Quan Luna, B., Van Westen, C., Christen, M., Malet, J., and van Asch, T. (2012). Parameterization of a numerical 2-d debris flow model with entrainment: a case study of the faucon catchment, southern french alps. *Nat. Hazards Earth Syst. Sci.* 12, 3075–3090. doi: 10.5194/nhess-12-3075-2012

Ijjasz-Vasquez, E., and Bras, L. (1995). Scaling regimes of local slope versus contributing area in digital elevation models. *Geomorphology* 12, 299–311. doi: 10.1016/0169-555X(95)00012-T

Imaizumi, F., Sidle, R. C., Tsuchiya, S., and Ohsaka, O. (2006). Hydrogeomorphic processes in a steep debris flow initiation zone. *Geophys. Res. Lett.* 33, 157–171. doi: 10.1029/2006GL026250

Iverson, R. M., Schilling, S. P., and Vallance, J. W. (1998). Objective delineation of lahar-hazard zones downstream from volcanoes. *Geol. Soc. Am. Bull.* 110, 972–984.

Jordan M. (1994). *Debris Flows in the Southern Coast Mountains, British Columbia: Dynamic Behaviour and Physical Properties*. PhD. thesis, University of British Coulumbia, Vancouver, BC.

Kean, J., McCoy, S. W., Tucker, G. E., Staley, D. M., and Coe, J. A. (2013). Runoff-generated debris flows: observations and modeling of surge initiation, magnitude and frequency. *J. Geophys. Res.* 118, 2190–2207. doi: 10.1002/jgrf.20148

Lanzoni, S., Gregoretti, C., and Stancanelli, M. (2017). Coarse-grained debris flow dynamics on erodible beds. *J. Geophys. Res.* 122, 592–614. doi: 10.1002/2016JF004046

Lenzi, M. A., D'Agostino, V., Gregoretti. C., and Sonda D. (2003). "A simplified numerical model for debris-flow hazard assessment: DEFLIMO," in *Third International Conference On Debris Flow Hazard Mitigations: Mechanics, Prediction and Assessment* (Davos).

Lo Brutto, M. C., and Meli, P. (2013). "Performance evaluation of 3d web-services and open-source software for digital modeling of archeological finds," in *Proceedings of Archeofoss*, eds F. Stanco and G. Gallo, 11–21.

Mattea, S., Franceschinis, C., Scarpa, R., and Thiene, M. (2016). Valuing landslide risk reduction programs in the Italian Alps: The effect of visual information on preference stability. *Land Use Policy* 59, 176–184. doi: 10.1016/j.landusepol.2016.08.032

McGlynn, B, L., and Seibert, J. (2003). Distributed assessment of contributing area and riparian buffering along stream networks. *Water Resour. Res.* 39:1082. doi: 10.1029/2002WR001521

McGuire, K. J., McDonnell, J. J., Weiler, M., Kendall, C., McGlynn, B. L., Welker, J. M., et al. (2005). The role of topography on catchment-scale water residence time. *Water Resour. Res.* 41:W05002. doi: 10.1029/2004WR003657

McGuire, L., Rengers, J., Kean, J., and Staley, D. (2017). Debris flow initiation by runoff in a recently burned basin: is grain-by-grain. *Geophys. Res. Lett.* 44, 7310–7319. doi: 10.1002/2017GL074243

Medina, V., Hurlimann, M., and Bateman, A. (2008). Application of flatmodel, a 2d a finite volume code to debris flows in the northeastern part of the iberian peninsula. *Landslide* 5, 127–142. doi: 10.1007/s10346-007-0102-3

Montgomery, D., and Foufoula-Georgiou, E. (1993). Channel network source representation using digital elevation models. *Water Resour. Res.* 29, 3925–3934. doi: 10.1029/93WR02463

Navratil, O., Liebault, F., Bellot, H., Travaglini, E., Theule, J., Chambon, G., et al. (2013). High-frequency monitoring of debris flows propagation along the real torrent, southern french alps. *Geomorphology* 201, 157–171. doi: 10.1016/j.geomorph.2013.06.017

Okano, K., Suwa, H., and Kanno, T. (2012). Characterization of debris flows by rainstorm condition at a torrent on the mount yakedake volcano, Japan. *Geomorphology* 136, 88–94. doi: 10.1016/j.geomorph.2011.04.006

Orlandini, S., and Rosso, R. (1996). Diffusion wave modeling of distributed catchment dynamics. *J. Hydrol. Eng.* 1, 103–113. doi: 10.1061/(ASCE)1084-0699(1996)1:3(103)

Reid, M. E., Coe, J. A., and Dianne, L. B. (2016). Forecasting inundation from debris flows that grows volumetrically during travel, with application to the Oregon Coast Range, USA. *Geomorphology* 273, 396–411. doi: 10.1016/j.geomorph.2016.07.039

Rengers, F. K., McGuire, L. A., Kean J. W., and Hobley, D. E. (2016). Model simulations of flood and debris flow timing in steep catchments after wildfire. *Water Resour. Res.* 52:6041. doi: 10.1029/2015WR018176

Rickenmann, D. (1999). Empirical relationships for debris flows. *Nat. Hazards* 19, 47–77. doi: 10.1023/A:1008064220727

Rosatti, G., and Begnudelli, L. (2013). Two dimensional simulations of debris flows over mobile beds: enhancing the trent2d model by using a well-balanced generalized roe-type solver. *Comput. Fluids* 71, 179–185. doi: 10.1016/j.compfluid.2012.10.006

Santi, P. M., deWolfe, V. G., Higgins, J. D., Cannon, S. H., and Gartner, J. E. (2008). Sources of debris flow material in burned areas. *Geomorphology* 96, 310–321. doi: 10.1016/j.geomorph.2007.02.022

Stancanelli, L. M., Peres, D. J., Cancelliere, A., and Foti, E. (2017). A combined triggering-propagation modeling approach for the assessment of rainfall induced debris flow susceptibility. *J. Hydrol.* 550, 130–143. doi: 10.1016/j.jhydrol.2017.04.038

Takahashi (2007). *Debris Flow, Mechanics, Prediction and Countermeasures*. Leiden: Taylor and Francis/Balkema.

Tarboton, D. (1997). A new method for the determination of flow directions and upslope areas in grid digital elevation models. *Water Resour. Res.* 33, 309–319. doi: 10.1029/96WR03137

Tarolli P., and Dalla Fontana G. (2009). Hillslope-to-valley transition morphology: new opportunities from high resolution DTMs. *Geomorphology* 113, 47–56. doi: 10.1016/j.geomorph.2009.02.006

Theule, J., Liebault, F., Loye, A., Laigle, D., and Jaboyedoff, M. (2012). Sediment budget monitoring of debris flow and bedload transport in the manival torrent, se france. *Nat. Hazard Earth Sci.* 12, 731–749. doi: 10.5194/nhess-12-731-2012

Thiene, M., Shaw, W. D., and Scarpa, R. (2017). Perceived risks of mountain landslides in Italy: stated choices for subjective risk reductions. *Landslides* 14, 1077–1089. doi: 10.1007/s10346-016-0741-3

Tiranti, D., Cavalli, M., Crema, S., Comiti, F., Zerbato, M., Graziadei, M., et al. (2016). Semi-quantitative method for the assessment of debris supply from slopes to river in ungauged catchments. *Sci. Total Environ.* 554–555, 337–448. doi: 10.1016/j.scitotenv.2016.02.150

Tiranti, D., Cavalli, M., Crema, S., and Deangeli, C. (2018). An integrated study to evaluate debris flow hazard in alpine environment. *Front. Earth Sci.* 6:60. doi: 10.3389/feart.2018.00060

Tiranti, D., and Deangeli, C. (2015). Modeling of debris flow depositional patterns according to the catchment and sediment source area characteristics. *Front. Earth Sci.* 3:8. doi: 10.3389/feart.2015.00008

Tognacca, C. (1999). *Beitrag zur Untersuchung der Entstehungsmechanismen von Murgängen*. Doctoral Thesis, ETH Zurich.

Tsubaki (1972). "Keikoku taiseki dosha no ryndo," in *XXVII Japanese National Congress on Civil Engineering*.

Wilson, J., and Gallant, J. (2000). *Terrain Analysis: Principles and Applications*. Newyork, NY: JohnWiley and Sons Inc.

Conflict of Interest Statement: The authors declare that the research was conducted in the absence of any commercial or financial relationships that could be construed as a potential conflict of interest.

NOMENCLATURE

The following symbols are used in this paper:

A = cell area;
A_T = threshold area for channel network;
A_B = basin area;
b_0 = outlet width;
b_1 = morphological exponent;
b_0 = outlet width;
c = sediment volumetric concentration of the mixture;
c_D = limit inferior sediment volumetric concentration for deposition;
c_F = solid volumetric concentration of the debris flow front;
c_* = solid volumetric concentration of dry bed;
C = conductance coefficient;
CN = curve number;
d = sediment diameter;
D = deposition rate;
E = erosion rate
f_c = infiltration rate
g = acceleration due to gravity;
h = flow depth in a cell;
I = rainfall intensity;
I_a = initial abstraction;
K = Egashira empirical coefficient;
k_S = Gauckler-Strickler roughness coefficient;
P = cumulative rainfall;
Pe = excess rainfall ;
$PeSCS$ = excess rainfall computed throug the SCS-CN method;
Q = solid-liquid discharge;
Q_p = peak solid-liquid discharge;
Q_0 = runoff peak discharge
Q_S = solid discharge;
S = potential maximum retention
SL_{MEAN} = mean slope;
SL_{MAX} = maximum slope;
t_{Ia} = time at which Ia occurs;
U = slope velocity along a possible flow direction;
V_{LIM} = limit superior velocity for deposition (V_{LIM-D}) or erosion (V_{LIM-E});
V_{max} = maximum velocity
z = bed level
z_O = basin outlet altitude;
z_M, mean basin altitude;
z_{MAX} = maximum basin altitude;
α = angle controlling deposition and entrainment
Δt = time step;
Δx = grid size;
θ = angle respect to the horizontal of the line joining the centers of two neighboring cells of DEM;
θ_{LIM} = limit superior angle for deposition (θ_{LIM-D}) or erosion (θ_{LIM-E});
Θ = angle respect to the horizontal of the line joining the centers of flow surface of two neighboring cells ;
AMC = Antecedent Moisture Content; CFL = Courant-Friedrichs-Levi; DEM = Digital Elevation Model; GIS = Geographical Information System; LiDAR = Light Detection and Ranging SCS = Soil Conservation Service;

frontiers in Earth Science

ORIGINAL RESEARCH
published: 07 November 2018
doi: 10.3389/feart.2018.00089

Evaluating the Differences of Gridding Techniques for Digital Elevation Models Generation and Their Influence on the Modeling of Stony Debris Flows Routing: A Case Study From Rovina di Cancia Basin (North-Eastern Italian Alps)

Mauro Boreggio, Martino Bernard and Carlo Gregoretti*

Department of Land Environment Agriculture and Forestry, University of Padova, Legnaro, Italy

OPEN ACCESS

Edited by:
Davide Tiranti,
Agenzia Regionale per la Protezione Ambientale (ARPA), Italy

Reviewed by:
Milad Janalipour,
K.N.Toosi University of Technology, Iran
Guy Jean-Pierre Schumann,
University of Bristol, United Kingdom

****Correspondence:***
Mauro Boreggio
mauro.boreggio@gmail.com

Specialty section:
This article was submitted to Quaternary Science, Geomorphology and Paleoenvironment, a section of the journal Frontiers in Earth Science

Received: *16 March 2018*
Accepted: *15 June 2018*
Published: *07 November 2018*

Citation:
Boreggio M, Bernard M and Gregoretti C (2018) Evaluating the Differences of Gridding Techniques for Digital Elevation Models Generation and Their Influence on the Modeling of Stony Debris Flows Routing: A Case Study From Rovina di Cancia Basin (North-Eastern Italian Alps). Front. Earth Sci. 6:89. doi: 10.3389/feart.2018.00089

Debris flows are among the most hazardous phenomena in mountain areas. To cope with debris flow hazard, it is common to delineate the risk-prone areas through routing models. The most important input to debris flow routing models are the topographic data, usually in the form of Digital Elevation Models (DEMs). The quality of DEMs depends on the accuracy, density, and spatial distribution of the sampled points; on the characteristics of the surface; and on the applied gridding methodology. Therefore, the choice of the interpolation method affects the realistic representation of the channel and fan morphology, and thus potentially the debris flow routing modeling outcomes. In this paper, we initially investigate the performance of common interpolation methods (i.e., linear triangulation, natural neighbor, nearest neighbor, Inverse Distance to a Power, ANUDEM, Radial Basis Functions, and ordinary kriging) in building DEMs with the complex topography of a debris flow channel located in the Venetian Dolomites (North-eastern Italian Alps), by using small footprint full-waveform Light Detection And Ranging (LiDAR) data. The investigation is carried out through a combination of statistical analysis of vertical accuracy, algorithm robustness, and spatial clustering of vertical errors, and multi-criteria shape reliability assessment. After that, we examine the influence of the tested interpolation algorithms on the performance of a Geographic Information System (GIS)-based cell model for simulating stony debris flows routing. In detail, we investigate both the correlation between the DEMs heights uncertainty resulting from the gridding procedure and that on the corresponding simulated erosion/deposition depths, both the effect of interpolation algorithms on simulated areas, erosion and deposition volumes, solid-liquid discharges, and channel morphology after the event. The comparison among the tested interpolation methods highlights that the ANUDEM and ordinary kriging algorithms are not suitable for building DEMs with complex topography. Conversely, the linear triangulation, the natural neighbor algorithm, and the thin-plate spline plus tension

and completely regularized spline functions ensure the best trade-off among accuracy and shape reliability. Anyway, the evaluation of the effects of gridding techniques on debris flow routing modeling reveals that the choice of the interpolation algorithm does not significantly affect the model outcomes.

Keywords: Digital Elevation Models (DEMs), interpolation algorithms, interpolation algorithms comparison, full-waveform LiDAR, LiDAR data accuracy assessment, DEMs accuracy assessment, stony debris flow, routing modeling

INTRODUCTION

Taking up the definition proposed by Iverson (2005), "debris flows can be defined as turbulent flowing mixtures of sediment and liquid in nearly equal proportions". Debris flows are found in a wide variety of mountainous environments worldwide (Berti et al., 1999), and in particular in the Dolomites area (North-eastern Italian Alps) they mainly initiate by mobilization of the channel-bed material due to surface runoff (Berti et al., 1999; Berti and Simoni, 2005; Gregoretti and Dalla Fontana, 2008; Theule et al., 2012; Tiranti and Deangeli, 2015). Debris flows seem to have increased in occurrence in the last few years, possibly by the rise of extreme rainfall events (Easterling et al., 2000; Floris et al., 2010), and the availability of debris material provided by the retreat of the glaciers and the permafrost areas to higher elevations (Degetto et al., 2015) owing to the global climatic change. In order to reduce debris flows hazard and the related socio-economic impact (Mattea et al., 2016; Thiene et al., 2017), it is common to couple structural and non-structural measurements, such as the zoning of risk prone areas and the development of emergency plans (Ghilardi et al., 2001).

Hazard mapping consists in identifying the areas that are threatened either historically or potentially by debris flows. The methods used to simulate potential hazard scenarios are both empirical-based (e.g., Scheidl and Rickenmann, 2010; Berti and Simoni, 2014) and model-based (e.g., Rickenmann et al., 2006; Deangeli, 2008; Medina et al., 2008; Armanini et al., 2009; Hussin et al., 2012; Gregoretti et al., 2018a). Since the topography is the major control over fluxes of water and sediments (Moore and Grayson, 1991; Hancock, 2006; Saksena and Merwade, 2015), the topographic data usually in the form of DEMs represent the most important input in debris flows routing models (e.g., Rickenmann et al., 2006; Sodnik et al., 2012).

A DEM can be defined as a mathematical representation of the bare earth in digital form (Erdogan, 2009; Vosselman and Maas, 2010), and it is commonly used to represent the surface morphology in three dimensions (Heritage et al., 2009). Two very well-known formats for the storage of DEMs data are the raster and the grid structure, also known as pixel- and lattice-model respectively (e.g., Wilson and Gallant, 2000; Wise, 2000, 2007; Pfeifer, 2005; Smith et al., 2005; Cilloccu et al., 2009; Hengl and Reuter, 2009; Vosselman and Maas, 2010; Höhle and Potuckova, 2011). Within the raster structure, each value represents the orthometric height of the whole area covered by the raster element (i.e., the square cell). Conversely, a grid structure represents the orthometric height information onto a regular two-dimensional array of points, which by convection are taken to lie in the center of square pixels. Clearly, it is the appropriate data format for DEMs, since the elevation estimates relate to points and not to areas.

The grid heights are determined starting from sample topographic data by means of deterministic or stochastic interpolation algorithms, in a basic step often referred to as gridding (Hengl and Reuter, 2009). Even if recent developments in the field of remote sensing allow to reach high sampling density (i.e., up to one point per square centimeter in non-vegetated areas for terrestrial laser scanner- and structure from motion-derived points clouds, Heritage and Large, 2009; Fonstad et al., 2013), artifacts (e.g., cut-offs, over-smoothing, and over-shooting) and uncertainties in DEMs may be formed during the gridding step whichever interpolation technique is used (Carrara et al., 1997; Smith et al., 2005; Heritage et al., 2009; Milan et al., 2011). However, the magnitude and spatial pattern of these uncertainties can greatly vary with different interpolation methods, since each technique considerably differs both in its sensitivity to the spatial distribution of the sampled data and their associated errors (Hengl and Reuter, 2009; Garnero and Godone, 2011), and in its ability to fit the real morphology (Smith et al., 2005). Consequently, the choice of the gridding methodology and its related parameters are very significant decisions in determining the realistic digital representation of the surface morphology (especially in uneven terrain, like the areas where debris flows occur), and thus for the reliability of routing modeling outcomes (Desmet, 1997; Blöschl and Grayson, 2000; Chaplot et al., 2006; Weng, 2006; Heritage et al., 2009; McDonnell and Lloyd, 2015).

Although many studies have compared the performance of many interpolation algorithms using different datasets related to several physical variables (e.g., hydrological, pedological, and topographical) and environments, the existing literature tends to be somewhat contradictory about the most reliable one. Furthermore, notwithstanding the general awareness about the potential impact of DEMs interpolation uncertainties on the numerical modeling, little work has been done to understand how these uncertainties affect the debris flow routing models

Abbreviations: DEM(s), Digital Elevation Model(s); LiDAR, Light Detection And Ranging; GIS, Geographic Information Systems; TIN(s), Triangulated Irregular Network(s); IDP, Inverse Distance to a Power function; RBFs, Radial Basis Functions; ALS, Airborne Laser Scanner; GPS, Global Positioning System; RTK-GPS, Real-Time Kinematic GPS; ESDA, Exploratory Spatial Data Analysis; NMAD, Normalized Median of Absolute Deviations; RMSE, Root Mean Square Error; MAE, Mean Absolute Error.

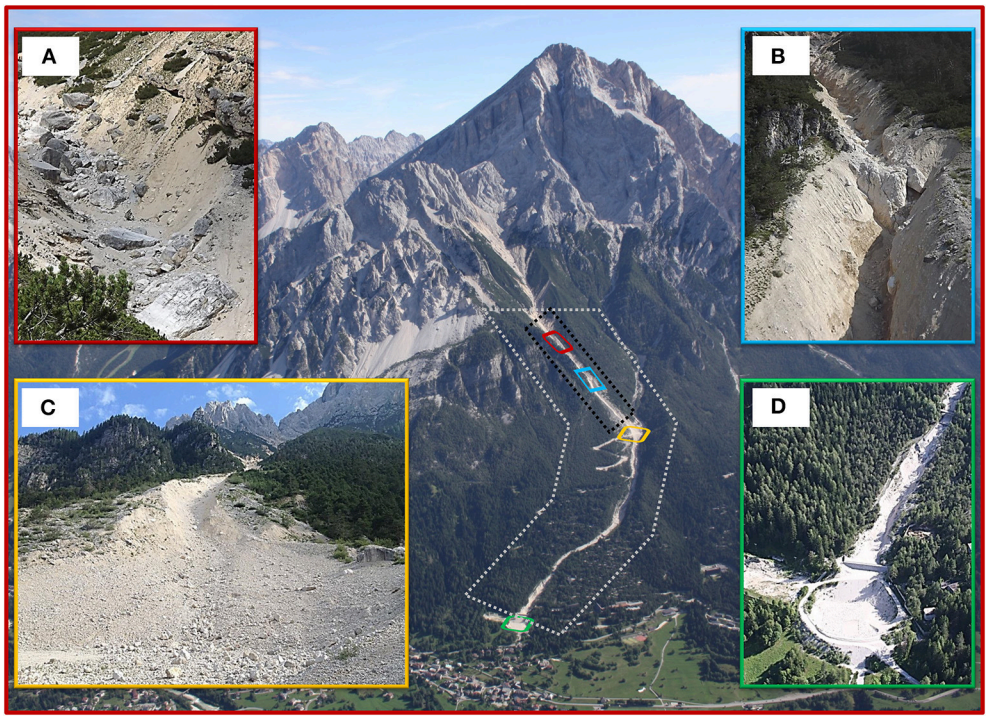

FIGURE 1 | Aerial view of the Rovina di Cancia study site. **(A)** Debris flow triggering area (∼1,670 m a.s.l.), **(B)** natural rock step located at the end of the debris flow triggering area (∼1,500 m a.s.l.), **(C)** man-built flat deposition area (∼1,340 m a.s.l.), **(D)** final flat circular deposition basin (∼1,000 m a.s.l.). Dotted white line: LiDAR data coverage and hydraulic model domain; dotted black line: RTK-GPS data coverage.

TABLE 1 | Computed standard and robust accuracy measures.

Accuracy measures	Values (m)	95% Confidence intervals (m)
Mean	0.032	[0.028, 0.038]
Standard deviation	0.304	[0.301, 0.308]
Root Mean Square Error (RMSE)	0.306	[–]
Threshold for the outliers removal (3*RMSE)	0.928	[–]
N. outliers (% of the error sample)	251 (1.98%)	[–]
Mean (after the outliers removal)	0.026	[0.022, 0.031]
Standard deviation (after the outliers removal)	0.260	[0.257, 0.263]
Median	0.020	[-0.020, 0.050]
Normalized Median of Absolute Deviations (NMAD)	0.237	[0.208, 0.267]
68.3% sample quantile of the absolute errors distribution	0.250	[0.220, 0.280]
95% sample quantile of the absolute errors distribution	0.630	[0.500, 0.780]

results. In order to fill this gap, in this study we first compare the performance of several commonly used digital terrain modeling algorithms in representing the complex topography of a debris flow channel located in the Venetian Dolomites, by using small footprint full-waveform LiDAR data. As one of the major remote sensing techniques which developed exponentially during the last decade in landslides investigation and hydraulic modeling is the LiDAR (e.g., French, 2003; Cavalli and Marchi, 2008; Scheidl et al., 2008; Jaboyedoff et al., 2012; Sodnik et al., 2012; Bossi et al., 2014; Tarolli, 2014), we assumed that nowadays this kind of data represents the most frequently used topographic information to create accurate and high-resolution DEMs of mountain catchments. In detail, the investigation is performed through a combination among statistical analysis of vertical accuracy, algorithm robustness, and spatial clustering of vertical errors, and multi-criteria shape reliability assessment. Finally, we assess the influence of the tested interpolation algorithms on the results of a GIS-based debris flows cell routing model. The assessment is carried out by investigating both the correlation between the DEMs heights uncertainty resulting from the interpolation procedure and that on the corresponding simulated erosion/deposition depths, both their effect on simulated areas, erosion and deposition volumes, solid-liquid discharges, and channel morphology after the event.

Therefore, this research may be useful for digital elevation data users involved in hazard modeling and prediction in morphologically complex areas, who are increasingly looking for a global, freely available, high-accuracy digital representation of the earth surface. It represents an up to date question, as demonstrated by the recent launch of the research topic in Frontiers in Earth Science "A global high-resolution digital elevation model: a paradigm shift in high impact research and applications."

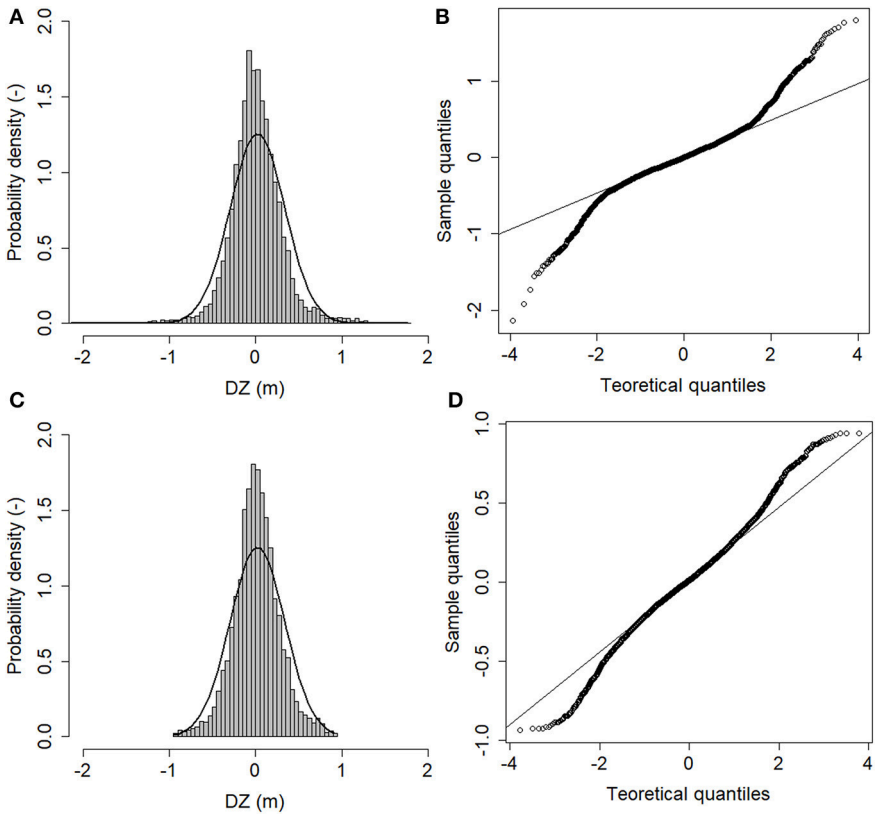

FIGURE 2 | (A) Histogram of the errors dataset. Superimposed, the normal distribution with mean and standard deviation estimated from the original errors dataset. **(B)** Normal Q-Q plot of the errors dataset. **(C)** Histogram of the errors dataset without outliers. Superimposed, the normal distribution with mean and standard deviation estimated from the thresholded errors dataset. **(D)** Normal Q-Q plot of the errors dataset without outliers. *DZ* denotes the vertical error.

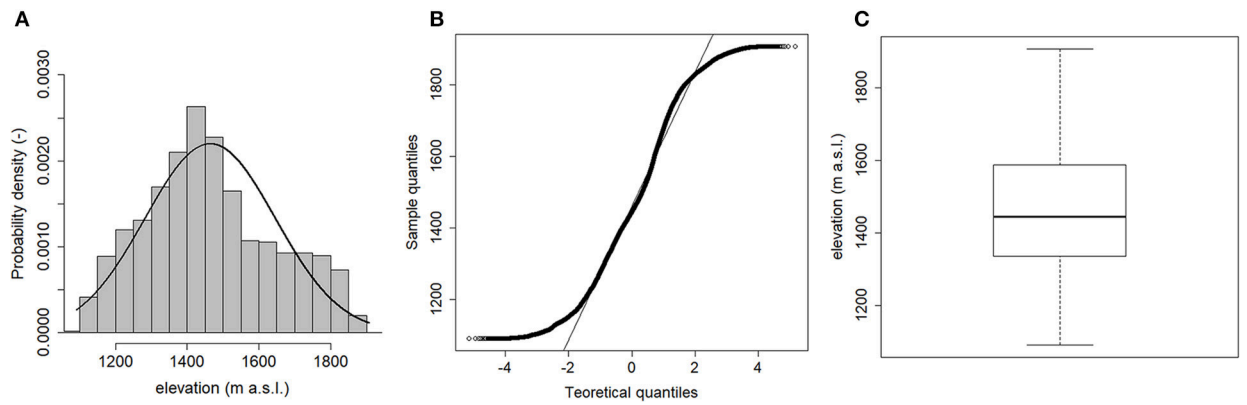

FIGURE 3 | Histogram with superimposed the normal distribution **(A)**, normal Q-Q plot **(B)**, and box-plot **(C)** of the LiDAR ground points dataset.

The paper is organized as it follows. After the description of the main works of previous authors on the topic of discrete spatial data interpolation shown in the **Supplementary Material**, the section Materials and Methods is outlined in six subsections. Here, after a short review of the theory underpinning the examined interpolation algorithms (subsection Background on the tested interpolation algorithms), the selected study site and the used topographic datasets are described (subsection Study area and data acquisition), along with the employed debris flow routing model (subsection GIS-based routing cell model). After that, the methodologies applied for the topographic data pre-processing, the investigation of interpolation algorithms performance, and the evaluation of their influence on routing modeling outcomes are explained in subsections LiDAR data

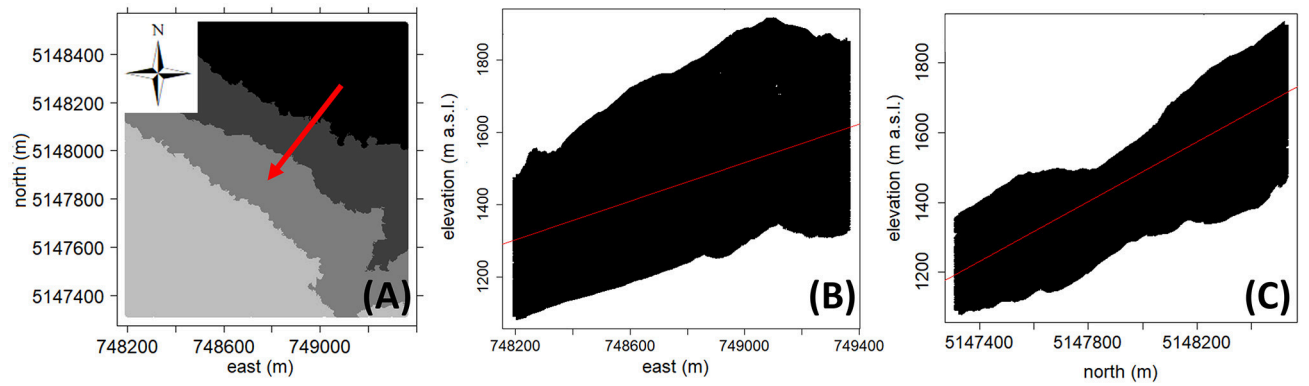

FIGURE 4 | Quantiles map of the variable elevation (the red arrow indicates the trend direction, which corresponds to the channel gradient) **(A)**, scatterplot elevation values versus east coordinate (rho Pearson = 0.48; rho Spearman = 0.47) **(B)**, and scatterplot elevation values versus north coordinate (rho Pearson = 0.82; rho Spearman = 0.84) **(C)**.

pre-processing and vertical accuracy analysis, DEMs generation and interpolation algorithms comparison, and Evaluation of the effects of the gridding techniques on debris flow routing model results, respectively. Lastly, the sections Results and Discussion and Conclusions complete the paper.

MATERIALS AND METHODS

Background on the Tested Interpolation Algorithms

Several interpolation and approximation methods were developed to predict the values of spatial phenomena in unsampled locations. In this study, twelve different algorithms commonly used for digital terrain modeling were applied using the software package ArcGIS™ (rel. 10.3): (i) linear triangulation, (ii) natural neighbor, (iii) nearest neighbor, (iv) Inverse Distance to a Power, (v) ANUDEM, Radial Basis Functions (among which: (vi) completely regularized spline function, (vii) thin-plate spline function, (viii) thin-plate spline plus tension function, (ix) multi-quadratic function, (x) inverse multi-quadratic function), (xi) point ordinary kriging, and (xii) block ordinary kriging. All the selected interpolators are already widely described in literature, so in the following we briefly summarize their main features in a narrative way. For in-depth theoretical and mathematical reviews concerning the techniques often used for gridding elevation data in connection with GIS, the reader is referred to the works of Mitas and Mitasova (1999), Blöschl and Grayson (2000), Johnston et al. (2001), El-Sheimy et al. (2005), Hengl and Reuter (2009), and McDonnell and Lloyd (2015).

Among the tested interpolation algorithms, the linear triangulation, the natural neighbor, and the nearest neighbor methods employ triangulated irregular networks (TINs), which consist in a sheet of continuous and connected triangular facets (defined according to the Delaunay's criterion) with vertices at the sampled points. Conversely, the Inverse Distance to a Power, the ANUDEM, the Radial Basis Functions, and the kriging algorithms directly apply on the set of scattered points.

The linear triangulation is the simplest method for fitting a continuous surface exploiting the Delaunay tessellation of the three-dimensional space. It represents a special case of piecewise polynomials interpolation, where each triangle containing a grid cell center is regarded as a local area, and a planar surface is fitted on each of them. Once the bivariate local linear function (i.e., the planar surface) is defined in this way, the value of the grid cell center can be estimated. It works effectively with a moderate amount of evenly distributed data points, and it allows an easy incorporation of topographic discontinuities and structural features. However, the interpolated values always lie within the range of the sampled values, and the resulting DEM may not be smooth due to the discontinuities created at the edges of each triangle.

The natural neighbor function uses a weighted average of the grid cell center nearest neighbors values, with weights dependent on proportions of the overlapping between the grid cell center Thiessen polygon and the Thiessen polygons of its surrounding sampled points. The resulting surface resembles a rubber-sheet passing through the input points, and it does not contain any peaks, pits, ridges or valleys that are not represented by the sampled data. It works equally well with regularly and irregularly distributed sampled data, often resulting in a smooth connection between the triangles edges. However, the interpolated values always lie within the range of the sampled values.

The nearest neighbor method assigns to the grid cell center the value of the sampled data point that is closest in space, often resulting in a polygon shaped surface. Since it often provides unrealistic results, the nearest neighbor algorithm is rarely used with topographic datasets. However, it could be useful for spatial fields with low (or nearly absent) spatial dependence, since in this case the sample data are considered reference values only for the surrounding area, and no gradation across the area boundaries is assumed.

The Inverse Distance to a Power function (IDP) is one of the most widely used methods for digital terrain modeling. It relies on a distance-weighted average of the values of the data points occurring within a neighborhood surrounding the grid

TABLE 2 | Global accuracy measures for each interpolated DEM (* the values refer to the errors distribution after the outliers removal).

	DEM resolution (m)	n. outliers (–)	median (m)	NMAD (m)	68.3% quantile (m)	95.0% quantile (m)	D'agostino K^2 test (p-value)*
Linear triangulation	1.00	27	−0.021	0.291	0.306	0.777	0.000
Natural neighbor	1.00	27	−0.021	0.291	0.306	0.777	0.000
IDP	1.00	27	−0.023	0.294	0.314	0.793	0.000
Nearest neighbor	1.00	23	−0.016	0.289	0.316	0.839	0.000
ANUDEM	1.00	20	−0.007	0.429	0.427	0.922	0.103
Completely regularized spline	1.00	26	−0.029	0.307	0.310	0.782	0.000
Thin-plate spline	1.00	30	−0.020	0.288	0.298	0.770	0.000
Thin-plate spline plus tension	1.00	26	−0.031	0.310	0.310	0.782	0.000
Multi-quadratic spline	1.00	26	−0.021	0.288	0.300	0.778	0.000
Inverse multi-quadratic spline	1.00	22	−0.026	0.339	0.351	0.840	0.000
Point ordinary kriging	1.00	21	0.018	0.390	0.406	0.945	0.000
Block ordinary kriging	1.00	21	0.018	0.390	0.406	0.945	0.000
Linear triangulation	0.50	35	−0.022	0.212	0.225	0.765	0.000
Natural neighbor	0.50	35	−0.022	0.212	0.225	0.765	0.000
IDP	0.50	37	−0.018	0.216	0.239	0.775	0.000
Nearest neighbor	0.50	26	−0.006	0.228	0.238	0.779	0.000
ANUDEM	0.50	24	−0.016	0.347	0.331	0.802	0.000
Completely regularized spline	0.50	32	−0.021	0.239	0.247	0.772	0.000
Thin-plate spline	0.50	41	−0.018	0.201	0.217	0.745	0.000
Thin-plate spline plus tension	0.50	31	−0.020	0.242	0.250	0.769	0.000
Multi-quadratic spline	0.50	40	−0.017	0.203	0.217	0.738	0.000
Inverse multi-quadratic spline	0.50	26	−0.023	0.286	0.302	0.825	0.000
Point ordinary kriging	0.50	21	0.034	0.337	0.406	0.945	0.000
Block ordinary kriging	0.50	21	0.034	0.337	0.354	0.898	0.000

cell center, with weights inversely proportional to a power of the Euclidean distance between the interpolated and the sampled data point. The greater the power exponent, the smaller effect the sample points far from the grid node have during the interpolation procedure. It usually results in an interpolated pattern that is smooth everywhere except at the sampled points, where local extrema (usually referred as bull's-eyes) are produced. The technique is particularly suitable for narrow datasets, where other gridding algorithms may be affected by errors. However, it does not work effectively with unevenly distributed data points, or in the presence of clustering and outliers. Furthermore, the interpolated values always lie within the range of the sampled values.

The ANUDEM algorithm is the only tested method based on a morphological approach specifically intended for digital terrain modeling. The approach couples the minimization of the sum of a user-specified roughness penalty and a weighted sum of squares of the residuals from the elevation data, with an automatic drainage enforcement algorithm ensuring a connected drainage structure and a sensible representation of ridges and streams in the fitted surface. It uses a multi-resolution, iterative, finite difference computational structure based on a regular two-dimensional grid. For scattered points dataset it can be regarded as a bivariate, discretised, smoothing thin-plate spline plus tension function, for which the tension parameter has been empirically determined in order to allow the interpolated DEM to follow abrupt changes in the land surface (e.g., streams and ridges). It is also a hybrid technique that allows to incorporate soft information (e.g., layers representing pits, streams, lake boundaries, ridges, cliffs, and coastline), thus assisting the interpolation procedure. Furthermore, it can predict values which are outside the range of the input data.

The Radial Basis Functions (RBFs) are a class of spline functions for interpolation (and approximation), frequently used for digital terrain modeling. They are based on the assumptions that the fitted surface should pass through (or close to) the data points and, at the same time, should be as smooth as possible. These conditions can be formulated within variational principles as the minimization of the sum of the deviations from the measured points and the smoothness seminorm of the spline function. The solution of this minimizing condition can be expressed as a sum of two components: a trend function described by means of a low order polynomial, and a linear combination of basis functions depending only to the Euclidean distance between the interpolated and the sampled data point. There are several basis functions (e.g., thin-plate spline, thin-plate spline plus tension, completely regularized spline, multi-quadratic spline, and the inverse multi-quadratic spline) according to the choice of the smoothness seminorm, and each of these yields a different gridded surface with its own

TABLE 3 | Supplementary DEM quality indices and global Moran'I index values for each tested interpolation algorithm and chosen spatial resolution (* the values refer to the errors distribution after the outliers removal).

	DEM resolution (m)	MAE (m)*	error range (m)*	slope (–)*	intercept (–)*	wR^2 (–)*	n. pits (–)	Moran's I index (–)
Linear triangulation	1.00	0.252	2.237	1.000	−0.928	1.000	11	0.339
Natural neighbor	1.00	0.252	2.237	1.000	−0.928	1.000	11	0.339
IDP	1.00	0.256	2.351	1.000	−0.859	1.000	14	0.316
Nearest neighbor	1.00	0.261	2.461	1.000	−0.655	1.000	22	0.242
ANUDEM	1.00	0.338	2.711	1.000	−1.695	1.000	3	0.466
Completely regularized spline	1.00	0.262	2.346	1.000	−1.050	1.000	12	0.372
Thin-plate spline	1.00	0.243	2.212	1.000	−0.823	1.000	19	0.316
Thin-plate spline plus tension	1.00	0.263	2.343	1.000	−1.063	1.000	12	0.374
Multi-quadratic spline	1.00	0.248	2.369	1.000	−0.896	1.000	30	0.301
Inverse multi-quadratic spline	1.00	0.289	2.454	1.000	−1.211	1.000	6	0.378
Point ordinary kriging	1.00	0.329	2.812	1.000	−1.801	1.000	17	0.501
Block ordinary kriging	1.00	0.329	2.812	1.000	−1.802	1.000	17	0.501
Linear triangulation	0.50	0.198	2.037	1.000	−1.028	1.000	104	0.445
Natural neighbor	0.50	0.198	2.037	1.000	−1.028	1.000	104	0.445
IDP	0.50	0.204	2.048	1.000	−0.974	1.000	102	0.414
Nearest neighbor	0.50	0.214	2.295	1.000	−0.813	1.000	190	0.329
ANUDEM	0.50	0.266	2.246	1.000	−1.641	1.000	2	0.531
Completely regularized spline	0.50	0.214	1.988	1.000	−1.195	1.000	32	0.489
Thin-plate spline	0.50	0.184	1.907	1.000	−0.888	1.000	177	0.428
Thin-plate spline plus tension	0.50	0.216	2.010	1.000	−1.204	1.000	29	0.490
Multi-quadratic spline	0.50	0.187	1.955	1.000	−0.901	1.000	273	0.424
Inverse multi-quadratic spline	0.50	0.251	2.222	1.000	−1.311	1.000	21	0.472
Point ordinary kriging	0.50	0.329	1.327	1.000	−1.801	1.000	64	0.583
Block ordinary kriging	0.50	0.298	2.597	1.000	−1.962	1.000	64	0.583

properties. Overall, the RBFs produce good results for gently varying landscapes, whereas they are inappropriate for irregular topographies where large changes in elevation within short horizontal distances can lead the functions to under- and over-shoot, even generating values outside the range of the sampled data.

"Kriging" is a generic term used to denote a number of closely related stochastic least-squares algorithms based on the regionalized variables theory, asserting that the fitted surface is one of the infinite possible realizations of a random process. It uses distance-weighted averages on punctual or block support, with weights depending on the spatial correlation of the random variable usually modeled by a function known as variogram. The kriging algorithm can be defined as the best linear unbiased estimator of a spatial variable, since it provides unbiased estimates with minimum variance. Linearity implies that the estimated value at any unknown point is a linear combination of its surrounding measurements, whose weights are calculated by solving a system of linear equations containing the semi-variances defined from a variogram function. Furthermore, the algorithm describes the variation of any spatial variable as a sum of three major components: a structural component or trend, a random but spatially correlated component, and a spatially uncorrelated Gaussian noise term. Depending on the assumptions underpinning the model, it is possible to recognize three principal kriging algorithms: the simple kriging which assumes a constant and known mean over the area of interest, the ordinary kriging which assumes a constant but unknown mean over the area of interest, and the universal kriging which assumes that an unknown mean changes smoothly over the area of interest. The ordinary kriging algorithm is the most popular one, and it serves well in many situations since its assumptions are easily satisfied. It is also robust regarding to both moderate departures from the underpinning assumptions, and a non-optimal choice of the variogram model. Overall, the kriging algorithm is not really appropriate for gridding elevation data mainly because: it causes a loss of sample variance under-estimating the largest sampled values and over-estimating the smallest ones, it ignores the hydrological connectivity of the terrain, and it is extremely sensitive to hot-spots causing many artifacts. In practice, the kriging algorithm and the RBFs can result in a very similar interpolated pattern. The main advantage of the kriging algorithm over the RBFs is that it provides direct estimates of the prediction quality in terms of estimation variance, so giving valuable information on the reliability of the interpolated values over the area of interest. Moreover, the measurement errors can be more directly introduced in the interpolation model by means of the so-called "nugget variance." However, it is less robust than the RBFs, and the predictions reliability heavily depends on the proper selection of the theoretical variogram model and on its fitting.

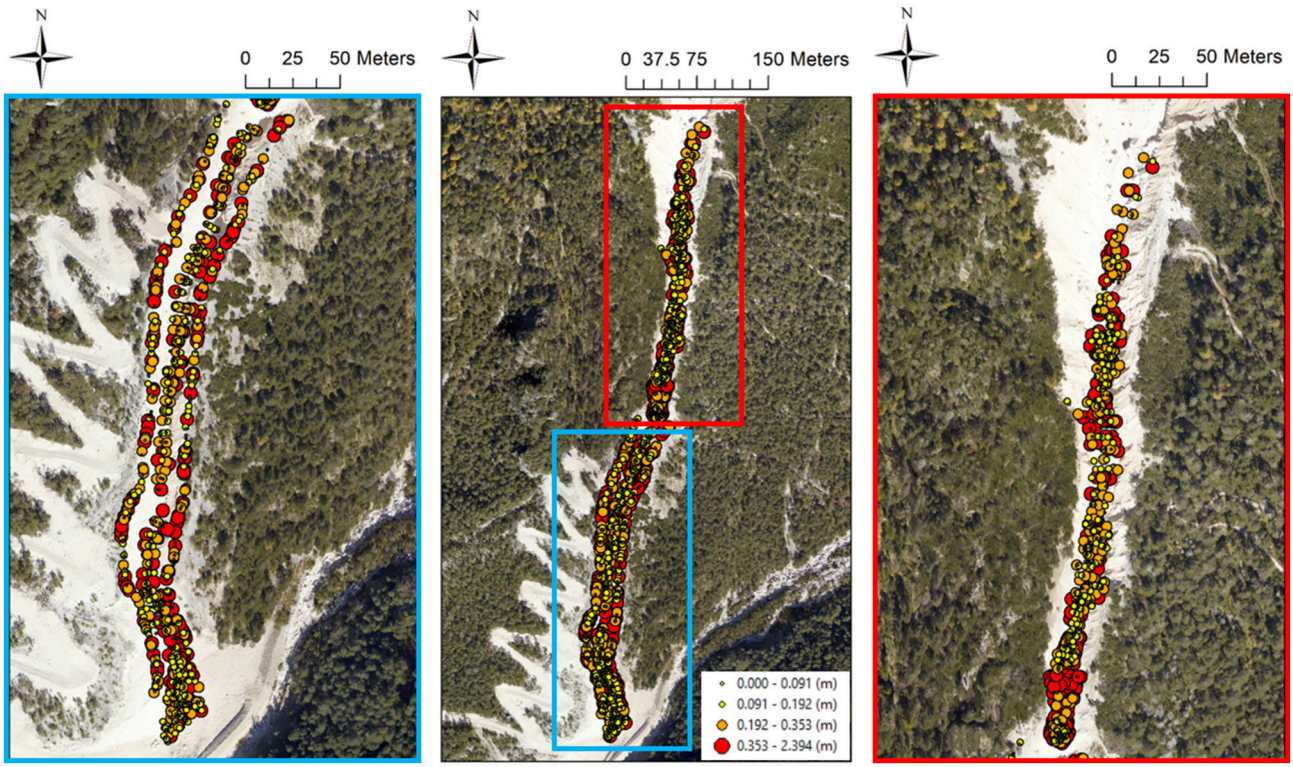

FIGURE 5 | Choropleth symbol map of the thin-plate spline function absolute errors (spatial resolution of 1.00 m). Note that the greatest absolute errors mainly occur at the top of the banks and in the rough upper part of the study area. Within the channel the spatial pattern of errors appears to be "random".

Study Area and Data Acquisition

Study Site

The research focused upon a 2 km length reach of the Rovina di Cancia debris flow channel (western slope of Mount Antelao, Venetian Dolomites, North-eastern Italian Alps, **Figure 1**). The channel originates in the scree at the base of Salvella fork (2,450 m a.s.l.), and the debris flows usually initiate at about 1,670 m a.s.l. (**Figure 1A**). The channel ends within a flat circular deposition basin bounded downstream by a gabion wall (1,000 m a.s.l., **Figure 1D**). At an altitude of 1,340 m a.s.l., just downstream a man-built flat deposition area (**Figure 1C**), the channel joins on the left with the Bus del Diau creek which basically provides a liquid input to the Rovina di Cancia debris flow.

From a geomorphological point of view, the debris flow catchment can be divided into three main sectors. In the upper part, massive rock cliffs prevail. They are composed of Upper Triassic to Lower Jurassic dolomites and limestones, underlined by the Raibl Formation, in a typical dolomitic stratigraphy configuration. The medium part is characterized by screes of poorly sorted and highly permeable debris, with boulders that can reach diameters of about 3–4 m, while the downstream part is covered by old debris flow deposits, including postglacial sediment material.

The Cancia area is prone to stony debris flows owing to the plenty availability of loose and coarse sediments, and the impulsive hydrological regime of the basin. In particular, the smaller grain sized material is provided by both the failure and the erosion of the banks, whereas gravel, pebbles and cobbles are provided by the upper part of the basin characterized by rocky material. The pluviometric regime of the area is characterized by short duration and high intensity rainfall events, usually occurring during the summer season (Gregoretti and Dalla Fontana, 2007).

Different stony debris flow events have been recorded in the past decades probably due to recent changes in the rainfall pattern. The most significant ones are those occurred on 2 July 1994, on 7 August 1996, and on 18 July 2009 (Simoni et al., 2018). The first flooded the inhabited fan with about 30,000 m^3 of debris. The second mobilized about 45,000–60,000 m^3 of debris damaging some houses and cars but without losses of human life, while the latter mobilized about 40,000 m^3 of debris and, after the filling of the retaining basin, it flooded some houses causing two casualties. The most recent debris flow events are those occurred on 23 July 2015 (about 30,000 m^3 of mobilized debris) and on 4 August 2015 (about 25,000 m^3 of mobilized debris).

Data Acquisition

Full-waveform aerial laser scanner survey

The study site of Rovina di Cancia was surveyed by Helica s.r.l. on 21 October 2015 by using a I-HBEP helicopter (Eurocopter AS 350 B3) equipped with a long-range, small footprint, full-waveform RIEGL LMS-Q780™ sensor. A comprehensive overview on the Airborne Laser Scanning (ALS) can be found in Vosselman and Maas (2010), while the state-of-the-art on

the full-waveform topographic LiDAR systems as well as on the related data processing techniques can be found in Mallet and Bretar (2009) and Wagner et al. (2006). The employed instrument works according to the time-of-flight distance measurement principle, and makes use of a powerful laser source, multiple-time-around processing, echo digitalization, and waveform analysis. This combination allows the operation at varying flying altitudes, and it is therefore ideally suited for aerial survey of wide areas and complex terrains. The ALS system was completed by five Global Positioning System (GPS) ground stations located within a maximum distance of 50 km from the surveyed area, which served as reference stations for the off-line differential GPS calculation. Furthermore, a Phaseone iXA 180 medium-format frame digital camera was accommodated on the scanner assembly ground plate, thus allowing the simultaneous acquisition of range and image data. The technical features of the employed laser-scan system as well as the employed flight parameters are reported in **Tables 1S, 2S** of the Supplementary Material, respectively.

After the aerial survey, the LiDAR data provider classified the raw points cloud into ground and non-ground echoes through the software package Terrascan^{TM}, setting parameters refined by the company itself over the years. For the study area of Rovina di Cancia (**Figure 1**), the mean LiDAR points density (i.e., ground and non-ground points density) was 20.79 points m^{-2}. After the filtering step, the mean LiDAR ground points density resulted in 3.33 points m^{-2}, corresponding to a mean ground points distance of 0.28 m.

Real-time kinematic GPS survey

To assess the vertical accuracy of both LiDAR data and interpolated DEMs (see subsections LiDAR data pre-processing and vertical accuracy analysis, and DEMs generation and interpolation algorithms comparison), over 3,000 independent Real-Time Kinematic GPS (rtkGPS) measurements were acquired on October-November 2015 by using a dual frequency Topcon HiPer V GPS base and rover system (**Figure 1** and **Figure 1SA** of the Supplementary Material). This ground-based survey technique ensures high-accuracy topographic measurements that can be regarded as control values for laser scanning- and photogrammetric-derived points clouds (Cilloccu et al., 2009; Caroti and Piemonte, 2010). As a matter of fact, the nominal positioning accuracy for dual-frequency GPS systems operating in kinematic mode and with baseline less than 20 km ranges between 0.02 and 0.05 m. Since the control values should be at least three times more accurate than data being evaluated (e.g., Höhle and Höhle, 2009; Höhle and Potuckova, 2011), it means that the rtkGPS measurements can be used to assess the accuracy of points clouds having positioning accuracy up to 0.06 m.

In order to describe the channel morphology as accurate as possible, a cross-sections morphological-guided spatial sampling scheme was adopted (e.g., Aguilar et al., 2005; Heritage et al., 2009). In detail, the ground measurements were acquired in coded cross-sections keeping orthogonal to the flow direction, and taking care to acquire relevant topographic features (e.g., talweg position, toe and top bank, **Figure 1SB** of the Supplementary Material). Both the ground points sampling distance and the cross-sections inter-distance were defined during the field survey according to the terrain roughness. The mean points sampling distance was 0.65 m (with a maximum of 2.73 m, and a minimum of 0.06 m), whereas the mean cross-sections inter-distance was 3.25 m (with a maximum of 9.80 m, and a minimum of 0.89 m).

The real-time three dimensional rover position was obtained by connecting via radio waves to a master station located at a maximum distance less than 1 km in order to minimize the measurement errors (**Figure 1SA** of the Supplementary Material). The positioning was based on phase solutions employing both L1 and L2 signal frequencies. To achieve the maximum accuracy, during the ground survey only fixed solutions were acquired. In addition, the three dimensional position of each surveyed ground point was calculated as the average of the measurements carried out on five epochs. This measurements redundancy allowed minimizing the influence of the inherent error sources (e.g., atmosphere delay, multipath, and clocks synchronization). The reported RTK-GPS data planimetric precision was 0.005 ± 0.001 m (with a maximum of 0.03 m), while the reported vertical precision was 0.008 ± 0.002 m (with a maximum of 0.05 m). The average planimetric dilution of precision value was 2.55 ± 0.45 (with a maximum of 3.50). The average number of GPS satellites viewed during the survey (GPS and GLONASS constellations) was 10 (with a maximum of 14).

The geographic coordinates of the rtkGPS measurements were projected in the coordinate system WGS84-UTM32 (i.e., the LiDAR data geodetic-cartographic datum, see subsection LiDAR data pre-processing and vertical accuracy analysis), whereas the orthometric heights were computed based on the local geoid model ITALGEO2005[1].

GIS-Based Routing Cell Model

The employed GIS-based debris flows cell routing model is able to simulate the routing and the entrainment-deposition processes of solid-liquid mixtures having a grain-collision dominated rheology (Gregoretti et al., 2018a), also known as stony debris flows (Takahashi, 2007). It represents the fully bi-phase version of the one proposed by Gregoretti et al. (2016a), and it allows a better simulation of the entrainment process.

The model discretizes the flow domain by using the square cells of a DEM. Each cell is hydraulically linked with its eight surrounding ones (**Figure 2SA** of the Supplementary Material), and the flow always occurs according to positive free surface drops (**Figures 2SB,SC** of the Supplementary Material). The governing equations of the mathematical model are those of mass and momentum conservation of both the overall sediment-water mixture and the solid phase, along with the Exner's equation in union with a modified version of the one dimensional empirical law of Egashira and Ashida (1987) for the rate of change of bed elevation.

[1]Nominal conversion accuracy equal to ± 0.035 m at 1σ.

In differential form, the continuity equations at the cell scale are:

$$A\frac{d(h+z)}{dt}+\sum_{k=1}^{8}Q_k=0 \quad (1)$$

$$A\frac{d(ch+c*z)}{dt}+\sum_{k=1}^{8}cQ_k=0 \quad (2)$$

where A is the area of the square cell, h is the flow depth, z is the bottom elevation, t is the time, c is the sediment volumetric concentration of the mixture, c_* is the dry sediment concentration (also known as maximum packaging concentration), and Q_k is the discharge exchanged by the reference cell with its surrounding ones, assumed to be positive if outflowing and negative otherwise.

In the model, the water-sediment mixture is supposed to be a continuous mean composed by granular material immersed in an interstitial fluid, with equal velocities for the two phases according to Rosatti and Begnudelli (2013). Following the kinematic wave approximation as in Lenzi et al. (2003) and Di Cristo et al. (2014), in the case of gravity-driven flow (**Figure 2SB** of the Supplementary Material) the momentum equation is that of uniform flow in a Chezy-like form. Conversely, in the case of flow along negative slopes (**Figure 2SC** of the Supplementary Material) the momentum equation is that of broad-crested weir. This latter equation is used to cope with flow routing in areas having local topographic depressions, and in the presence of obstacles like hydraulic structures and houses. The two momentum equations are:

$$Q_k = Ch\ \ \Delta x w_k\sqrt{g\,h\,sin\,\vartheta_k}\ \ w_k=\frac{\sin\vartheta_k}{\sum_{k=1}^{n}\sin\vartheta_k} \quad (3)$$

$$Q_k = 0.385\,\Delta x s_k\sqrt{2g}(h-z_k)^{1.5}\ \ s_k=\frac{h-z_k}{\sum_{k=1}^{m}(h-z_k)} \quad (4)$$

where C is the conductance coefficient (Tsubaki, 1972) representative of the grain-inertial rheology (Takahashi, 1978, 2007), Δx is the cell size, w_k and s_k are weighting functions introduced in order to allow multi-flow directions, g is the gravity acceleration, h is the flow depth, z is the bottom elevation, and ϑ_k is the angle formed with the horizontal by the line joining the center of the reference cell with its surrounding ones.

The Exner's equation is:

$$\frac{dz}{dt}=-i_b \quad (5)$$

$$i_b = KU_{MAX}\,(sin\alpha_{MAX}-sin\vartheta_{LIM}) \quad (6)$$

where i_b is the rate of change of bed elevation as proposed in Gregoretti et al. (2016a), K is an empirical constant ranging between 0 and 1, U_{MAX} is the velocity corresponding to the steepest of the eight possible flow directions k_{MAX}, α_{MAX} is equal to $\vartheta k_{\mathrm{MAX}}$ in the case of gravity-driven flow, otherwise α_{MAX} is equal to $(\vartheta_{\mathrm{K}}+\Theta_k)_{MAX}$ being Θ_k the angle that the horizontal forms with the line joining the flow surface of the reference cell with that of the cell where the flow is directed, ϑ_{LIM} and U_{LIM} are limit values for ϑ and U, respectively. The parameters ϑ_{LIM} and U_{LIM} assume different values for erosion ($U_{LIM\text{-}E}$ and $\vartheta_{LIM\text{-}E}$) and deposition ($U_{LIM\text{-}D}$ and $\vartheta_{LIM\text{-}D}$), and they should be determined by field measurements or numerical back-analysis. The erosion velocity i_b is positive if $U_{MAX} > U_{LIM\text{-}E}$ and $\alpha_{MAX} > \vartheta_{LIM\text{-}E}$, whereas it is negative if $U_{MAX} < U_{LIM\text{-}D}$ and $\alpha_{MAX} < \vartheta_{LIM\text{-}D}$. Erosion and deposition are computed only along the steepest downslope flow direction because considering all the possible flow directions could lead to unrealistically large deposition rate along directions transverse to the steepest downslope flow direction, and a cell could be subjected to both erosion and deposition in the same time interval. Erosion is only computed for increasing flow depths ($dh/dt > 0$), according to the instrumental field observations of Berger et al. (2011). Other two constrains are imposed to erosion and deposition processes: entrainment of sediment by the overflowing mixture is possible only if c is smaller than the physic limiting upper value of $0.9c_*$ (Takahashi, 2007); similarly, deposition occurs only if c is larger than a limiting lower sediment concentration for debris flow (c_D) assumed equal to 0.05.

From a numerical point of view, the governing equations are solved by using the finite difference technique with an explicit scheme subject to the Courant-Friedrichs-Lewy stability condition. The initial conditions are represented by the inflow solid-liquid hydrograph computed by means of a triggering model (e.g., Gregoretti et al., 2016b, 2018a,b). The computation procedure starts defining for each cell the possible solid-liquid discharges toward its eight surrounding ones according to Equations (3, 4). Then, the rate of change of bed elevation corresponding to the steepest downslope flow direction is computed by Equation (6). At the end of each computational time step, the cell free surface and bed elevation are simultaneously updated based on the computed outflow/inflow and deposited/entrained volumes.

LiDAR Data Pre-processing and Vertical Accuracy Analysis

Raw and filtered LiDAR datasets were delivered in ASCII files consisting of X, Y, Z coordinates (ellipsoidal heights related to the reference ellipsoid WGS84) and intensity data, arranged in 1 × 1 km tiles based on the projected coordinate system WGS84-UTM32. Although at national and regional level the geodetic-cartographic datum Roma40-Gauss Boaga represents the formally accepted coordinate system, no datum transformation was performed in order to avoid accuracy loss in the delivered topographic datasets. Conversely, the ellipsoidal heights were converted in orthometric heights based on the local geoid model ITALGEO2005, thus allowing the direct comparison with the GPS validation measurements (see subsection Real-time kinematic GPS survey). No additional attributes (e.g., GPS time for every laser shot, scan angle, edge of flight line information, echo amplitude, echo width) were included within the delivered datasets.

Before analysing the vertical accuracy of the aerial laser data, the filtered LiDAR dataset was converted in LAS format and then critically examined to check for classification errors (i.e., commission and omission errors). It represents a key step since the LiDAR-derived DEMs quality strongly depends on the correct classification of the raw points cloud into terrain and off-terrain echoes (e.g., Vosselman and Maas, 2010). The

visual inspection of the LiDAR data via LASview™[2] highlighted many data voids in morphologically complex areas, mainly due to misclassified LiDAR points as non-ground when they truly represented ground features such as big boulders within the channel (**Figure 3S** of the Supplementary Material). As this kind of classification errors could heavily affect the routing model outcomes, the delivered raw points cloud was re-classified into ground and non-ground points within the software package LAStools™. For the study area of Rovina di Cancia, the re-classification procedure yielded a mean LiDAR ground points density equal to 4.34 points m^{-2} (i.e., 30% more than the density of the delivered LiDAR ground points dataset), with an observed mean ground points distance corresponding to 0.25 m.

Since a number of error sources can affect the accuracy of LiDAR points clouds determining systematic errors and many outliers (e.g., accuracy in the aircraft absolute positioning and attitude data, accuracy of system calibration as determination of boresight angles and offsets between instruments, internal scanner errors, automated processing of the points cloud), an extensive vertical accuracy assessment was carried out on the re-classified LiDAR ground points dataset by using the independent rtkGPS measurements. An automated routine based on a proximal point algorithm (e.g., Reutebuch et al., 2003; Webster and Dias, 2006; Pourali et al., 2014) was then coded in order to directly compare the LiDAR and the validation data. This approach is suitable to accurate heights comparison since the errors introduced through the data gridding are eliminated (Hodgson and Bresnahan, 2004; Höhle and Potuckova, 2011; Pourali et al., 2014). The validation technique involves a user specified horizontal search radius around the GPS control point for comparison with the LiDAR ground points. In order to limit the influence of channel slope on the computed elevation residuals, a horizontal search radius equal to 0.50 m was used. It has also allowed an average number of LiDAR ground points within the search radii equal to four, thus ensuring a sufficient sample size for reliable accuracy measures. All LiDAR ground points within that search area are selected, and then their orthometric heights are compared to that of the GPS validation point. The computed elevation differences were regarded as vertical "errors," and they were statistically analyzed within the R open-source software package (R Development Core Team, 2008).

The derivation of accuracy measures has to take into account that outliers may exist, and that the distribution of the errors might not be normal. For this reason, the framework outlined in Höhle and Potuckova (2011), based on the standard (e.g., mean error, standard deviation, and their confidence intervals) and robust accuracy measures (e.g., median, Normalized Median of Absolute Deviations (NMAD), sample quantiles of absolute errors, and their confidence intervals) reported in **Table 3S** of the Supplementary Material, was followed. The reader is referred to the works of Höhle and Höhle (2009) and Höhle and Potuckova (2011) for a complete dissertation of the method.

It is worth pointing out that we compared two points datasets having different measurement support size, location, and spatial distribution, which poses inherent uncertainties on the accuracy assessment results.

DEMs Generation and Interpolation Algorithms Comparison

DEMs Interpolation

Prior to DEMs interpolation, a thoroughly Exploratory Spatial Data Analysis (ESDA) was performed on the re-classified LiDAR ground points dataset. This analysis was carried out at the purpose of gaining insight into the studied spatial variable. A number of features of the topographic dataset were investigated by the ESDA tools of the Geostatistical Analyst™ module (ArcGIS™, rel. 10.3), among which: spatial and marginal distribution via Voronoi's polygon map, points pattern analysis, and standard statistic plots and indices; second-order or intrinsic stationarity by trend analysis; and spatial dependency through variography.

Among the tested interpolation methods, the TIN-based routines (i.e., linear triangulation, natural neighbor, and nearest neighbor) does not require a dataset specific parametrization. Conversely, the remaining deterministic (i.e., Inverse Distance to a Power, ANUDEM, and Radial Basis Functions) and geostatistical (i.e., point ordinary kriging, and block ordinary kriging) methods were parameterized as it follows.

The most important parameters of IDP and RBFs algorithms were optimized via cross-validation, by minimizing the mean square prediction error. As a matter o fact, in its common form of "leave one out" it represents the most frequently used exploratory mean to find the best dataset specific algorithm parametrization (Erdogan, 2009). According to Oliver and Webster (2014), these algorithms were also parametrized to use during the interpolation procedure a number of neighbors ranging from 7 to 25. Furthermore, the presence of a linear global trend following the channel gradient (see subsection Exploratory spatial data analysis results and **Figure 4A**) led to the use of a one sector elliptical search neighborhood, oriented according to the direction of the greatest spatial continuity (i.e., the direction perpendicular to the trend). The ellipse major semi-axis was set equal to the range of the directional empirical variogram computed along the direction of the greatest spatial continuity. Conversely, the ellipse minor semi-axis, corresponding to the direction of the least spatial continuity (i.e., the trend direction), was defined by cross-validation. This search strategy allowed to favor during the interpolation procedure the points with the greatest spatial correlation. The ANUDEM algorithm was tested using only the re-classified LiDAR ground points as input data. The algorithm roughness penalty was defined as a mixture of minimum curvature and minimum potential, and the drainage enforcement option was enabled. Moreover, the standard vertical error and the first elevation tolerance were set equal to the computed random vertical error of the re-classified LiDAR points dataset (see subsection LiDAR data vertical accuracy assessment and **Table 1**). The geostatistical interpolation was performed through the ordinary kriging algorithm, employing a Gaussian theoretical variogram model fitted on the directional empirical one computed perpendicularly to the trend. In fact, as suggest by Chiles (1984) and Oliver and Webster (2014), a statistically

[2]Isenburg, M. (2017). LAStools - efficient LiDAR processing software (version 170608, unlicensed).

sound procedure to kridge points dataset with a dominant linear global trend consists in applying the ordinary kriging algorithm using a theoretical variogram model fitted on the directional empirical one computed along the direction of the greatest spatial continuity. This theoretical variogram can be regarded as the variogram of the residuals (i.e., the theoretical variogram of the spatially correlated component of the studied variable). The nugget parameter of the theoretical variogram was set equal to the square of the computed random vertical error of the re-classified LiDAR points dataset, so predicting filtered (or, "error-free") values. Furthermore, the points dataset was kridged using both a punctual and a block support, with a block dimension corresponding to 0.50 and 1.00 m (i.e., the DEMs spatial resolution, see below). For the upscaling procedure, the number of averaged punctual predictions within each block was defined according to the LiDAR footprint, which represents the input data support dimension. All the employed interpolation techniques parametrizations are summarized in **Table 4S** of the Supplementary Material.

The spatial resolution of DEMs was set according to the rules outlined by Hengl (2006). In detail, the author proposed empirical and analytical criteria to select the optimal grid resolution for points dataset interpolation, including those based on GPS horizontal error, map scale, size and shape of the smallest objects being mapped, points pattern geometry, and spatial correlation. Many of the described methods refer to the Whittaker-Nyquist-Kotelnikov-Shannon sampling theorem (e.g., El-Sheimy et al., 2005), which states that an original continuous signal can be reconstructed from the sampled data (without any loss of information) only if the sampling frequency is twice than the original one (Nyquist frequency). Thus, a raster grid cell size that retains the highest information content of the original points dataset is equal to half the average spacing between the closest points pairs. The re-classified ground LiDAR points were randomly distributed with an average mutual distance equal to 0.29 m. However, the 5% quantile of the nearest neighbor distances distribution was 0.10 m, while the 95% quantile was 0.57 m (**Table 5S** of the Supplementary Material). Therefore, a spatial resolution of 0.05–0.30 m was deemed to be appropriate for the employed LiDAR dataset. Nevertheless, the processing power of the available hardware along with the data management efficiency of GIS software limit the ability to generate digital surfaces at these very fine spatial resolutions. Thus, for each combination of interpolator and related parameters, DEMs were generated with a spatial resolution equal to 0.50 and 1.00 m (corresponding to 2.17 and 4.34 ground LiDAR points per cell, respectively). Notably, a spatial resolution of 0.50 m matches the source data information content according to the root mean square slope criterion developed by Hutchinson (1996).

Comparison of Interpolation Methods

Once the DEMs were generated, the overall performance of each tested interpolation algorithm was assessed by computing the vertical bias and accuracy of the corresponding gridded digital surface through the independent rtkGPS points dataset. In detail, the accuracy measures were statistically derived starting from the differences between the rtkGPS height value and the elevation value of the grid cell center containing the rtkGPS point itself. In order to choose between standard or robust accuracy measures (see subsection LiDAR data pre-processing and vertical accuracy analysis and **Table 3S** of the Supplementary Material), the sample error distributions were firstly check for outliers and normality. The outliers threshold was set equal to three times the Root Mean Square Error (RMSE) according to the rules outlined by Höhle and Höhle (2009), whereas the sample error distributions normality was tested both graphically by means of the normal Q-Q plot, both statistically through the D'Agostino K^2 omnibus test. This statistical test was choosen for its reliability with large data samples having kurtosis slightly higher than the normal distribution (Gallay et al., 2013). Therefore, the median of the vertical errors was chosen as robust estimator of the DEMs vertical bias, whereas, for the vertical accuracy of DEMs, the NMAD along with the 68.3 and 95% quantiles of the absolute errors distribution were chosen as robust estimators. The Mean Absolute Error (MAE), the minimum and maximum vertical error and the corresponding range, the weighted determination coefficient (Krause et al., 2005) along with the slope and the intercept parameters of the linear regression between measured and interpolated values, and the total drainage sink area (i.e., number and extension of raster cells whose neighbors are all of higher elevation) were also used as supplementary DEM quality indices. This latter index was used here as interpolation errors indicator, since the higher the number of interpolation artifacts in the gridded DEM, the larger the total drainage sink area will be (Wise, 2000, 2007; Setiawan et al., 2013).

It is worth pointing out that all these descriptive statistics are aspatial (i.e., spatially uniform) summary accuracy indices. However, a number of authors suggested that the vertical error of DEMs is not spatially uniform, but it can assume some form of spatial pattern (e.g., Li, 1993; Wood and Fisher, 1993; Wood, 1996; Yang and Hodler, 2000; Weng, 2006; Erdogan, 2009). Since DEMs with identical global accuracy values may have a different spatial pattern of errors (with digital surfaces having evenly distributed error values more reliable than those with high error clustering), to evaluate the performance of an interpolation method it is also important to investigate the spatial distribution of the vertical errors and their clustering extension. For deterministic gridding methods, the best way to examine the spatial distribution of the vertical errors is by means of accuracy maps obtained after comparing the interpolated DEM with a second more accurate surface. These maps have the advantage of clearly indicate where serious and perhaps anomalous errors occur. Unfortunately, as in this study, the availability of a more accurate control surface for comparison is rare. Thus, the spatial distribution of the vertical errors was graphically investigated through choropleth symbol maps, in which the size and the color of each independent validation point is established according to the error magnitude. Conversely, the error clustering extent was statistically assessed by means of both global and local indicators of spatial autocorrelation (i.e., the Global Moran's I index and the Anselin Local Moran's I index, respectively). The Global Moran's I index measures the overall spatial autocorrelation based on both features location and features value simultaneously, so evaluating whether the pattern expressed is clustered (index value approaching to 1), dispersed (index value approaching to

−1), or random (index value approaching to 0). Noteworthy, it indicates clustering of high or low error values, but without showing where the clusters are. To overcome this drawback, the Anselin Local Moran's I index was also used in the error clustering assessment. As the name suggests, it represents the local form of the Global Moran's I index, and it is used to graphically detect local pockets of dependence.

Since a critical concern in assessing the reliability of a gridding method is represented by its sensitivity with respect to changes in certain parameters (e.g., search neighborhood) or conditions (e.g., sample size; Yang and Hodler, 2000), we further evaluated the stability (or robustness) of each tested interpolation algorithm focusing on the sample size. In detail, we investigated the change in the performance of each tested gridding method considering a decreasing number of LiDAR ground points. Therefore, thinned datasets were obtained by randomly splitting the re-classified LiDAR ground points at densities equal to 95%, 75%, and 50% (which correspond to 4.13, 3.29, and 2.64 points m^{-2}, respectively). These thinned sample datasets were therefore interpolated at the spatial resolution of 0.50 and 1.00 m, keeping unchanged for each gridding technique the optimized model parameters (**Table 4S** of the Supplementary Material). After that, on each thinning-derived DEM, a comprehensive accuracy assessment was carried out following the approach above outlined, and the results obtained at the vary sample densities were finally compared. Note that a total of 96 DEMs were generated for this investigation.

As recognized by vary authors the success of a digital terrain modeling algorithm mainly depends on the purposes (e.g., Hengl and Reuter, 2009; Schwendel et al., 2012). Unlike DEMs for ortho-photos production where the absolute accuracy of the elevation values is the most important feature, DEMs for hydrological and hydraulic modeling must represent the catchment and channel shape realistically and close to the sampled topographic data. It ensures that slopes and flow paths are correctly represented in the interpolated DEM. For this reason, the shape reliability of each generated DEM was investigated by combining visualization techniques and residual analysis. The shape reliability is here defined as the degree of maintenance of the channel shape (as described by the sampled topographic data) in the interpolated DEM. In a pre-selection phase, for each generated DEM derivatives like slope, aspect, and curvature, along with shaded relief and surface roughness maps, were visually examined in order to identify interpolation artifacts. For the gridded surfaces that ensured a satisfactory representation of the channel topography, a multi-criteria morphological based comparison was then undertaken. The established morphological criteria include the plano-altimetric representation of longitudinal and transversal linear features (e.g., channel margins, hydraulic structures, and steps), and the representation of channel bottom forms (e.g., sediment sheets, boulders, and rugged reaches). They were defined considering the morphological features of the channel that need to be correctly maintained in the interpolated DEM in order to guarantee a reliable numerical modeling of debris flows routing. Noteworthy, this approach relies on qualitative analysis depending on the expert judgment of a user, and it represents its main limit. Therefore, in order to overcome this drawback, the ability of each tested gridding method to fulfill the topographic sampled data (i.e., the ability to faithfully represent the surveyed topography) was quantitatively assessed through a residual analysis.

Evaluation of the Effects of the Gridding Techniques on Debris Flow Routing Model Results

The hydraulic simulation of the Rovina di Cancia debris flow was carried out by using the cell routing model proposed by Gregoretti et al. (2018a) and described in subsection GIS-based routing cell model.

Since the effects of the digital elevation uncertainty resulting from the gridding procedure on debris flows routing modeling could be masked by an inaccurate model parametrization, the input parameters of the cell model were previously calibrated against two real debris flow events (occurred at Rovina di Cancia on 18 July 2009 and on Ru Secco the 4th of August 2015, respectively). In detail, the calibration procedure was undertaken by comparing the simulation results with both the observed erosion/deposition depth maps and the witnessed routing times. Both the back-analysis provided the same optimal model parametrization, thus guaranteeing a certain high degree of predictivity (for further details see Gregoretti et al., 2018a,b).

For all the model runs, both the calibrated values of the input parameters (i.e., C, K, $U_{LIM\text{-}D}$, $U_{LIM\text{-}E}$, $\vartheta_{LIM\text{-}D}$, and $\vartheta_{LIM\text{-}E}$) and the initial conditions (i.e., the upstream solid-liquid hydrograph) were kept unchanged, varying only the initial topographic surface generated according to the twelve tested interpolation algorithms. Therefore, this approach allowed the investigation of the influence of the algorithms itself on modeling outcomes.

Two event scenarios, corresponding respectively to 50- and 300-years return period, were defined by means of a coupled hydrological and triggering model (e.g., Gregoretti et al., 2016b, 2018a,b), starting from the rainfall depth-duration frequencies curves. It enabled to investigate the influence of the gridding methods on debris flows routing model results for events having different magnitude, characteristics of two usual design return periods.

For the sake of simplicity, in the different model runs we employed only the full dataset- and the 50% thinning-derived 1-meter resolution DEMs as input topographic data, carrying out a total of 48 simulations (i.e., twelve DEMs, two points densities, and two event scenarios).

To evaluate the influence of the gridding methods on debris flows routing modeling, we initially explored the relationship between the uncertainties on digital elevation and on the model results. In detail, for each combination of points density and event scenario we correlated the pixel-wise standard deviation of the twelve DEMs heights (i.e., the standard deviation at the cell scale of the elevation values of the twelve input topographic data of the routing model) and the pixel-wise standard deviation of the corresponding twelve simulated erosion/deposition depths (i.e., the standard deviation at the cell scale of the corresponding twelve routing model outputs). This allowed elucidating if the cells with high uncertainty in the simulated erosion/deposition depths were spatially linked to those with high topographic

uncertainty. It must be noted that the correlation was investigated both globally (i.e., at the channel extent) and locally by means of moving windows. The moving window size was set equal to 3 × 3 and 5 × 5 m, according to the spatial continuity of the correlated variables. The bivariate moving windows correlation analysis was carried out through the R package developed by Evans (2017). After that, for each combination of data density and event scenario, we compared the model run results in terms of simulated areas, erosion and deposition volumes, solid-liquid discharges, and channel morphology after the event.

RESULTS AND DISCUSSION

LiDAR Data Vertical Accuracy Assessment

The results of the vertical accuracy assessment carried out on the re-classified LiDAR points cloud are summarized in **Table 1**. It turns out that the outliers have a great influence on the mean and standard deviation of the vertical errors values. Respectively, they drop from 0.032 to 0.026 m and from 0.304 to 0.260 m after the outliers removal. The histogram and the normal Q-Q plot shown respectively in **Figures 2A,B** highlight that the vertical errors distribution is non-normal. In particular, the histogram shows that the kurtosis of the vertical errors distribution is positive (i.e., the distribution has a more acute peak around the mean and fatter tails than the normal one). Furthermore, the normal Q-Q plot deviates from the straight line at the extremes, which clearly indicates the presence of outliers in the vertical errors sample. After the outliers removal, the values of the mean and standard deviation of the vertical errors decrease (**Table 1**), remaining any way somewhat greater than the corresponding robust ones (i.e., greater than the values of the median and NMAD of the vertical errors; see subsection LiDAR data pre-processing and vertical accuracy analysis and **Table 3S** of the Supplementary Material). Furthermore, the histogram and the normal Q-Q plot shown respectively in **Figures 2C,D** highlight that the thresholded vertical errors distribution does not follow the normal one.

The median of the vertical errors is 0.020 m, and it represents the systematic vertical shift between the re-classified LiDAR points cloud and the rtkGPS validation data. This altimetric bias has been eliminated by means of a 2.5D calibration procedure (i.e., a rigid translation in the Z dimension of the re-classified LiDAR points cloud). After the calibration procedure, the vertical accuracy of the re-classified LiDAR points cloud only depends on its random vertical error component, and it can be evaluated by means of the standard deviation of the vertical errors. In this case, the robust estimator of the standard deviation is equal to 0.237 m, and it corresponds approximately to the 68.3% quantile of the absolute vertical errors distribution.

Figure 4S of the Supplementary Material depicts the difference between the employed accuracy measures. It has been obtained by superimposing to the vertical errors sample distribution the normal ones calculated by using the mean and the standard deviation of the vertical errors sample, the mean and the standard deviation of the vertical errors sample without outliers, and the median and the NMAD of the vertical errors sample, respectively. On one hand, the graph shows that the standard accuracy measures are not able to match the vertical errors sample distribution. Furthermore, even the application of an outliers threshold does not eliminate each of them from the vertical errors sample, and so the standard accuracy measures remain inaccurate. On the other hand, since the robust accuracy measures are able to apply a smoother transition between accepting or rejecting an observation from the vertical errors sample, they fit the vertical errors sample distribution best, both near the mean and at the tails. This finding validates the suggestions proposed by Höhle and Höhle (2009), who recommend the use of robust accuracy measures (i.e., median, NMAD, and sample quantiles of the absolute errors distribution)

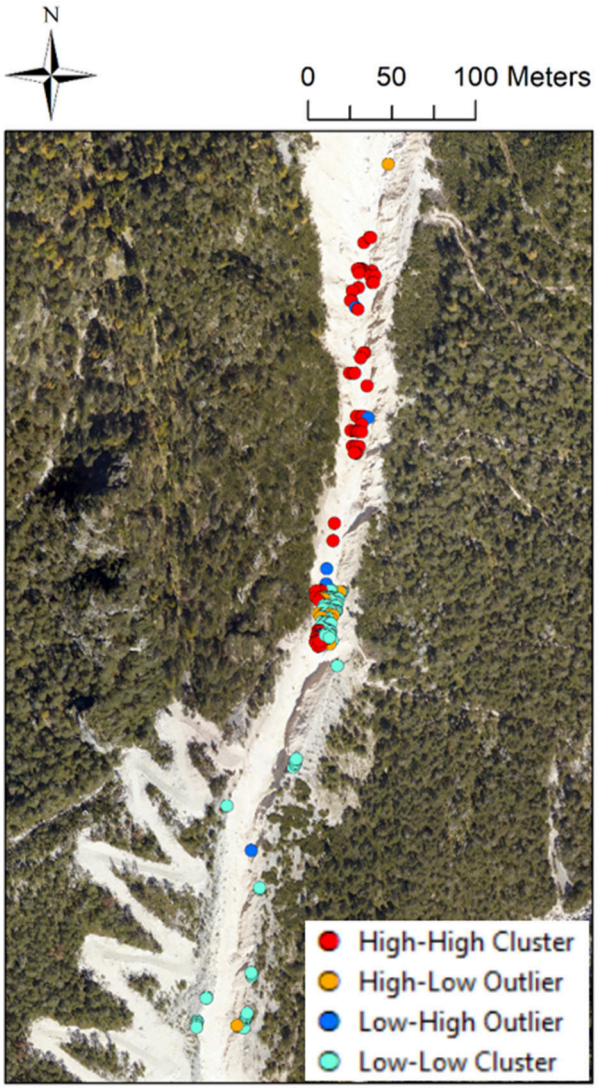

FIGURE 6 | Local Moran's I index map of the thin-plate spline function absolute errors (spatial resolution of 1.00 m). Note the local clusters of high and low errors values mainly located along the upper part of the channel where the topographic roughness is higher due to the presence of boulders and bank failures. Furthermore, local outliers concentrate near the rock step at an altitude of about 1,500 m a.s.l..

when the histogram (or the normal Q-Q plot) of the errors sample distribution reveals non-normality, since they are not influenced by the outliers or by the distribution skewness.

Exploratory Spatial Data Analysis Results

The results of the spatial distribution analysis carried out on the re-classified LiDAR points dataset are summarized in **Table 5S** of the Supplementary Material. The mean Voronoi's influence area of the LiDAR ground points is equal to 0.237 m^2, with an interquartile range corresponding to 0.174 m^2. It means that the spread of the influence area values is small, and so the sampling network can be considered homogeneous. Moreover, the average mutual distance between closest LiDAR points pairs is equal to 0.29 m $\pm$ 0.13 m, with a maximum of 3.48 m. The 5% quantile of the mutual distances distribution corresponds to 0.10 m, while the 95% quantile is equal to 0.57 m. The former statistic can be regarded as a robust measure of the minimum distance between closest ground points pairs, whereas the latter as a robust measure of their maximum distance.

As shown in **Figure 3A**, the marginal distribution of the re-classified LiDAR dataset is roughly unimodal, approximatively symmetric (skewness coefficient equal to 0.30), and approximatively mesokurtic (kurtosis equal to 2.40). However, the normal Q-Q plot deviates from the straight line at the extremes (**Figure 3B**), thus indicating that the elevation values distribution is non-normal. Moreover, the box-plot shown in **Figure 3C** does not reveal the presence of outliers within the dataset, as also confirmed by a coefficient of variation value lesser than one.

The quantiles map of the elevation values (**Figure 4A**) clearly shows a trend in the NE-SW direction. It means that the variable to be interpolated is not stationary within the domain since its mean changes smoothly in the space. To find the trend degree, the correlation between the elevation values and the east-north spatial coordinates has been analyzed through the scatter-plots shown respectively in **Figures 4B,C**. The Pearson's correlation coefficient (referred as "rho Pearson"), which provides a measure of the linear relationship between two variables, is equal to 0.48 and 0.82 along the east and north direction, respectively. Often, it is useful to supplement the linear correlation coefficient with the Spearman's rank correlation coefficient (referred as "rho Spearman"), which represents a further measure of the relationship strength (Isaaks and Srivastava, 1989). Unlike the Pearson's coefficient, the Spearman's rank coefficient is not strongly influenced by extreme pairs, and large differences between the two correlation coefficients values may be due to the presence of few erratic pairs or to a non-linear relationship between the two variables. For the study area, the Spearman's rank coefficient is equal to 0.47 and 0.84 along the east and north direction, respectively. Since both along the east and north direction the differences between the Pearson's and Spearman's correlation coefficients values are small, it can be stated that the variable to be interpolated exhibits a linear global trend.

The directional empirical variogram of the elevation values computed perpendicularly to the channel gradient (i.e., along the direction of the greatest spatial continuity) is shown in **Figure 5SA** of the Supplementary Material, with overlying the fitted Gaussian theoretical variogram model. The theoretical variogram levels off at a range of about 180 m, reaching a plateau of 450 m^2. Furthermore, it exhibits a parabolic structure near the origin (**Figure 5SB** of the Supplementary Material), followed by an inflection point. The nugget to sill ratio along the considered variogram modeling direction is close to zero, thus indicating the presence of a strong spatial structure.

Comparison of Interpolation Methods

The computed global accuracy measures for each interpolated DEM are summarized in **Table 2**. For both the chosen spatial resolutions, all the tested interpolation algorithms provide a comparable small number of outliers (corresponding at about 1% of the vertical errors sample), however affecting the standard accuracy measures. Moreover, all the vertical errors sample distributions are non-normal (the only exception is the ANUDEM algorithm that yields a K^2 omnibus test p-value equal to 0.10 at the spatial resolution of 1.00 m). Overall, the median of the vertical errors is centimetric (smaller than $\pm$ 0.040 m), meaning that the interpolation bias can be regarded as negligible. However, a closer look of the computed median values reveals that only the ordinary kriging algorithm provides positive values (0.018 and 0.034 m at the spatial resolutions of 1.00 and 0.50 m, respectively). Furthermore, the ANUDEM and nearest neighbor algorithms yield the lowest median values at both the chosen spatial resolutions (respectively, -0.007 and -0.016 m at the spatial resolution of 1.00 m, and -0.016 and -0.006 m at the spatial resolution of 0.50 m), whereas the highest values are provided by the thin-plate spline plus tension (-0.031 m at the spatial resolution of 1.00 m) and ordinary kriging (0.034 m at the spatial resolution of 0.50 m) algorithms. The NMAD values range from 0.288 to 0.429 m, and from 0.201 to 0.337 m at the spatial resolutions of 1.00 and 0.50 m, respectively. At both the grid cell sizes, the thin-plate spline and multi-quadratic basis functions yield the lowest values (respectively, 0.288 and 0.288 m at the spatial resolution of 1.00 m, and 0.201 and 0.203 m at the spatial resolution of 0.50 m), whereas the ANUDEM and ordinary kriging algorithms show the lowest performance (i.e., the highest NMAD values, equal to 0.429 and 0.390 m at the spatial resolution of 1.00 m, and 0.347 and 0.337 m at the spatial resolution of 0.50 m, respectively). It must be noted that for all the tested gridding methods, the higher the spatial resolution of the interpolated DEM (i.e., the smaller the raster grid cell size), the smaller the corresponding NMAD value (i.e., the better the interpolation). This finding is in general agreement with that observed for example by Bater and Coops (2009), who noticed an improvement on the interpolation algorithms performance as the spatial resolution of the generated DEMs increased from 1.50 to 0.50 m. However, the percentages of NMAD variation (i.e., how much an interpolator increases its prediction accuracy as the spatial resolution increases) change according to the considered gridding algorithm. In detail, the thin-plate spline and multi-quadratic basis functions exhibit the greatest percentages of NMAD variation (corresponding to 29.90 and 29.38%, respectively), where the ordinary kriging algorithm along with the inverse multi-quadratic basis function show the smallest ones (corresponding to 13.69 and 15.72%, respectively).

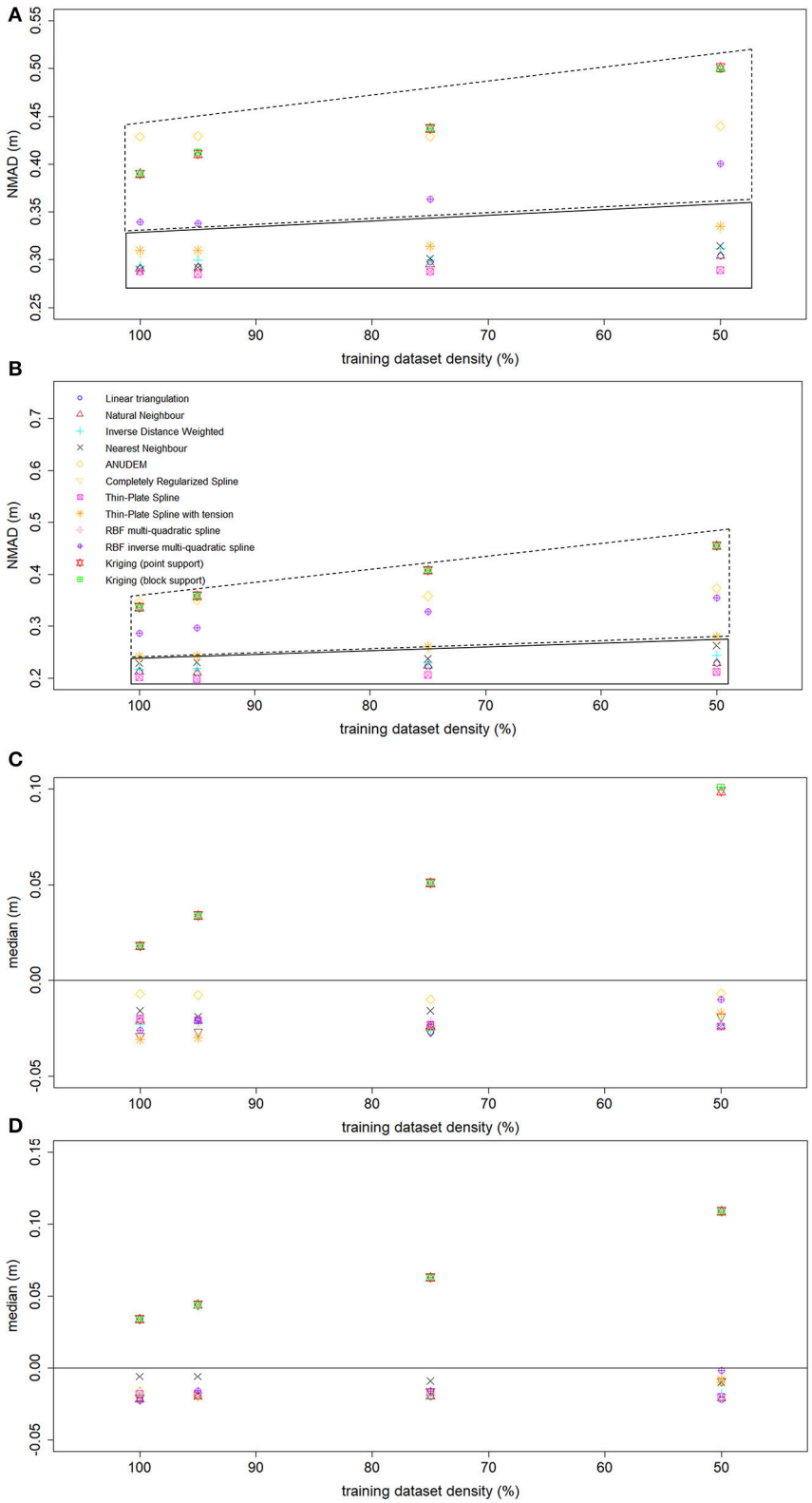

FIGURE 7 | NMAD values variation as a function of the sample density (**A**, spatial resolution equal to 1.00 m, and **B**, spatial resolution equal to 0.50 m). Median values variation as a function of the sample density (**C**, spatial resolution equal to 1.00 m, and **D**, spatial resolution equal to 0.50 m).

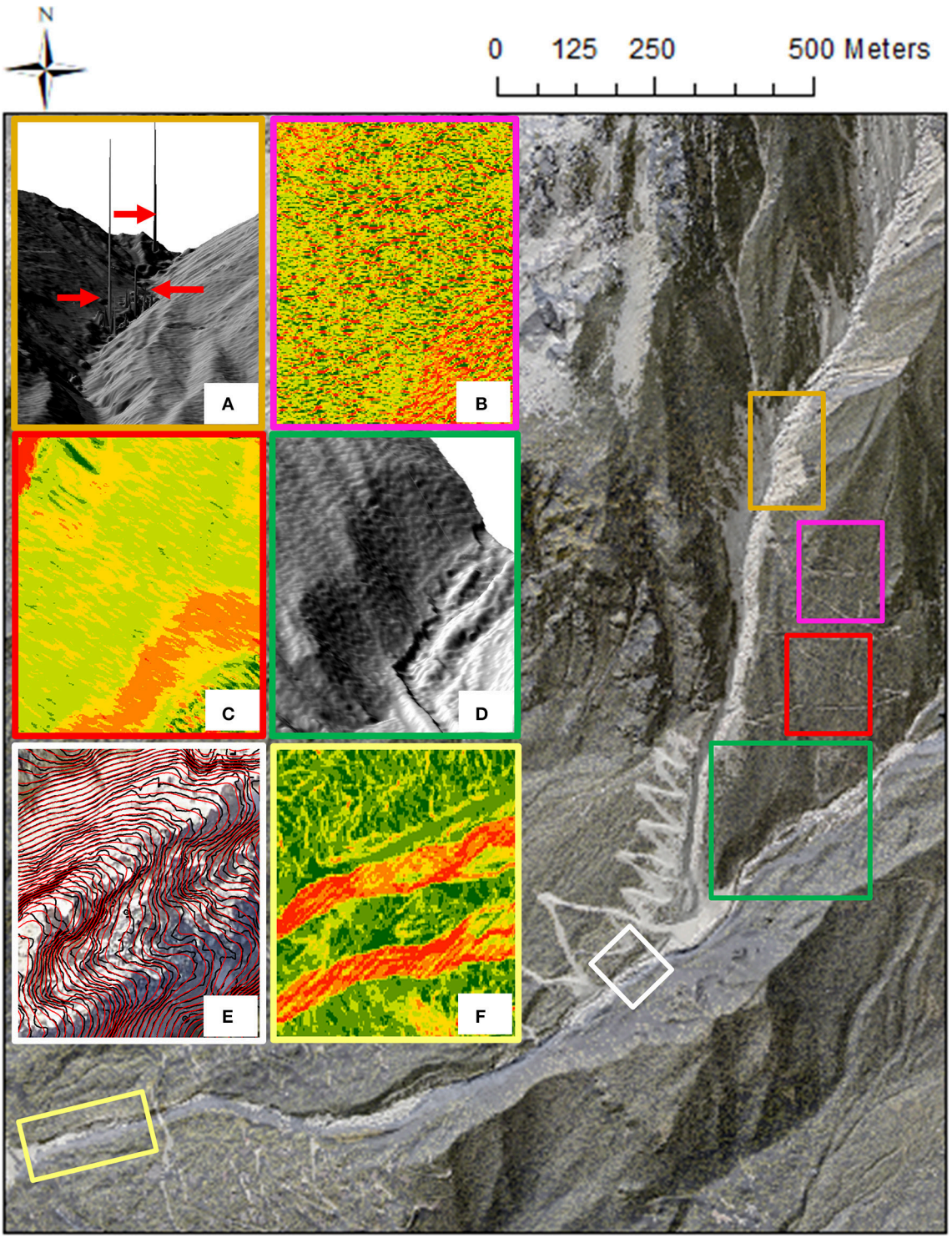

FIGURE 8 | Overview of the detected interpolation artifacts: **(A)** spiky features in the upper part of the debris flow channel due to function under- and over-shooting in correspondence of slope discontinuities, **(B)** noisy relief with a discontinuos spatial pattern of slopes, **(C)** striping effect oriented according to the direction of variogram modeling, **(D)** undulating surface, **(E)** over-smoothed surface (red lines: 1-meter interval contour lines of the ANUDEM-derived DEM, black lines: 1-meter interval contour lines of the natural neighbor-derived DEM), **(F)** striping effect oriented according to the sampling direction.

It means that although all the tested interpolation algorithms improve their performance as the chosen raster grid cell size decreases, for some of them the choice of an optimal spatial resolution is a more critical concern. The 95% sample quantiles of the absolute vertical errors distributions range from 0.770 to 0.945 m, and from 0.738 to 0.945 m at the spatial resolutions of 1.00 and 0.50 m, respectively. This statistic can be regarded as a robust measure of the maximum (unsigned) interpolation vertical error. For both the chosen spatial resolutions, the thin-plate spline and multi-quadratic basis functions yield the lowest quantiles values (respectively, 0.770 and 0.778 m at the spatial resolution of 1.00 m, and 0.745 and 0.738 m at the spatial resolution of 0.50 m), along with the linear triangulation (0.777 m) and the natural neighbor algorithm (0.777 m) only at the spatial resolution of 1.00 m. Conversely, the ANUDEM and ordinary kriging algorithms perform worst (i.e., yield the highest sample quantile values, equal to 0.922 and 0.945 m at the spatial resolution of 1.00 m, and 0.802 and 0.945 m at the spatial resolution of 0.50 m, respectively), along with the inverse multi-quadratic basis function (0.825 m) only at the spatial resolution of 0.50 m. It is worth pointing out that overall no significant differences in the computed accuracy measures are found among point and block ordinary kriging.

The supplementary DEMs quality measures along with the Global Moran's I index values are reported in **Table 3**. The MAE values range from 0.243 to 0.338 m, and from 0.184 to 0.329 m at the spatial resolutions of 1.00 and 0.50 m, respectively. At both the grid cell sizes, the thin-plate spline and multi-quadratic basis functions yield the lowest MAE values (respectively, 0.243 and 0.248 m at the spatial resolution of 1.00 m, and 0.184 and 0.187 m at the spatial resolution of 0.50 m), whereas the ANUDEM and ordinary kriging algorithms show the lowest performance (i.e., the highest MAE values, corresponding to 0.338 and 0.329 m at the spatial resolution of 1.00 m, and 0.266 and 0.329 m at the spatial resolution of 0.50 m, respectively). The vertical error range is between 2.212 and 2.812 m, and between 1.327 and 2.597 m at the spatial resolutions of 1.00 and 0.50 m respectively. The lowest error ranges are provided by the thin-plate spline (2.212 and 1.907 m, at the spatial resolutions of 1.00 and 0.50 m, respectively). Conversely, the ANUDEM and ordinary kriging algorithms return the highest error range values at the spatial resolution of 1.00 m (respectively, 2.711 and 2.812 m), whereas the ordinary block kriging performs worst at the spatial resolution of 0.50 m (2.597 m). Respect to the linear regression parameters, the intercept values are all negative at both the chosen spatial resolutions, with the worst results provided by the ANUDEM and ordinary kriging algorithms (approximatively −2.00 m). On the other hand, both the slope and the weighted regression coefficient values does not reveal noteworthy differences among the tested gridding methods, with all of them equal to one. The analysis of the total drainage sink area points out a correspondence between the spatial resolution increment and the number of pits, irrespective to the gridding algorithm. The only exception is the ANUDEM algorithm, which also provides (as expected) the lowest number of sinks at both the chosen spatial resolutions (respectively, 3 and 2). Conversely, the multi-quadratic basis function performs worst (i.e., it yields the highest number of sinks) at both the grid cell sizes (respectively, 30 and 273). It must be noted that the increase in the total drainage sink area is not only related to the cell size halving, but also to an increment in the number of pits. In other words, the higher the spatial resolution, the higher the number of interpolation artifacts. This finding is clearly in contrast with the previous one. However, it should be noted that the vertical accuracy assessment carried out on the interpolated DEMs has been performed by comparing two points datasets (i.e., the rtkGPS points and the grid cells centers containing the rtkGPS points themselves) that do not spatially overlap. Therefore, the better accuracy (i.e., the smaller NMAD values) of the finer gridded surfaces might be only due to the lower distances between the grid cell center and the rtkGPS validation point.

The analysis of the absolute errors spatial pattern by means of the visual inspection of choropleth symbol maps (**Figure 5**) reveals that for all the tested interpolation algorithms the greatest (unsigned) vertical errors occur in correspondence of breaks of slope (e.g., at the top of the banks) and in morphologically complex areas (e.g., in the upper part of the channel due to the presence of big boulders, and at the rock step located about 200 m downstream the initiation area (∼1,500 m a.s.l.), **Figure 1B**), regardless of both the points density of the dataset used during the interpolation procedure and the chosen raster grid cell size. Moreover, within the channel there are subtle differences among the tested interpolation algorithms, and the spatial pattern of the vertical errors visually appears to be random. However, a closer look of these maps highlights some local pockets of spatial dependence common to all the tested methods, as also confirmed by the Anselin local Moran's I index maps (**Figure 6**). The Global Moran's I index values range from 0.242 to 0.501, and from 0.329 to 0.583 at the spatial resolutions of 1.00 and 0.50 m, respectively. It means that all the tested interpolation algorithms yield a considerable degree of error clustering, with the highest values provided by the ANUDEM and ordinary kriging algorithms (respectively, 0.466 and 0.501 at the spatial resolution of 1.00 m, and 0.531 and 0.583 at the spatial resolution of 0.50 m). Noteworthy, for all the tested gridding methods, the higher the spatial resolution, the higher the degree of error clustering, with the highest percentages of variation provided by the thin-plate spline and multi-quadratic basis functions (35.44 and 40.86%, respectively).

The results of the interpolation algorithms robustness analysis in terms of NMAD and median of the vertical errors values variation on the basis of the sample density are summarized in **Figure 7**. The graphs of **Figures 7A**,**B** can be divided in two distinct regions. The first region (continuous border line) includes the interpolation algorithms which are stable (or robust) in relation to the sample density (i.e., the NMAD value does not change as the number of points used in the interpolation procedure decreases). Conversely, the second one (dotted border line) includes the routines whose prediction accuracy changes according to the sample density (the only exception is the ANUDEM algorithm, which provides consistent NMAD values). Furthermore, in the two delineated regions the spread of the NMAD values for each sample density differs. As a matter

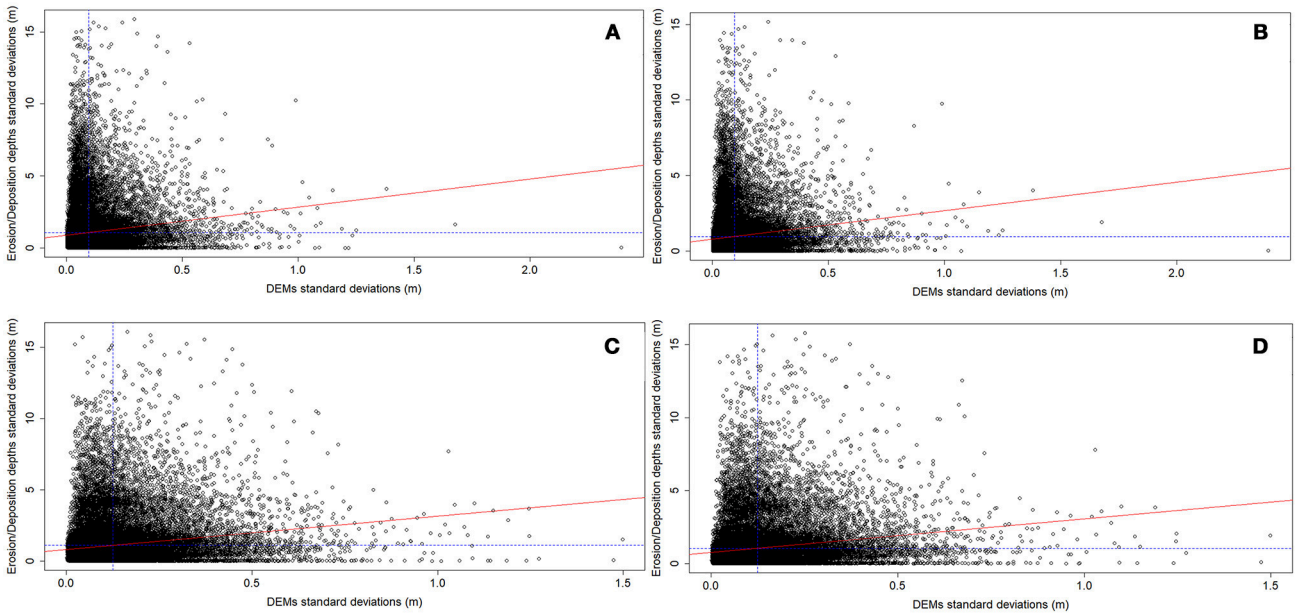

FIGURE 9 | Scatterplot of the pixel-wise standard deviations of the twelve 1-meter resolution DEMs heights and the pixel-wise standard deviation of the corresponding twelve simulated erosion/deposition depths: **(A)** full dataset-derived DEMs and 300-years return period (rho Pearson = 0.126, rho Spearman = 0.205), **(B)** full dataset-derived DEMs and 50-years return period (rho Pearson = 0.129, rho Spearman = 0.208), **(C)** 50% thinning-derived DEMs and 300-years return period (rho Pearson = 0.167, rho Spearman = 0.252), and **(D)** 50% thinning-derived DEMs and 50-years return period (rho Pearson = 0.172, rho Spearman = 0.256). The continuous red line corresponds to the linear regression line, whereas the dotted blue lines correspond to the marginal mean of the two correlated variables.

of fact, in the first region the spread of the values is smaller than that of the values in the second one, meaning that the interpolators within the first region yield similar accuracy values at each sample density. For both the chosen spatial resolutions, the thin-plate spline and multi-quadratic basis functions yield the more consistent NMAD values, which are also the lowest for each sample density. They are followed by the TIN-based interpolation algorithms and the Inverse Distance to a Power method. Conversely, at both the grid cell sizes, the ordinary kriging algorithm and the inverse multi-quadratic radial basis function are the least robust interpolation algorithms, along with the completely regularized spline function (only at the spatial resolution of 0.50 m). Furthermore, the graphs of **Figures 7C,D** highlight that all the tested gridding methods yield consistent vertical biases (i.e., the median of the vertical errors does not significantly change according to the sample density). The only exception is the ordinary kriging algorithm, which also provides positive median values (up to 0.10 m at a sample density equal to 50%). It is worth noting out that at the lowest sample densities (i.e., 75 and 50%) the kriging algorithm performs worst in terms of both systematic and random vertical error. This evidence is clearly in contrast with what reported in McDonnell and Lloyd (2015), who stated that for irregular spatial fields as the sample density decreases the kriging algorithm outperforms the deterministic interpolation methods.

The visual inspection carried out on the DEMs derivatives highlights that all the generated gridded surfaces contain noticeable interpolation artifacts (e.g., triangular facets; spiky features; striping effect; undulating, noisy, or over-smoothed relief; and discontinuos spatial pattern of slope and curvature), regardless of both the points density of the dataset used during the interpolation procedure and the chosen raster grid cell size (**Figure 8**). However, for the linear triangulation, natural neighbor, ANUDEM, completely regularized spline, thin-plate spline plus tension, and ordinary kriging algorithms, they do not prevent an overall satisfactory visual representation of the channel morphology. Conversely, the Inverse Distance to a Power, nearest neighbor, and inverse multi-quadratic basis function algorithms yield overly noisy DEMs. Furthermore, despite their excellent statistical performance, also the thin-plate spline and multi-quadratic radial basis functions do not ensure a realistic representation of the study site topography mainly due to function under- and over-shooting. As a consequence, relevant spiky features in correspondence of slope discontinuities are generated, both internally and externally to the channel area (**Figure 8A**). This finding endorses the importance of integrating statistical and qualitative techniques when an interpolation algorithm performance analysis is undertaken, as suggested by a number of earlier studies (e.g., Wood and Fisher, 1993; Declercq, 1996; Wood, 1996; Desmet, 1997; Yang and Hodler, 2000; Chaplot et al., 2006; Podobnikar, 2009; Setiawan et al., 2013). The multi-criteria morphological based comparison points out that the completely regularized spline and the thin-plate spline plus tension functions ensure the most realistic plano-altimetric representation of both longitudinal and transversal linear features, both channel bottom forms. Conversely, the ANUDEM and ordinary kriging methods prove the lowest shape reliability mainly due to surface over-smoothing, with slope

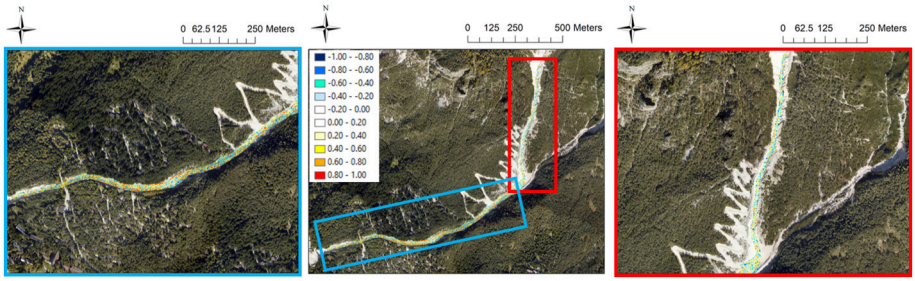

FIGURE 10 | 5 × 5 moving windows Pearson's correlation coefficient between the pixel-wise standard deviations of the twelve 50% thinning-derived 1-meter resolution DEMs heights and the pixel-wise standard deviation of the corresponding twelve 50-years return period simulated erosion/deposition depths.

discontinuities and channel bottom forms not well defined in the corresponding DEMs. Moreover, a meaningful striping effect perpendicular to the trend direction (i.e., along the considered variogram modeling direction) affecting the kriging-derived DEMs suggests that the methodology here followed to kridge the LiDAR points dataset does not represent a suitable procedure to interpolate DEMs for hydrological and hydraulic modeling (**Figure 8C**). The linear triangulation and the natural neighbor algorithm perform in an intermediate position, with an overall realistic representation of channel features although the contours in some cases appear irregular or with spurious shapes. The results of the residual analysis carried out on the full dataset-derived 0.50 meters-resolution DEMs are shown (as an example) in **Figure 6S** of the Supplementary Material. It turns out that the ANUDEM algorithm has the lowest ability to fulfill the topographic sampled data, followed by the ordinary kriging algorithm. On the other hand, no significant differences in the ability of honoring the sampled topographic data are detected among the remaining tested gridding methods.

Effects of the Gridding Techniques on Debris Flow Routing Modeling

For the two modeled event scenarios (i.e., 50 and 300-years return periods), the results of the global (i.e., at the channel extent) correlation analysis between the pixel-wise standard deviation of the twelve full dataset-derived 1-meter resolution DEMs heights and the pixel-wise standard deviation of the corresponding twelve simulated erosion/deposition depths are summarized in **Figures 9A,B**, respectively. For both the event scenarios, the Pearson's and the Spearman's rank correlation coefficient approach similar low values, respectively equal to 0.13 and 0.21 (i.e., about 15–20% of the perfect positive correlation between the two analyzed variables). Only a slight improvement in the correlation strength is gained by using the 50% thinning-derived 1-meter resolution DEMs in the model runs (**Figures 9C,D**). Furthermore, also the moving windows correlation analysis does not emphasize a strong spatial link between the cells with high uncertainty in the simulated erosion/deposition depths and those with high uncertainty in the input topographic data (**Figure 10**), regardless of both the magnitude of the modeled event scenario and the points density of the dataset used during the interpolation procedure.

For the 50% thinning-derived 1-meter resolution DEMs, we report (as an example) the 50-years return period run results in terms of: simulated erosion/deposition areas and volumes (**Table 4**), solid-liquid discharges (**Figure 11**), and channel morphology after the event (**Figure 12**). Overall, the results do not highlight a noteworthy change in the routing model behavior depending on the used topographic surface, regardless of both the magnitude of the modeled event scenario and the points density of the dataset used during the interpolation procedure. In detail, in **Table 4** the spread of the simulated flooded area values is smaller than 2,000 m^2 (i.e., smaller than 10% of the mean of all the simulated flooded area values), whereas for the simulated erosion and deposition areas it corresponds to 854 m^2 (i.e., 7% of the mean of all the simulated erosion area values) and 1,191 m^2 (i.e., 6% of the mean of all the simulated deposition area values), respectively. Similarly, the spread of the simulated erosion and deposition volume values is equal to 6,166 m^3 (i.e., 14% of the mean of all the simulated erosion volume values) and 3,217 m^3 (i.e., 13% of the mean of all the simulated deposition volume values), respectively. Clearly, these differences can be regarded as negligible when the cell routing model is used at forecasting purposes, or to identify the areas mainly subjected to large erosion and deposition phenomena. The solid-liquid hydrographs shown in **Figure 11** relate to two cross-sections located in the upper part of the channel, just downstream the triggering area of the Rovina di Cancia debris flow. All the hydrographs show a comparable well-defined triangular shape with similar values of peak discharge, time to peak, and duration. It means that the dynamic of the simulated flow is not strongly influenced by the topographic uncertainty due to the different tested interpolation algorithms. This finding is also confirmed by the cross-section profiles of the pre- (continuous line) and post-event (dotted lines) DEMs shown in **Figure 12**. The reported cross-section profiles are representative of a channel reach mainly subject to erosion processes (**Figure 12A**), deposition processes (**Figure 12B**), and mixed erosion and deposition processes (**Figure 12C**). For all the cross-sections, the DEMs profiles do not highlight meaningful differences in the channel morphology after the event. Even more important, the detected differences in the erosion and deposition profiles do not appear to be linked to the profiles variability of the input DEMs.

TABLE 4 | 50% thinning-derived 1-meter resolution DEMs model run results (50-years return period).

	Flooded area (m^2)	Erosion area (m^2)	Deposition area (m^2)	Erosion volume (m^3)	Deposition volume (m^3)
Linear triangulation	30,525.00	11,850.00	18,675.00	−42,041.18	24,300.35
Natural neighbor	30,574.00	11,862.00	18,712.00	−41,672.18	24,265.99
IDP	31,050.00	11,911.00	19,139.00	−44,062.71	25,315.81
Nearest neighbor	30,515.00	11,748.00	18,767.00	−42,104.00	24,376.84
ANUDEM	30,233.00	11,990.00	18,243.00	−42,796.95	22,933.06
Completely regularized spline	30,788.00	11,956.00	18,832.00	−44,627.68	24,732.76
Thin-plate spline	29,885.00	11,519.00	18,366.00	−40,776.85	23,228.63
Thin-plate spline plus tension	30,313.00	11,769.00	18,544.00	−41,283.94	23,278.35
Multi-quadratic spline	30,544.00	11,905.00	18,639.00	−42,873.98	24,501.13
Inverse multi-quadratic spline	31,338.00	12,292.00	19,046.00	−45,422.73	25,621.91
Point ordinary kriging	31,807.00	12,373.00	19,434.00	−46,715.08	26,150.98
Block ordinary kriging	31,630.00	12,315.00	19,315.00	−46,943.16	26,002.85

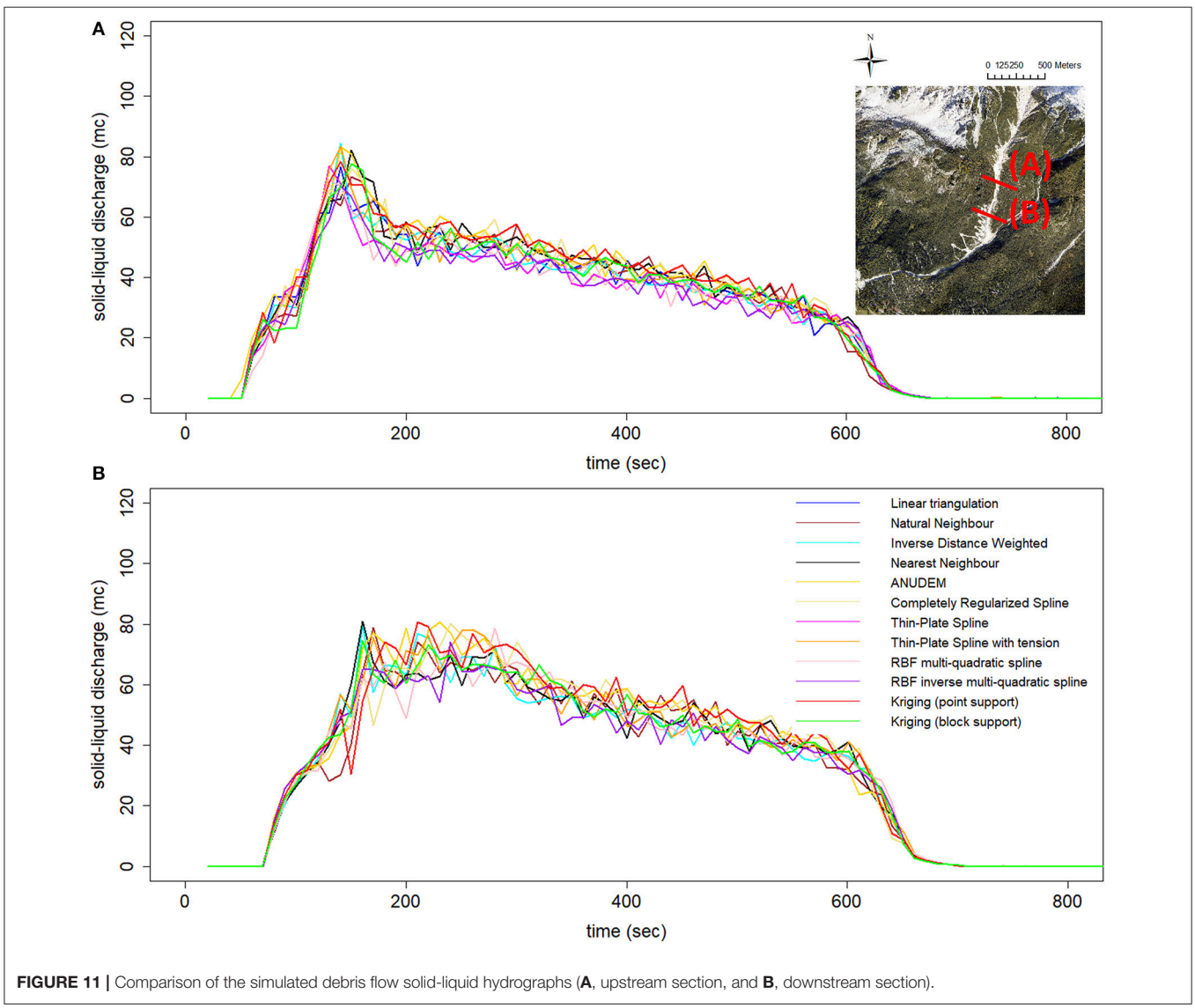

FIGURE 11 | Comparison of the simulated debris flow solid-liquid hydrographs (**A**, upstream section, and **B**, downstream section).

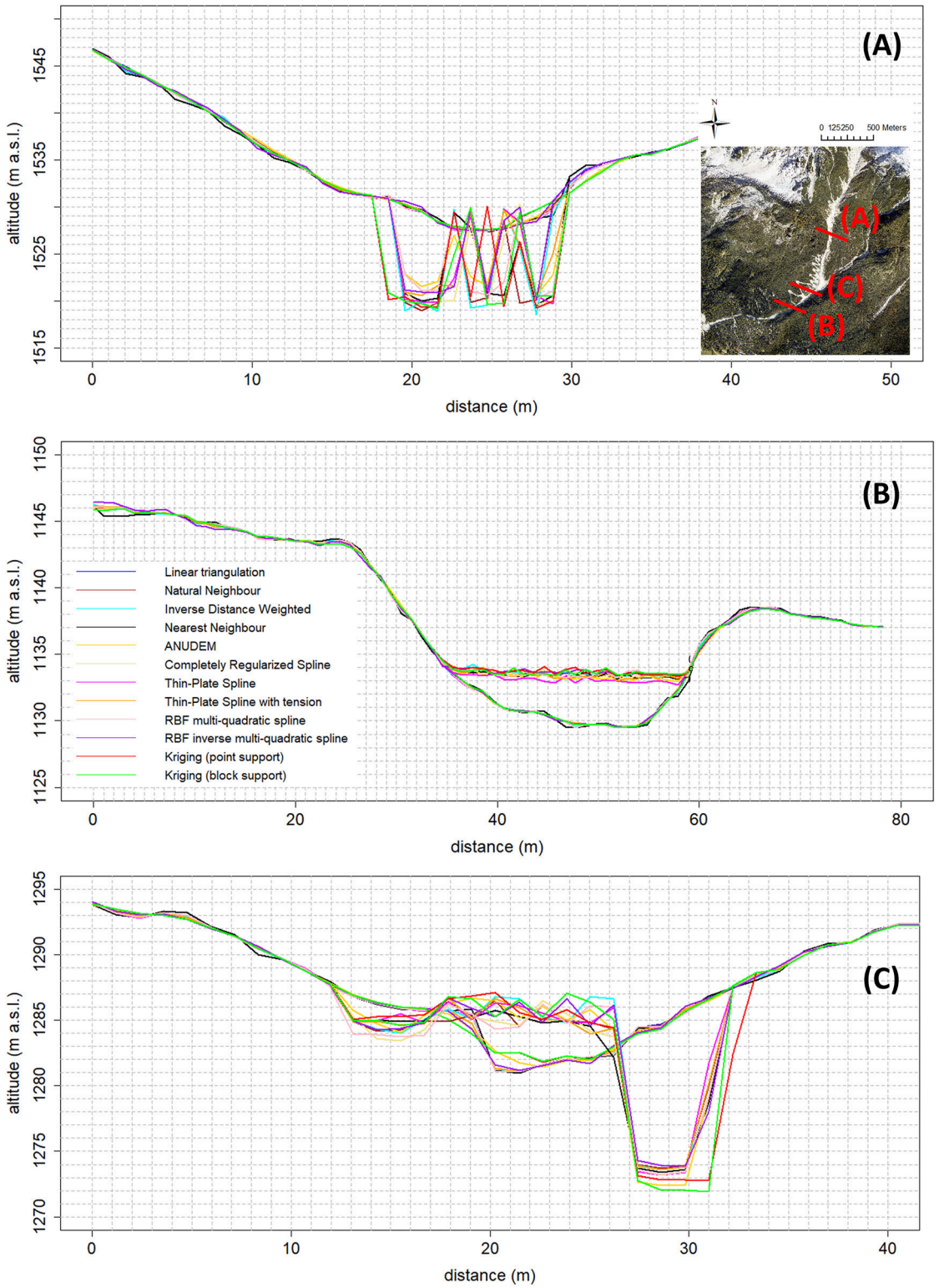

FIGURE 12 | Comparison of the pre- (continuous lines) and post-event (dotted lines) DEMs cross-section profiles (erosional **(A)**, depositional **(B)**, and mixed erosional-depositional reach **(C)** of the Rovina di Cancia debris flow channel).

CONCLUSIONS

In this study we compared the performance of twelve gridding algorithms (i.e., linear triangulation, natural neighbor, nearest neighbor, Inverse Distance to a Power, ANUDEM, completely regularize spline function, thin-plate spline function, thin-plate spline plus tension function, multi-quadratic function, inverse multi-quadratic function, point ordinary kriging, and block ordinary kriging) in building DEMs with the complex topography of a debris flow channel located in the Venetian Dolomites. After that, we paid special attention in assessing the relationship existing between the digital elevation uncertainty due to the use of the different tested interpolation methods and the uncertainty on the results of a GIS-based cell model for simulating stony debris flows routing.

The investigation carried out on the performance of the tested interpolation algorithms highlighted that the ordinary kriging algorithm, applied according to the followed methodology (i.e., employing a theoretical variogram model fitted on the directional empirical one computed perpendicularly to the linear global trend), is not suitable for reproducing the complex topography of the debris flow channel. As a matter of fact, it has demonstrated an overall unsatisfactory statistical performance, a low robustness, and a poor shape reliability. Also the ANUDEM algorithm has exhibited an overall unsatisfactory performance (from both the quantitative and qualitative point of view), despite it represents the only tested interpolation method specifically intended for digital terrain modeling. Conversely, the thin-plate spline function proved to be the most accurate and stable interpolation algorithm, along with the multi-quadratic radial basis function. However, they have demonstrated a low ability in faithfully representing the shape of the channel, mainly due to function under- and over-shooting causing relevant spiky features in correspondence of slope discontinuities. This lead to the conclusion that when the absolute accuracy of the elevation values is the most important feature, these algorithms could represent the best choice also in natural landscapes featuring a high morphological complexity. On the other hand, when also the realistic representation of surface shape is important, the linear triangulation, the natural neighbor algorithm, and the thin-plate spline plus tension and completely regularized spline basis functions could represent a better choice, since they ensure a proper trade-off among accuracy and shape reliability.

The evaluation of the effects of the gridding techniques on debris flows routing modeling revealed that the correlation between the uncertainty in the cell elevations due to the different tested interpolation methods and the uncertainty in the corresponding simulated erosion/deposition depths was weak, regardless of both the magnitude of the modeled event scenario and the points density of the dataset used during the interpolation procedure. Also the results of the different model runs in terms of simulated areas, erosion and deposition volumes, solid-liquid discharges, and channel morphology after the event did not highlight a significant change in the model behavior depending on the used topographic surface. This leads to the conclusion that the choice of the interpolation algorithm does not represent a determining factor for debris flows routing modeling.

However, the extrapolation of the latter conclusion must be done with care at least for two reasons. In fact, the investigation was performed focusing on a channelized-debris flow, whose flow depths are larger than the DEMs height uncertainty resulting from the interpolation procedure. So, future researches have to be carried out in order to test the influence of the gridding algorithms on non-channelized debris flows, since in this case small interpolation errors might have a greater impact on the dynamic of the simulated flow, and thus on the resulting erosional/depositional pattern. Furthermore, also the use of different rheological models and/or sediments erosion and deposition process schematizations might lead to different conclusions. Therefore, in order to confirm the finding of this paper more work has to be done also by testing different debris flows routing models.

AUTHOR CONTRIBUTIONS

MBo carried out the analysis on the topographic data, the interpolation of DEMs, the comparison among the different gridding routine, the numerical simulations, and the analysis on the obtained results. MBe carried out the hydrological simulations, performed the rtkGPS surveys, and helped building a code for GIS analysis. CG contributed to the triggering and hydraulic simulations. Furthermore, he, supervised, checked, and reviewed the work.

ACKNOWLEDGMENTS

The authors wish to thank the Regional Civil Work Agency of Veneto for the ortho-photos and full-waveform LiDAR data. We also thank the Environmental Protection Agency of Veneto (ARPAV) for providing the meteorological data used in the hydrological modeling. Data are available under request to the corresponding author.

SUPPLEMENTARY MATERIAL

The Supplementary Material for this article can be found online at: https://www.frontiersin.org/articles/10.3389/feart.2018.00089/full#supplementary-material

REFERENCES

Aguilar, F. J., Agüera, F., Aguilar, M. A., and Carvajal, A. F. (2005). Effects of Terrain Morphology, Sampling Density, and Interpolation Methods on Grid DEM Accuracy. *Photogram. Eng. Remote Sens.* 71, 805–816. doi: 10.14358/PERS.71.7.805

Armanini, A., Fraccarollo, L., and Rosatti, G. (2009). Two-dimensional simulation of debris flows in erodible channels. *Comput. Geosci.* 35, 993–1006. doi: 10.1016/j.cageo.2007.11.008

Bater, C. W., and Coops, N. C. (2009). Evaluating error associated with lidar-derived DEM interpolation. *Comput. Geosci.* 35, 289–300. doi: 10.1016/j.cageo.2008.09.001

Berger, C., McArdell, B. W., and Schlunegger, F. (2011). Direct measurement of channel erosion by debris flows, Illgraben, Switzerland. *J. Geophys. Res.* 116:F01002. doi: 10.1029/2010JF001722

Berti, M., Genevois, R., Simoni, A., and Tecca, R. P. (1999). Field observations of a debris flow event in the Dolomites. *Geomorphology* 29, 265–274. doi: 10.1016/S0169-555X(99)00018-5

Berti, M., and Simoni, A. (2005). Experimental evidences and numerical modeling of debris flow initiated by channel runoff. *Landslides* 2, 171–182. doi: 10.1007/s10346-005-0062-4

Berti, M., and Simoni, A. (2014). DFLOWZ: a free program to evaluate the area potentially inundated by a debris flow. *Comput. Geosci.* 67, 14–23. doi: 10.1016/j.cageo.2014.02.002

Blöschl, G., and Grayson, R. (2000). Spatial Observations and Interpolation. *Spat. Patt. Catch. Hydrol.* 113, 13–16.

Bossi, G., Cavalli, M., Crema, S., Frigerio, S., Luna, B. Q., and Mantovani, M. (2014). Multi temporal LiDAR-DTMs as a tool for modeling a complex landslide: a case study in the Rotolon catchment (Eastern Italian Alps). *Natl. Hazards Earth Syst. Sci. Discus.* 2, 6453–6474. doi: 10.5194/nhessd-2-6453-2014

Caroti, G., and Piemonte, A. (2010). *Analisi Dei Dati Altimetrici Disponibili Per Il Territorio Comunale Di Pisa, Geomatica le Radici Del Futuro*. Pavia: Edizioni SIFET.

Carrara, A., Bitelli, G., and Carla, R. (1997). Comparison of techniques for generating digital terrain models from contour lines. *Int. J.Geogr. Inform. Sci.* 11, 451–472. doi: 10.1080/136588197242257

Cavalli, M., and Marchi, L. (2008). The effectiveness of airborne LiDAR's data in the recognition of channel-bed morphology. *Catena* 75, 249–260. doi: 10.1016/j.catena.2007.11.001

Chaplot, V., Darboux, F., Bourennane, H., Leguedois, S., Silvera, N., and Phachomphon, K. (2006). Accuracy of interpolation techniques for the derivation of digital elevation models in relation to landform types and data density. *Geomorphology* 77, 126–141. doi: 10.1016/j.geomorph.2005.12.010

Chiles, J. P. (1984). "Simulation of a nickel deposit: problems encountered and practical solutions," in *Geostatistics for Natural Resources Characterization*, eds G. Verly, M. David, A. G. Journel, and A. Makchal. Dordrecht; Hollan: Reidel, Springer.

Cilloccu, F., Dequal, S., Brovelli, M., Crespi, M., and Lingua, A. (2009). Ortoimmagini 1:10.000 e modelli altimetrici. *Linee Guida*. Roma: CISIS - Centro Interregionale per i Sistemi Informatici, Geografici e Statistici.

Deangeli, C. (2008). Laboratory granular flows generated by slope failures. *Rock Mech. Rock Eng.* 41 , 199–217. doi: 10.1007/s00603-007-0131-1

Declercq, F. A. N. (1996). Interpolation methods for scattered sample data: accuracy, spatial patterns, processing time. *Cartogr. Geogr. Inform. Sys.* 23, 128–144. doi: 10.1559/152304096782438882

Degetto, M., Gregoretti, C., and Bernard, M. (2015). Comparative analysis of the differences between using LiDAR and contour-based DEMs for hydrological modeling of runoff generating debris flows in the Dolomites. *Front. Earth Sci.* 3:21. doi: 10.3389/feart.2015.00021

Desmet, P. J. J. (1997). Effects of interpolation errors on the analysis of DEMs. *Earth Surf. Process. Landforms* 22, 563–580. doi: 10.1002/(SICI)1096-9837(199706)22:6<563::AID-ESP713>3.0.CO;2-3

Di Cristo, C., Iervolino, M., and Vacca, A. (2014). Applicability of kinematic, diffusion and quasi-steady dynamic wave models to shallow mud flows. *J. Hydrol. Eng.* 19, 956–965. doi: 10.1061/(ASCE)HE.1943-5584.0000881

Easterling, D. R., Evans, J. L., Groisman, P. Y., Karl, T. R., Kunkel, K. E., and Ambenje, P. (2000). Observed variability and trends in extreme climate events: a brief review. *Bull. Am. Meteorol. Soc.* 81, 417–425. doi: 10.1175/1520-0477(2000)081<0417:OVATIE>2.3.CO;2

Egashira, S., and Ashida, K. (1987). "Sediment transport in steep slope flumes," in *Proceedings of Roc Japan Joint Seminar on Water Resources*.

El-Sheimy, N., Valeo, C., and Habib, A. (2005). *Digital Terrain Modeling Acquisition, Manipulation, and Applications; Artech House:* Boston, MA.

Erdogan, S. (2009). A comparison of interpolation methods for producing digital elevation models at the field scale. *Earth Surf. Proc. Land.* 34, 366–376. doi: 10.1002/esp.1731

Evans, J. S. (2017). *SpatialEco.* R package version 0.0.1-7. Available online at: https://CRAN.R-project.org/package=spatialEco

Floris, M., D'Alpaos, A., Squarzoni, C., Genevois, R., and Marani, M. (2010). Recent changes in rainfall characteristics and their influence on thresholds for debris flow triggering in the Dolomitic area of Cortina d'Ampezzo, north-eastern Italian Alps. *Nat. Hazards Earth Syst. Sci.* 10, 571–580. doi: 10.5194/nhess-10-571-2010

Fonstad, M. A., Dietrich, J. T., Courville, B. C., Jensen, J. L., and Carbonneau, P. E. (2013). Topographic structure from motion: a new development in photogrammetric measurement. *Earth Surface Proces. Landf.* 38, 421–430. doi: 10.1002/esp.3366

French, J. R. (2003). Airborne LiDAR in support of geomorphological and hydraulic modeling. *Earth Surf. Process. Landf.* 28, 321–335. doi: 10.1002/esp.484

Gallay, M., Lloyd, C. D., McKinley, J., and Barry, L. (2013). Assessing modern ground survey methods and airborne laser scanning for digital terrain modeling: a case study from the Lake District, England. *Comput. Geosci.* 51, 216–227. doi: 10.1016/j.cageo.2012.08.015

Garnero, G., and Godone, D. (2011). *Accuratezza Nell'interpolazione dei DTM: Analisi dei fattori Determinanti*. Colorno: Atti del XV Conferenza Nazionale ASITA.

Ghilardi, P., Natale, L., and Savi, F. (2001). Modeling debris-flow propagation and deposition. *Phys. Chem. Earth C* 26, 651–656. doi: 10.1016/S1464-1917(01)00063-0

Gregoretti, C., and Dalla Fontana, G. (2007). "Rainfall threshold for the initiation of debris flows by channel bed failure of the dolomites," in *Proceedings of the Fourth International Conference on Debris Flow Hazards Mitigation*, eds C. L. Chen and J. J. Major (Chengdu: Balkema), 11–21.

Gregoretti, C., and Dalla Fontana, G. (2008). The triggering of debris flow due to channel-bed failure in some alpine headwater basins of the Dolomites: analyses of critical runoff. *Hydrol. Process.* 22, 2248–2263. doi: 10.1002/hyp.6821

Gregoretti, C., Degetto, M., Bernard, M., and Boreggio, M. (2018b). The debris flow occurred at Ru Secco Creek, Venetian Dolomites, on 4 August 2015: analysis of the phenomenon, its characteristics and reproduction by models. *Front. Earth Sci.* 6:367817. doi: 10.3389/feart.2018.00080

Gregoretti, C., Degetto, M., Bernard, M., Crucil, G., Pimazzoni, A., De Vido, G., et al. (2016b). Runoff of small rocky headwater catchments: Field observations and hydrological modeling. *Water Resour. Res.* 52, 8138–8158. doi: 10.1002/2016WR018675

Gregoretti, C., Degetto, M., and Boreggio, M. (2016a). GIS-based cell model for simulating debris flow runout on a fan. *J. Hydrol.* 534, 326–340. doi: 10.1016/j.jhydrol.2015.12.054

Gregoretti, C., Stancanelli, L., Bernard, M., Degetto, M., Boreggio M., and Lanzoni S. (2018a). Relevance of erosion processes when modelling in-channel gravel debris flows for efficient hazard assessment. *J. Hydrol.* doi: 10.1016/j.jhydrol.2018.10.001

Hancock, G. R. (2006). The impact of different gridding methods on catchment geomorphology and soil erosion over long timescales using a landscape evolution model. *Earth Surf. Process. Landforms* 31, 1035–1050. doi: 10.1002/esp.1306

Hengl, T. (2006). Finding the right pixel size. *Comput. Geosci.* 32, 1283–1298. doi: 10.1016/j.cageo.2005.11.008

Hengl, T., and Reuter, H. I. (eds.). (2009). *Geomorphometry: Concepts, Software, Applications. Developments in Soil Science,* Vol. 33. Amsterdam; Oxford, UK: Elsevier.

Heritage, G. L., and Large, A. R. G. (2009). *Laser Scanning for the Environmental Sciences*. London: Wiley-Blackwell.

Heritage, G. L., Milan, D. J., Large, A. R. G., and Fuller, I. (2009). Influence of survey strategy and interpolation model upon DEM quality. *Geomorphology* 112, 334–344. doi: 10.1016/j.geomorph.2009.06.024

Hodgson, M. E., and Bresnahan, P. (2004). Accuracy of Airborne Lidar-Derived Elevation. *Photogram. Eng. Remote Sens.*70, 331–339. doi: 10.14358/PERS.70.3.331

Höhle, J., and Höhle, M. (2009). Accuracy assessment of digital elevation models by means of robust statistical methods. *ISPRS J. Photogramm. Remote Sens.* 64, 398–406. doi: 10.1016/j.isprsjprs.2009.02.003

Höhle, J., and Potuckova, M. (2011). *Assessment of the Quality of Digital Terrain Models*. Amsterdam: European Spatial Data Research, Official Publication n. 60.

Hussin, H. Y., Quan Luna, B., van Westen, C. J., Christen, M., Malet, J. P., and van Asch Th,. W. J. (2012). Parameterization of a numerical 2-D debris flow model with entrainment: a case study of the Faucon catchment, Southern French Alps. *Nat. Hazards Earth Syst. Sci.* 12, 3075–3090. doi: 10.5194/nhess-12-3075-2012

Hutchinson, M. F. (1996). "A locally adaptive approach to the interpolation of digital elevation models," in *Proceedings, Third International Conference/Workshop on Integrating GIS and Environmental Modeling, Santa Fe, NM, January 21-26, 1996* (Santa Barbara, CA: National Center for Geographic Information and Analysis).

Isaaks, E. H., and Srivastava, R. M. (1989). *An Introduction to Applied Geostatistics*. Oxford: Oxford University Press.

Iverson, R. M. (2005). "Debris-flow mechanics," in *Debris-Flow Hazards and Related Phenomena*, eds M. Jakob and O. Hungr (Berlin; Heidelberg: Springer-Praxis), 105–134.

Jaboyedoff, M., Oppikofer, T., Abellán, A., Derron, M. H., Loye, A., Metzger, R., et al. (2012). Use of LIDAR in landslide investigations: a review. *Natl. Hazards* 61, 5–28. doi: 10.1007/s11069-010-9634-2

Johnston, K., Ver Hoef, J., Krivoruchko, K., and Neil, L. (2001). *Using Arcgis Geostatistical Analyst*. Redlands, CA: ESRI Press.

Krause, P., Boyle, D. P., and Bäse, F. (2005). Comparison of different efficiency criteria for hydrological model assessment. *Adv. Geosci.* 5, 89–97. doi: 10.5194/adgeo-5-89-2005

Lenzi, M. A., D'Agostino, V., Gregoretti, C., and Sonda, D. (2003). "A simplified numerical model for debris-flow hazard assessment: DEFLIMO," in *Third International Conference On Debris Flow Hazard Mitigations: Mechanics, Prediction and Assessment* (Davos), 10–12.

Li, Z. (1993). Theoretical models of the accuracy of digital terrain models: an evaluation and some observations. *Photogram. Record* 14, 651–660. doi: 10.1111/j.1477-9730.1993.tb00775.x

Mallet, C., and Bretar, F. (2009). Full-waveform topographic LiDAR: state-of-the-art. *ISPRS J. Photogram. Remote Sensing* 64, 1–16. doi: 10.1016/j.isprsjprs.2008.09.007

Mattea, S., Franceschinis, C., Scarpa, R., and Thiene, M. (2016). Valuing landslide risk reduction programs in the Italian Alps: the effect of visual information on preference stability. *Land Use Policy* 59, 176–184. doi: 10.1016/j.landusepol.2016.08.032

McDonnell, R. A., and Lloyd, C. D. (2015). *Principles of Geographical Information Systems*. Oxford, UK: Oxford University Press.

Medina, V., Hurlimann, M., and Bateman, A. (2008). Application of FLATModel, a 2D finite volume code, to debris flows in the Northeastern part of Iberian Peninsula Experimental evidences and numerical modeling of debris flow initiated by channel runoff. *Landslide* 5, 127–142. doi: 10.1007/s10346-007-0102-3

Milan, D. J., Heritage, G. L., Large, A. R. G., and Fuller, I. C. (2011). Filtering spatial error from DEMs: implications for morphological change estimation. *Geomorphology* 125, 160–171. doi: 10.1016/j.geomorph.2010.09.012

Mitas, L., and Mitasova, H. (1999). Spatial interpolation. *Geogr. Inf. Syst. Principles Tech. Manag. Appl.* 1, 481–492.

Moore, I. D., and Grayson, R. B. (1991). Terrain-based catchment partitioning and runoff prediction using vector elevation data. *Water Resour. Res.* 27, 1177–1191. doi: 10.1029/91WR00090

Oliver, M. A., and Webster, R. (2014). Catena A tutorial guide to geostatistics: computing and modeling variograms and kriging. *Catena* 113, 56–69. doi: 10.1016/j.catena.2013.09.006

Pfeifer, N. (2005). A subdivision algorithm for smooth 3D terrain models. *ISPRS J. Photogram. Remote Sensing* 59, 115–127. doi: 10.1016/j.isprsjprs.2004.09.002

Podobnikar, T. (2009). Methods for visual quality assessment of Digital Terrain Model. *J. SAPIENS* 2, 15–24.

Pourali, S., Arrowsmith, C., and Chrisman, N. (2014). "Vertical accuracy assessment of LiDAR ground points using minimum distance approach," in *Research at Locate'14*, eds S. Winter and C. Rizos (Canberra, ACT: Rheinisch-Westfaelische Technische Hochschule Aache), 86–96.

R Development Core Team (2008). *R: A Language and Environment for Statistical Computing*. Vienna: R Foundation for Statistical Computing.

Reutebuch, S. E., McGaughey, R. J., Andersen, H. E., and Carson, W. W. (2003). Accuracy of a high-resolution lidar terrain model under a conifer forest canopy. *Can. J. Remote Sensing* 29, 527–535. doi: 10.5589/m03-022

Rickenmann, D., Laigle, B., McArdell, B. W., and Hubl, J. (2006). Comparison of 2D debris-flow simulation models with field events. *Comput. Geosci.* 10, 241–264 doi: 10.1007/s10596-005-9021-3

Rosatti, G., and Begnudelli, L. (2013). Two-dimensional simulation of debris flows over mobile bed: enhancing the TRENT2D model by using a well-balanced generalized Roe-type solver. *Comput. Fluids* 71, 179–185. doi: 10.1016/j.compfluid.2012.10.006

Saksena, S., and Merwade, V. (2015). Incorporating the effect of DEM resolution and accuracy for improved flood inundation mapping. *J. Hydrol.* 530, 180–194. doi: 10.1016/j.jhydrol.2015.09.069

Scheidl, C., and Rickenmann, D. (2010). "TopFlowDF-A simple GIS based model to simulate debris-flow runout on the fan," in *Proceedings of the Fifth International Conference on Debris Flow Hazards Mitigation* (Padova), 253–262.

Scheidl, C., Rickenmann, D., and Chiari, M. (2008). The use of airborne LiDAR data for the analysis of debris flow events in Switzerland. *Nat. Hazards Earth Syst. Sci.* 8, 1113–1127. doi: 10.5194/nhess-8-1113-2008

Schwendel, A. C., Fuller, I. C., and Death, R. G. (2012). Assessing DEM interpolation methods for effective representation of upland stream morphology for rapid appraisal of bed stability. *River Res. Applic.* 28, 567–584. doi: 10.1002/rra.1475

Setiawan, M. A., Rutzinger, M., Wichmann, V., Stoetter, J., and Sartohadi, J. (2013). Evaluation of Methods for Digital Elevation Model Interpolation of Tillage Systems. *J. Natl. Resour. Develop.* 3, 1 28–139. doi: 10.5027/jnrd.v3i0.13

Simoni, A., Bernard, M., Berti, M., Boreggio, M., Lanzoni, S., Stancanelli, L. M., et al. (2018). "Observation of initiation conditions and role of sediment availability in run-off generated debris flows at Cancia (North Eastern Italian Alps)," in *Geographical Research Abstract. Vol. 20, EGU2018-9091* (Vienna: EGU General Assembly 2018).

Smith, S., Holland, D., and Longley, P. (2005). "The importance of understanding error in LiDAR digital elevation models," *20 th ISPRS Conference* (Istanbul), 12–34.

Sodnik, J., Podobnikar, T., and Mikoš, M. (2012). "Using LiDAR data for debris flow modeling," in *12th Congress INTERPRAEVENT 2012* (Grenoble), 573–583.

Takahashi, T. (1978). Mechanical characteristics of debris flow. *J. Hydr. Div. ASCE* 104, 1153–1169.

Takahashi, T. (2007). *Debris Flow Mechanics, Prediction and Countermeasures*. London; Leiden: Taylor and Francis, Balkema.

Tarolli, P. (2014). High-resolution topography for understanding Earth surface processes: opportunities and challenges. *Geomorphology* 216, 295–312, doi: 10.1016/j.geomorph.2014.03.008

Theule, J. I., Liebault, F., Loye, A., Laigle, D., and Jaboyedoff, M. (2012). Sediment budget monitoring of debris flow and bedload transport in the Manival Torrent, SE France. *Natl. Hazard Earth Sci.* 12, 731–749. doi: 10.5194/nhess-12-731-2012

Thiene, M., Shaw, W. D., and Scarpa R. (2017). Perceived risks of mountain landslides in Italy: stated choices for subjective risk reductions. *Landslides* 14, 1077–1089. doi: 10.1007/s10346-016-0741-3

Tiranti, D., and Deangeli, C. (2015). Modeling of debris flow depositional patterns according to the catchment and sediment source area characteristics. *Front. Earth Sci.* 3:8. doi: 10.3389/feart.2015.00008

Tsubaki (1972). "Keikoku taiseki dosha no ryndo," in *XXVII Japanese National Congress on Civil Engineering (in japanese)*.

Vosselman, G. V., and Maas, H. G. (eds.). (2010). *Airborne and Terrestrial Laser Scanning*. Scotland, UK: Whittles.

Wagner, W., Ullrich, A., Ducic, V., Melzer, T., and Studnicka, N. (2006). Gaussian decomposition and calibration of a novel small-footprint full-waveform digitising airborne laser scanner. *ISPRS J. Photogramm. Remote Sens.* 60, 100–112. doi: 10.1016/j.isprsjprs.2005.12.001

Webster, T. L., and Dias, G. (2006). An automated GIS procedure for comparing GPS and proximal LIDAR elevations. *Comput. Geosci.* 32, 713–726. doi: 10.1016/j.cageo.2005.08.009

Weng, Q. (2006). "An evaluation of spatial interpolation accuracy of elevation data," in *Progress in Spatial Data Handling*, eds A. Riedl, W. Kainz, G. A. Elmes (Berlin: Springer-Verlag), 805–824.

Wilson, J. P., and Gallant, J. C. (2000). "Digital terrain analysis," in Terrain Analysis: Principles and Applications, eds J. P. Wilson and J. C. Gallant (New York, NY: Wiley), 1–28.

Wise, S. M. (2000). Assessing the quality for hydrological applications of digital elevation models derived from contours. *Hydrol. Process.* 14, 1909–1929. doi: 10.1002/1099-1085(20000815/30)14:11/12<1909::AID-HYP45>3.0.CO;2-6

Wise, S. M. (2007). Effect of differing DEM creation methods on the results from a hydrological model. *Comput. Geosci.* 33, 1351–1365. doi: 10.1016/j.cageo.2007.05.003

Wood, J. D. (1996). *The Geomorphological Characterisation of Digital Elevation Models*. Unpublished Doctoral Thesis, University of Leicester.

Wood, J. D., and Fisher, P. F. (1993). Assessing Interpolation Accuracy in Elevation Models. *IEEE Comput. Graph. Applic.* 13, 48–56. doi: 10.1109/38.204967

Yang, X., and Hodler, T. (2000). Visual and statistical comparisons of surface modeling techniques for point-based environmental data. *Cartogr. Geogr. Inform. Sci.* 27, 165–175. doi: 10.1559/152304000783547911

Conflict of Interest Statement: The authors declare that the research was conducted in the absence of any commercial or financial relationships that could be construed as a potential conflict of interest.

frontiers in Earth Science

ORIGINAL RESEARCH
published: 23 May 2018
doi: 10.3389/feart.2018.00060

An Integrated Study to Evaluate Debris Flow Hazard in Alpine Environment

Davide Tiranti[1]*, *Stefano Crema*[2], *Marco Cavalli*[2] and *Chiara Deangeli*[3]

[1] Department of Forecasting Systems, Regional Agency for Environmental Protection of Piemonte, Turin, Italy, [2] National Research Council, Research Institute for Geo-Hydrological Protection, Padua, Italy, [3] Department of Environment, Land and Infrastructure Engineering, Politecnico di Torino, Turin, Italy

Debris flows are among the most dangerous natural processes affecting the alpine environment due to their magnitude (volume of transported material) and the long runout. The presence of structures and infrastructures on alluvial fans can lead to severe problems in terms of interactions between debris flows and human activities. Risk mitigation in these areas requires identifying the magnitude, triggers, and propagation of debris flows. Here, we propose an integrated methodology to characterize these phenomena. The methodology consists of three complementary procedures. Firstly, we adopt a classification method based on the propensity of the catchment bedrocks to produce clayey-grained material. The classification allows us to identify the most likely rheology of the process. Secondly, we calculate a sediment connectivity index to estimate the topographic control on the possible coupling between the sediment source areas and the catchment channel network. This step allows for the assessment of the debris supply, which is most likely available for the channelized processes. Finally, with the data obtained in the previous steps, we modeled the propagation and depositional pattern of debris flows with a 3D code based on Cellular Automata. The results of the numerical runs allow us to identify the depositional patterns and the areas potentially involved in the flow processes. This integrated methodology is applied to a test-bed catchment located in Northwestern Alps. The results indicate that this approach can be regarded as a useful tool to estimate debris flow related potential hazard scenarios in an alpine environment in an expeditious way without possessing an exhaustive knowledge of the investigated catchment, including data on historical debris flow events.

Keywords: torrential mass movement, sediment connectivity, cellular automata, hazard assessment, Northwestern Italy

OPEN ACCESS

Edited by:
Daniel Nývlt,
Masaryk University, Czechia

Reviewed by:
Radek Tichavsky,
University of Ostrava, Czechia
Vincenzo Amato,
University of Molise, Italy

***Correspondence:**
Davide Tiranti
davide.tiranti@arpa.piemonte.it

Specialty section:
This article was submitted to Quaternary Science, Geomorphology and Paleoenvironment, a section of the journal Frontiers in Earth Science

Received: *29 January 2018*
Accepted: *07 May 2018*
Published: *23 May 2018*

Citation:
Tiranti D, Crema S, Cavalli M and Deangeli C (2018) An Integrated Study to Evaluate Debris Flow Hazard in Alpine Environment. Front. Earth Sci. 6:60. doi: 10.3389/feart.2018.00060

INTRODUCTION

In the last decades, several studies have focused on analyzing channel processes in relation to hydrological, geomorphological and ecological systems; in particular, the concepts of coupling and connectivity are largely adopted for studying the interaction of hillslope and channel flows in order to model the hydrological response of catchments (Rickenmann, 1999; Michaelides and Wainwright, 2002; Glade, 2005; Michaelides and Chappell, 2009) and sediment dynamics (Iverson, 2003; Rickenmann et al., 2003; Berti and Simoni, 2005).

Sediment connectivity is a measure of the degree of linkage between sediment sources and downstream areas (Cavalli et al., 2013) and its spatial characterization in a catchment gives an estimation of the possible paths of sediment to reach a target zone. The geomorphic effect of the rainfall acting on sediment deposits may result in debris flow occurrence. Debris flows are one of the most dangerous phenomena within the Italian alpine environment. In fact, they have been responsible for the 36% of fatalities in the Italian alpine region during the last century (Tropeano et al., 2006). Mitigation of debris flow effects on human life has become one of the most important challenges of the scientific community.

The complexity of such a type of catchment processes, resulted in several research field focused on particular aspects governing the behavior of these flows events.

The aspects related to debris flows are typically investigated with emphasis on:

1. triggering conditions (Ellen and Flaming, 1987; Gregoretti, 2000; Beylich and Sandberg, 2005; Wieczorek and Glade, 2005; Cannon et al., 2008; Tiranti et al., 2008; Stoffel et al., 2011, 2014; Kean et al., 2013; Brunetti et al., 2015; Marra et al., 2015; Cavalli et al., 2017a)
2. propagation and deposition (Chang and Chao, 2006; Rickenmann et al., 2006; Deangeli et al., 2015; Gregoretti et al., 2016);
3. magnitude evaluation (Bovis and Dagg, 1988; Marchi and D'Agostino, 2004; Jakob et al., 2005; Hungr et al., 2008; Brardinoni et al., 2012; Rickenmann, 2015; Tiranti et al., 2016a; Cavalli et al., 2017b);
4. rheological behavior (Pierson and Costa, 1987; Costa, 1988; Hungr, 1995, 2002; Ancey, 2007; Von Boetticher et al., 2016);
5. geomorphological and sedimentary processes (Moscariello et al., 2002; Wilford et al., 2004);
6. evolution mechanisms (Sassa, 1985; Segre and Deangeli, 1995; Prancevic et al., 2014);
7. hydrologic modeling (Johnson and Sitar, 1990; Harvey, 1994; Hürlimann et al., 2006; Gregoretti et al., 2016).

In this paper, an integrated study to gain insight into potential hazard linked to debris flows is presented. The proposed methodology starts from the classificati of the catchment and the characterization of the main active processes. Considering the characteristics of the dominant bedrock lithology in the area (Tiranti et al., 2014) it is possible to infer a potential frequency of occurrence of debris flows, the total rainfall needed for their triggering, together with the sedimentological and rheological characteristics of the flow (viscosity, evolution, and depositional style). The second step consists in the characterization of sediment source areas, including their degree of coupling to the main channel by using a sediment connectivity index (IC) proposed by Cavalli et al. (2013). The final step concerns the propagation and deposition of material from sediment source areas actually involved in debris flow process by a Cellular Automata Model (Deangeli, 2008) simulating the mechanisms of flow routing and deposition patterns. One of the advantages of the presented integrated approach relies on the fact that there's no need to simulate past debris flow events to define its deposition areas, but it takes into account a likely volume based on the availability and distribution of sediment source areas and a compatible deposition pattern with the alluvial fan architecture and the processes behavior characterizing the catchments, according to the CWI classification proposed by Tiranti et al. (2008, 2014, 2016a), Tiranti and Deangeli (2015). The aim of the simulations is to match the predominant observed depositional style on the alluvial fan and the channel bed. In this way, the model can be applied in absence of a detailed report (actual magnitude, deposition areas, etc.) of a debris flow event used as calibration test. In this way, it is possible to get close to the most likely behavior of a given catchment. The methodology has been applied to an alpine test-bed catchment, for which historical documentation on debris flow occurrence is available, thus helping in the validation of the obtained results.

Study Area

The Rio Frejus catchment, located at the head of Susa Valley (upper Susa Valley, Municipality of Bardonecchia, Turin, North-western Italy), covers an area of about 22 km^2 and is composed by several sub-catchments: Comba Merdovine, Comba del Frejus, Comba Gaudet, Comba Cougna, Comba Gautier, and Rio Chaulet (**Figure 1**).

The upper Susa Valley is dominated by dry climate with average annual precipitations is under 800 mm, whereas the annual average is about 1,200 mm in Piemonte. The average number of annual rainy days is about 50 with a very low precipitation density, <10 mm/day (Fratianni and Motta, 2002).

Rio Frejus is characterized by a complex geomorphology due to the combined action of several processes, such as landslides, rock falls, debris flows and cryogenic processes (permafrost degradation and nival processes) at the head of catchments. Shallow deposits linked to the glacial activity are infrequent and almost completely reworked by the action of streams and landslides. For more details on geomorphological settings of Rio Frejus see Bosco et al. (2007) and Tiranti et al. (2016b).

The pre-Quaternary bedrock of Rio Frejus belongs primarily to the Tectonostratigraphic Unit of the Lago Nero (Polino et al., 2002), formed by carbonate or phylladic calc-schists. The outcropping of thick-bedded serpentinites, ophicalcites and quartzites is subordinate. The outcrops percentages consist of 74.2% shallow deposits (including colluvial cover), 27.28 schists, 0.22% serpentinites/ophicalcites and 0.03% quartzites (**Figure 2**).

The main structural setting is represented by slightly-dip overthrust contacts and subvertical faults. The intensely fractured rock masses exhibit poor geomechanical characteristics. The phylladic-rich calc-schists are extremely degraded and can be classified as blocky/disturbed/seamy according to the Geological Strength Index (GSI; Marinos et al., 2005). Such conditions favor weathering with high generation of fine loose materials and slope instability. The main characteristics of Rio Frejus are reported in **Table 1**.

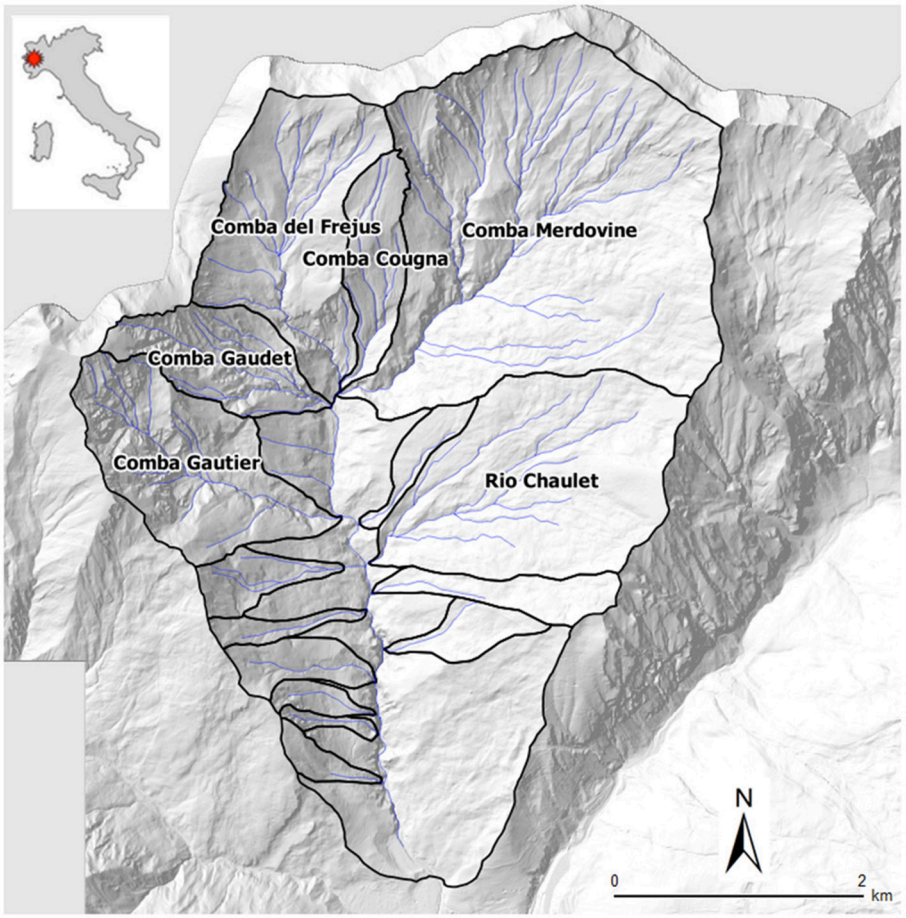

FIGURE 1 | Rio Frejus catchment and its sub-catchments.

METHODS

Clay Weathering Index (CWI) and Catchment Classification

North-western alpine catchments were classified by Tiranti et al. (2014) into three main catchment lithology classes by using the Clay Weathering Index (CWI). This index defines the propensity of a certain lithotype to weather into clay or other fine minerals with clay-like rheology behavior (e.g., phyllosilicate groups). Following this approach, Excellent Clay Maker (ECM) catchments are characterized by particularly degradable rocks due to their weak geotechnical characteristics. Debris flow frequency for these catchments is therefore high (two events/year) due to the abundance of unconsolidated material available along the channel network in spring, summer and autumn with indicative minimum triggering rainfall threshold of 20 mm/h. In Good Clay Maker (GCM) catchments, rocks are degradable and consequently, the unconsolidated material is less abundant if compared to ECM ones. Debris flows for this class occur usually in late-spring, with an indicative minimum triggering rainfall threshold of 30 mm/h. In Bad Clay Maker (BCM) catchments, bedrocks are more resistant to the weathering and inclined to produce coarse debris (blocks and boulders in silt-sandy matrix). Debris flows are triggered by infrequently heavy rainfall. In this case, the debris flows average frequency is <1 event every 20 years and the main seasons of occurrence are fall and early spring (very uncommon during summer). Identified minimum triggering rainfall threshold is 50 mm/h.

Sediment Connectivity Index (IC)

The Sediment Connectivity Index (IC) was originally proposed by Borselli et al. (2008) with an application to agricultural catchments. Cavalli et al. (2013) made important modifications to this approach to take advantage of high-resolution Digital Terrain Models (DTMs) and to make it suitable for applications to mountain environment. IC is a distributed morphometric index focused on the topography influence on sediment connectivity representing the degree of coupling among different portions of the catchment with respect to a selected target (e.g., main channel network).

Mathematically IC is expressed by the logarithm of the ratio between the upslope and the downslope components

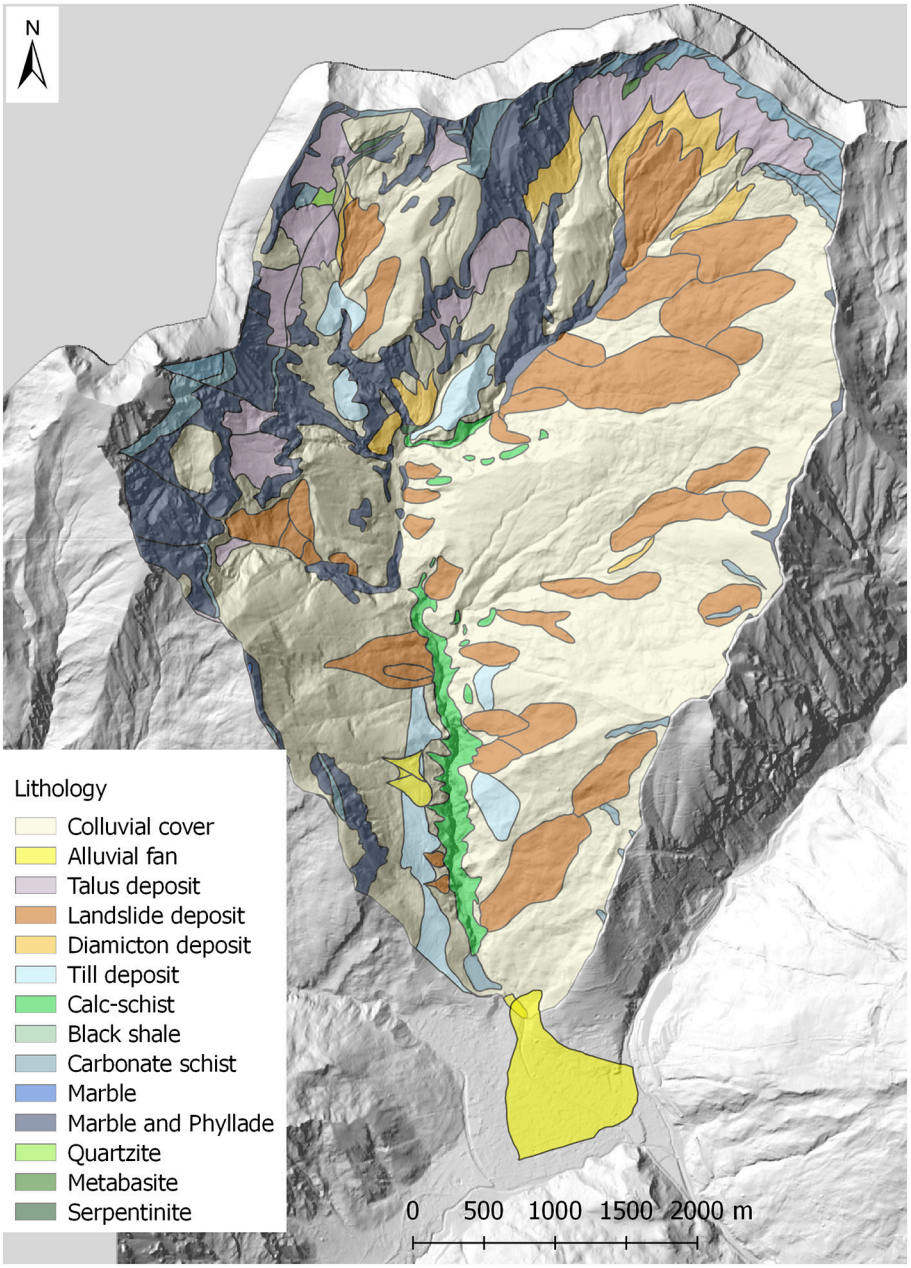

FIGURE 2 | The geological sketch map of Rio Frejus catchment.

(Equation 1):

$$IC = log\left(\frac{D_{up}}{D_{dn}}\right) \quad (1)$$

This index indicates the potential for downward routing of sediments produced upslope and the (weighted) flow path length to the nearest target or sink.

To model the impedance to runoff and sediment fluxes, a weighting factor is included in both components of IC. In mountain catchments, high-resolution DTMs can represent an important input for deriving surface roughness in order to include an objective measure of flow impedance in the connectivity assessment. We computed the roughness index as the standard deviation of residual topography according to Cavalli et al. (2008). The roughness index was used to calculate the weighting factor by using the following equation (Equation 2; Cavalli et al., 2013):

$$W = 1 - \left(\frac{RI}{RI_{max}}\right) \quad (2)$$

TABLE 1 | A synthesis of the Rio Frejus catchment characteristics (modified from Tiranti and Deangeli, 2015).

Catchment area (km^2)	22.32
Average catchment slope (°)	28.1
Average elevation (m asl)	2,169
Alluvial fan area (km^2)	0.63
Fan/catchment area ratio (%)	2.83
Outcrops area [Quaternary formations and rocks (km^2)]	11.91
Outcrops area [rocks (km^2)]	3.28
Outcrops area [Quaternary formations (km^2)]	8.63
Outcrop density [rocks (%)]	14.69
Outcrop density [Quaternary formations (%)]	38.67
Eluvial-colluvial cover area (km^2)	10.42
Eluvial-colluvial cover area (%)	46.68
Average rock condition	Sheared
Average shallow deposit type	Clast supported, poorly-cohesive
Main debris flow rheology	Viscoplastic
Main depositional style	Steep-asymmetrical levee and flat lobe

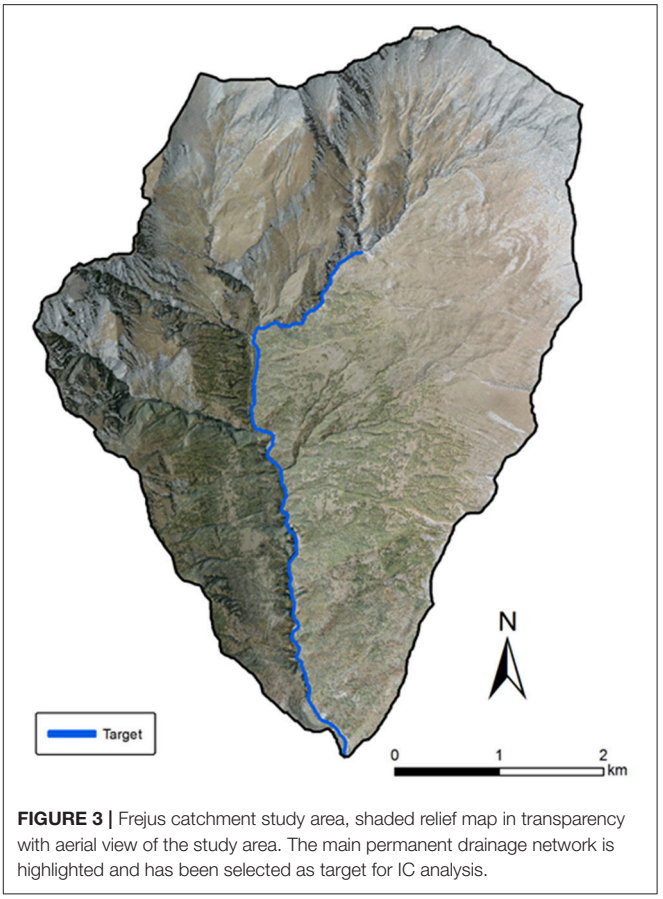

FIGURE 3 | Frejus catchment study area, shaded relief map in transparency with aerial view of the study area. The main permanent drainage network is highlighted and has been selected as target for IC analysis.

Where RI is the roughness index value and RI_{max} is the maximum value of RI in the study area.

As the DTM of the study area is at 5-m resolution, we considered as an optimal spatial scale a moving window of 3 × 3 pixel in order to derive a flow-impedance related roughness index and the related weighting factor.

The determination of the information necessary to identify sediment source areas were carried out with field surveys coupled with an analysis of the existent cartography (regional geologic and geomorphologic maps).

We carried out an assessment of sediment connectivity based on the computation of IC (Cavalli et al., 2013) in order to select the areas effectively coupled to the main channel system (i.e., areas accountable for sediment supply). The results of this analysis were interpreted and integrated with field observations to characterize connectivity patterns at the catchment scale with a focus on sediment source areas.

The main drainage system was extracted on an empirical basis from the DTM, adopting an area threshold approach (**Figure 3**) to extract a synthetic network corresponding to the presence of permanent drainage lines from field evidence. The main permanent drainage network was selected as a target for IC analysis.

We used the extent of the main channel system to determine the threshold area for the stream network extraction (i.e., 4.8 km^2). IC map, surface roughness and the weighting factor were computed using the freely available SedInConnect application (Crema et al., 2015; Crema and Cavalli, 2018).

Cellular Automata Model

Debris flow propagation and deposition patterns were simulated by a 3D numerical code based on Cellular Automata Method (Segre and Deangeli, 1995; Deangeli, 2008). In this code, the computational domain is discretized into elementary squared cells. Each cell is characterized by columns of rigid substratum and mobilizable debris material. The volume of debris material is characterized by rheological parameters, depending on the selected constitutive law. Two constitutive laws are implemented: a frictional/collisional law (Segre and Deangeli, 1995), based on the Bagnold dilatant fluid behavior (Takahashi, 1978, 1991), and a viscoplastic law (Deangeli et al., 2013; Tiranti and Deangeli, 2015), based on Bingham fluid behavior. The solid-liquid mixture is considered as a single-phase fluid.

The linear momentum conservation equation, the mass balance, and the constitutive law are combined and integrated to obtain flow velocity. The average velocity is used for flow rate calculation at each cell.

The evolution of the system occurs in discrete time-steps, based on the Courant criterion. At each time-step, an initiation rule dependent on flow rheology is verified in each cell. If the initiation rule is satisfied for a cell, a sediment flow rate, proportional to the time-step, is calculated and stored. When all the cells are checked, the system is simultaneously updated, at the end of the time-step. Deposition and remobilization of debris can occur at each time-step and when no cell can receive or supply a rate of solid-liquid mixture the simulation ends. This numerical tool was successfully applied to analyze flume experiments (Deangeli, 2008) and the evolutive behavior of actual flows, occurred in different

settings and contexts (Deangeli and Grasso, 1996; Deangeli and Giani, 1998; Deangeli et al., 2013, 2015; Tiranti and Deangeli, 2015).

The numerical analyses for the definition of depositional scenarios were carried out for each sub-catchment in the viscoplastic regime (Bingham fluid), as the basin was classified as an Excellent Clay Maker. The rheological parameters, i.e., the yield strength and the viscosity of the fluid, used in the numerical runs are based on a study of Tiranti and Deangeli (2015). In this study, the authors analyzed deposition styles and scenarios of different basins, and also the main Rio Frejus channel. They estimated the yield strength from the mean basal shear stress at the time of deposition, and the viscosity from the maximum debris flow velocity. Tiranti and Deangeli (2015) found that the yield strength was equal to $\tau_y = 1{,}400$ Pa and the viscosity was equal to $\mu = 80$ Pa*s, by assuming a solid concentration equal $c = 0.4$. An analysis of deposition style sensitivity to yield strength and viscosity, indicated that in the Rio Frejus the deposition pattern did not vary substantially in the range $\tau_y = 1{,}400$–$2{,}000$ Pa and $\mu = 80$–100 Pa*s. Based on this finding, in our numerical runs we used the following values of yield strength and the viscosity: $\tau_y = 1{,}400$ Pa, $\mu = 80$ Pa*s.

RESULTS AND DISCUSSION

This section reports the results of the integrated study presented step-by-step to underline the single contribute for each method and how them can give some more exhaustive results compared with those resulting from more classical approaches based only on debris flow routing model output calibrated on debris flow events of the past (e.g., Bertolo and Bottino, 2008; Pirulli and Marco, 2010) applied in similar geological and geomorphological contest.

CWI Classification of Catchment

Based on the dominant bedrock lithology characteristics reported in section "Study Area," Rio Frejus is classified as Excellent Clay Maker based on the Clay Weathering Index (CWI) classification (Tiranti et al., 2014; **Table 2**).

Due to the dominant lithology (phyllosilicates-rich schist), the catchment is characterized by a very high production of unconsolidated material which is rich in clay or clay-like

TABLE 3 | Observed processes from 26 historical events occurred between 1934 and 2015.

Sub-catchment	Date	Process type
?	August-3-1934	Mud/debris flow
?	June-12-1947	?
?	September-5-1948	?
Comba Merdovine	May-2-1949	Mud/debris flow
Comba Merdovine	May-27-1951	Mud/debris flow
?	June-21-1954	Mud/debris flow
?	August-21-1954	Mud/debris flow
?	June-8-1955	Mud flow
?	June-14-1957	?
?	October-19-1966	?
?	Nuvember-4-1968	Mud/debris flow
Comba Gautier	August-7-1997	Mud/debris flow
Comba Gautier	June-21-2002	Mud/debris flow
Comba Gautier	August-6-2004	Mud flow
Comba Gautier	July-25-2006	Mud flow
Combas Gautier, Merdovine, and Gaudet	August-?-2006	Mud flow
Comba Gautier	July-16-2013	Mud flow
?	July-17-2013	Mud flow
?	August-9-2015	Mud flow

TABLE 2 | Dominant lithologies of Rio Frejus.

Outcrop type	Structure*/Texture	Cohesion/Strength**	Main lithology group (CWI)	Area (km^2)	%
Glacial deposits	Clast supported	Cohesive	Schist (ECM)	0.28	2.37
Talus deposits	Openwork	Non-cohesive	Crystalline (BCM)	0.04	0.34
Talus deposits	Openwork	Non-cohesive	Schist (ECM)	1.96	16.49
Alluvial fans	Clast supported	Poorly-cohesive	Schist (ECM)	0.06	0.49
Diamicton	Clast supported	Poorly-cohesive	Schist (ECM)	0.09	0.72
Glacial deposits	Clast supported	Poorly-cohesive	Schist (ECM)	0.35	2.96
Landslide deposits	Clast supported	Poorly-cohesive	Schist (ECM)	0.43	3.68
Landslide deposits	Clast supported	Poorly-cohesive	Schist (ECM)	5.41	45.42
Serpentinites	Blocky	Extremely strong	Crystalline (BCM)	0.03	0.22
Marble and phyllades	Blocky/Disturbed/Seamy	Medium strong	Schist (ECM)	2.37	19.87
Carbonate schists	Blocky/Disturbed/Seamy	Medium strong	Schist (ECM)	0.17	1.42
Laminated limestones and black shales	Blocky/Disturbed/Seamy	Medium strong	Schist (ECM)	0.24	2.05
Black shales	Laminated/Sheared	Medium strong	Schist (ECM)	0.36	2.97
Calc-schists	Very blocky	Strong	Schist (ECM)	0.12	0.97
Quartzites	Very blocky	Very strong	Crystalline (BCM)	0.004	0.03

Bedrock and deposits are classified according to CWI classification based on characteristics of lithofacies forming deposits sediment and the bedrock rocks.
**Sensu* *Marinos and Hoek (2001),* ***Sensu* *Hoek and Brown (1997).*

minerals. This material favors the occurrence of cohesive debris flows showing a viscoplastic rheology, as resulting from the analysis of historical reports on torrential processes occurred in the Rio Frejus catchment (**Table 3**).

FIGURE 4 | An example of main type of torrential process that most frequently reaches the Rio Frejus's alluvial fan area (6th August 2004).

Debris flows occurred along the Rio Frejus show high viscosity and on average 45% of material is commonly deposited along the channels while only 55% of sediment reaches the alluvial fan as mud flow or mud/debris flow (Tiranti and Deangeli, 2015) as shown in **Figure 4**.

For this reason, the Rio Frejus alluvial fan shows a rather small area ("starved alluvial fan" sensu Tiranti and Deangeli, 2015) compared to the feeding catchment (see **Figure 2** and **Table 1**), according to CWI classification.

Index of Connectivity and Sediment Source Areas

We identified extensive sediment source areas primarily as landslide deposits (**Figure 5**), typically incised by several gullies (**Figure 6a**), covering 58% of the catchment, with 35% of active phenomena. The most frequent debris flow initiation points occur at the landslide deposits intersected by channel network. In these zones the sediments are chaotic and heterometric, characterized by a prevalent gravel and clayey silt-forming matrix. These deposits represent the main sediment source for erodible clayey sediments.

Moreover, the colluvial cover (<2 m) on steep slope is affected by shallow landslides and widespread rill erosion. Another important sediment source is represented by the abundant

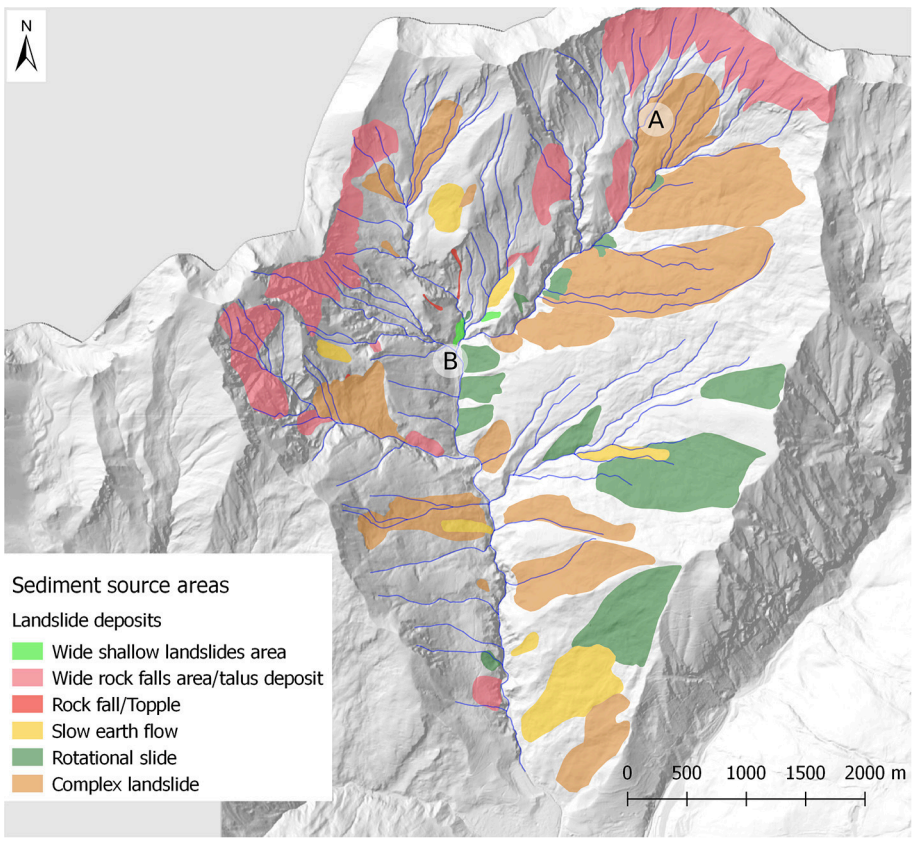

FIGURE 5 | Distribution of sediment source areas within the Rio Frejus catchment. A and B represent the location of example deposits shown in **Figure 7**.

presence of past debris-flow deposits along the main incised channel (**Figure 6b**).

IC map (**Figure 7A**), resulting from the analysis reported in section "Methods," was subdivided into 4 classes (i.e., Low, Medium-Low, Medium-High, High), using the Natural Breaks (Jenks, 1967) classification algorithm (**Figure 7A**) as proposed by Crema and Cavalli (2018) and Tiranti et al. (2016a).

Figure 7B shows the results of IC analysis based on two classes (high/low) This analysis was carried out to highlight potentially coupled and decoupled areas. **Figure 7** clearly shows that three sub-catchments seem characterized by a general decoupled behavior. Two of these sub-catchments, located in the upper and western portion of the study area, exhibit signs of geomorphic activity and active erosional processes, but also a structural decoupling barrier can be detected at the outlet of these sub-catchments. This physical barrier could account for the upstream low IC values playing an important role in the catchment morphological evolution. Unlike these two cases, the decoupled subcatchments in the eastern portion of the study area do not show important ongoing erosional processes. The disconnectivity here could be related to the presence of flatter areas and gentler slopes that affect primarily the flow paths in the downslope component of IC.

The comparison between coupled and decoupled results are shown in **Figure 8**. in which it is clear how the high connectivity

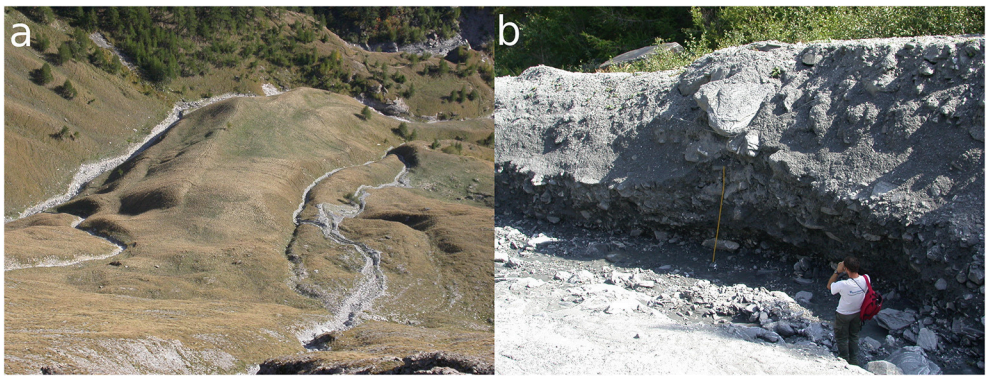

FIGURE 6 | Example of deposits located at the head of Rio Frejus catchment: **(a)** A slow earth flow landslide deposit incised by gullies. **(b)** A thick debris flow deposit near a main incised channel located at the catchment head.

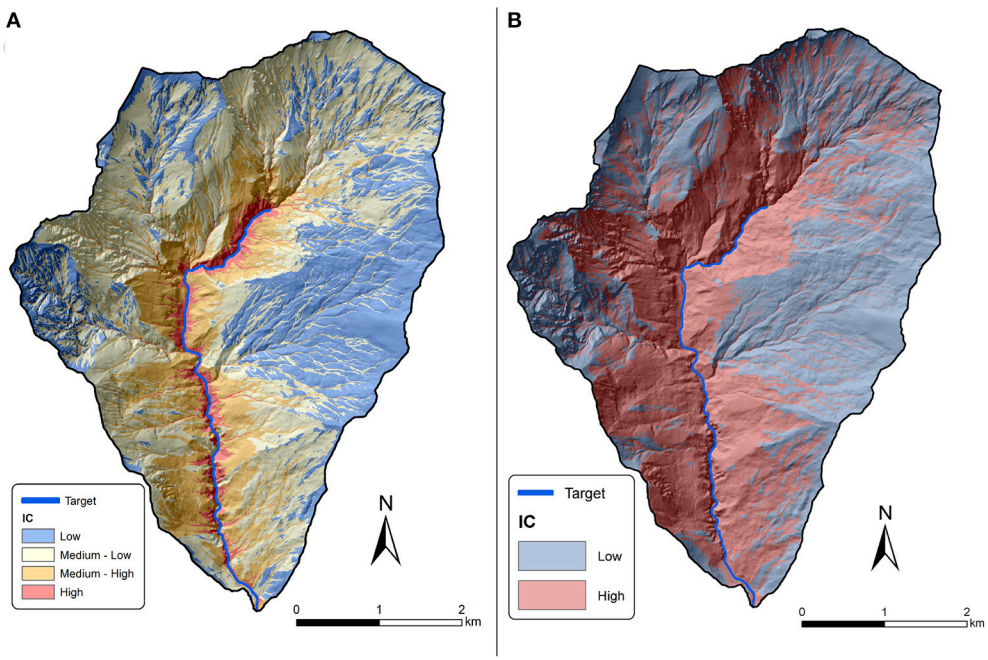

FIGURE 7 | (A) Results of IC analysis with the main river as a target. Results are divided in four classes according to Natural Breaks algorithm. **(B)** Results of IC analysis grouping the values in two classes.

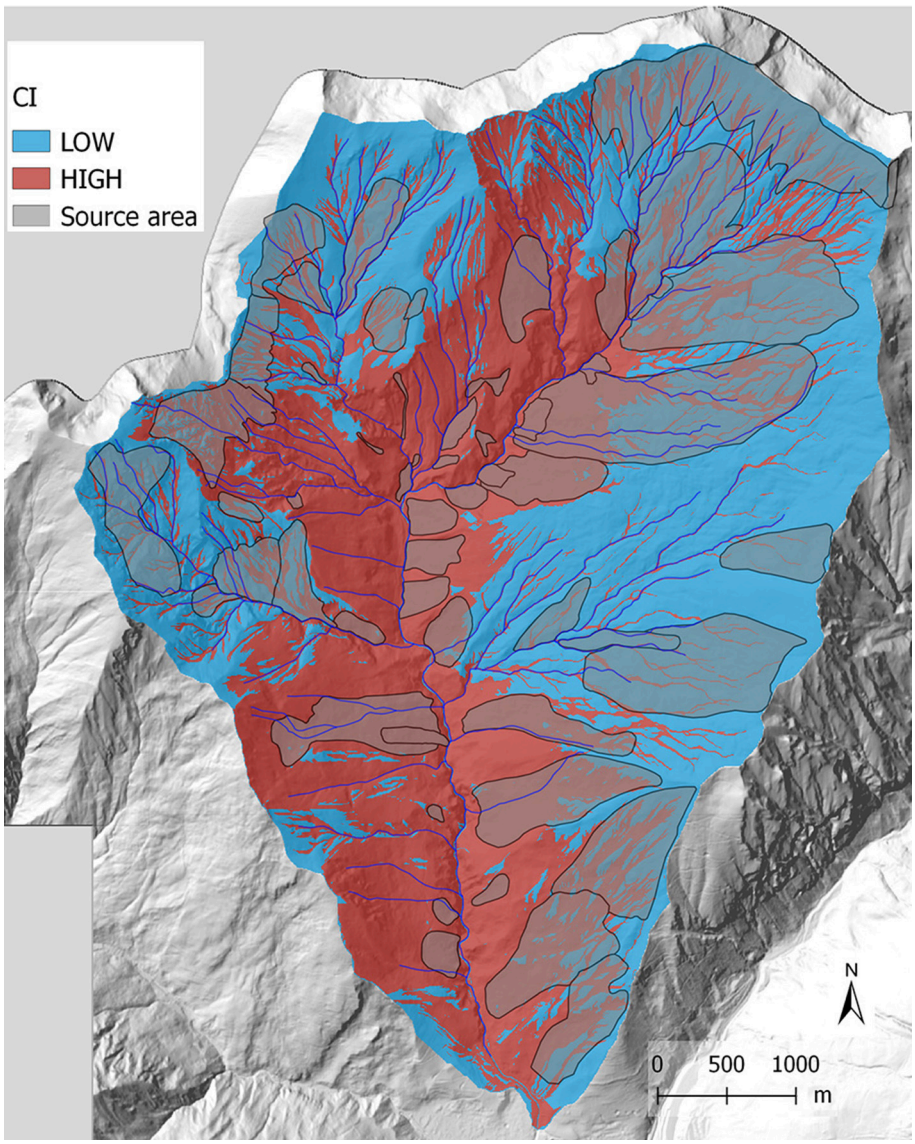

FIGURE 8 | Intersection between sediment source areas and IC map.

distribution is mainly close to the gullies related to large sediment source areas.

The most likely amount of sediment that actually can contribute to a debris flow of usual magnitude by selecting the source areas on the basis of the IC distribution and the intersection with the channel network within 50 m buffering from channels axes is showed in **Figure 9**, according to Bosco et al. (2007).

Based on field observations, we estimated the average depth of detachment surfaces for each deposit in order to determine the mobilizable volume from slope sediment source areas.

We compared the resulting volumes with standard volumes of the same deposit types available in the literature (Hungr et al., 1984; Dadson et al., 2004; Marchi and D'Agostino, 2004; Guzzetti et al., 2009; Tiranti et al., 2016a). The identified portion of sediment source areas represents the effective total sediment volume potentially mobilizable by debris flows that can reach the channel network. In order to find the total sediment volume, we considered the average thickness for each type mobilizable deposit (1.5 m for rockfall accumulation areas, 1 m for areas subject to wide shallow landslides, 2.5–3 m for slow earth flows, 3–5 m for marginal/surficial portions of complex landslides, 2–7 m for rotational landslides) according to the method proposed by Tiranti et al. (2016a). We calculated a likely maximum sediment volume equal to 3,342,286 m^3.

Routing Model (Cellular Automata Model)

Based on the results of IC analyses and field observations, the source areas and the volumes of sediments were identified for each sub-catchment. These outcomes were used as

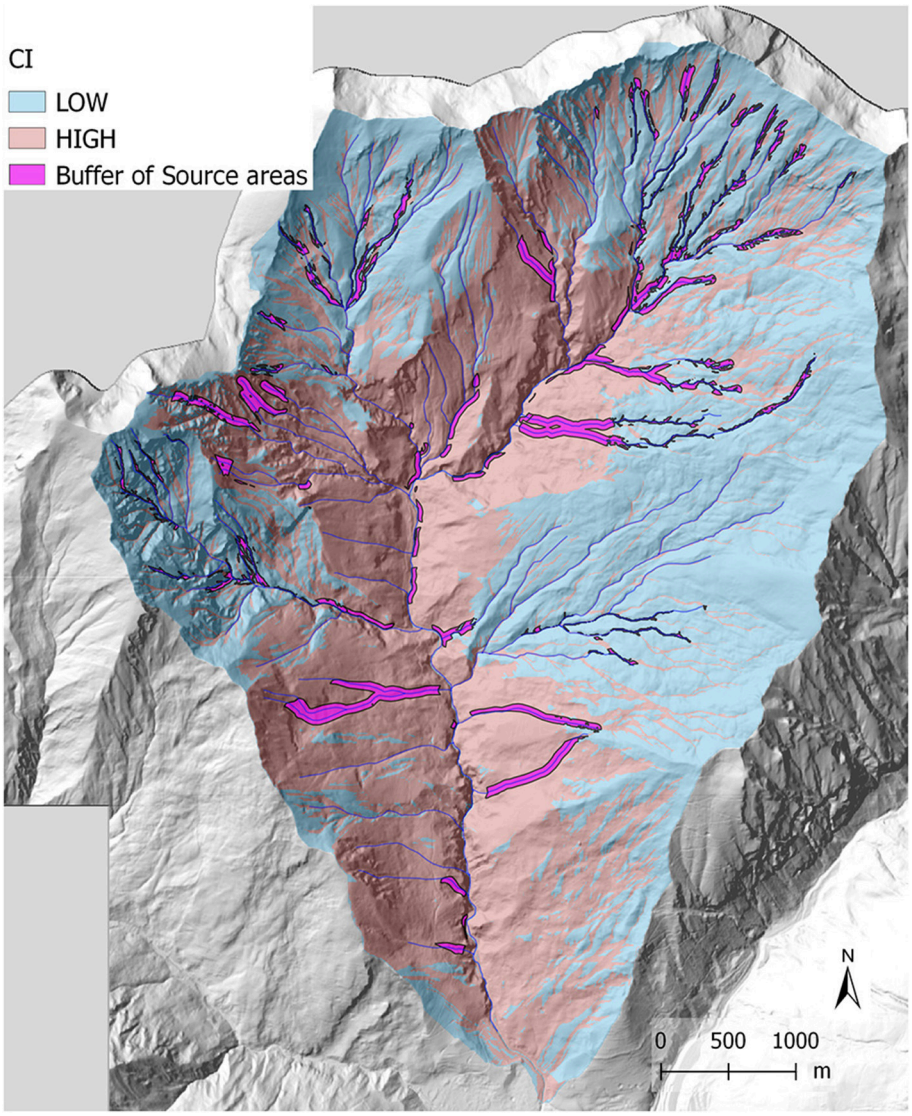

FIGURE 9 | Sediment source areas resulting from intersection between source deposits and a 50 m buffer of the channel network.

an input to simulate sub-catchment dynamics through deposition scenarios with the Cellular Automata Model. **Figure 10** shows the initial sediment input determined from the intersection of buffered source areas and IC map.

In the numerical simulations, we subdivided the whole catchment area into a West area and East area. Each area was further subdivided into sub-catchments, characterized by a potential mobilizable volume of sediments:

- West area. Comba Merdovine sx_1 and Comba Merdovine sx_2 with potential mobilizable volume of 258,784 m^3 and 323,856,32 m^3 respectively; Rio Chaulet and unnamed channels (sx_3) with a mobilizable volume of 554,578 m^3 (**Figure 11**).
- East area. Comba del Frejus (dx_1) with potential mobilizable volume of 678,918 m^3; Comba Gaudet and Gautier (dx_2) with potential mobilizable volume of 827,388 m^3; unnamed channels (dx_3) with potential mobilizable volume of 532,745 m^3 (**Figure 12**).

Figures 11, **12** show the results of the simulations in the West area and East area, respectively. All the sediment flows reach the target channel, in agreement with the IC spatial pattern. A part of the initial deposits of sediments remains in the original place or propagates for a small distance on channels belonging to the sub-catchments. This outcome is related to the local morphology of each sub-catchment and to the viscoplastic rheology of the mixture and agrees with *in situ* observations. Furthermore, the results also show a significant sediment deposition along the

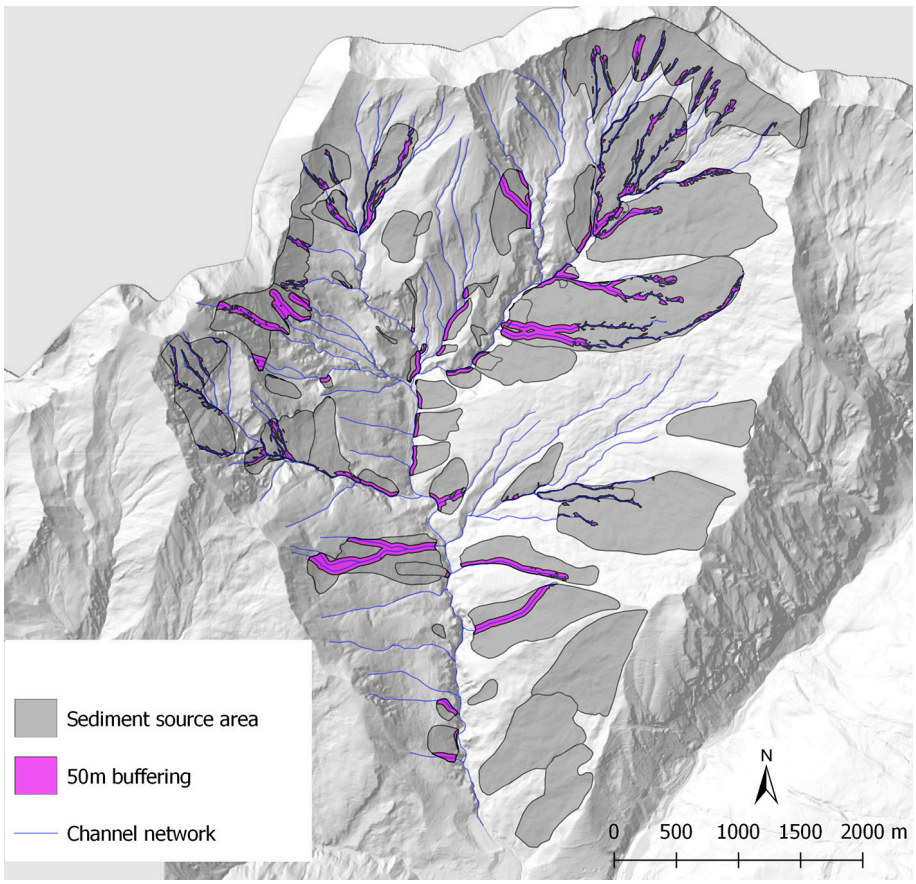

FIGURE 10 | Initial sediment input used in the numerical runs.

main channel, in agreement with *in situ* observation and CWI class of catchments. Only the debris flows occurring in sub catchments with the higher initial sediment volumes reach the valley bottom, with very low deposition thicknesses. This result agrees with the characteristics of the fan highlighted from *in situ* observations.

For this reason, we stress herein the fact that the evaluation of debris flow hazard needs to be considered in a dynamic way as an evolving process, with continuous updates.

CONCLUSIONS

The presented integration of different methodology to characterize debris flows initiation, propagation and deposition allows to define hazard scenarios without refer the simulations to past debris flow events. Thanks to the application of the Clay Weathering Index classification it is possible to infer "a priori" the potential typology of torrential processes that can occur and its evolution according to flow rheology and transported sediment characteristics. The characterization of sediment source areas by applying of a sediment connectivity index permitted to include into the analysis a potential for the sediment to be coupled to the main drainage system. Finally, the scenarios of debris flow propagation and deposition can be modeled using a 3D cellular automata model. Through this third step, it is possible to obtain numerous propagation and deposition scenarios considering only the sediment source areas that can actually feed a debris flow. Thanks to the proposed integrated approach, it is possible to gain accurate insights into the most likely impacts of a debris flow, characterizing its dynamics from the initiation areas to the alluvial fan. Moreover, the study demonstrates that the maximum expected magnitude of a debris flow can be forecasted excluding all the sediment source areas not connected to the main channel network, with interesting applications also in urban planning and hazard mitigation strategies.

The limits of this integrated method are mainly linked to the availability of territorial dataset (detailed geological and geomorphological maps, high resolution DTM, knowledge of nature and distribution of potential sediment source areas).

Moreover, this study represents the beginning of the experimentation of the integrated method, which must be applied to catchments characterized by different geomorphological geologic contexts before being considered sufficiently reliable to be used as a decision makers' support tool.

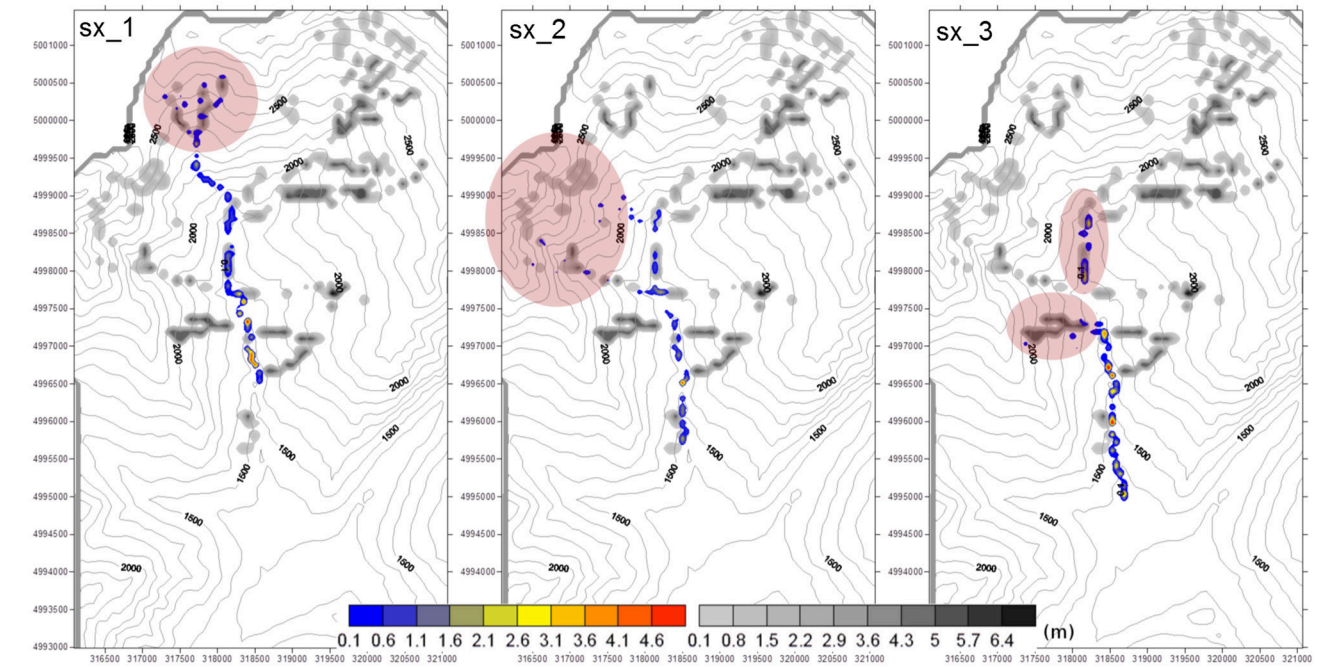

FIGURE 11 | Results of the numerical runs performed in the West area. Colored scale: simulated deposition patterns. Gray scale: initial deposits of sediments.

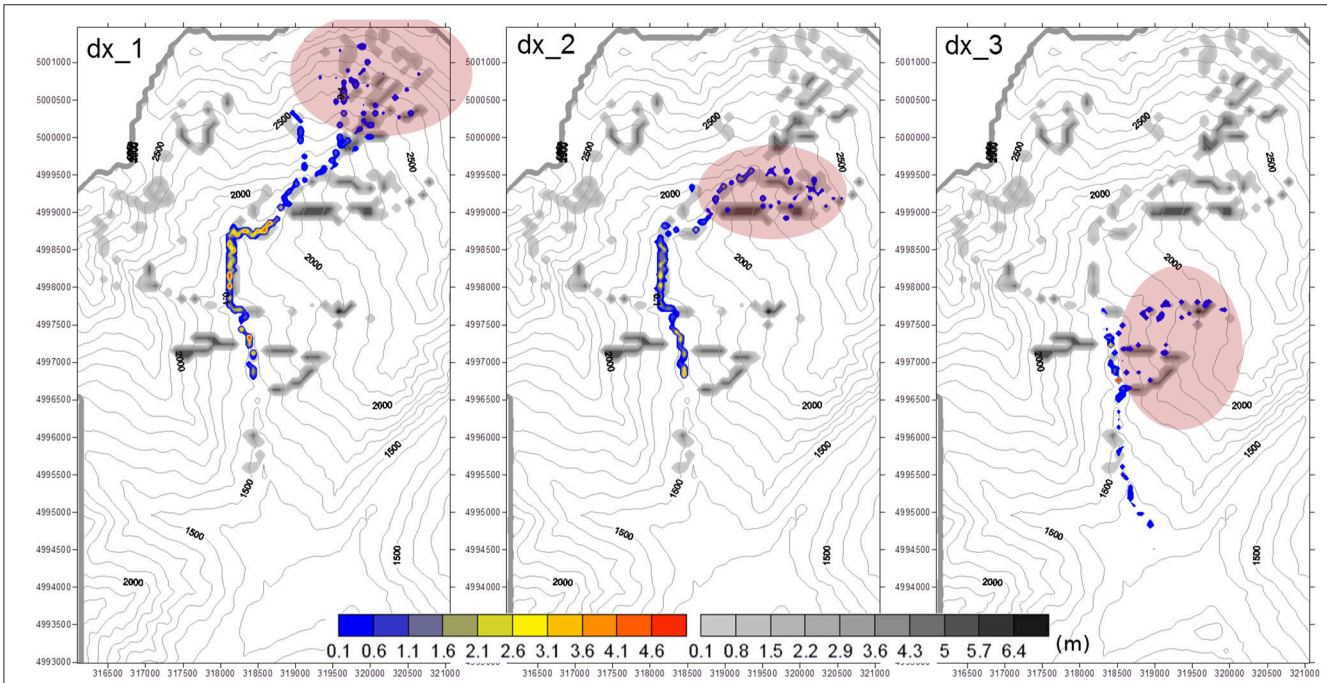

FIGURE 12 | Results of the numerical runs performed in the East area. Colored scale: simulated deposition patterns. Gray scale: initial deposits of sediments.

Another point of future development will consist in comparing the here proposed method with others already widely tested and available in the literature.

At this moment, the presented study represents an interesting line of research that will provide a new and useful tool for debris flow hazard assessment.

AUTHOR CONTRIBUTIONS

DT dealt with the characterization and classification of catchment, debris flow processes and sediment source areas. MC and SC determined the connectivity index to identify the sediment source areas available to generate debris flows. CD applied a Cellular Automata model to define the propagation and deposition scenarios of debris flows in the studied catchment.

REFERENCES

Ancey, C. (2007). Plasticity and geophysical flows: a review. *J. Nonnewton. Fluid Mech.* 142, 4–35. doi: 10.1016/j.jnnfm.2006.05.005

Berti, M., and Simoni, A. (2005). Experimental evidences and numerical modelling of debris flow initiated by channel runoff. *Landslides* 2, 171–182. doi: 10.1007/s10346-005-0062-4

Bertolo, P., and Bottino, G. (2008). Debris-flow event in the Frangerello Stream-Susa Valley (Italy)-calibration of numerical models for the back analysis of the 16 October, 2000 rainstorm. *Landslides* 5, 19–30. doi: 10.1007/s10346-007-0099-7

Beylich, A. A., and Sandberg, O. (2005). Geomorphic effects of the extreme rainfall event of 20–21 July, 2004 in the Latnjavagge catchment, northern Swedish Lapland. *Geogr. Ann.* 87A, 409–419. doi: 10.1111/j.0435-3676.2005.00267.x

Borselli, L., Cassi, P., and Torri, D. (2008). Prolegomena to sediment and flow connectivity in the landscape: a GIS and field numerical assessment. *CATENA* 75, 268–277. doi: 10.1016/j.catena.2008.07.006

Bosco, F., Gandini, D., Giudici, I., Marco, F., Paro, L., Tararbra, M., et al. (2007). "The mass movement of the Rio Frejus (Bardonecchia, NW Italian Alps) on August 6th, 2004," in *Evaluation and Prevention of Natural Risks*, eds S. Campus, S. Barbero, S. Bovo, and F. Forlati (London: Taylor and Francis Group, Balkema), 409–447.

Bovis, M. J., and Dagg, B. R. (1988). A model for debris accumulation and mobilization in steep mountain streams. *Hydrol. Sci.* 33, 589–604. doi: 10.1080/02626668809491292

Brardinoni, F., Church, M., Simoni, A., and Macconi, P. (2012). Lithologic and glacially conditioned controls on regional debris-flow sediment dynamics. *Geology* 40, 455–458. doi: 10.1130/G33106.1

Brunetti, M. T., Luino, F., Vennari, C., Peruccacci, S., Biddoccu, M., Valigi, D., et al. (2015). "Rainfall thresholds for possible occurrence of shallow landslides and debris flows in Italy," in *Dating Torrential Processes on Fans and Cones, Advances in Global Change Research*, eds M. Schneuwly-Bollschweiler, M. Stoffel, and F. Rudolf-Miklau (Springer Science), 327–339.

Cannon, H. S., Gartner, J. E., Wilson, R. C., Bowers, J. C., and Laber, J. L. (2008). Storm rainfall conditions for floods and debris flows from recently burned areas in Southwestern Colorado and Southern California. *Geomorphology* 96, 250–269. doi: 10.1016/j.geomorph.2007.03.019

Cavalli, M., Crema, S., Trevisani, S., and Marchi, L. (2017a). GIS tools for preliminary debris-flow assessment at regional scale. *J. Mt. Sci.* 14, 2498–2510. doi: 10.1007/s11629-017-4573-y

Cavalli, M., Goldin, B., Comiti, F., Brardinoni, F., and Marchi, L. (2017b). Assessment of erosion and deposition in steep mountain basins by differencing sequential digital terrain models. *Geomorphology* 291, 4–16. doi: 10.1016/j.geomorph.2016.04.009

Cavalli, M., Tarolli, P., Marchi, L., and Dalla Fontana, G. (2008). The effectiveness of airborne LiDAR data in the recognition of channel-bed morphology. *CATENA* 73, 249–260. doi: 10.1016/j.catena.2007.11.001

Cavalli, M., Trevisani, S., Comiti, F., and Marchi, L. (2013). Geomorphometric assessment of spatial sediment connectivity in small Alpine catchments. *Geomorphology* 188, 31–41. doi: 10.1016/j.geomorph.2012.05.007

Chang, T. C., and Chao, R. J. (2006). Application of back-propagation networks in debris flow prediction. *Eng. Geol.* 85, 270–280 doi: 10.1016/j.enggeo.2006.02.007

Costa, J. E. (1988). "Rheologic, geomorphic, and sedimentologic differentiation of water floods, hyperconcentrated flows, and debris flows," in *Flood Geomorphology,* eds V. R. Baker, R. C. Kochel, and R. C. Patton (New York, NY: John Wiley and Sons), 113–122.

Crema, S., and Cavalli, M., (2018). SedInConnect: a stand-alone, free and open source tool for the assessment of sediment connectivity. *Comput. Geosci.* 111, 39–45. doi: 10.1016/j.cageo.2017.10.009

Crema, S., Schenato, L., Goldin, B., Marchi, L., and Cavalli, M. (2015). Toward the development of a stand-alone application for the assessment of sediment connectivity. *Rendiconti Online Della Soc. Geol. Ital.* 34, 58–61. doi: 10.3301/ROL.2015.37

Dadson, S. J., Hovius, N., Chen, H., Dade, W. B., Lin, J. C., and Hsu, M. L. (2004). Earthquake-triggered increase in sediment delivery from an active mountain belt. *Geology* 32, 733–736. doi: 10.1130/G20639.1

Deangeli, C. (2008). Laboratory granular flows generated by slope failures. *Rock Mech. Rock Eng.* 41, 199–217. doi: 10.1007/s00603-007-0131-1

Deangeli, C., and Giani, G. P. (1998). "Physical and Numerical models to rehabilitate a waste disposal site," in *Proceedings of the 8th International Congress IAEG* (Vancouver, BC; Balkema; Rotterdam), 1813–1818.

Deangeli, C., and Grasso, P. (1996). "The evolutive mechanism of debris flows: analysis and protection works," in *Proceedings of 7th International Symposium on Landslides* (Trondheim; Balkema; Rotterdam), 1183–1188.

Deangeli, C., Paltrinieri, E., and Tiranti, D. (2013). Debris flow analysis: from lithological classification of the basin to deposition," in *Landslide Science and Practice*, *Vol. 3, Spatial Analysis and Modeling Chap. 2: Rapid Landslide Runout Analysis*, eds C. Margottini, P. Canuti, and K. Sassa (Springer), 301–307.

Deangeli, C., Tiranti, D., Marco, F., and Volpato, M. (2015). "Comparison of Debris flow depositional scenarios using different DTMs," in *Engineering Geology for Society and Territory*, *Vol. 2,* eds G. Lollino, D. Giordan, G. B. Crosta, J. Corominas, R. Azzam, J. Wasowski, and N. Sciarra (Springer International Publishing), 1667–1671.

Ellen, S. D., and Flaming, R. W. (1987). *Mobilization of Debris Flows From Soil Slips, San Francisco Bay Region. GSA Reviews in Engineering Geology.*

Fratianni, S., and Motta, L. (2002). *Andamento Climatico in Alta Val Susa Negli Anni 1990*-1999. Regione Piemonte; Studi Climatologici in Piemonte.

Glade, T. (2005). Linking debris-flow hazard assessment with geomorphology. *Geomorphology* 66. 189–213. doi: 10.1016/j.geomorph.2004.09.023

Gregoretti, C. (2000). Experimental evidence from the triggering of debris flow along a granular slope. *J. Phys. Chem. Earth B Hydrol. Oceans Atmosphere* 25, 387–390. doi: 10.1016/S1464-1909(00)00031-9

Gregoretti, C., Degetto, M., and Boreggio, M. (2016). GIS-based cell model for simulating debris flow runout on a fan. *J. Hydrol.* 534, 326–340. doi: 10.1016/j.jhydrol.2015.12.054

Guzzetti, F., Ardizzone, F., Cardinali, M., Rossi, M., and Valigi, D. (2009). Landslide volumes and landslide mobilization rates in Umbria, central Italy. *Earth Planetary Sci. Lett.* 279, 222–229. doi: 10.1016/j.epsl.2009.01.005

Harvey, A. M. (1994). "Influence of slope/stream coupling on process interactions on eroding gully slopes, Howgill Fells, Northwest England," in *Process Models and Theoretical Geomorphology*, ed M. J. Kirkby (Chichester: John Wiley and Sons), 247–270.

Hoek, E., and Brown, E. T. (1997). Practical estimates of rock mass strength. *Int. J. Rock Mech. Min. Sci.* 34, 1165–1186. doi: 10.1016/S1365-1609(97)80069-X

Hungr, O. (1995). A model for the run out analysis of rapid flow slides, debris flows and avalanches. *Can. Geotechnical J.* 32, 610–623. doi: 10.1139/t95-063

Hungr, O. (2002). "*Analytical Models for Slide Sand Flows*," in *Proceedings of the International Symposium on Landslide Risk Mitigation and Protection of Cultural and Natural Heritage,* ed K. Sassa (Kyoto: KyotoUniversity), 559–586.

Hungr, O., McDougall, S., Wise, M., and Cullen, M. (2008). Magnitude–frequency relationships of debris flows and debris avalanches in relation to slope relief. *Geomorphology* 96, 355–365. doi: 10.1016/j.geomorph.2007.03.020

Hungr, O., Morgan, G. C., and Kellerhals, R. (1984). Quantitative analysis of debris torrent hazard for design of remedial measures. *Can. Geotech. J.* 21, 663–677 doi: 10.1139/t84-073

Hürlimann, M., Copons, R., and Altimir, J. (2006). Detailed debris flow hazard assessment in Andorra: a multidisciplinary approach. *Geomorphology* 78, 359–372. doi: 10.1016/j.geomorph.2006.02.003

Iverson, R. M. (2003). "The debris flow rheology myth," in *Third International Conference on Debris-Flow Hazard Mitigation: Mechanics, Prediction and Assessment*, eds Rickenmann and C. L. Chen (New York, NY: American Society of Civil Engineers), 303–314.

Jakob, M., Bovis, M., and Oden, M. (2005). The significance of channel recharge rates for estimating debris-flow magnitude and frequency. *Earth Surf. Process. Landf.* 30, 755–766. doi: 10.1002/esp.1188

Jenks, G. F. (1967). The data model concept in statistical mapping. *Int. Cartogr.* 7, 186–190.

Johnson, K. A., and Sitar, N. (1990). Hydrologic conditions leading to debris-flow initiation. *Can. Geotech. J.* 27, 789–801. doi: 10.1139/t90-092

Kean, J. W., McCoy, S. W., Tucker, G. E., Staley, D. M., and Coe, J. A. (2013), Runoff-generated debris flows: observations and modeling of surge initiation, magnitude, and frequency. *J. Geophys. Res. Earth Surf.* 118, 2190-2207. doi: 10.1002/jgrf.20148

Marchi, L., and D'Agostino, V. (2004). Estimation of debris-flow magnitude in the Estern Italian Alps. *Earth Surf. Process. Landforms* 29, 207–220. doi: 10.1002/esp.1027

Marinos, P., and Hoek, E. (2001). Estimating the geotechnical properties of heterogeneous rock masses such as flysch. *Bull. Eng. Geol. Environ.* 60, 85–92. doi: 10.1007/s100640000090

Marinos, V., Marinos, P., and Hoek, E. (2005). The geological strength index: applications and limitations. *Bull. Eng. Geol. Environ.* 64, 55–65. doi: 10.1007/s10064-004-0270-5

Marra, F., Nikolopoulos, E. I., Creutin, J. D., and Borga, M. (2015). Space–time organization of debris flows-triggering rainfall and its effect on the identification of the rainfall threshold relationship. *J. Hydrol.* 541, 246–255. doi: 10.1016/j.jhydrol.2015.10.010

Michaelides, K., and Chappell, A. (2009). Connectivity as a concept for characterising hydrological behaviour. *Hydrological Process.* 23, 517–522. doi: 10.1002/hyp.7214

Moscariello, A., Marchi, L., Maraga, F., and Mortara, G. (2002). Alluvial fans in the Alps: sedimentary facies and processes. *Spec. Publ. Int. Ass. Sediment* 32, 141–166.

Pierson, T. C., and Costa, J. E. (1987). A rheologic classification of subaerial sediment–water flows. *Geol. Soc. Am. Rev. Eng. Geol.* 7, 1–12. doi: 10.1130/REG7-p1

Pirulli, M., and Marco, F. (2010). Description and numerical modelling of the October 2000 Nora debris flow, Northwestern Italian Alps. *Can. Geotech. J.* 47, 135–146 doi: 10.1139/T09-082

Polino, R., Dela Pierre, F., Fioraso, G., Giardino, M., and Gattiglio, M. (2002). *Foglio 132-152-153 "Bardonecchia" Carta Geologica d'Italia, scala 1:50,000*. Servizio Geologico d'Italia.

Prancevic, J. P., Lamb, P. M., and Fuller, B. M. (2014). Incipient sediment motion across the river to debris-flow transition. *Geology* 42, 191–194, doi: 10.1130/G34927.1

Rickenmann, D. (1999). Empirical relationships for debris flows. *Nat. Hazards* 19, 47–77.

Rickenmann, D. (2015). "Debris-flow hazard assessment and methods applied in engineering practice," in *International Conference on Debris-Flow Hazards Mitigation: Mechanics, Prediction, and Assessment, Proceedings*, 23–24.

Rickenmann, D., Laigle, D., McArdell, B. W., and Hubl, J. (2006). Comparison of 2D debris-flow simulation models with field events. *Comput. Geosci.* 10, 241–264. doi: 10.1007/s10596-005-9021-3

Rickenmann, D., Weber, D., and Stepanov, B. (2003). "Erosion by debris flows in field and laboratory experiments," in *Debris-Flow Hazards Mitigation: Mechanics, Prediction, and Assessment,* eds D. Rickenmann and C. L. Chen (Rotterdam: Millpress), 883–894.

Sassa, K. (1985). "The mechanism of debris flow," in *Proceedings of XI International Conference on Soil Mechanics and Foundation Engineering* (San Francisco, CA), 1173–1176.

Segre, E., and Deangeli, C. (1995). Cellular automaton for realistic modelling of landslides. *Nonlinear Process. Geophys.* 2, 1–15. doi: 10.5194/npg-2-1-1995

Stoffel, M., Bollschweiler, M., and Beniston, M. (2011). Rainfall characteristics for periglacial debris flows in the Swiss Alps: past incidences–potential future evolutions. *Clim. Change* 105, 263–280. doi: 10.1007/s10584-011-0036-6

Stoffel, M., Tiranti, D., and Huggel, C. (2014). Climate change impacts on mass movements – case studies from the European Alps. *Sci. Total Environ.* 493, 1255–1266. doi: 10.1016/j.scitotenv.2014.02.102

Takahashi, T. (1978). Mechanical characteristics of debris flow. *J. Hydraulics Div.* 104, 1153–1169.

Takahashi, T. (1991). *Debris Flow. IAIIR Monograph*. Rotterdam: Balkema.

Tiranti, D., Bonetto, S., and Mandrone, G. (2008). Quantitative basin characterization to refine debris-flow triggering criteria and processes: an example from the Italian Western Alps. *Landslides* 5, 45–57. doi: 10.1007/s10346-007-0101-4.

Tiranti, D., Cavalli, M., Crema, S., Zerbato, M., Graziadei, M., Barbero, S., et al. (2016a). Semi-quantitative method for the assessment of debris supply from slopes to river in ungauged catchments. *Sci. Total Environ.* 554–555, 337–348. doi: 10.1016/j.scitotenv.2016.02.150

Tiranti, D., Cremonini, R., Asprea, I., and Marco, F. (2016b). Driving factors for torrential mass-movements occurrence in the Western Alps. *Front. Earth Sci.* 4:16. doi: 10.3389/feart.2016.00016

Tiranti, D., Cremonini, R., Marco, F., Gaeta, A. R., and Barbero, S. (2014). The DEFENSE (DEbris Flows triggEred by storms-Nowcasting SystEm): an early warning system for torrential processes by radar storm tracking using a Geographic Information System (GIS). *Comput. Geosci.* 70, 96–109. doi: 10.1016/j.cageo.2014.05.004

Tiranti, D., and Deangeli, C. (2015). Modeling of debris flow depositional patterns according to the catchments and source areas characteristics. *Front. Earth Sci.* 3:8. doi: 10.3389/feart.2015.00008

Tropeano, D., Luino, F., and Turconi, L. (2006). *Eventi di Piena e Frana in Italia Settentrionale nel Periodo 2002-2004*. CNR-IRPI/GNDCI.

Von Boetticher, A., Turowski, J. M., McArdell, B. W., Rickenmann, D., and Kirchner, J. W. (2016). DebrisInterMixing-2.3: a finite volume solver for three-dimensional debris-flow simulations with two calibration parameters-Part 1: model description. *Geosci. Model Dev.* 9, 2909–2923. doi: 10.5194/gmd-9-2909-2016

Michaelides, K., and Wainwright, J. (2002). Modelling the effects of hillslope–channel coupling on catchment hydrological response. *Earth Surf. Process. Landforms* 27, 1441–1457. doi: 10.1002/esp.440

Wieczorek, G. F., and Glade, T. (2005). "Climatic factors influencing occurrence of debris flow," in *Debris Flow Hazard and Related Phenomena,* eds Jacob and Hungr (Springer), 325–352.

Wilford, D. J., Sakals, M. E., Innes, J. L., Sidle, R. C., and Bergerud, W. A. (2004). Recognition of debris flow, debris flood and flood hazard through watershed morphometrics. *Landslides* 1, 61–66.

Conflict of Interest Statement: The authors declare that the research was conducted in the absence of any commercial or financial relationships that could be construed as a potential conflict of interest.

frontiers in Earth Science

ORIGINAL RESEARCH
published: 21 November 2018
doi: 10.3389/feart.2018.00210

Multi-Source Glacial Lake Outburst Flood Hazard Assessment and Mapping for Huaraz, Cordillera Blanca, Peru

Holger Frey[1], Christian Huggel[1], Rachel E. Chisolm[2†], Patrick Baer[1†], Brian McArdell[3], Alejo Cochachin[4] and César Portocarrero[5†]*

[1] Department of Geography, University of Zurich, Zurich, Switzerland, [2] Center for Research in Water Resources, University of Texas at Austin, Austin, TX, United States, [3] Mountain Hydrology and Mass Movements Research Unit, Swiss Federal Institute for Forest, Snow and Landscape Research (WSL), Birmensdorf, Switzerland, [4] Autoridad Nacional del Agua – Unidad de Glaciología y Recursos Hídricos (ANA-UGRH), Huaraz, Peru, [5] Área Glaciares, Instituto Nacional de Investigación en Glaciares y Ecosistemas de Montaña (INAIGEM), Huaraz, Peru

OPEN ACCESS

Edited by:
Davide Tiranti, Agenzia Regionale per la Protezione Ambientale (ARPA), Italy

Reviewed by:
Dhananjay Anant Sant, Maharaja Sayajirao University of Baroda, India
Fabio Matano, Consiglio Nazionale Delle Ricerche (CNR), Italy

***Correspondence:**
Holger Frey
holger.frey@geo.uzh.ch

†Present Address:
Patrick Baer, Geotest AG, Zollikofen, Switzerland
César Portocarrero, Independent Consultant, Huaraz, Peru
Rachel E. Chisolm, Austin Water, Austin, TX, United States

Specialty section:
This article was submitted to Geohazards and Georisks, a section of the journal Frontiers in Earth Science

Received: *17 July 2018*
Accepted: *31 October 2018*
Published: *21 November 2018*

Citation:
Frey H, Huggel C, Chisolm RE, Baer P, McArdell B, Cochachin A and Portocarrero C (2018) Multi-Source Glacial Lake Outburst Flood Hazard Assessment and Mapping for Huaraz, Cordillera Blanca, Peru. Front. Earth Sci. 6:210. doi: 10.3389/feart.2018.00210

The Quillcay catchment in the Cordillera Blanca, Peru, contains several glacial lakes, including Lakes Palcacocha (with a volume of 17 $\times$ 10^6 m^3), Tullparaju (12 $\times$ 10^6 m^3), and Cuchillacocha (2 $\times$ 10^6 m^3). In 1941 an outburst of Lake Palcacocha, in one of the deadliest historical glacial lake outburst floods (GLOF) worldwide, destroyed large parts of the city of Huaraz, located in the lowermost part of the catchment. Since this outburst, glaciers, and glacial lakes in Quillcay catchment have undergone drastic changes, including a volume increase of Lake Palcacocha between around 1990 and 2010 by a factor of 34. In parallel, the population of Huaraz grew exponentially to more than 120,000 inhabitants nowadays, making a comprehensive assessment and mapping of GLOF hazards for the Quillcay catchment and the city of Huaraz indispensable. Here we present a scenario-based multi-source GLOF hazard mapping, applying a chain of interacting numerical models to simulate involved cascading mass movement processes. Susceptibility assessments for rock-ice avalanches and breach formation at moraine dams were used to define scenarios of different magnitudes and related probabilities, which are then simulated by corresponding mass movement models. The evaluation revealed, that (1) the three investigated lakes pose a significant GLOF hazard to the Quillcay Catchment and the city of Huaraz, (2) in some scenarios the highest hazard originates from the lake with the smallest volume (Cuchillacocha), and (3) current moraine characteristics of Lake Palcacocha cannot be compared to the situation prior and during the 1941 outburst. Results of outburst floods obtained by the RAMMS model were then converted into intensity maps and corresponding hazard levels according to national and international standards, and eventually combined into the GLOF hazard map for the entire Quillcay catchment, including the urban area of Huaraz. Besides technical aspects of such a multi-source model-based hazard mapping, special attention is also paid to approval and dissemination aspects in a complex institutional context. Finally, some general conclusions are drawn and recommendations are given, that go beyond the presented case of the Quillcay Catchment.

Keywords: dissemination, GLOF, hazard assessment and mapping, process chains, numerical modeling, hazard and risk communication, institutional aspects, DRR

INTRODUCTION

Outburst floods of glacial lakes often involve cascades of interacting processes at, above, and below the lake (Richardson and Reynolds, 2000; Huggel et al., 2004b), posing particular challenges for the numerical modeling of such events (Worni et al., 2014; Mergili, 2016). Nevertheless, as glacier lake outburst floods (GLOFs) have the farthest potential reach among the various hazards in glacierized mountain regions, integrative hazard assessments of potentially critical glacier lakes are needed for efficient planning of effective disaster risk reduction measures.

Different components of the high mountain cryosphere have diverging response times to currently observed and projected future climatic changes. Glaciers are retreating worldwide and will largely disappear in mid and low latitudes during the coming decades (Huss and Hock, 2015; Zemp et al., 2015). At the same time new lakes are forming and growing behind moraine walls and in glacier bed depressions revealed by retreating glaciers (Gardelle et al., 2011; Linsbauer et al., 2015). On the other hand, permafrost degradation (Noetzli and Gruber, 2009; Haeberli et al., 2016) and de-buttressing of steep rock walls due to glacier retreat in the surrounding of such lakes are acting on century to millennia time scales (Fischer et al., 2010; McColl and Davies, 2013), leading to destabilized mountain flanks and increased availability of mobile loose material located above new and growing water bodies. In addition to the constantly changing environmental conditions, catastrophic events related to glaciers are often of a unique nature and not reoccurring, such as the failure of a dam, for instance. Therefore, the assessment of glacier related hazards cannot rely on historical records of past events. Potentially critical situations in high mountains, without historical precedence, thus, require scenario-based modeling approaches for the assessment of current and potential future hazards and risks (Schaub et al., 2013; Schneider et al., 2014; Allen et al., 2016). In GAPHAZ (2017), the Standing Group on Glacier and Permafrost Hazards (GAPHAZ) of the International Association of Cryospheric Sciences and International Permafrost Association (IACS/IPA) provides an overview of the related scientific state of the art together with recommendations for such quantitative hazard assessment and mapping.

The Cordillera Blanca in Peru is a global hot spot of high mountain hazards and risks. Extreme topography with peaks above 6,500 m a.s.l., extensive glaciation, a high number of glacier lakes, and the densely populated Santa Valley in close vicinity at its western foot result in a high-risk combination of vulnerable population and infrastructure directly exposed to high hazard potentials. Since 1941, this manifested in more than 30 glacier disasters in this mountain range, claiming more than 15,000 lives (Carey, 2005). Besides the catastrophic mass flows originating from Mount Huascaran in 1962 and 1970, with a death toll of about 7000 (Evans et al., 2009), the catastrophic outburst of lake Palcacocha, located above the regional capital of Huaraz, is to our knowledge the deadliest outburst event of a glacial lake in historic times. In December 1941 this GLOF destroyed about a third of the city of Huaraz and Independencia (hereafter only called Huaraz for convenience) and killed more than 1,800 people (Wegner, 2014). As a consequence of this disaster, a series of pioneer works in structural risk reduction measures at glacial lakes, such as lake volume control and dam reinforcements, have been implemented since the 1970s at more than 35 critical lakes in the Cordillera Blanca (Portocarrero, 2014; Emmer et al., 2016). In parallel, the high mountain environments of the Cordillera Blanca, including the Quillcay catchment above Huaraz with several glacial lakes, have undergone drastic changes. Since more than a decade, Lake Palcacocha along with two other glacial lakes in the Quillcay catchment pose again a significant threat to Huaraz and its population despite the implementation of remedial works, and requires new risk reduction measures.

In this paper we present a scenario-based elaboration of a GLOF hazard map for the entire Quillcay catchment, considering multiple hazard sources and using interacting numerical models in order to simulate involved chains of cascading processes. We illustrate how model results can be translated in a hazard map and also focus on institutional and practical aspects of disseminating this hazard map and related information to the potentially affected population, an important but challenging task in a context of low confidence and mistrust of the population toward governmental institutions and authorities (Carey, 2005, 2010; Carey et al., 2012).

STUDY SITE

In 2003, glacier coverage in the Cordillera Blanca was reported to be between 530 km^2 (ANA, 2014a) and 595 km^2 (Racoviteanu et al., 2008), depending on the source, and 830 glacial lakes are registered in the national glacial lake inventory (ANA, 2014b). At the same time, half a million people in the Santa Valley live straight below these glacierized mountains in smaller settlements and larger towns like Caraz, Yungay, Carhuaz, or the city of Huaraz, the regional capital, with more than 120,000 inhabitants (Carey, 2005).

The Quillcay catchment, a sub-catchment of the Santa River basin, is located on the western flank of the Cordillera Blanca. It drains toward the city of Huaraz, where the confluence with the main Santa River is located. From northwest to southeast it can be further subdivided into the Cojup Valley with lake Palcacocha in its headwater, the Auqui Valley with the lakes Cuchillacocha and Tullparaju, and the minor Shallap Valley (**Figure 1**).

Based on aerial photography interpretations and topographic analyses, the volume of Lake Palcacocha before its outburst in 1941 is estimated to have been around 9 to 11 $\times$ 10^6 m^3 (Vilímek et al., 2005). The trigger of the lake outburst event of 13 December 1941 is unclear; an impact of a larger ice or combined rock-ice avalanche is a likely explanation, considering the hanging glaciers in the steep faces of Mount Palcaraju (6,264 m a.s.l.) and Mount Pucaranra (6,156 m a.s.l.) straight above the lake (Vilímek et al., 2005; Emmer and Vilimek, 2014; Wegner, 2014). The overtopping water initiated retrogressive erosion at the moraine dam, leading to the formation of a breach and eventually draining Lake Palcacocha almost completely. After the outburst, a small lake with a volume of about 0.5 $\times$ 10^6 m^3 remained at the bottom of the valley, dammed by a younger, 8 m high moraine wall,

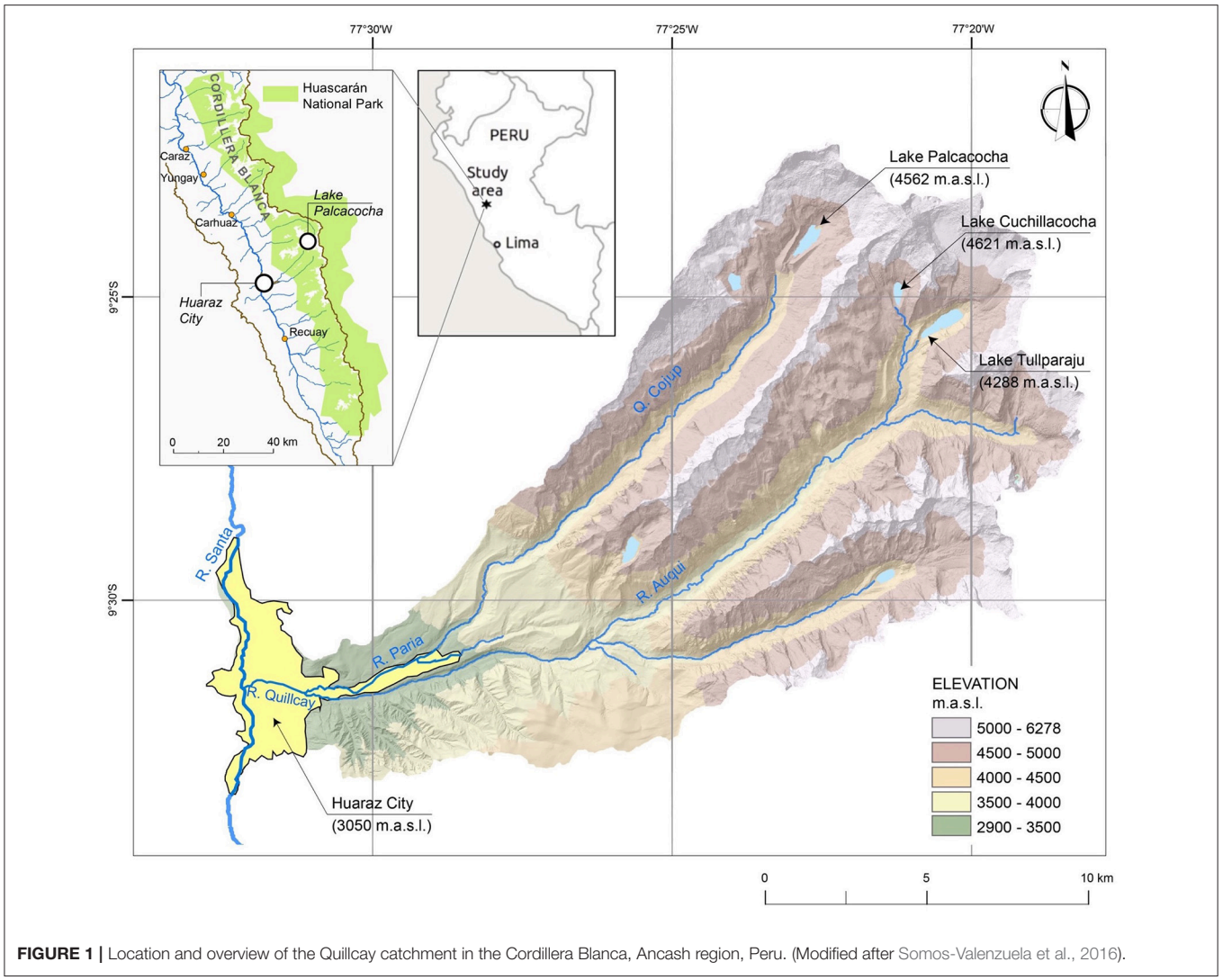

FIGURE 1 | Location and overview of the Quillcay catchment in the Cordillera Blanca, Ancash region, Peru. (Modified after Somos-Valenzuela et al., 2016).

with a lake level at about 47 m below pre-outburst conditions (Vilímek et al., 2005). In the 1970s the lake level was stabilized by installing a drainage pipe and the drainage channel was capped by an 8-m artificial dam. At the same time the secondary natural outflow at the right side of the moraine dam was reinforced in order to prevent erosion in case of overtopping displacement waves (Portocarrero, 2014). Since the 1990s, accelerated glacier retreat led to a strong increase of lake area and volume. In 2009 a bathymetric survey revealed a lake volume of more than 17×10^6 m^3 (ANA, 2014b), i.e., an increase by a factor of 34 within <20 years (**Figure 2**).

In parallel to this extreme increase in lake volume, the city of Huaraz has undergone an enormous growth since the GLOF disaster in 1941, despite the destructions of large parts of the city by the Ancash Earthquake in 1970. According to census data from the National Statistical Institute (INEI), the population of Huaraz grew from <20,000 inhabitants in 1941 to more than 127,000 inhabitants in 2015 (INEI, 2015). This strong growth of the population can be used as a rough proxy for the increase in damage potential in the form of population and urban infrastructure located in the city of Huaraz, in the trajectories of potential outburst floods of glacial lakes.

Besides Lake Palcacocha, four other glacial lakes are located in the Quillcay catchment: Cuchillacocha, Tullparaju, Churup, and Shallap (from north to south). Due to their considerable hazard potential for the city of Huaraz, besides Lake Palcacocha, structural hazard mitigation measures have been undertaken as well at Lakes Cuchillacocha (2×10^6 m^3) and Tullparaju (12×10^6 m^3) (ANA, 2014b, cf. **Figure 1**). These works include lake level lowering and stabilization by the construction of artificial drainage channels, capped by artificial dams reinforcing the natural moraine dams and ensuring a fixed freeboard (Portocarrero, 2014). All three lakes are considered for the hazard assessment and mapping presented here. Such a multi-source assessment of GLOF hazards considering different lakes of a catchment rather than a single lake, run though from a susceptibility assessment down to the final hazard mapping has to our knowledge so far not been done for any catchment

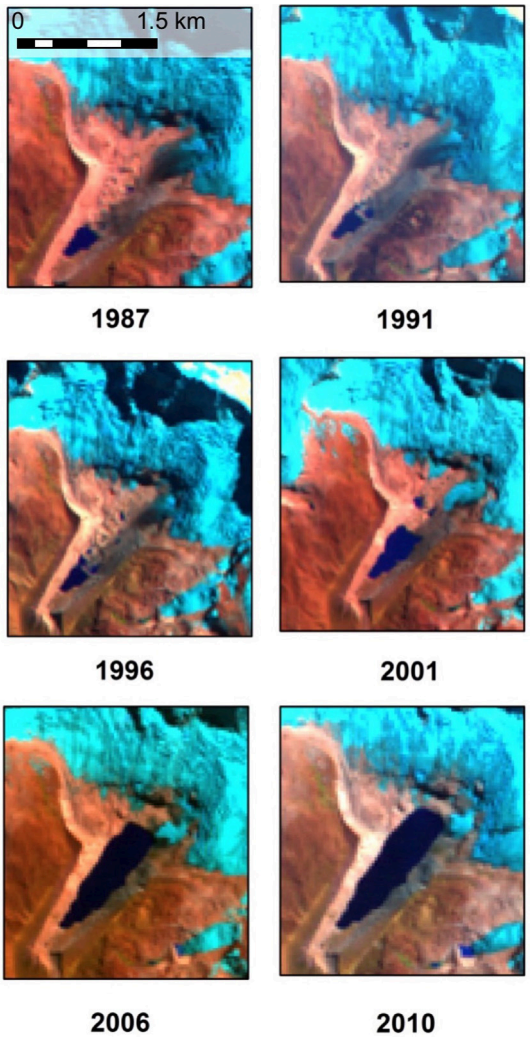

FIGURE 2 | Satellite imagery documenting the evolution of Lake Palcacocha from 1987 to 2010. Glacier ice is shown in cyan, rock and debris in orange, and water in dark blue. The lake volume increased from about 2×10^6 m^3 in 1987 to 17×10^6 m^3 in 2010. Images acquired by Landsat 5 (1987, 1991, 1996, and 2001) and Landsat 7 (2006 and 2010), all scenes from July or August.

worldwide. Schneider et al. (2014) presented a GLOF hazard map for the Chucchún catchment and the city of Carhuaz, located 30 km north of Huaraz. They applied a series of compatible numerical models to simulate the chain of involved processes. Somos-Valenzuela et al. (2016) applied a similar approach to Lake Palcacocha. Results of this study are also considered here as a reference and for model comparison.

METHODS

Hazard assessments in general rely on the determination of (i) the probability of occurrence of a potential event and (ii) intensities of involved processes at a given point in space (UNISDR, 2009). Generally, these two components of hazard are determined either by historical data or scientific analyses. Due to the characteristics of glacier related hazards as outlined above, (i) should rely on scenarios of potential events, rather than historical records of past events. Despite the outburst in 1941, this is also true for Lake Palcacocha, where current conditions cannot be compared to the setting prior to the 1941 event, as the pre-1941 dam was destroyed by the formation of the dam breach, and the lake after 1941 until today has been dammed by a younger moraine with a different geometry and geotechnical characteristics (Vilímek et al., 2005; Somos-Valenzuela et al., 2016). Numerical models for the simulation of the involved processes can be applied to evaluate and quantify (ii), spatially distributed intensities of potential events. Hence, a scenario-based hazard assessment approach using interacting numerical models, was applied here as described below for the hazard mapping of the three lakes Palcacocha, Tullparaju, and Cuchillacocha.

Scenario Definitions

Considering past events at Lake Palcacocha and other glacial lakes in the Cordillera Blanca and taking into account structural remedial safety measures at all three lakes, the only potential outburst triggers are major ice or combined rock-ice avalanches impacting a glacial lake. The definition of GLOF scenarios therefore included (1) the identification of potential detachment zones for ice or rock-ice avalanches, and (2) the determination of involved avalanche volumes for the three scenarios to be modeled. For this, a susceptibility assessment similar to the approach presented by Schaub et al. (2015) was performed, based on analyses of glacier topography, crevasse patterns, and traces of recent avalanches combined with rough estimates of ice thicknesses. In view of displacement waves causing overtopping at the dam, impact directions parallel to the longitudinal axes of the lakes, i.e., perpendicular to the dam orientations, constitute the most unfavorable constellation, as the main kinetic energy from the avalanche impact is directed straight to the dam.

Since a definition of return periods is virtually impossible due to the lacking information of the frequency-magnitude relation of such avalanches (Schneider et al., 2014; GAPHAZ, 2017), only qualitative probabilities of occurrence (high, medium, low) were assigned to the three different magnitudes of the scenarios (small, medium, large, respectively) (Raetzo et al., 2002). For the evaluation of avalanche volumes for the three scenarios, current glacier surface geometry, topography, and crevasse patterns were analyzed. Average ice-thicknesses of hanging glaciers were assumed to be 20 to 40 m, according to on-site observations of exposed ice cliffs and evidences from recent ice avalanches in the Cordillera Blanca (cf. Schaub et al., 2015). For the determination of total avalanche volumes, it has to be taken into consideration that considerable volumes of underlying bedrock material, potentially under (warm) permafrost conditions (cf. Carey et al., 2012; Schneider et al., 2014), might be incorporated in a combined rock-ice avalanche. Corresponding total volumes were also set in relation to other comparable events as reported from around the world (Schneider et al., 2011). Avalanche volumes of the medium scenarios eventually were set in between the volumes of the large and small scenario, according to the

topographic situation and geometry of the respective detachment zones.

The avalanches described above are the initial triggers of a chain of processes eventually leading to a GLOF. The only other process which needs to be evaluated separately in terms of a scenario, is the susceptibility of the involved moraine dams for breach formation. All other processes involved in the cascade of GLOF related mass movements are directly determined by the characteristics of these initial avalanches and therefore are not further considered in the definition of scenarios.

Numerical Modeling of Mass Movement Process Chains

Numerical modeling of cascading chains of mass movements is a relatively new field of research. There are models aiming at the integration of the different involved processes into single model frameworks (e.g., Mergili et al., 2017, 2018). Here, an approach to combine different models of the individual processes into a compatible model chain was chosen, using model results as input for subsequent modeling (Schneider et al., 2014; Westoby et al., 2014; Worni et al., 2014). For each scenario, the entire process chain of avalanche, displacement wave, and overtopping, down to the eventual outburst flood, was simulated (**Figure 3**, top).

Ice and rock-ice avalanches were modeled using the RAMMS model (Christen et al., 2010). This model is based on the 2-D shallow water equations, using a Voellmy approach incorporating a dry Coulomb friction μ and a turbulent friction ξ (Bartelt et al., 1999) and has been successfully applied to the simulation of large ice and rock-ice avalanches all around the world (Schneider et al., 2010, 2014; Worni et al., 2014), including the simulation of potential avalanches impacting Lake Palcacocha (Somos-Valenzuela et al., 2016).

Different hydrodynamic models are available for physically-based simulations of impact wave generation and propagation, and run-up height calculations at the dam. Such models include, for instance, IBER (IBER, 2010) or FLOW3D (Flow Science, 2012). Such models require 3D topographical information of the lake bathymetry, which was available for the three lakes investigated here from the Glaciology and Water Resources Unit of the Peruvian National Water Authority (Unidad de Glaciología y Recursos Hídricos, UGRH; Autoridad Nacional del Agua, ANA). However, besides bathymetry, these hydrodynamic models as well need a large number of parameters to be defined, typically not available for specific glacial lakes, implying considerable uncertainties, as discussed by Schneider et al. (2014) for the modeling of the displacement wave at Lake 513 with IBER. Somos-Valenzuela et al. (2016) applied FLOW3D to lake Palcacocha, replacing the impacting avalanche by a corresponding mass of water.

Empirically-based approaches for engineering purposes provide a valuable alternative to the above mentioned hydrodynamic models. Heller et al. (2009) provide a manual with a suite of equations allowing for the estimation a large variety of parameters of displacement waves in reservoirs generated by impacting landslide processes. Schneider et al. (2014) used Heller et al.'s 2009 approach for the calibration of the IBER model. Also Somos-Valenzuela et al. (2016) compared their FLOW3D results to Heller et al. (2009) estimates and concluded that FLOW3D is possibly overestimating wave height. In a more recent study Chisolm and McKinney (2018) further investigated the impact waves at Lake Palcacocha and came to a closer agreement of 3D modeling results and the empirical relations, but still with larger wave heights indicated by the numerical models. In this study, equations from Heller et al. (2009) were used to estimate wave heights, run-up heights at the dam, and overtopping volumes. Resulting hydrographs, which were later used as input for the GLOF modeling, were estimated based on overtopping volumes from the Heller et al. (2009) equations and typical durations of overtopping waves as simulated by the hydrodynamic models mentioned above. Furthermore, historical analyses of landslide and avalanche impacts on lakes revealed that in case of an impacting mass >10% of the lake volume, complete drainage of the lake is possible (Huggel et al., 2004a). This had to be considered in particular for Lake Cuchillacocha, with its relatively small volume compared to potential avalanches occurring form a hanging glacier straight above the lake.

Besides overtopping, such as typically observed for lakes with solid rock dams, it is important to evaluate the stability of moraine dams and to assess their susceptibility to the formation of a breach due to retrogressive erosion, which can increase the total flood volume dramatically compared to the volume of the overtopping wave, such as seen, for instance, during the 1941 outburst of lake Palcacocha. BASEMENT is a software able to simulate the erosional processes involved in the formation of a breach at a moraine dam (Worni et al., 2012; Vetsch et al., 2018). Somos-Valenzuela et al. (2016) applied BASEMENT to the dam of Lake Palcacocha; here we draw on the related findings from this study and adopt them to the other two lakes Tullparaju and Cuchillacocha.

For the final modeling of resulting lake outburst floods, again the RAMMS debris flow module was applied. RAMMS also in the past had been successfully applied to modeling of large debris flows (Hussin et al., 2012; Scheidl et al., 2013; Schraml et al., 2015) and GLOF modeling (Schneider et al., 2014; Frey et al., 2016). GLOFs typically undergo several flow type transformations along their trajectory, depending on slope, material, and water availability (Worni et al., 2012; Schneider et al., 2014; GAPHAZ, 2017). This was taken into account by using a RAMMS version allowing for the incorporation of erosional processes within predefined zones. These zones were defined based on field evidences of such flow type changes from the Palcacocha 1941 outburst and relating them to surface slope inclinations.

For both the avalanche and GLOF modeling, a LIDAR digital elevation model (DEM) from 2010 with 5 m spatial resolution, provided by the Peruvian Ministry of the Environment (Ministerio del Ambiente, MINAM) could be used.

Hazard Mapping Based on Numerical Model Results

For translating the GLOF modeling results into a hazard map (cf. lower panel of **Figure 3**), in a first step the spatially distributed

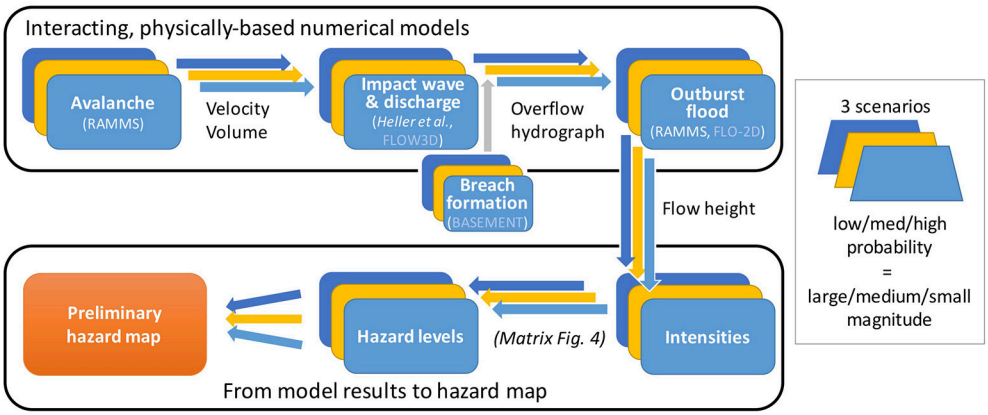

FIGURE 3 | Chain of involved interacting processes and numerical models applied to each of the three scenarios. Each set of boxes corresponds to a process and related numerical models (in brackets). Italic model names represent empirical approaches, models that were not directly applied in this study in transparent letters. Arrows indicate results from the previous models that are used as input for the subsequent model. Breach formation, i.e., the evaluation of dam stability, is only applied to moraine dammed glacial lakes. Cf. matrix in **Figure 4** for details of the translation of model results to hazard levels (bottom part of the chart).

		Probability			
		high small scenario	medium medium scenario	low large scenario	(very low) worst-case scenario
Intensity	high *[flow height ≥ 1m]*	very high	very high	very high	low
	medium *[flow height < 1m]*	high	high	medium	

FIGURE 4 | Matrix of hazard levels based on probability and intensity. Intensity levels are based on modeled flow heights; probability levels correspond to the different scenarios. The four hazard levels low, medium, high, and very high and related colors correspond to the Peruvian national standards.

GLOF flow heights for each of the three scenarios were translated to GLOF intensities. To do so, thresholds of modeled GLOF flow heights were set according to existing debris flow intensity definitions from Hürlimann et al. (2006) and Raetzo et al. (2002): High intensity corresponds to areas where maximum GLOF flow heights exceed 1 m, medium intensity corresponds to areas with maximum flow heights of <1 m. Low intensity does by definition not exist for debris flows. Then, in a second step, resulting GLOF intensities of each scenario were translated into hazard levels, according to the probability of occurrence (low, medium, high) of the respective scenario (cf. **Figure 4**).

The applied hazard classification matrix is based on three hazard levels, as used in different countries, including Switzerland (Raetzo et al., 2002). However, Peruvian national standards, determined by the National Center for Disaster Risk Estimation, Prevention, and Reduction (Centro Nacional de Estimación, Prevención y Reducción del Riesgo de Desastres, CENEPRED), consider four hazard levels (CENEPRED, 2015). In order to meet these national standards, the low hazard level was assigned to areas potentially affected by an extremely low probability, but possibly high impact event. With this modification of the hazard level matrix, a worst-case scenario could be included in the hazard assessment and mapping. This helped to reduce uncertainties induced by the scenario definitions significantly, as the formation of a dam-breach is still reflected in the resulting hazard map, although based on the moraine dam stability modeling it was excluded from the three main scenarios.

RESULTS

Scenarios

Detachment zones of the different avalanche scenarios are shown in **Figure 5**. For Palcacocha (P) and Cuchillacocha (C) one detachment zone was considered (Somos-Valenzuela et al., 2016 used the same detachment zone for their modeling study at Palcacocha). For Tullparaju two situations were taken into account, as a smaller avalanche from the eastern part of the glacier (T2 in **Figure 3**) might cause a similar wave at the dam as a larger avalanche from the western detachment zone (T1), due to the different impact angles of the avalanche trajectories compared to the longitudinal lake axis of the lake.

Avalanche volumes for the three scenarios for each of the four detachment zones are given in **Table 1**. Volumes for the small scenario were defined based on experiences from the 1991 and 2010 avalanches at Mount Hualcán (Carey et al., 2012; Schneider et al., 2014; Schaub et al., 2015). Volumes of the large scenarios correspond to worst-case estimates, reaching volumes of up to 3×10^6 m^3 for the detachment zones above Palcacocha (P in **Figure 5**), and Tullparaju (T1 in **Figure 5**) based on potentially unstable parts of steep hanging glacies with areas of about 500,000 m^2 and depths of 60 m (including ice and bedrock). For the medium scenario values in between the small and the large scenarios were chosen, based on the site specific topographic characteristics of involved hanging glaciers. For the Palcacocha avalanches, avalanche scenarios were defined in agreement with the scenarios used by Somos-Valenzuela et al. (2016).

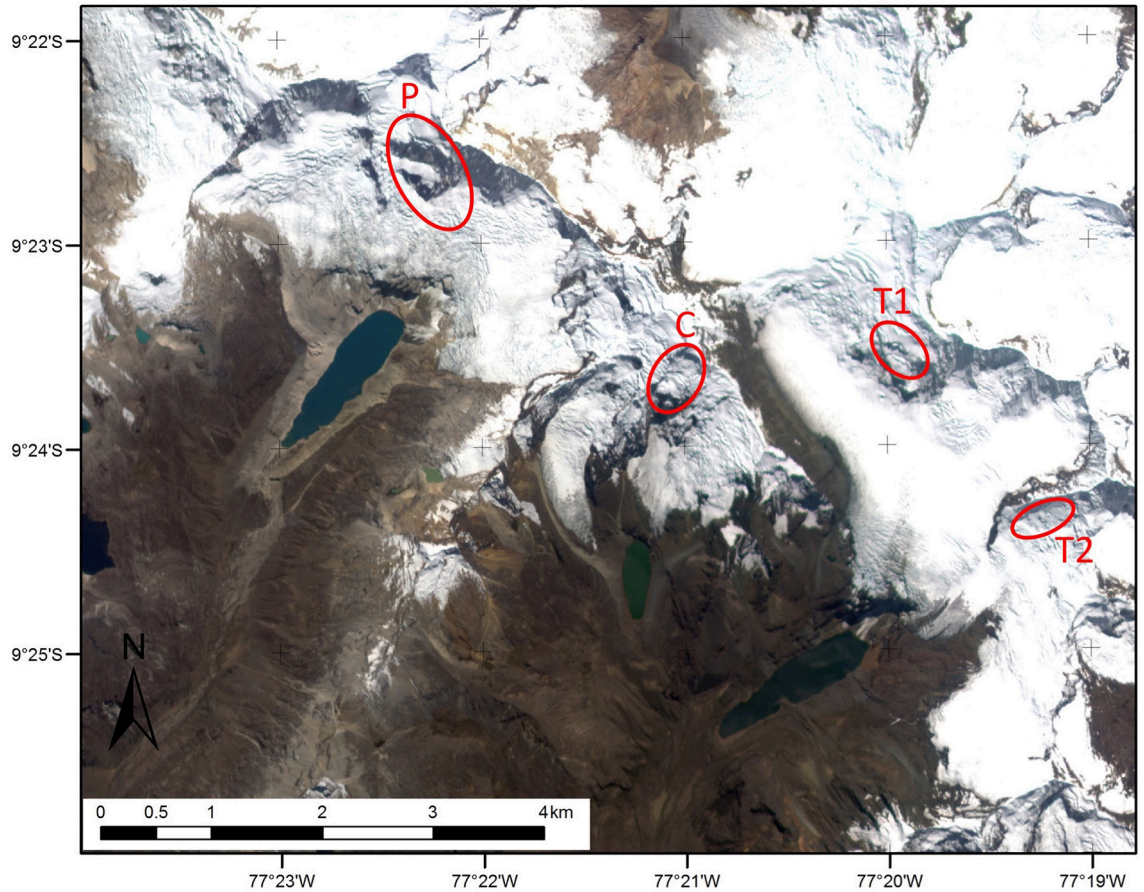

FIGURE 5 | Release areas of modeled ice or rock-ice avalanches. P, Palcacocha avalanche; C, Cuchillacocha avalanche; T1, Tullparaju west avalanche; T2, Tullparaju east avalanche. Background: RapidEye scene from 14 July 2012.

Numerical Modeling

Avalanche Simulations

Friction parameters for the RAMMS avalanche simulations were set to $\mu = 0.12$ (dry Coulomb) and $\xi = 1{,}000\ \mathrm{m\ s^{-1}}$ (turbulent), according to Schneider et al. (2014) and Somos-Valenzuela et al. (2016). At Cuchillacocha all three scenarios reach the lake, in the medium and large scenario the impacting avalanche volume is larger than 10% of the lake volume (impacting avalanche volume $>200{,}000\ \mathrm{m^3}$; lake volume $2 \times 10^6\ \mathrm{m^3}$), which is important for lake drainage considerations (cf. above and below). The small avalanche scenario from the Tullparaju west detachment zone (T1 in **Figure 5**) does not reach the lake but stops in the flat glacier part between the peak and the lake. All other avalanche scenarios from the two detachment zones at Tullparaju reach the lake. **Figure 6** shows maximum flow heights of the RAMMS modeling of the large avalanche scenarios at Tullparaju. It can also be seen, that besides impact volume, also impact direction plays a crucial role for the determination of potential overtopping at the dam. For Palcacocha results were identical to Somos-Valenzuela et al. (2016).

TABLE 1 | Volumes of rock-ice avalanche scenarios (in $10^6\ \mathrm{m^3}$).

	Small scenario	Medium scenario	Large scenario
Palcacocha (P)	0.5	1	3
Cuchillacocha (C)	0.2	0.75	1.3
Tullparaju west (T1)	0.3	0.75	3
Tullparaju east (T2)	0.1	0.3	0.75

Impact Wave

Based on results from the RAMMS avalanche modeling, impact wave properties were estimated based on Heller et al.'s 2009 equations. Mass and angles of the impacting avalanche were extracted from RAMMS results and the DEM, density was set to $1{,}000\ \mathrm{kg\ m^{-3}}$, such as applied as well by Schneider et al. (2014) and Somos-Valenzuela et al. (2016). Geometrical properties of the reservoir and the dam were extracted from the bathymetric data, the DEM and topographic surveys, all provided by ANA. Evaluated wave parameters included H_M, maximum wave height in the reservoir; R, run-up height at the dam (typically R is larger than H_M); and V, the overtopping volume per unit length at the dam crest (in case R is higher than the freeboard F). **Table 2** gives

an overview of the estimated impact wave characteristics of the different avalanche scenarios for the three lakes.

It is noteworthy that none of the Tullparaju west (T1) scenarios result in overtopping at the dam, despite the much larger avalanche volumes compared to the Tullparaju east (T2) avalanches. The reason for this is the impact direction of the avalanche trajectories which in the case of the T1 avalanches are almost perpendicular to the longitudinal axis of the lake, as indicated in **Figure 6**. This leads to very high run-up height at the proximal moraine opposite to the impact, but much lower wave and run-up heights in the direction of the dam. For Cuchillacocha, both the medium and large scenarios lead to significant overtopping. However, due to the relatively small lake volume compared to the impacting avalanche mass, according to Huggel et al. (2004a), even complete drainage of the lake has to be considered for these two scenarios. Thus, both for the medium and the large scenario, the overtopping volume corresponds to the lake volume (2×10^6 m^3, cf. **Table 2**). This is remarkable, as—at least for the medium scenario—the highest GLOF volume originates from the smallest lake, which is contradicting assessment schemes that consider lake area as a criterion for hazard level determination.

Moraine Dam Stability

A detailed analysis of the susceptibly for breach formation with BASEMENT by Somos-Valenzuela et al. (2016) revealed that breach form at the moraine dam of Lake Palcacocha is very unlikely. For the large scenario, the simulation indicates significant erosion at the distal face of the dam, nevertheless the back-propagating of the erosion is not enough to reach the lake and thus form a breach. This result is based on the assumption of unfavorable, worst-case setting of related soil parameters (i.e., most favorable for erosion) (Somos-Valenzuela et al., 2016). Dam conditions at Lake Tullparaju are much more stable than at Lake Palcacocha, due to the predominance of clayish material that has a much higher resistance against erosion (Portocarrero, 2014). Given this, in combination with the much higher freeboard of the Tullparaju dam, breach formation is considered to be even more unlikely at the Tullparaju moraine than at Lake Palcacocha, and thus was not further considered here. For Lake Cuchillacocha, as mentioned above, drainage of the complete lake by overtopping was considered for the medium and large scenario due to the high avalanche impact volume compared to the lake volume, making a more detailed stability assessment of the dam obsolete.

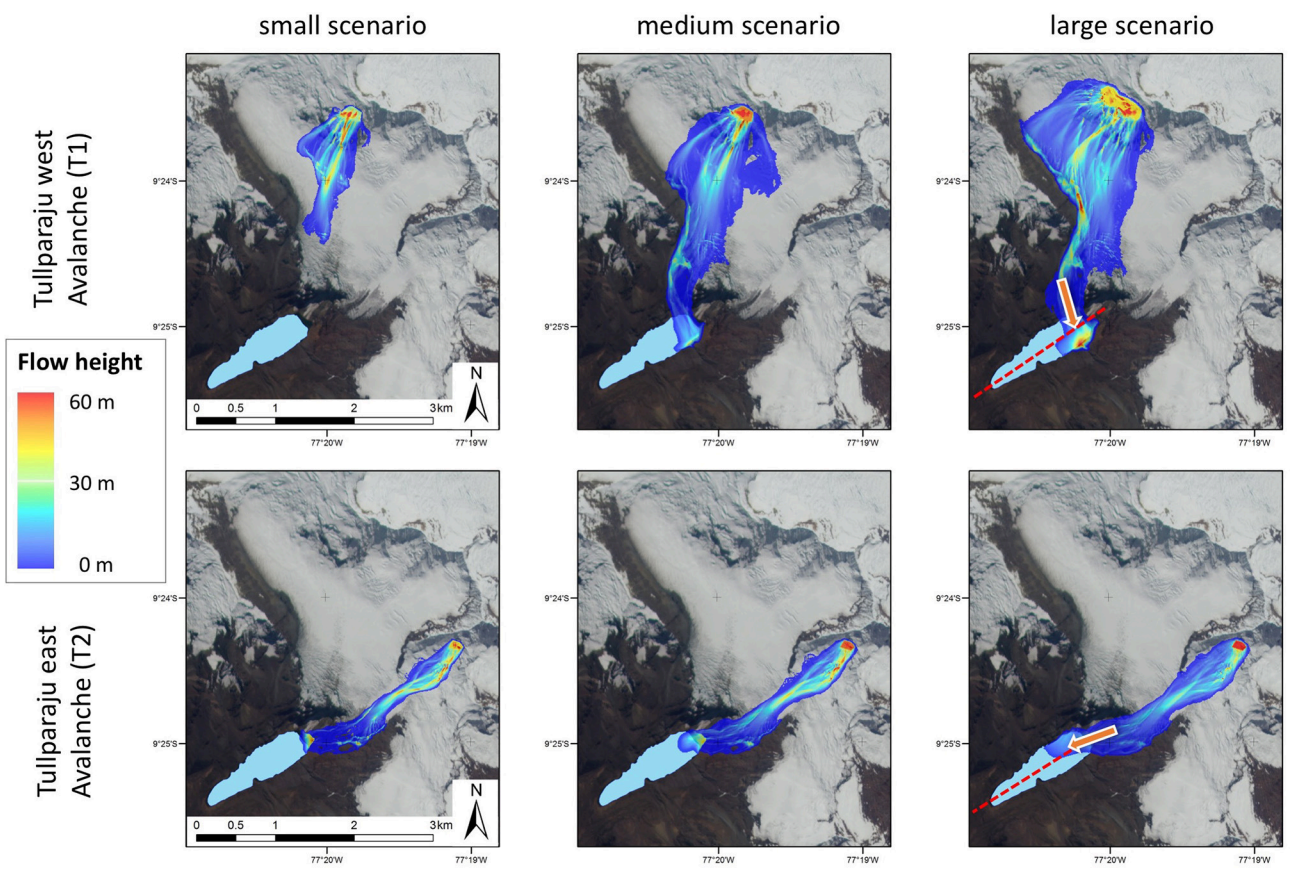

FIGURE 6 | RAMMS results of the three scenarios for avalanches from the two detachment zones above Lake Tullparaju (T1 and T2 in **Figure 5**). Note the angle between the impact direction (orange arrow) and the longitudinal axis of the lake (dashed red line) in the two panels for the large scenarios (right). Background: RapidEye scene from 14 July 2012.

TABLE 2 | Wave characteristics according to Heller et al. (2009) for the four avalanche sites, cf. **Figure 5**. Overtopping only occurs if wave run-up height R > Freeboard F. Lake characteristics according to ANA (2014b) and Portocarrero (2014).

Lake	Avalanche site (Figure 5)	Wave parameters	Small scenario	Medium scenario	Large scenario
Palcacocha	P	Wave height H_M [m]	8.8	21.1	42.2
Area = 514.100 m^2		Run-up height R [m]	15.1	20	29.7
Vol. = 17 × 10^6 m^3		Overtopping volume V [10^6 m^3]	0.15	0.5	1.8
Freeboard F = 8 m					
Cuchillacocha	C	Wave height H_M [m]	5	11.3	14.8
Area = 145.700 m^2		Run-up height R [m]	13.7	35.7*	48.8*
Vol. = 2 × 10^6 m^3		Overtopping volume V [10^6 m^3]	0 (R < F)	2*	2*
Freeboard F = 16 m					
Tullparaju	T1 (Tullparaju west)	Wave height H_M [m]	*Not*	2.5	4.5
Area = 463.700 m^2		Run-up height R [m]	*reaching*	5.1	10.1
Vol. = 12 × 10^6 m^3		Overtopping volume V [10^6 m^3]	*the lake*	0 (R < F)	0 (R < F)
Freeboard F = 18 m	T2 (Tullparaju east)	Wave height H_M [m]	3.1	6.1	13.4
		Run-up height R [m]	7.4	16.5	41.3
		Overtopping volume V [10^6 m^3]	0 (R < F)	0 (R < F)	1

**Entire lake volume considered for outburst as these scenarios at Lake Cuchillacocha include impacting avalanche volumes >10% of the total lake volume.*

To take uncertainties related to these evaluations into account and reflect them in the hazard map, an additional very low probability scenario has been considered, complementing the three scenarios defined and described above (section Scenarios). This scenario consists of the combination of the large avalanche scenario followed by the formation of a dam breach at Lake Palcacocha (cf. Somos-Valenzuela et al., 2016; **Figure 4** above and section Hazard map below).

Outburst Flood Modeling

GLOF volumes have been determined based on overtopping volumes as described in **Table 2**. Eventual GLOFs have been modeled using the RAMMS debris flow module allowing for taking erosional processes into account. In this RAMMS version, sections of the mass movement trajectory can be selected, where erosion is considered by the model, and others where this is not the case. Traces of the 1941 Palcacocha outburst still visible in the field provide evidence for flow type transformations related to changes of the erosional regime: Erosion took place mainly in the breach of the moraine, but the eroded material was mainly deposited within several hundred meters below the dam. Then, in the relatively flat Cojup Valley no erosional traces are visible, supposing a hyperconcentrated flow of mainly water with only fine-grained sediment. After having washed away Lake Jircacocha on its way (Vilímek et al., 2005), erosion took place again at the lower mouth of the Cojup Valley, about 10 km upstream of the city of Huaraz, where surface slopes increase again. Field visits and comparisons of flow type evidences from the 1941 outburst to surface slope inclinations revealed that erosion occurred mainly on river sections with slopes of more than 10%. An analysis of the longitudinal valley profiles shows the characteristic shape of a first short but steep section straight blow the lakes, followed by a long and flat valley, and then again an increase in surface slope in the section between the lower mouths of the Cojup and Auqui valleys and the city of Huaraz (**Figure 7**). Thus, erosion was considered for the modeling in regions with an overall slope of more than 10%, indicated by the gray rectangle in **Figure 7**, and frictional parameters were set accordingly to simulate a viscous debris flow ($\mu = 0.08$ and $\xi = 500\,m\,s^{-1}$) in these steeper regions, whereas for less inclined sections, i.e., the relatively flat valley floors below the lakes, erosion was neglected and friction parameters were set according to a hyperconcentrated flow with relatively high amounts of liquid water ($\mu = 0.04$ and $\xi = 500\,m\,s^{-1}$) (cf. Schneider et al., 2014). Resulting maximum flow heights for the large GLOF scenarios from Lakes Palcacocha and Tullparaju are shown in **Figure 8**.

Hazard Map

Maximum flow heights of the three lakes investigated were combined for each of the three scenarios. In cases of two or more overlapping outburst trajectories (e.g., below the dams of Lakes Cuchillacocha, and Tullparaju, and at the confluence of the Auqui and the Cojup Rivers), the highest value within each DEM pixel was considered for the combined maximum flow height maps of each scenario. These maximum flow height maps were then translated into intensity maps for each scenario, according to the threshold of 1 m flow height. Then, the intensity maps for each scenario were converted into hazard maps for each scenario, according to the probability of occurrence of the different scenarios (cf. **Figure 4**). Finally, these three hazard maps were combined into the preliminary, raw hazard map by selecting the highest hazard level within the tree scenarios for each DEM pixel, such as illustrated in **Figure 3**.

In Peru, hazard maps consist of four hazard levels, according to CENEPRED (2015). Here, GLOF modeling results of the three scenarios were translated into the three hazard levels medium, high, and very high (cf. **Figure 4**). In order to meet this national standard of four hazard levels and to take into consideration, an additional unlikely but not entirely impossible worst-case

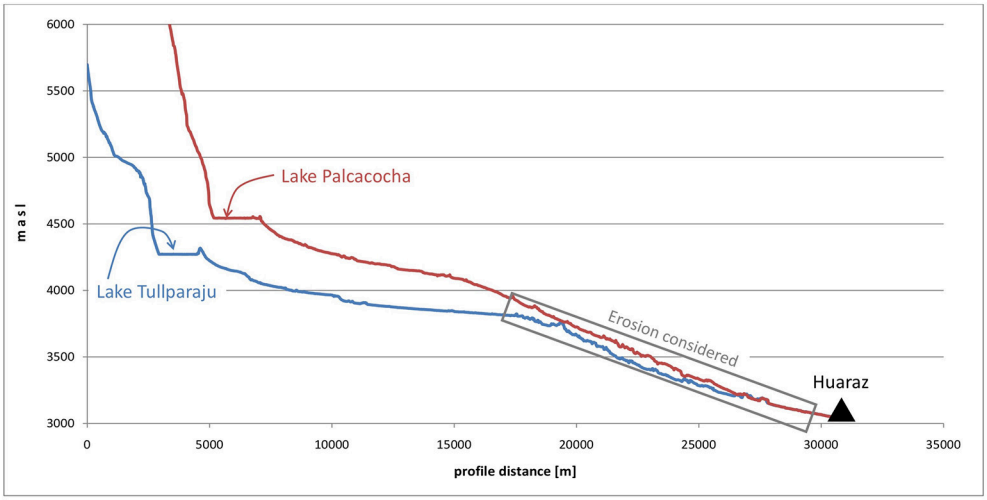

FIGURE 7 | Longitudinal profiles of the Cojup Valley (red) with Lake Palcacocha and the Auqui Valley (blue) with Lakes Tullparaju (and Lake Cuchillacocha, not on the profile line). Note the flat sections (Pampas) below the lakes in both valleys. In the steeper sections, directly about the city of Huaraz, indicated by the gray rectangle, erosion is considered in the GLOF modeling.

scenario of a breach formation at Lake Palcacocha (cf. section Moraine Dam Stability) was considered as well. In contrast to the three regular scenarios, maximum flow height results of this worst-case scenario were not translated into intensity maps, but a low hazard level was assigned to the entire area potentially affected in such a scenario. This on the one hand takes into account the extremely low probability of such a breach formation (cf. Somos-Valenzuela et al., 2016), but on the other hand eliminates uncertainties that would be induced when completely neglecting this worst-case scenario. In other hazard mapping standards, as for instance the Swiss system, such extreme events with very low probabilities of occurrence but high potential impacts are often translated into a so-called residual hazard.

For obtaining the final hazard map, the raw hazard map was generalized according to cartographic generalization rules, i.e., simplifying polygons of the same hazard level, eliminating isolated pixels and filling small holes and thus converting the speckled "raw" map in continuous and contiguous map (cf. **Figure 9**). This resulted in a model-based hazard map of multi-source GLOF hazards for the entire Quillcay catchment. An excerpt of the urban area of Huaraz of this map is shown in **Figure 9**, green areas (low hazard) correspond to areas only affected in case of a dam breach at Lake Palcacocha, see above and **Figure 4**.

INSTITUTIONAL ASPECTS AND DISSEMINATION

The assessment of multiple GLOF hazards and the development of a hazard map was part of a larger institutional process. In response to imminent GLOF hazards from lake Palcacocha an interinstitutional commission of responsible authorities and technical expert institutions was formed, consisting of representatives of the Municipalities of Huaraz, and Independencia with their Civil Defense departments, the regional Ancash government, technical government institutions including ANA and INAIGEM (Instituto Nacional de Investigación en Glaciares y Ecosistemas de Montaña), the National Park Huascarán, NGO's (CARE and the Mountain Institute), and international scientific experts from the University of Zurich and University of Texas. The lead was with the Mancomunidad Waraq, an administrative association between the two municipalities of Huaraz and Independencia that promotes climate change adaptation and risk management.

This commission mandated the technical local and international institutions to develop this GLOF hazard map for Huaraz for GLOF hazards in the Quillcay catchment. The approval process of hazard maps is in principle defined by CENEPRED but in practice still considerable doubts and missing clarity prevails. Specifically, it is not sufficiently clear whether a technical institution competent in the respective field can approve the hazard map or whether this role is taken in a centralized way by CENEPRED. In the first case questions are raised that a single institution cannot be both judge and judged at the same time, i.e., a technical institution would be mandated to develop the hazard map and would then validate and approve their own work.

In our case the hazard map was approved by the inter-institutional commission. One of the critical issues in this respect is the purpose of the hazard map. For Quillcay, the hazard map was found to be appropriate as a basis for evacuation plans and procedures, including early warning, but not for detailed urban land-use planning. This is due to the lack of consideration of high-resolution urban topography and in particular the effects of built structures (houses, roads, etc.) on GLOF flow dynamics. A follow-up process was foreseen to develop a high-resolution hazard map apt to urban planning.

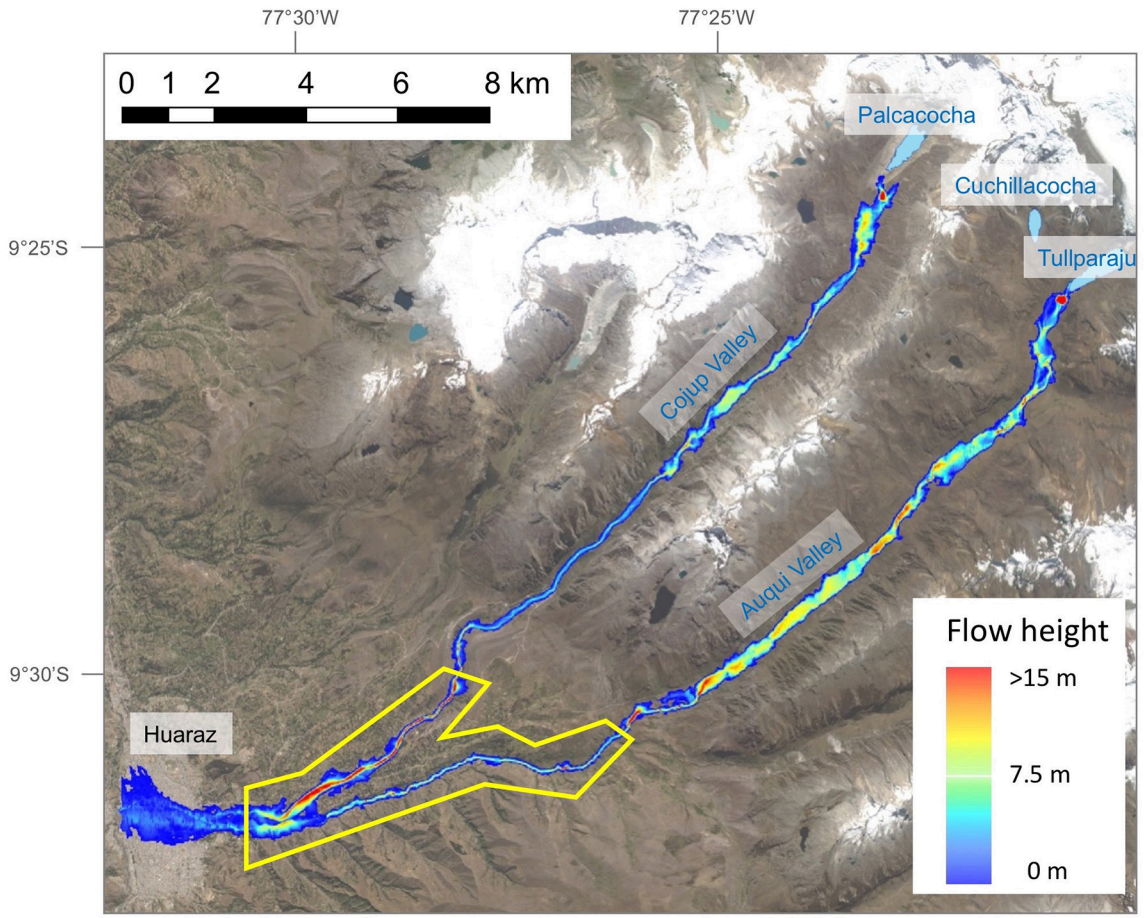

FIGURE 8 | Combined results (maximum flow height) of GLOF model runs with RAMMS for the large outburst scenarios of Lakes Palcacocha and Tullparaju. The yellow polygon indicates the zone of steeper slopes (cf. gray rectangle in **Figure 7**), where frictional parameters of a viscous debris flow were chosen and erosion was considered in simulations with RAMMS. For other areas, no erosion was considered and frictional parameters of a hyperconcentrated flow were chosen. Background: RapidEye scene from 14 July 2012.

Communication of hazards and risks to the population is a critical but fundamentally important task, in particular when considering the context of mistrust by the local population in authorities, governments, and technical experts (Carey, 2005). The dissemination of the hazard map to local population was implemented by the municipalities of Huaraz and Independencia and the NGO CARE. For this purpose, a leaflet was produced (**Figure 10**), containing a catchment-scale hazard map and a popular illustrative cartoon explaining the process and purpose of a hazard map, indicating what to do in case of emergency and a self-evaluation of how well prepared the own family is for GLOF emergencies. A second dissemination product was an evacuation map for which the hazard map formed the basis. The evacuation map indicated the main routes of evacuation in case of a GLOF for the hazardous parts of the city. A large campaign was run that covered about 4,000 households by face to face contacts and interactions with the urban population located in the potentially affected zones in Huaraz. The evacuation map was provided to and discussed with each household individually to make sure that the emergency preparations were at an appropriate level. This campaign also allowed the institutions to better understand the perceptions of GLOF hazards by the local population. Furthermore, the evacuation maps are also shown in public buildings, shops, restaurants, pharmacies, and travel agencies.

The hazard and evacuation map helped raising the awareness of authorities about the latent threat these lakes are posing to Huaraz, and eventually also formed an important basis for the design and implementation of an early warning system for GLOFs in the Quillcay catchment. The early warning system was foreseen as an immediate measure to protect people's lives from GLOFs but the institutional and administrative processes were complicated, and together with low institutional capacities combined with high instabilities, especially concerning the regional government, enormously delayed the implementation. The slow and multi-stage procedures for technical approval and financing of the early warning system resulted to be a major barrier to efficient and effective response to GLOF risks. The hazard and evacuation maps represent indispensable

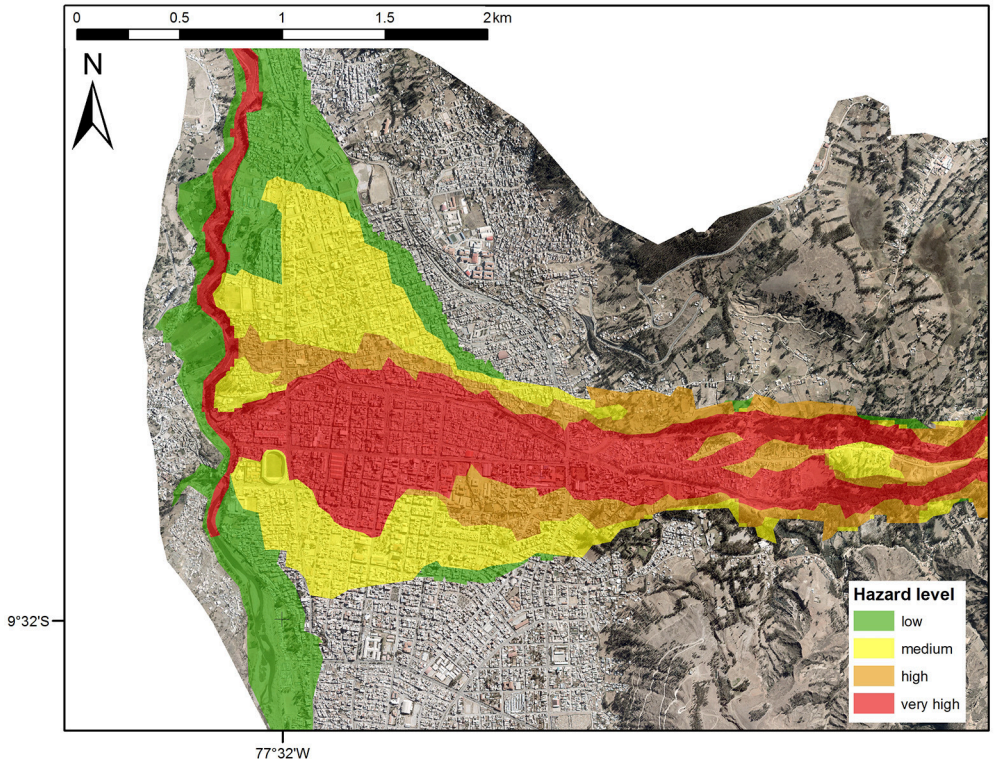

FIGURE 9 | Excerpt of the final hazard map for the urban area of Huaraz. Hazard levels and related colors according to the Peruvian national standards defined by CENEPRED.

FIGURE 10 | Information leaflet (in Spanish) distributed to households in the hazard zone of Huaraz. **Top**: front side with the hazard map of the entire catchment with some population information **(Left)** and characteristics of the evaluated glacial lakes **(Right)**. **Bottom**: reverse side with five points with cartoons and explanations and information on the map (1) What's a hazard map? (2)Why is it important? (3) How was it elaborated? (4) Which lakes have been considered? (5) Who elaborated the map? (6) What's the meaning of the different colors? (7) How much time is left in case of a GLOF alarm and eventually a questionnaire for a self-evaluation of the preparedness. (Courtesy of CARE Peru).

elements for several of the early warning system components, such as for understanding the risks, and for response. After about 4 years of technical studies and administrative procedures the early warning system process in mid-2018 reached the phase of public tender for the construction of the system.

DISCUSSION

The elaboration of a multi-source GLOF hazard map using a scenario-based modeling approach involves different kinds of uncertainties. Involved uncertainties are related to different sources, including (i) the numerical models, (ii) their input data, (iii) introduced simplifications, and (iv) the definitions of scenarios.

Chosen numerical models need to be able to simulate and represent the physical behavior of simulated processes and to provide results which are compatible with models for subsequent processes. This is generally the case here, but the extreme dimensions, magnitudes, and context are certainly at the limits of capabilities of such models. For instance, the simulation of GLOFs with volumes of several millions m^3 is not the main purpose RAMMS was designed for. "Normal" debris flows of comparable volumes probably occur in several pulses or surges, whereas in a GLOF the entire mass can be involved in one major mass movement (Frey et al., 2016). Such extreme applications could even lead to numerical instabilities of the applied models, however, comparison to evidences from other comparable events and results from independent simulations with other models provide a certain control on the validness of obtained modeling results. In this case, RAMMS results were compared to FLO-2D results obtained by Somos-Valenzuela et al. (2016) for identical GLOF scenarios of Lake Palcacocha. Considerable differences were observed regarding maximum flow depth values between results from RAMMS and FLO-2D. However, regarding the critical criteria for hazard mapping, in this case the area affected and the spatial distribution of maximum flow heights above and below 1 m (= threshold for intensity classification), are similar. After generalizing the raw hazard map combining the three scenarios, the remaining differences can be neglected.

The input data for the models used here is generally adequate for its purposes, but as well includes certain limitations. On the one hand, physically-based numerical models often require a large set of parameters which is not available from site specific measurements, but needs to be taken from literature. Even more important is the fact that the DEM used here is a true elevation or terrain model, representing the topography of the earth surface without vegetation and infrastructure, such as bridges or buildings. In particular in urban areas like the city of Huaraz, the latter have a significant influence on flow behavior. For a more accurate and detailed hazard mapping within the urban center of Huaraz, further works would be required, including high-precision surveys of the buildings and other infrastructure, detailed flow modeling based on a digital surface model comprising such infrastructure, and thorough validation and adjustments in the field, considering for instance also passages and channels for the GLOF which are not detectable from a vertical air or space borne perspective. Such improvements would also require an analysis of the suitability of RAMMS model, for instance, which has not been tested for this type of applications. These kind of works is also very cost and labor intensive and related investments could only be justified if a clear benefit could be drawn from related improvement, such as for instance, detailed urban land-use planning or (re-)definitions of real-estate values (cf. section Institutional aspects and dissemination).

However, the biggest source of uncertainty in the entire hazard mapping approach is related to the definition of scenarios. Due to the lack of historic recordings of involved processes, often also due to the unique nature of certain mass movement events, scenario definitions cannot rely on empirically established, site specific frequency-magnitude relations, as it is the case for various other hazardous processes. Taking into account worst-case considerations at all stages of the process chain allow to better account for these uncertainties by including much more conservative assumptions on moraine dam stability. Here, this was addressed first by considering worst-case scenarios for the GLOF triggering rock-ice avalanches, and second by including a breach formation scenario as the low hazard level, despite its very low probability of occurrence according to the susceptibility analysis with a physically-based numerical model.

Besides ice or combined rock-ice avalanches, no other potential triggers were considered here. In principle also slope instabilities at steep inner moraine slopes can cause displacement waves, such as observed in a landslide event 2003 at the inner Palcacocha moraine (Vilímek et al., 2005). However, this event caused a displacement wave only marginally higher than the freeboard at the dam, and did not lead to a larger overtopping wave. A detailed evaluation by Klimes et al. (2016) revealed, that this 2003 event was among the largest landslides that are possible form the Palcacocha moraine, and that comparable landslides will not lead to substantial displacement waves, mainly due to the elongated shapes of the involved lakes. Another aspect that has not been considered here are effects of earthquakes. However, for instance the 2015 Gorkha Earthquake in Nepal only affected a very small number of moraine dams of glacial lakes and did not lead to a single GLOF, despite the large number of glacial lakes in the Himalayas (Kargel et al., 2016). Nevertheless, more detailed site-specific analyses would be required to assess the potential impacts of earthquakes on moraine dam, in particular since the Cordillera Blanca is located in very active seismic zone.

As outlined in section Institutional aspects and dissemination, considerations of the social and institutional context, as well as, dissemination activities are key for a successful communication and implementation of the elaborated hazard map. Based on the analysis of experiences of hazard map development, approval and dissemination at Quillcay and Huaraz we conclude the following which we consider relevant beyond this case study:

- Missing clarity about the process from mandating to developing and producing a hazard map affects the integration of the hazard map into operational and institutional processes, as well as, the acceptance by the authorities and the population. In countries with limited or not established regulations concerning this process, developing hazard maps intended to substantially reach beyond academic studies, is a major challenge. Clear regulations also increase the legitimacy and credibility of the institutions and experts involved, which is particularly important in case of multiple competing institutions with unclearly defined

responsibilities—a situation prevailing in many countries of the world and bearing significance much beyond just GLOF hazards.

- The assessment of GLOF hazards and development of hazards maps needs to follow a transparent method and be based on the international state of the art. The GAPHAZ (2017) guidance document was produced exactly in recognition of this need. This document represents a consensus of international experts and therefore forms a major international reference.
- The approval process of a hazard map is important for its acceptance and further use. In many countries there is still missing clarity about it which limits the practical effectiveness of hazard aps and therefore this gap should be closed wherever possible.
- The purpose and use of hazard maps should be clearly defined before or during the development process. This is particularly important because worldwide (and even within countries) different types of hazard maps exist. As seen here missing (high-resolution) data, time, financial, or human resources can limit the use of a hazard map for certain purposes (e.g., apt for early warning systems but not for urban planning).
- The dissemination of a GLOF hazard map should be an integral part of the complete planning process and represents a major effort on its own. Multiple aspects (perceptions, credibility of institutions and experts, poverty, existing information, etc.) influence the success of the dissemination in terms of how effective a hazard map is to reduce GLOF related risks. A thorough analysis of these aspects is recommended but in practice often difficult due to time and financial constraints.

Knowledge and understanding of local perceptions of hazards and risks are fundamentally important for successful hazard and risk communication, but also for the willingness of governments and authorities to invest in related mitigation measures. After a GLOF event, fast-onset glacier related hazards typically receive high attention. But within a few years' time, this perception can move toward other hazards and risks, in particular in societies with a relatively high dependency on agriculture, including subsistence farming, where slow-onset hazards, such as droughts, have severe and immediate impacts on the well-being. In the case of the Quillcay catchment such a prioritization applies also the different lakes. Lake Palcacocha receives highest attention, probably due to its history with the 1941 outburst, whereas the hazard assessment performed here revealed, that in particular also Lake Cuchillacocha, despite its smaller volume compared to the other lakes, comprises a significant hazard potential.

CONCLUSIONS

Rapid changes of environmental conditions in high-mountain regions currently observed all over the world require scenario-based hazard assessment and mapping approaches, as current situations often are beyond historical precedence. Despite considerable uncertainties related to such assessments, the use of numerical models for the simulation of involved processes yields objectivity and traceability needed to meet scientific standards. With smart scenario definitions and well-reflected worst-case considerations, the degree of uncertainty can be lowered substantially. The GLOF hazard assessment and mapping procedure applied in the present paper to the Quillcay Catchment in the Cordillera Blanca demonstrated that approaches successfully tested for single lake assessments can also be applied to a multi-hazard-source setting such as an entire catchment containing several potentially hazardous lakes.

The assessments of rock-ice avalanche and dam breach susceptibility and impact revealed, that the situation of Lake Palcacocha, which in 1941 caused one of the deadliest GLOFs in recent history, today is different than it was in the 1940's, and a breach formation in case of an overtopping impact wave is very unlikely nowadays (Somos-Valenzuela et al. (2016)). Nevertheless, a substantial hazard is emanated by this lake to the Quillcay Catchment and the city of Huaraz, urgently requiring complementary disaster risk prevention measures. Besides the prominent Lake Palcacocha, also the lakes Tullparaju and Cuchillacocha need to be considered when evaluating the GLOF hazard in this catchment. We found that in particular Lake Cuchillacocha poses the highest hazard of the three lakes in the medium scenario, due to its proximity to a large hanging glacier, which has the potential to completely drain this 2-million m^3 lake even by an impact of an avalanche of the medium magnitude scenario. These findings contradict to some extent common local risk perceptions, which are often biased by historical events (here the 1941 Palcacocha outburst); highlighting the importance of integrative, unprejudiced, and objective hazard assessments.

In order to convert the resulting hazard map in a useful disaster risk reduction tool allowing for hazard communication, spatial planning, and the design of complementary structural and non-structural prevention measures, etc., national standards and institutional aspects need to be taken into consideration. In many countries, related processes and regulations are not clearly established, resulting in challenging situations for the transformation of a hazard map as a scientific result into an official, legally binding document, serving the authorities as a basis for decision-making and planning.

In a context of mistrust by the population in their government, authorities and experts, such as it is the case in the Cordillera Blanca (Carey, 2005; Carey et al., 2012), the dissemination of a hazard map is a challenging, but fundamentally important task, requiring major efforts. For the dissemination of the hazard map presented here, successful experiences have been made by a massive door-to-door information campaign, accompanied by the positive effect of more detailed insights into risk perceptions by the population.

Future efforts might aim at improving the hazard mapping within the urban area, including a detailed evaluation of the effects of urban infrastructure on the flow behavior of GLOFs. This is a major task, as scientific knowledge and experiences are currently still very limited in this regard. However, the presented hazard map provides an important planning tool for subsequent DRR measures, aiming at reducing

the GLOF risk in the Quillcay catchment and the city of Huaraz.

AUTHOR CONTRIBUTIONS

HF led the study, coordinated works of co-authors, wrote the main part of the manuscript and elaborated most figures. CH helped designing the study, advised modeling works and wrote the dissemination section. RC provided information and data on the works done by Somos-Valenzuela et al. (2016), was involved in the design of the modeling works and provided a figure. PB did most of the modeling work with RAMMS and the empirical wave estimates. BM provided advice regarding the RAMMS modeling, especially to the beta version able to consider erosional processes. AC and CP were the contacts of the national institutions involved in the hazard mapping and members of the technical commission, provided DEM and bathymetric data and other site specific information and liaised with involved local governmental authorities and other institutions.

ACKNOWLEDGMENTS

The work presented in this study are part of the activities of the Proyecto Glaciares+, funded by the Swiss Agency for Development and Cooperation (SDC). Support from and collaboration with CARE Peru, the implementing partner of the University of Zurich in Proyecto Glaciares+, and the regional Ancash office of CARE in Huaraz is warmly acknowledged. Previous works by the University of Texas at Austin were supported by the USAID Climate Change Resilient Development (CCRD) project. DEM and RapidEye imagery provided by the Peruvian Ministry of the Environment (MINAM); Landsat imagery (**Figure 2**) provided by US Geological Survey (USGS). The Swiss Federal Institute for Forest, Snow and Landscape Research (WSL) and its Institute for Snow and Avalanche Research (SLF) provided access and support to the RAMMS debris flow module and the beta version allowing for the simulation of erosional processes. We thank the editor D. Tiranti and the two reviewers for their comments and suggestions, which helped to improve this article.

REFERENCES

Allen, S. K., Linsbauer, A., Randhawa, S. S., Huggel, C., Rana, P., and Kumari, A. (2016). Glacial lake outburst flood risk in Himachal Pradesh, India: an integrative and anticipatory approach considering current and future threats. *Nat. Hazards* 84, 1741–1763. doi: 10.1007/s11069-016-2511-x

ANA (2014a). *Inventario Nacional de Glaciares y Lagunas – Glaciares*. Huaraz, Peru.

ANA (2014b). *Inventario Nacional de Glaciares y Lagunas – Lagunas*. Huaraz, Peru.

Bartelt, P., Salm, L. B., and Gruber, U. (1999). Calculating dense-snow avalanche runout using a Voellmy-fluid model with active/passive longitudinal straining. *J. Glaciol.* 45, 242–254. doi: 10.1017/S002214300000174X

Carey, M. (2005). Living and dying with glaciers: people's historical vulnerability to avalanches and outburst floods in Peru. *Glob. Planet. Change* 47, 122–134. doi: 10.1016/j.gloplacha.2004.10.007

Carey, M. (2010). *In the Shadow of Melting Glaciers: Climate Change and Andean Society*. Oxford, UK: Oxford University Press.

Carey, M., Huggel, C., Bury, J., Portocarrero, C., and Haeberli, W. (2012). An integrated socio-environmental framework for climate change adaptation and glacier hazard management: lessons from Lake 513, Cordillera Blanca, Peru. *Clim. Change* 112, 733–767. doi: 10.1007/s10584-011-0249-8

CENEPRED (2015). *Manual Para La Evaluación de Riesgos Originados Por Fenómenos Naturales, 2nd Edn*. Lima: Centro Nacional de Estimación, Prevención y Reducción del Riesgo de Desastres (CENEPRED).

Chisolm, R. E., and McKinney, D. C. (2018). Dynamics of avalanche-generated impulse waves: three-dimensional hydrodynamic simulations and sensitivity analysis. *Nat. Hazards Earth Syst. Sci.* 18, 1373–1393. doi: 10.5194/nhess-18-1373-2018

Christen, M., Kowalski, J., and Bartelt, P. (2010). RAMMS: numerical simulation of dense snow avalanches in three-dimensional terrain. *Cold Regions Sci. Technol.* 63, 1–14. doi: 10.1016/j.coldregions.2010.04.005

Emmer, A., and Vilimek, V. (2014). New method for assessing the susceptibility of glacial lakes to outburst floods in the Cordillera Blanca, Peru. *Hydrol. Earth Syst. Sci.* 18, 3461–3479. doi: 10.5194/hess-18-3461-2014

Emmer, A., Vilímek, V., and Luyo, M. Z. (2016). Hazard mitigation of glacial lake outburst floods in the cordillera blanca (Peru): the effectiveness of remedial works. *J. Flood Risk Manage.* 11, S489–S501. doi: 10.1111/jfr3.12241

Evans, S. G., Bishop, N. F., Smoll, L. F., Murillo, P. V., Delaney, K. B., and Oliver-Smith, A. (2009). A re-examination of the mechanism and human impact of catastrophic mass flows originating on Nevado Huascarán, Cordillera Blanca, Peru in 1962 and 1970. *Eng. Geol.* 108, 96–118. doi: 10.1016/j.enggeo.2009.06.020

Fischer, L., Amann, F., Moore, J. R., and Huggel, C. (2010). Assessment of periglacial slope stability for the 1988 Tschierva rock avalanche (Piz Morteratsch, Switzerland). *Eng. Geol.* 116, 32–43. doi: 10.1016/j.enggeo.2010.07.005

Flow Science (2012). *FLOW3D Documentation: Release 10.1.0*. Santa Fe, NM: Flow Science, Inc., 811.

Frey, H., Huggel, C., Bühler, Y., Buis, D., Burga, M. D., Choquevilca, W., et al. (2016). A robust debris-flow and GLOF risk management strategy for a data-scarce catchment in Santa Teresa, Peru. *Landslides* 13, 1493–1507. doi: 10.1007/s10346-015-0669-z

GAPHAZ (2017). "Assessment of glacier and permafrost hazards in Mountain Regions," in Joint Standing Group on Glacier and Permafrost Hazards in High Mountains (GAPHAZ) of the International Association of Cryospheric Sciences (IACS) and the International Permafrost Association (IPA), eds S. K. Allen, H. Frey, and C. Huggel (Zurich; Lima). Available online at: http://gaphaz.org/files/Assessment_Glacier_Permafrost_Hazards_Mountain_Regions.pdf (Accessed November, 2018).

Gardelle, J., Arnaud, Y., and Berthier, E. (2011). Contrasted evolution of glacial lakes along the Hindu Kush Himalaya mountain range between 1990 and 2009. *Glob. Planet. Change* 75, 47–55. doi: 10.1016/j.gloplacha.2010.10.003

Haeberli, W., Schaub, Y., and Huggel, C. (2016). Increasing risks related to landslides from degrading permafrost into new lakes in de-glaciating mountain ranges. *Geomorphology* 293, 405–417. doi: 10.1016/j.geomorph.2016.02.009

Heller, V., Hager, W. H., and Minor, H-E. (2009). *Landslide Generated Impulse Waves in Reservoirs*. Zurich: Mitteilungen Versuchsanstalt für Wasserbau, Hydrologie und Glaziologie (VAW), ETH Zürich.

Huggel, C., Haeberli, W., Kääb, A., Bieri, D., and Richardson, S. (2004a). An assessment procedure for glacial hazards in the Swiss Alps. *Can. Geotech J.* 41, 1068–1083. doi: 10.1139/t04-053

Huggel, C., Kääb, A., and Salzmann, N. (2004b). GIS-Based modelling of glacial hazards and their interactions using Landsat-TM and IKONOS imagery. *Norsk Geografisk Tidskrift - Norwegian J. Geogr.* 58, 61–73. doi: 10.1080/00291950410002296

Hürlimann, M., Copons, R., and Altimir, J. (2006). Detailed debris flow hazard assessment in Andorra: a multidisciplinary approach. *Geomorphology* 78, 359–372. doi: 10.1016/j.geomorph.2006.02.003

Huss, M., and Hock, R. (2015). A new model for global glacier change and sea-level rise. *Front. Earth Sci.* 3:54. doi: 10.3389/feart.2015.00054

Hussin, H. Y., Luna, B. Q., van Westen, C. J., Christen, M., Malet, J. P., and van Asch, T. W. J. (2012). Parameterization of a numerical 2-D debris flow model with entrainment: a case study of the Faucon catchment, Southern French Alps. *Nat. Hazards Earth Syst. Sci.* 12, 3075–3090. doi: 10.5194/nhess-12-3075-2012

IBER (2010). *Two-Dimensional Modeling of Free Surface Shallow Water Flow, Hydraulic Reference Manual*. IBER v1.0. Available online at: www.iberaula.es (Accessed July, 2018)

INEI (2015). *Día Mundial de la Población*. Lima: INEI.

Kargel, J. S., Leonard, G. J., Shugar, D. H., Haritashya, U. K., Bevington, A., Fielding, E. J., et al. (2016). Geomorphic and geologic controls of geohazards induced by Nepals 2015 Gorkha earthquake. *Science* 351:aac8353. doi: 10.1126/science.aac8353

Klimes, J., Novotný, J., Novotná, I., Urries, B. J., Vilímek, V., Emmer, A., et al. (2016). Landslides in moraines as triggers of glacial lake outburst floods: example from PalcacochaLake (Cordillera Blanca, Peru). *Landslides* 13, 1461–1477. doi: 10.1007/s10346-016-0724-4

Linsbauer, A., Frey, H., Haeberli, W., Machguth, H., Azam, M. F., and Allen, S. (2015). Modelling glacier-bed overdeepenings and possible future lakes for the glaciers in the Himalaya–Karakoram region. *Ann. Glaciol.* 57, 119–130. doi: 10.3189/2016AoG71A627

McColl, S. T., and Davies, T. R. H. (2013). Large ice-contact slope movements: glacial buttressing, deformation and erosion. *Earth Surf. Process. Landforms* 38, 1102–1115. doi: 10.1002/esp.3346

Mergili, M. (2016). Observation and Spatial Modeling of Snow- and Ice- Related Mass Movement Hazards. Oxford University Press.

Mergili, M., Emmer, A., Juricová, A., Cochachin, A., Fischer, J.-T., Huggel, C., et al. (2018). How well can we simulate complex hydro-geomorphic process chains? The 2012 multi-lake outburst flood in the Santa Cruz Valley (Cordillera Blanca, Perú). *Earth Surf. Process. Landforms* 43, 1373–1389. doi: 10.1002/esp.4318

Mergili, M., Fischer, J-T., Krenn, J., and Pudasaini, S. P. (2017). r.avaflow v1, an advanced open-source computational framework for the propagation and interaction of two-phase mass flows. *Geosci. Model Dev.* 10, 553–569. doi: 10.5194/gmd-10-553-2017

Noetzli, J., and Gruber, S. (2009). Transient thermal effects in Alpine permafrost. *Cryosphere* 3, 85–99. doi: 10.5194/tc-3-85-2009

Portocarrero, C. (2014). *The Glacial Lake Handbook*. Washington, DC: USAID.

Racoviteanu, A. E., Arnaud, Y., Williams, M., and Ordoñez, J. (2008). Decadal changes in glacier parameters in the Cordillera Blanca, Peru, derived from remote sensing. *J. Glaciol.* 54, 499–509. doi: 10.3189/002214308785836922

Raetzo, H., Lateltin, O., Bollinger, D., and Tripet, J. (2002). Hazard assessment in Switzerland - Codes of practice for mass movements. *Bull. Eng. Geol. Environ.* 61, 263–268. doi: 10.1007/s10064-002-0163-4

Richardson, S., and Reynolds, J. (2000). An overview of glacial hazards in the Himalayas. *Quaternary Int.* 65–66, 31–47. doi: 10.1016/S1040-6182(99)00035-X

Schaub, Y., Haeberli, W., Huggel, C., Künzler, M., and Bründl, M. (2013). "Landslides and new lakes in deglaciating areas: a risk management framework," in *Landslide Science and Practice: Social and Economic Impact and Policies*, eds C. Margottini, P. Canuti, and K. Sassa (Berlin; Heidelberg: Springer), 31–38.

Schaub, Y., Huggel, C., and Cochachin, A. (2015). Ice-avalanche scenario elaboration and uncertainty propagation in numerical simulation of rock-/ice-avalanche-induced impact waves at Mount Hualcán and Lake 513, Peru. *Landslides* 13, 1–15. doi: 10.1007/s10346-015-0658-2

Scheidl, C., Rickenmann, D., and McArdell, B. W. (2013). "Runout prediction of debris flows and similar mass movements," in *Landslide Science and Practice: Spatial Analysis and Modelling* Vol. 3, eds C. Margottini, P. Canuti, and K. Sassa (Berlin, Heidelberg: Springer Berlin Heidelberg), 221–229.

Schneider, D., Bartelt, P., Caplan-Auerbach, J., Christen, M., Huggel, C., and McArdell, B. W. (2010). Insights into rock-ice avalanche dynamics by combined analysis of seismic recordings and a numerical avalanche model. *J. Geophys. Res.* 115, 1–20. doi: 10.1029/2010JF001734

Schneider, D., Huggel, C., Cochachin, A., Guillén, S., and García, J. (2014). Mapping hazards from glacier lake outburst floods based on modelling of process cascades at Lake 513, Carhuaz, Peru. *Adv. Geosci.* 35, 145–155. doi: 10.5194/adgeo-35-145-2014

Schneider, D., Huggel, C., Haeberli, W., and Kaitna, R. (2011). Unraveling driving factors for large rock-ice avalanche mobility. *Earth Surf. Process. Landforms* 36, 1948–1966. doi: 10.1002/esp.2218

Schraml, K., Thomschitz, B., McArdell, B. W., Graf, C., and Kaitna, R. (2015). Modeling debris-flow runout patterns on two alpine fans with different dynamic simulation models. *Nat. Hazards Earth Syst. Sci.* 15, 1483–1492. doi: 10.5194/nhess-15-1483-2015

Somos-Valenzuela, M. A., Chisolm, R. E., Rivas, D. S., Portocarrero, C., and McKinney, D. C. (2016). Modeling a glacial lake outburst flood process chain: the case of Lake Palcacocha and Huaraz, Peru. *Hydrol. Earth Syst. Sci.* 20, 2519–2543. doi: 10.5194/hess-20-2519-2016

UNISDR (2009). *UNISDR Terminology on Disaster Risk Reduction*. Geneva: United Nations.

Vetsch, D., Siviglia, A., Caponi, F., Ehrbar, D., Gerke, E., Kammerer, S., et al. (2018). System manuals of BASEMENT. zurich: laboratory of hydraulics, glaciology and hydrology (VAW). ETH zurich. Available online at: http://www.basement.ethz.ch (Accessed July 2018).

Vilímek, V., Zapata, M., Klimes, J., Patzelt, Z., and Santillan, N. (2005). Influence of glacial retreat on natural hazard of the Palcacocha Lake area, Peru. *Landslides* 2, 107–115. doi: 10.1007/s10346-005-0052-6

Wegner, S. A. (2014). *Lo Que el Agua se Llevó. Notas Técnicas Sobre Cambio Climático 7*. Lima: Ministerio del Ambiente Peru, 88.

Westoby, M. J., Glasser, N. F., Brasington, J., Hambrey, M. J., Quincey, D. J., and Reynolds, J. M. (2014). Modelling outburst floods from moraine-dammed glacial lakes. *Earth Sci. Rev.* 134, 137–159. doi: 10.1016/j.earscirev.2014.03.009

Worni, R., Huggel, C., Clague, J. J., Schaub, Y., and Stoffel, M. (2014). Coupling glacial lake impact, dam breach, and flood processes: a modeling perspective. *Geomorphology* 224, 161–176. doi: 10.1016/j.geomorph.2014.06.031

Worni, R., Stoffel, M., Huggel, C., Volz, C., Casteller, A., and Luckman, B. (2012). Analysis and dynamic modeling of a moraine failure and glacier lake outburst flood at Ventisquero Negro, Patagonian Andes (Argentina). *J. Hydrol.* 444–445, 134–145. doi: 10.1016/j.jhydrol.2012.04.013

Zemp, M., Frey, H., Gärtner-Roer, I., Nussbaumer, S. U., Hoelzle, M., Paul, F., et al. (2015). Historically unprecedented global glacier decline in the early 21st century. *J. Glaciol.* 61, 745–762. doi: 10.3189/2015JoG15J017

Conflict of Interest Statement: The authors declare that the research was conducted in the absence of any commercial or financial relationships that could be construed as a potential conflict of interest.

frontiers in Earth Science

ORIGINAL RESEARCH
published: 20 June 2018
doi: 10.3389/feart.2018.00085

Combination of Rainfall Thresholds and Susceptibility Maps for Dynamic Landslide Hazard Assessment at Regional Scale

Samuele Segoni, Veronica Tofani, Ascanio Rosi, Filippo Catani and Nicola Casagli*

Department of Earth Sciences, University of Firenze, Firenze, Italy

We propose a methodology to couple rainfall thresholds and susceptibility maps for dynamic landslide hazard assessment at regional scale. Both inputs are combined in a purposely-built hazard matrix to get a spatially and temporally variable definition of landslide hazard: while statistical rainfall thresholds are used to accomplish a temporal forecasting with very coarse spatial resolution, landslide susceptibility maps provide static spatial information about the probability of landslide occurrence at fine spatial resolution. The test site is the Northern part of Tuscany (Italy), where a recent landslide susceptibility map and a set of recently updated rainfall thresholds are available. These products were modified and updated to meet the requirements of the proposed procedure: the susceptibility map was reclassified and the threshold set was expanded defining additional thresholds. The hazard matrix combines three susceptibility classes (S1, low susceptibility; S2 medium susceptibility; S3 high susceptibility) and three rainfall rate classes (R1, R2, R3), defining five hazard classes, from H0 (null hazard) to H4 (high hazard). A key passage of the procedure is the appropriate calibration and validation of the matrix, letting the hazard classes have a precise meaning in terms of expected consequences and hazard management. The employ of the proposed procedure in a regional warning system brings two main advantages: (i) it is possible to better hypothesize when and where landslide are expected and with which hazard degree, thus fostering a more effective hazard and risk management (e.g., setting priorities of intervention); (ii) the spatial resolution of the regional scale warning system is markedly refined because from time to time the areas where landslides are expected represent only a fraction of the alert zone.

Keywords: landslide, hazard, rainfall thresholds, susceptibility maps, northern Apennines

OPEN ACCESS

Edited by:
Davide Tiranti,
Agenzia Regionale per la Protezione Ambientale (ARPA), Italy

Reviewed by:
Matthieu Kervyn,
Vrije Universiteit Brussel, Belgium
Milad Janalipour,
K.N.Toosi University of Technology, Iran

****Correspondence:***
Veronica Tofani
veronica.tofani@unifi.it

Specialty section:
This article was submitted to Quaternary Science, Geomorphology and Paleoenvironment, a section of the journal Frontiers in Earth Science

Received: *16 March 2018*
Accepted: *04 June 2018*
Published: *20 June 2018*

Citation:
Segoni S, Tofani V, Rosi A, Catani F and Casagli N (2018) Combination of Rainfall Thresholds and Susceptibility Maps for Dynamic Landslide Hazard Assessment at Regional Scale. Front. Earth Sci. 6:85. doi: 10.3389/feart.2018.00085

INTRODUCTION

Since landslides are continuously responsible of damages and casualties worldwide, landslide hazard assessment is a cogent research topic, aiming to determine the spatial and temporal probability of occurrence of landslides (Fell et al., 2008; Corominas et al., 2013).

Spatial occurrence is called susceptibility. A landslide susceptibility map subdivides the terrain into zones with differing likelihoods that landslides of a certain type may occur (Fell et al., 2008). A large part of the quantitative methods to produce landslide susceptibility maps relies on regression

or classification approaches (Aleotti and Chowdhury, 1999; Fell et al., 2008). The techniques most widely used are discriminant analysis (Carrara, 1983; Chung and Fabbri, 1995; Baeza and Corominas, 1996), logistic regression (Hosmer and Lemeshow, 2000; Lee, 2005; Manzo et al., 2013), artificial neural networks (ANN) (Bianchi and Catani, 2002; Lee et al., 2003, 2004; Ermini et al., 2005; Yilmaz, 2009; Lu et al., 2012), linear regression (Atkinson and Massari, 1998), fuzzy membership (Kanungo et al., 2006), conditional probability or Bayesian methods (Yilmaz, 2010; Catani et al., 2013).

The temporal occurrence of landslides is normally expressed in terms of frequency, return period, or exceedance probability (Corominas et al., 2013). Usually the approaches followed to determine the temporal occurrence of landslides are: heuristic methods (judgmental approaches) (Lee et al., 2000; Wong, 2005), physically based methods (Montgomery and Dietrich, 1994; Pack et al., 1998; Iverson, 2000; Crosta and Frattini, 2003; Baum et al., 2005; Godt et al., 2008; Mercogliano et al., 2013; Rossi et al., 2013; Tofani et al., 2017) and empirical/statistical rainfall thresholds (Guzzetti et al., 2008; Segoni et al., 2018; and references therein).

Hazard assessment can be quantitative or qualitative. It is generally preferable to determine the actual frequency of landsliding in a quantitative way but in some situations it may not be practical to assess frequencies sufficiently accurately and a qualitative system based on hazard classes may be adopted (Catani et al., 2005; Fell et al., 2008). Landslide susceptibility maps and hazards assessments are static products that provide a detailed quantitative or qualitative scenario with a good spatial resolution. In this regard, they have complementary characteristics respect to rainfall thresholds, which are widely employed in regional scale landslide warning systems with good temporal resolution but with very coarse spatial resolutions, since warnings are usually issued over large alert zones (Segoni et al., 2018). Indeed, the joint use of rainfall thresholds and landslide susceptibility maps has already proven to be a promising tool in advanced landslide hazard assessment. Hong and Adler (2008) hypothesized a real-time detection system at global scale where a prototype global landslide susceptibility map was overlaid with satellite-based observations of rainfall intensity-duration, to identify the location and time of landslide hazards when areas with significant landslide susceptibility are receiving heavy rainfall. Segoni et al. (2015b) integrated a landslide susceptibility map into a regional scale landslide waning system based on rainfall thresholds to increase the spatial resolution of a warning system used in Emilia Romagna (Italy). Jemec Auflič et al. (2016) described a prototype prediction system for rainfall-induced landslides in Slovenia based on a landslide susceptibility map and a rainfall threshold.

In this work we propose a methodology to couple rainfall thresholds and susceptibility maps for dynamic landslide hazard assessment at regional scale, according to the workflow shown in **Figure 1**. While statistical rainfall thresholds are used to accomplish a dynamic temporal forecasting with good temporal resolution but very coarse spatial resolution, landslide susceptibility maps provide static spatial information about the probability of landslide occurrence with a finer resolution. The test site is the Northern part of Tuscany (Italy), where a recent landslide susceptibility map (Segoni et al., 2016) and a set of recently updated rainfall thresholds (Rosi et al., 2015) are available. This work provides an added value to these two products because for the first time two very different techniques are coupled together to establish a landslide hazard management tool. The proposed approach is based on the definition of a purposely-built hazard matrix that provides different qualitative level of landslide hazard based on different intensity-duration rainfall thresholds and susceptibility classes. In the discussion section, the potential application to real time hazard management is outlined.

MATERIALS AND METHODS

Test Site

The test area is located in Northern Tuscany (Italy), including part of the northern Apennines with an extension of 3,103 Km^2 (**Figure 2**). We selected this area as a test site since we have at disposal the results of a recent landslide susceptibility study (Segoni et al., 2016) and a set of recently updated rainfall thresholds (Rosi et al., 2015), regarding five alert zones (namely A3, A4, B3, B4, and B5) of the Tuscany regional warning system (Segoni et al., 2015a) (**Figure 2**).

The Northern Apennines is a complex thrust-belt system made up by the juxtaposition of several tectonic units, piled during the Tertiary under a compressive regime that was followed by extensional tectonics from the Upper Tortonian. The latter phase produced a sequence of horst-graben structures with an alignment NW-SE that resulted in the emplacement of Neogene sedimentary basins, mainly of marine (to the West) and fluvio-lacustrine (to the East) origin (Vai and Martini, 2001). Today, the morphology is dictated by the presence of NW-SE trending ridges where Mesozoic and Tertiary flysch and calcareous units outcrop, separated by Pliocene-Quaternary basins.

These geological settings clearly affect the typology and occurrence of surface processes, primarily through the differences in the mechanical properties linked to the various prevalent lithologies while the rainfall is the main triggering factor. In particular, the study area shows two different geological settings in the east and west sectors respectively (Tofani et al., 2017). In the west sector carbonaceous rocks and metamorphic sandstone and phyllitic–schist mainly outcrop. The slopes are largely characterized by soils that are rather thin (0.5–2 m thick). On the contrary, the calcareous and dolomitic slopes are usually rocky or with very thin soil cover. The east sector shows a more uniform geological condition with the prevalence of flysch formation rock-type (Macigno) which is composed of quartz and feldspar sandstone alternated with layers of siltstone. The slope gradient varies from 0° in the plain to 55°. In the mid and upper sections of the valley, where most landslides usually occur, the stratigraphy consists of a 1.5–5 m thick layer of colluvial soil overlying the bedrock (Tofani et al., 2006, 2017).

In the study area, mean annual precipitation varies from about 800 mm/y in the southern valleys to about 1,800 mm/y on the north-western mountain ridges. During the year, rainfalls

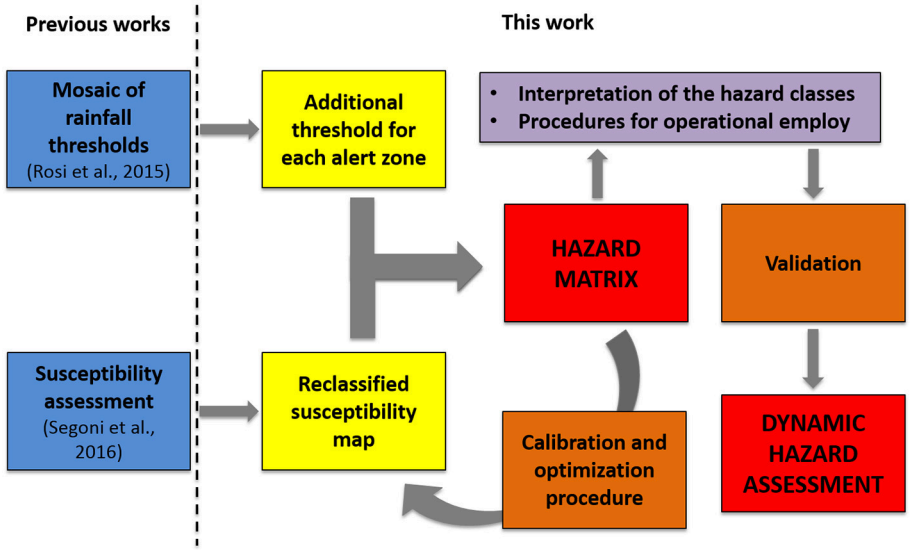

FIGURE 1 | Workflow.

concentrate in autumn and spring, with November and March being the rainiest months, while summer is typically dry, except for occasional short and intense storms (Rosi et al., 2012).

Northern Tuscany is affected by serious geological hazards as landslides and subsidence (Rosi et al., 2014, 2018). According to the Inventario dei Fenomeni Franosi Italiani (IFFI) (Trigila et al., 2010, 2013) database, more than 5,000 landslides are present. Their dimensions range from 10^2 to 10^6 m^2 (Rosi et al., 2018) and they are almost entirely categorized as rotational/translational slides (37% of the entire database) of or as complex movements (63%), i.e., shallow landslides or soil slips evolving into flows. It is worth to notice that the hazard assessment procedure that we propose in this work is related only to these types of landslides involving mainly soil material, while we do not take into account rock falls and topples (less than 1% of the database).

Data and Previous Works

Rainfall Thresholds

Tuscany is covered by a prototype regional warning system based on a set of rainfall thresholds differentiated for 25 alert zones (Segoni et al., 2014b, 2015a). Rainfall thresholds are based on intensity and duration and were defined with a highly automated procedure using a purposely developed software called MaCumBA (Segoni et al., 2014a). The subdivision into 25 alert zones following the main regional divides allows relating each threshold to a hydrographic basin with homogeneous meteorological and geomorphological settings, thus strengthening the forecasting effectiveness of the system (Segoni et al., 2014b). In the alert zones extending over the study area, the thresholds have been recently updated using an extended landslide dataset (Rosi et al., 2015).

The source of landslide data is mainly constituted by event reports performed by the regional Civil Protection offices and by a catalog of geotagged internet news (Battistini et al., 2017), which was automatically obtained using a purposely-developed web-based semantic search engine called SECAGN (Battistini et al., 2013). These landslide data were also used to calibrate the hazard matrix, which is the main objective of this work (section Hazard Assessment).

To date, each alert zone of the regional warning systems is monitored by a rainfall threshold, calibrated at the 95% confidence level, that discriminates between "warning" and "no warning." The high confidence level is a conservative choice that allows having a high "hits" rate at the cost of a not negligible number of false positives (Rosi et al., 2015).

Susceptibility Model

In the study area, a susceptibility assessment has been recently carried out (Segoni et al., 2016) using "Random forest," a machine-learning algorithm for non-parametric multivariate classification (Breiman, 2001). Although this methodology can be considered relatively new, it has already been consolidated in landslide studies through different applications (Brenning, 2005; Vorpahl et al., 2012; Catani et al., 2013; Trigila et al., 2013; Segoni et al., 2015b; Pourghasemi and Kerle, 2016; Youssef et al., 2016). Random Forest has the advantage of handling both numerical and categorical variables without requiring assumptions about the distribution of the input data. Moreover, it can use a large number of input parameters, then a procedure of forward selection, which accounts also for interactions and nonlinearities among variables, discards the ones that do not bring a positive contribution and selects the optimal configuration. The landslide susceptibility analysis was performed using the software ClaReT (Lagomarsino et al., 2017), which uses a random forest implementation based on Matlab [Matworks, version 7.11, treebagger object (RFtb) and methods].

Two kinds of input parameters were considered as explanatory variables for the susceptibility map: morphometric

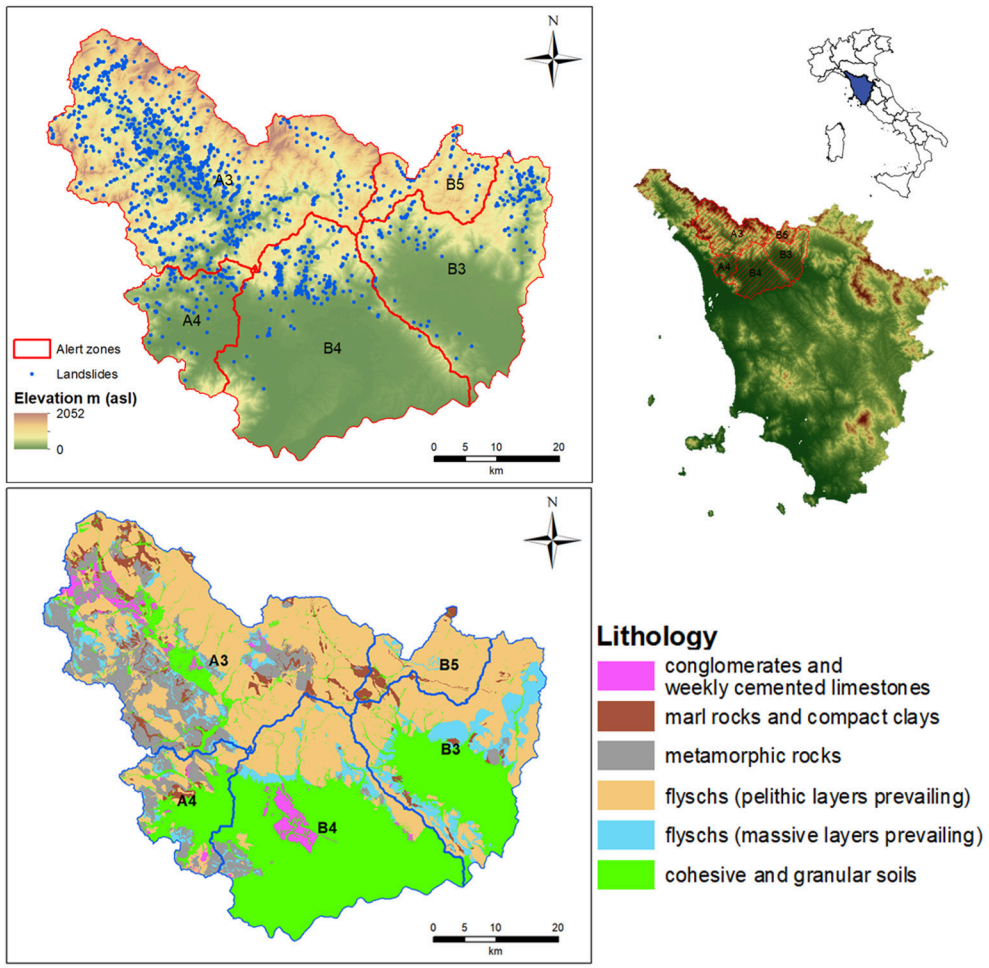

FIGURE 2 | Study area, subdivision into Alert Zones, morphology and lithology.

attributes and attributes derived from thematic maps. In particular, the morphometric attributes are: curvature, flow accumulation, topographic wetness index, elevation, profile curvature, planar curvature, slope gradient, aspect. The thematic attributes are: land use and lithology. Topographic attributes were derived from the official and most recent 10 m resolution DEM (Digital Elevation Model) produced by Tuscany Region. Land use was derived from CORINE Land Cover Map (1:50,000), updated in 2006 (https://www.eea.europa.eu/publications/COR0-landcover) which in the study area was reclassified into 9 classes: urban areas, crops, grasslands, heterogenic rural areas, forests (broad-leaved); forests (conifers); shrubs; bare rocks; humid areas. Lithology was derived from Regional Geological Maps at the 1:10,000 scale, by reclassifying each geological formation into six lithological classes (Segoni et al., 2016): conglomerates and weekly cemented limestones; marl rocks and compact clays; metamorphic rocks; flyschs (pelithic layers prevailing); flyschs (massive layers prevailing); cohesive and granular soils (**Figure 2**).

The IFFI database (Trigila et al., 2010), the Italian national inventory of landslides at 1:10,000 scale, was used to train and validate the susceptibility model.

As described in Segoni et al. (2016) the grid for each morphometric or thematic attribute was resampled to a 100 m pixel size and split into two variables: the average value encountered in the 100 × 100 m cell (mean value for numerical attributes and prevailing class for categorical values), and the variability inside the 100 × 100 m cell (standard deviation for numerical attributes and number of classes for categorical values). For the slope gradient and all kinds of curvature we have considered also the maximum value. The total number of input parameters used is 23 (Segoni et al., 2016).

To calibrate the "Random forest" classification algorithm, the study area was randomly sampled to select 10% of the pixels for training and 10% for testing. Such percentages have been proved to be a good compromise between quality of the results and speed of the calculations (Catani et al., 2013); indeed, a validation of the susceptibility map provided satisfactory results, with an AUC (area under ROC curve) value of 0.84 (Segoni et al., 2016),

highlighting a good agreement with the observed truth and the potentiality of new landslide activations in the future (Segoni et al., 2016).

The raw output data of the susceptibility assessment is a raster map with a 100 m cell size, where each pixel has a percentage value expressing the probability of being affected by a landslide. The map has a range of susceptibility values from 0% to 91.

In this work, these raw data will be reclassified in three classes: low susceptibility (S1), medium susceptibility (S2), and high susceptibility (S3). The definition of the thresholds values between the susceptibility classes is part of the calibration of our hazard model; therefore, it is explained in the following section.

Hazard Assessment

To assess the landslide hazard, the rainfall levels defined from the rainfall thresholds have been integrated with the susceptibility classes. The basic assumption of this work is that if the susceptibility map is classified in a number of classes that equals the number of possible alert levels featured in the threshold system, a square matrix can be built and it is possible to establish a straightforward correspondence between hazard, rainfall rates and susceptibility classes.

The general classification scheme is reported in **Figure 3**, where the hazard matrix, based on susceptibility classes (S1, low susceptibility; S2, medium susceptibility; S3, high susceptibility) and rainfall classes (R1, low rainfall; R2, medium rainfall; R3, high rainfall), defines five hazard classes from H0 (null hazard) to H4 (very high hazard). The hazard matrix is based on the assumption that the higher the susceptibility, the lower the rainfall level that could trigger landslides.

To obtain the needed number of rainfall classes to build a square matrix, in each alert zone an additional threshold has been defined to discriminate between low and high criticality. To define this threshold, we simply translated upward the original threshold until a consistent reduction of false alarms (i.e., rainfall events above the thresholds without triggering landslides) is obtained. The downward or upward translation of a previously defined threshold to defining different alert levels is a quite consolidated approach in the international literature (Guzzetti et al., 2008; Segoni et al., 2018). In this work, three warning levels have been defined for each alert zone: R1 (low rainfall rate), R2 (medium rainfall rate), and R3 (high rainfall rate) (**Table 1**).

For each alert zone, the three susceptibility classes have been defined separately using, in order to define the class breaks, a simple trial and error optimization procedure. All 1,761 landslides used in the rainfall threshold analysis were taken into account and they were associated to: (i) a landslide susceptibility value (by means of a simple elaboration in GIS environment); (ii) a rainfall class as defined above (querying the database of past events of the regional warning systems). Then, optimal susceptibility class breaks have been defined after this procedure:

- First, the class breaks from Segoni et al. (2016) have been taken into account and the hazard matrix (**Figure 3**) has been defined.
- The S1/S2 limit has been progressively lowered until no occurrence was found in the S1/R1 cell of the hazard matrix.
- In case the S1/R1 cell was already at zero, the S1/S2 limit was progressively raised to the highest susceptibility value that allows maintaining a count of zero landslides in the S1/R1 cell.
- The S2/S3 limit has been lowered or raised until the count of landslides in the H2, H3, and H4 classes was 90% of the total.

This procedure has been applied separately to every Alert Zone. Therefore, every AZ is expected to have a characteristic set of susceptibility values defining the susceptibility classes.

	S1	S2	S3
R1	H0	H1	H2
R2	H1	H2	H3
R3	H2	H3	H4

FIGURE 3 | Combination of susceptibility classes and rainfall rates into the hazard matrix: H0, null hazard; H1, low hazard; H2, medium hazard; H3, high hazard; H4, very high hazard.

RESULTS

Hazard Matrix Implementation

According to the methodology described in the previous section, susceptibility classes have been defined with class break values very different from ZA to ZA (**Table 2**). **Figure 4** displays the reclassified susceptibility map for the whole test site.

An original feature the proposed reclassification is that the classes are conceived to be used in conjunction to rainfall thresholds and to become hazard classes of different severity according to the dynamic outputs of the regional warning system based on rainfall thresholds. In other words, based on the rainfall rate (R1, R2, or R3) of each alert zone, the landslide susceptibility classes are transformed into hazard classes according to the scheme reported in **Figure 3**.

TABLE 1 | The system of rainfall threshold proposed for this work.

Alert zone	R2 (Rosi et al., 2015)	R3 (this work)
A3	$I = 32.702\ D^{-0.577}$	$I = 61.850\ D^{-0.577}$
A4	$I = 37.220\ D^{-0.635}$	$I = 61.134\ D^{-0.635}$
B3	$I = 93.553\ D^{-0.828}$	$I = 145.50\ D^{-0.828}$
B4	$I = 48.643\ D^{-0.737}$	$I = 66.00\ D^{-0.737}$
B5	$I = 46.529\ D^{-0.810}$	$I = 93.00\ D^{-0.810}$

The lower bound of the intermediate rainfall rate (R2) is represented by a literature threshold, while the lower bound of the most critical rainfall rate (R3) is an original outcome of this work.

To test this approach, we performed a back-analysis on the whole landslides dataset: each landslide was associated to a hazard class according to the susceptibility class of its location and to the rainfall rate provided by the thresholds of the warning system for the day in which the landslide was triggered. **Table 3** shows the results of this test counting the hazard level associated to each landslide. In **Table 3**, the count is provided separately for each alert zone and it is also aggregated over the whole test site. It can be easily verified that only about 10% of the landslides is in the H1 class and no landslide is in the H0 class.

Validation

The proposed approach was validated using an independent dataset, pertaining to the period from 01-01-2017 to 30-4-2108. The validation consists in simulating an operational employ of the dynamic hazard matrix through the whole validation period and to check what is the hazard class associated to each landslide occurred in the study area during that period.

SECAGN search engine (Battistini et al., 2013, 2017) was applied to retrieve online news of landslides occurred in the study area during the validation period. The result was a catalog of 39 landslides for which triggering time is known with hourly or daily approximation. For each landslide, the rainfall level (R) provided by the warning system during the day of occurrence and the landslide susceptibility class characterizing the landslide location were combined to get the corresponding hazard level (according to **Figure 3**).

It was possible to ascertain that in a hypothetic operational employ of the proposed dynamic hazard assessment, 9 landslides

TABLE 2 | Class break values for the susceptibility classes of each alert zone.

Alert zone	S1–S2 (%)	S2–S3 (%)
A3	4	18
A4	7	15
B3	7	22
B4	4	22
B5	7	26

TABLE 3 | Back-analysis of the landslides dataset: each landslide is associated to a hazard class according to the susceptibility class of its location and to the rainfall rate provided by the thresholds of the warning system.

	A3	A4	B3	B4	B5	TOT	
H0	0	0	0	0	0	0	0%
H1	115	8	17	23	9	172	10%
H2	179	27	24	66	8	304	17%
H3	425	25	106	113	62	731	42%
H4	435	39	35	36	9	554	31%
TOT	1,154	99	182	238	88	1,761	100%

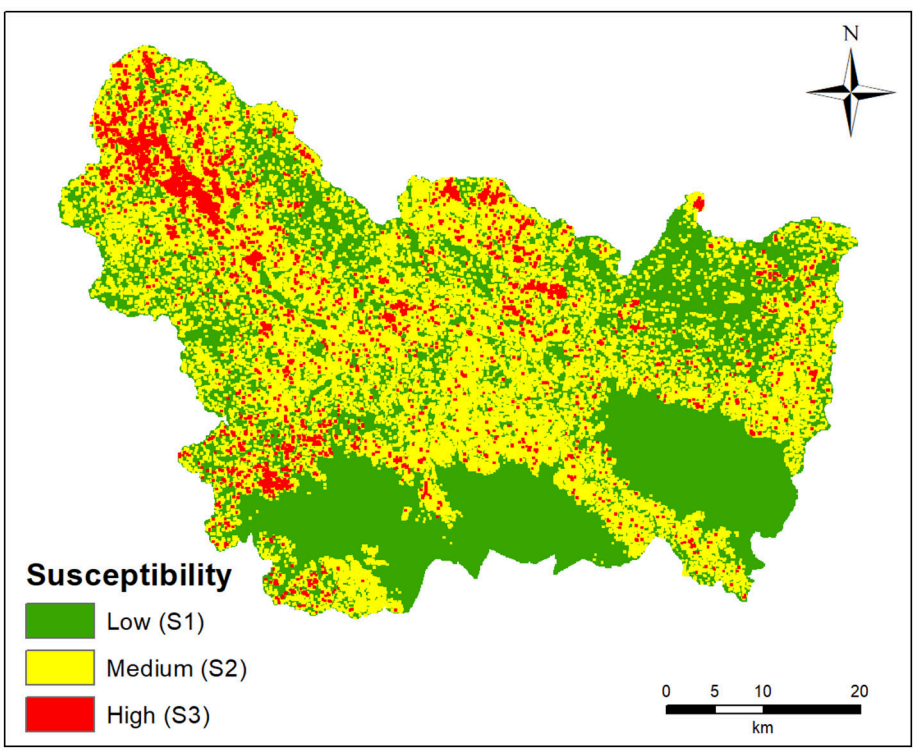

FIGURE 4 | Reclassified susceptibility map.

would have occurred in H4 class, 14 in H3, 15 in H2, 1 in H1 and none in H0. These numbers are in accordance with the criteria used for the hazard assessment calibration: no landslides would have occurred in the "no hazard class," less than 10% (namely, a single landslide) in the H1 class and 38 out of 39 would have been associated to one of the hazard levels interpreted as very likely to be associated with landslides.

Although the validation results are encouraging, we are aware that the dataset used for validation is limited; therefore, further tests should be performed before deeming the proposed procedure ready for the operational employ in the risk management.

DISCUSSION

Hazard Interpretation

Given the physical meaning of the input susceptibility and rainfall classes and the outcomes of the back-analysis, the qualitative hazard classes obtained with the proposed approach could be interpreted as follows:

- H0 - null hazard. No landslides are expected. This hazard class can originate only from the intersection of R1 and S1 classes: it represents a condition for which both the susceptibility map and the threshold model calculated the minimum level of hazard. A landslide occurrence in this box would represent an error of the proposed methodology, as it would occur in a pixel deemed as stable by the susceptibility assessment and during a time when no alarm in terms of rainfall duration and intensity (neither moderate nor high) is issued. Therefore, the hazard matrix was calibrated to have no landslides in this cell, in an effort to account also for the errors and the uncertainties in the data and in the two input models (susceptibility and rainfall thresholds) originating the hazard matrix.
- H1 - low hazard. Theoretically, no landslides should be expected. However, this class encompasses a residual possibility of landslide occurrence because of errors in one of the input models (susceptibility model or rainfall thresholds model), uncertainties in the data, or triggers other than rainfall (e.g., snow melting). The hazard matrix has been calibrated to encompass only 10% of the known landslides dataset in this hazard class. This hazard class can be generated in two different cases:
  - R1/S2. Landslides occurred here represent an error of the proposed hazard model, because harmless rainfalls (no alarms issued by the rainfall thresholds) actually triggered some landslides in a medium susceptibility area.
  - R2/S1. Landslides occurred here represent an error of the proposed hazard model, because mild rainfalls (medium criticality level provided by the rainfall thresholds) triggered some landslides in an area where landslides should not be expected (low susceptibility).
- H2 - medium hazard. In this hazard class, landslides are expected, since one of the inputs is high and the other is low, or they both are medium:
  - R1/S3. Landslides are located in the highest susceptibility class but in the low rainfall rate class. These situations represent errors of the rainfall thresholds model, for example situations related to snow melting, which is not taken into account in the rainfall thresholds definition. Therefore, with this class the proposed dynamic hazard approach is capable of accounting also for occurrences that would be missed by the original warning system.
  - R3/S1. Conversely, this class could be associated to an intrinsic error of the susceptibility model, since landslides occur in an area with low susceptibility, but according to our hazard approach this could be possible only in rainfall conditions belong to the highest rainfall class.
  - R2/S2. In this class, both input models provide the intermediate level of criticality, thus resulting in an intermediate hazard level.
- H3 - high hazard. In this hazard class, one of the input models provides the maximum level of criticality while the other provides the intermediate one:
  - R3/S2. The interpretation of this class is that when the rainfall rate is at the maximum level, landslides can be expected also in areas with medium landslide susceptibility.
  - R2/S3. Where the susceptibility to landslides is at the highest level, landslides can be triggered also when the rainfall rate is at a medium level of criticality.
- H4 - very high hazard. This hazard class originates only from the intersection of R3 and S3 classes, thus representing a condition for which both the susceptibility assessment and the threshold model calculated the highest possible level of spatial and temporal (respectively) hazard.

Possible Use

The methodology presented could be easily integrated into the regional landslide warning system and used to obtain real time dynamic hazard maps. Since the warning system combines rainfall forecasts and real time rainfall data recorded at hourly time step by a network of automated rain gauges, the hazard scenarios could be displayed both for the real-time condition and for the future.

In addition, the dynamic hazard scenario may change as soon as new outputs of the warning systems are provided. If the system is running in now-casting mode, every hour the dynamic hazard map can be refreshed and a new scenario can be built using the new rainfall data coming from the regional network of rain gauges providing hourly rainfall measures. If the system is run in forecast mode, whenever a new forecast of distributed rainfall field is available (normally, twice a day), the dynamic hazard map can be refreshed and updated.

Traditionally, regional warning systems provide a spatially constant alert level for the whole area of application or for large subdivisions called alert zones. The actual consequence of the application of our methodology is that when a rainfall rate (R1, R2, and R3) is recorded/forecasted in a given alert zone, its territory is automatically partitioned in three hazard classes, thanks to the availability of the susceptibility map (**Figure 5**). Therefore, a double advantage is obtained:

1. It is possible to better hypothesize where landslides are expected and with which hazard degree, thus fostering a more

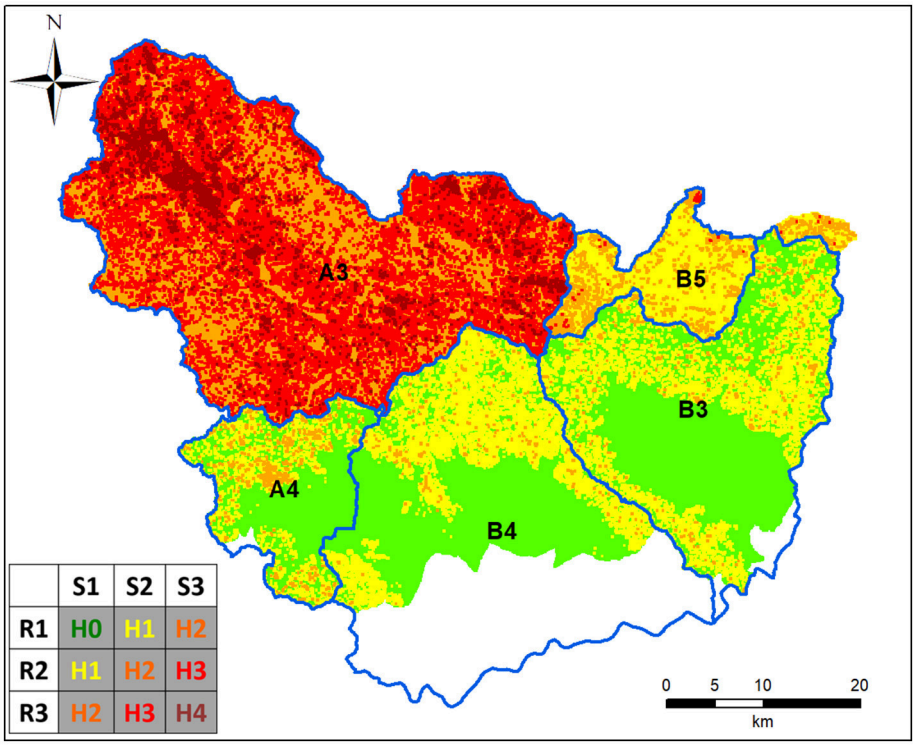

FIGURE 5 | Example of dynamic hazard map for a complex rainfall scenario, with different rainfall rates (R3, R1, R1, R1, R2) in the alert zones (A3, A4, B2, B3, B5, respectively).

effective hazard and risk management (e.g., setting priorities of intervention);

2. The spatial resolution of the warning system is markedly refined because from time to time the areas where landslides should be expected are only a fraction of the alert zone.

Table 4 quantifies to which extent the spatial resolution of the warning system can be refined by the proposed approach: at every time, the territory of each alert zone is partitioned into three out of the five proposed hazard classes, depending on the current rainfall rate. As instance, when the maximum rainfall rate is encompassed (R3: rainfall above the highest threshold), in 26% of the territory of the A3 alert zone the landslide hazard is medium, in 52% is high and in 21% is very high. Taking into account the rainfall threshold warning system alone, the whole alert zone territory would be considered at the maximum hazard level. Therefore, the proposed methodology can be used to obtain a consistent refinement of the spatial resolution of the hazard assessment providing a dynamic hazard classification, which can be used in hazard and risk management.

Comments on the Physical Settings

Rainfall thresholds and susceptibility maps are products that are traditionally created independently for different needs (namely: temporal forecasting for warning purposes and spatial assessment for land management). The objective of this work is finding a dependence between the two approaches to couple the temporal and the spatial forecasting. Form this point of view, rainfall thresholds and susceptibility maps can be considered as complimentary products that can be conveniently coupled to have a dynamic hazard assessment. These two methodologies can be considered complimentary also from another point of view: while rainfall thresholds relate landslide initiation with the main triggering factor (rainfall), susceptibility maps relate landslide occurrence to the predisposing factors (e.g., morphometry, lithology, and land use). It is important to note that both approaches neglect an explicit analysis of the physic behind the landslide initiation: both rainfall thresholds and susceptibility maps used a statistical approach and not a physically based one. As a consequence, the same can be said for the resulting hazard matrix and hazard assessment proposed in this work. However, some characteristics of the hazard assessment can be put into close correlation with some physical features of the test site.

The study area is wide and presents heterogeneous physical features; therefore the approach of subdividing the site into alert zones calibrated independently allowed strengthening the statistical correlation between landslide initiation and triggering/predisposing factors. The very different threshold equations (**Table 1**) and the difference in susceptibility values used to separate susceptibility classes (**Table 2**) corroborates further the effectiveness of the approach consisting in partitioning the study area into independent physiographic units. Among these, A3 is the most prone to landslides: here landslide density is higher than in the other alert zones (Segoni

TABLE 4 | Spatial extension of the hazard classes determined in each alert zone in case of rainfall rates R1, R2, or R3.

		R1 (%)	R2 (%)	R3 (%)
A3	H0	26	N.A.	N.A.
	H1	52	26	N.A.
	H2	21	52	26
	H3	N.A.	21	52
	H4	N.A.	N.A.	21
A4	H0	54	N.A.	N.A.
	H1	40	54	N.A.
	H2	6	40	54
	H3	N.A.	6	40
	H4	N.A.	N.A.	6
B3	H0	55	N.A.	N.A.
	H1	41	55	N.A.
	H2	4	41	55
	H3	N.A.	4	41
	H4	N.A.	N.A.	4
B4	H0	54	N.A.	N.A.
	H1	43	54	N.A.
	H2	3	43	54
	H3	N.A.	3	43
	H4	N.A.	N.A.	3
B5	H0	61	N.A.	N.A.
	H1	37	61	N.A.
	H2	2	37	61
	H3	N.A.	2	37
	H4	N.A.	N.A.	2

et al., 2014b; Battistini et al., 2017), due to the higher slope gradients, the highest altitudes and the presence of lithologies very susceptible to landslides (pelitic flyschs and shistose metamorphic rocks). This is also reflected by the outcomes of the calibration procedure: A3 has the lowest rainfall thresholds combined with the lowest susceptibility, while B3 shows the highest ones. The subdivision of the study area into alert zones to be monitored independently allow also the better encompass the spatial and temporal variability of the rainfall variable: a check on the validation period revealed that in 39% of the days, the rainfall amounts were so different from an alert zone to another that the systems returned different rainfall rate classes (R1, R2, R3), and this occurred mainly during storms: during the validation period it never happened that all the alert zones were at the R2 or R3 level during the same day.

According to the validation procedure, the dynamic hazard assessment proposed in this work underestimated landslide hazard only in one circumstance out of 39. A thorough investigation of this error revealed that it is related to a single landslide event occurred in a S2 spot of the alert zone A3, in a day when the warning system state was in R1 mode, thus providing a H1 (low hazard) matrix output. In this case, both the rainfall threshold system and the susceptibility map underestimated the hazard: the former because no threshold was overcome, the latter because probably some anthropic predisposing factor were not take into account properly (indeed, the landslides occurred close to a mountain road and to a drainage system, which both could have favored the triggering mechanism). This was the only circumstance for which the proposed hazard assessment could not encompass properly the inherent uncertainty of the two original models that were combined into the matrix, but it is a flaw within the error limits imposed by the calibration and optimization procedure explained in section Hazard Assessment.

CONCLUSION

We propose a dynamic landslide hazard assessment procedure based on the combination of rainfall thresholds and susceptibility maps. Inside each alert zone, the dynamic but spatially constant input provided by a warning system based on rainfall thresholds is combined with the spatially variable but static input provided by a susceptibility map into a matrix defining five possible hazard levels.

The proposed hazard classification scheme underwent a calibration procedure against a large landslide dataset, counting 1,761 landslides, to ensure a good constraint between hazard classification and experimental data. This allowed minimizing the number of landslide occurrences in the lowest hazard classes and to provide an interpretation of the hazard classes. A validation procedure was performed against an independent dataset simulating an operational employ of the dynamic hazard assessment through a 16 months period. The validation provided encouraging results, as 38 landslides out of 39 would have been associated to a consistent hazard level.

The proposed procedure could be easily applied to early warning systems based on rainfall thresholds bringing two main advantages: a consistent refinement of the spatial resolution of the forecasts and a robust tool to assist hazard and risk management and spatial-temporal forecasting of rainfall induced landslides at regional scale.

AUTHOR CONTRIBUTIONS

SS has written the manuscript, conceived the work and assisted the data interpretation. VT has conceived the work and she has provided a specific contribution to the methodological part with special reference to the susceptibility assessment. AR has contributed to the rainfall thresholds assessment and to the data elaboration. FC and NC have supervised the work.

ACKNOWLEDGMENTS

This research has been performed in the framework of the project SARnet, funded by the Italian Department of Civil Protection, Presidency of the Council of Ministers.

REFERENCES

Aleotti, P., and Chowdhury, R. (1999). Landslide hazard assessment: summary, review and new perspectives. *Bull. Eng. Geol. Environ*. 58, 21–44. doi: 10.1007/s100640050066

Atkinson, P. M., and Massari, R. (1998). Generalized linear modeling of susceptibility to landsliding in the central Apennines, Italy, *Comput. Geosci*. 24, 373–385. doi: 10.1016/S0098-3004(97)00117-9

Baeza, C., and Corominas, J. (1996). "Assessment of shallow landslide susceptibility by means of statistical techniques," in *Proceedings of the Seventh International Symposium on Landslides,* ed K. Senneset (A.A. Balkema: Trondheim), 147–152.

Battistini, A., Rosi, A., Segoni, S., Lagomarsino, D., Catani, F., and Casagli, N. (2017). Validation of landslide hazard models using a semantic engine on online news. *Appl. Geogr*. 82, 59–65. doi: 10.1016/j.apgeog.2017.03.003

Battistini, A., Segoni, S., Manzo, G., Catani, F., and Casagli, N. (2013). Web data mining for automatic inventory of geohazards at national scale. *Appl. Geogr*. 43, 147–158. doi: 10.1016/j.apgeog.2013.06.012

Baum, R., Coe, J., Godt, J., Harp, E., Reid, M., Savage, W., et al. (2005). Regional landslide-hazard assessment for Seattle, Washington, USA. *Landslides* 2, 266–279. doi: 10.1007/s10346-005-0023-y

Bianchi, F., and Catani, F. (2002). "Landscape dynamics risk management in Northern Apennines (ITALY)," in *Development and Application of Computer Techniques to Environmental Studies, Development and Application of Computer Techniques to Environmental Studies*, eds F. Bianchi, F. Catani, C. A. Brebbia, and P. Zannetti (Southampton: WIT Press), 319–328.

Breiman, L. (2001). Random forests. *Mach. Learn.* 45, 5–32. doi: 10.1023/A:1010933404324

Brenning, A. (2005). Spatial prediction models for landslide hazards: review, comparison and evaluation. *Nat. Haz. Earth Syst. Sci.* 5, 853–862. doi: 10.5194/nhess-5-853-2005

Carrara, A. (1983). Multivariate methods for landslide hazard evaluation. *Math. Geol*. 15, 403–426. doi: 10.1007/BF01031290

Catani, F., Casagli, N., Ermini, L., Righini, G., and Menduni, G. (2005). Landslide hazard and risk mapping at catchment scale in the Arno river basin. *Landslides* 2, 329–342. doi: 10.1007/s10346-005-0021-0

Catani, F., Lagomarsino, D., Segoni, S., and Tofani, V. (2013). Landslide susceptibility estimation by random forests technique: sensitivity and scaling issues. *Natl. Haz. Earth Syst. Sci.* 13, 2815–2831. doi: 10.5194/nhess-13-2815-2013

Chung, C. F., and Fabbri, A. G. (1995). "Multivariate regression analysis for landslide hazard zonation," in *Geographical Information Systems in Assessing Natural Hazards*, eds A. Carrara and F. Guzzetti (Dordrecht: Kluwer Academic), 107–142.

Corominas, J., van Westen, C., Frattini, P., Cascini, L., Malet, J., Fotopoulou, S., et al. (2013). Recommendations for the quantitative analysis of landslide risk. *Bull. Eng. Geol. Environ.* 73, 209–263. doi: 10.1007/s10064-013-0538-8

Crosta, G. B., and Frattini, P. (2003). Distributed modelling of shallow landslides triggered by intense rainfall. *Nat. Hazards Earth Syst. Sci*. 3, 81–93. doi: 10.5194/nhess-3-81-2003

Ermini, L., Catani, F., and Casagli, N. (2005). Artificial neural networks applied to landslide susceptibility Assessment. *Geomorphology* 66, 327–343. doi: 10.1016/j.geomorph.2004.09.025

Fell, R., Corominas, J., Bonnard, C., Cascini, L., Leroi, E., and Savage, W. Z. (2008). Guidelines for landslide susceptibility, hazard and risk zoning for land use planning. *Eng. Geol.* 102, 85–98. doi: 10.1016/j.enggeo.2008.03.022

Godt, J. W., Baum, R. L., Savage, W. Z., Salciarini, D., Schulz, W. H., and Harp, E. L. (2008). Transient deterministic shallow landside modelling: requirements for susceptibility and hazard assessment in a GIS framework. *Eng. Geol.* 102, 214–226. doi: 10.1016/j.enggeo.2008.03.019

Guzzetti, F., Peruccacci, S., Rossi, M., and Stark, C. P. (2008). The rainfall intensity–duration control of shallow landslides and debris flows: an update. *Landslides* 5, 3–17. doi: 10.1007/s10346-007-0112-1

Hong, Y., and Adler, R. F. (2008). Predicting global landslide spatiotemporal distribution: integrating landslide susceptibility zoning techniques and real-time satellite rainfall estimates. *Int. J. Sediment Res.* 23, 249–257. doi: 10.1016/S1001-6279(08)60022-0

Hosmer, D. W., and Lemeshow, S. (2000). *Applied Logistic Regression*. New York, NY: John Wiley and Sons.

Iverson, R. (2000). Landslide triggering by rain infiltration. *Water Resour. Res*. 36, 1897–1910. doi: 10.1029/2000WR900090

Jemec Auflič, M., Šinigoj, J., Krivic, M., Podboj, M., Peternel, T., and Komac, M. (2016). Landslide prediction system for rainfall induced landslides in Slovenia (Masprem). *Geologija* 59, 259–271. doi: 10.5474/geologija.2016.016

Kanungo, D. P., Arora, M. K., Sarkar, S., and Gupta, R. P. (2006). A comparative study of conventional, ANN black box, fuzzy and combined neural and fuzzy weighting procedures for landslide susceptibility zonation in Darjeeling Himalayas. *Eng. Geol*. 85, 347–366. doi: 10.1016/j.enggeo.2006.03.004

Lagomarsino, D., Tofani, V., Segoni, S., Catani, F., and Casagli, N. (2017). A tool for classification and regression using random forest methodology: applications to landslide susceptibility mapping and soil thickness modeling. *Environ. Model. Assess*. 22, 201–214. doi: 10.1007/s10666-016-9538-y

Lee, E. M., Brunsden, D., and Sellwood, M. (2000). "Quantitative risk assess- ment of coastal landslide problems," in *Landslides in Research Theory and Practice: Eighth International Symposium on Landslides,* eds E. Bromhead, N. Dixon, and M-L. Ibsen (London: Thomas Telford), 2, 899–904.

Lee, S. (2005). Application of logistic regression model and its validation for landslide susceptibility mapping using GIS and remote sensing data. *Int. J. Remote Sens*. 26, 1477–1491. doi: 10.1080/01431160412331331012

Lee, S., Choi, J., and Min, K. (2004). Probabilistic landslide hazard mapping using GIS and remote sensing data at Boun, Korea. *Int. J. Remote Sens*. 25, 2037–2052. doi: 10.1080/01431160310001618734

Lee, S., Ryu, J. H., Lee, M. J., and Won, J. S. (2003). Use of an artificial neural network for analysis of the susceptibility to landslides at Boun, Korea. *Environ. Geol*. 44, 820–833. doi: 10.1007/s00254-003-0825-y

Lu, P., Casagli, N., Catani, F., and Tofani, V. (2012). Persistent scatterers interferometry hotspot and cluster analysis (PSI-HCA) for detection of extremely slow-moving landslides. *Int. J. Remote Sens.* 33, 466–489. doi: 10.1080/01431161.2010.536185

Manzo, G., Tofani, V., Segoni, S., Battistini, A., and Catani, F. (2013). GIS techniques for regional-scale landslide susceptibility assessment: the Sicily (Italy) case study. *Int. J. Geogr. Inform. Sci.* 27, 1433–1452. doi: 10.1080/13658816.2012.693614

Mercogliano, P., Segoni, S., Rossi, G., Sikorsky, B., Tofani, V., Schiano, P., et al. (2013). Brief communication: a prototype forecasting chain for rainfall induced shallow landslides. *Nat. Hazards Earth Syst. Sci.* 13, 771–777. doi: 10.5194/nhess-13-771-2013

Montgomery, D. R., and Dietrich, W. E. (1994). A physically based model for the topographic control on shallow landsliding. *Water Resour. Res.* 30, 1153–1171. doi: 10.1029/93WR02979

Pack, R., Tarboton, D., and Goodwin, C. (1998). "The sinmap approach to terrain stability mapping," in *8th Congress of the International Association of Engineering Geology,* eds D. Moore and O. Hungr (Vancouver, BC).

Pourghasemi, H. R., and Kerle, N. (2016). Random forests and evidential belief function-based landslide susceptibility assessment in western Mazandaran province, Iran. *Environ. Earth Sci.* 75:185. doi: 10.1007/s12665-015-4950-1

Rosi, A., Agostini, A., Tofani, V., and Casagli, N. (2014). A procedure to map subsidence at the regional scale using the persistent scatterer interferometry (PSI) technique. *Remote Sens*. 6, 10510–10522. doi: 10.3390/rs61110510

Rosi, A., Lagomarsino, D., Rossi, G., Segoni, S., Battistini, A., and Casagli, N. (2015). Updating EWS rainfall thresholds for the triggering of landslides. *Nat. Hazards* 78, 297–308. doi: 10.1007/s11069-015-1717-7

Rosi, A., Segoni, S., Catani, F., and Casagli, N. (2012). Statistical and environmental analyses for the definition of a regional rainfall thresholds system for landslide triggering in Tuscany (Italy). *J. Geogr. Sci.* 22, 617–629. doi: 10.1007/s11442-012-0951-0

Rosi, A., Tofani, V., Tanteri, L., Stefanelli, C. T., Agostini, A., Catani, F., et al. (2018). The new landslide inventory of Tuscany (Italy) updated with PS-InSAR: geomorphological features and landslide distribution. *Landslides* 15, 5–19. doi: 10.1007/s10346-017-0861-4

Rossi, G., Catani, F., Leoni, L., Segoni, S., and Tofani, V. (2013). HIRESSS: a physically based slope stability simulator for HPC applications. *Nat. Hazards Earth Syst. Sci*. 13, 151–166. doi: 10.5194/nhess-13-151-2013

Segoni, S., Battistini, A., Rossi, G., Rosi, A., Lagomarsino, D., Catani, F., et al. (2015a). Technical note: an operational landslide early warning system at

regional scale based on space–time-variable rainfall thresholds. *Natl. Hazards Earth Syst. Sci.* 15, 853–861. doi: 10.5194/nhess-15-853-2015

Segoni, S., Lagomarsino, D., Fanti, R., Moretti, S., and Casagli, N. (2015b). Integration of rainfall thresholds and susceptibility maps in the Emilia Romagna (Italy) regional-scale landslide warning system. *Landslides* 12, 773–785. doi: 10.1007/s10346-014-0502-0

Segoni, S., Piciullo, L., and Gariano, S. L. (2018). A review of the recent literature on rainfall thresholds for landslide occurrence. *Landslides* 1–19. doi: 10.1007/s10346-018-0966-4

Segoni, S., Rossi, G., Rosi, A., and Catani, F. (2014a). Landslides triggered by rainfall: a semiautomated procedure to define consistent intensity-duration thresholds. *Comput. Geosci.* 3063, 123–131. doi: 10.1016/j.cageo.2013.10.009

Segoni, S., Rosi, A., Rossi, G., Catani, F., and Casagli, N. (2014b). Analysing the relationship between rainfalls and landslides to define a mosaic of triggering thresholds for regional-scale warning systems. *Nat. Hazards Earth Syst. Sci.* 14, 2637–2648. doi: 10.5194/nhess-14-2637-2014

Segoni, S., Tofani, V., Lagomarsino, D., and Moretti, S. (2016). Landslide susceptibility of the Prato–Pistoia–Lucca provinces, Tuscany, Italy. *J. Maps* 12, 401–406. doi: 10.1080/17445647.2016.1233463

Tofani, V., Bicocchi, G., Rossi, G., Segoni, S., D'Ambrosio, M., Casagli, N., et al. (2017). Soil characterization for shallow landslides 390 modeling: a case study in the Northern Apennines (Central Italy). *Landslides* 14, 755–770. doi: 10.1007/s10346-017-0809-8

Tofani, V., Dapporto, S., Vannocci, P., and Casagli, N. (2006). Infiltration, seepage and slope instability mechanisms during the 20–21 November 2000 rainstorm in Tuscany, central Italy. *Nat. Hazards Earth Syst. Sci.* 6, 1025–1033. doi: 10.5194/nhess-6-1025-2006

Trigila, A., Casagli, N., Catani, F., Crosta, G., Esposito, C., Frattini, P., et al. (2013). "Landslide susceptibility mapping at national scale: the Italian case study," in *Landslide Science and Practice*, *Vol. 1: Landslide Inventory and Susceptibility and Hazard Zoning*, eds C. Margottini, P. Canuti and K. Sassa (Rome: Springer), 287–295.

Trigila, A., Iadanza, C., and Spizzichino, D. (2010). Quality assessment of the Italian landslide inventory using GIS processing. *Landslides* 7, 455–470. doi: 10.1007/s10346-010-0213-0

Vai, G. B., and Martini, I. P. (2001). *Anatomy of an Orogen (2001). The Appennines and adjacent Mediterranean Basins*. Dortdrecht; Boston; London: Kluver Academic Publishers.

Vorpahl, P., Elsenbeer, H., Märker, M., and Schröder, B. (2012). How can statistical models help to determine driving factors of landslides? *Ecol. Model.* 239, 27–39. doi: 10.1016/j.ecolmodel.2011.12.007

Wong, H. N. (2005). "Landslide risk assessment for individual facilities— state of the art report," in *Proceedings of the International Conference on Land- slide Risk Management,* eds O. Hungr, R. Fell, R. Couture, and E. Eberhardt (London: Taylor & Francis), 237–296.

Yilmaz, I. (2009). Landslide susceptibility mapping using frequency ratio, logistic regression, artificial neural networks and their comparison: a case study from Kat landslides (Tokat-Turkey). *Comput. Geosci.* 35, 1125–1138. doi: 10.1016/j.cageo.2008.08.007

Yilmaz, I. (2010). Comparison of landslide susceptibility mapping methodologies for Koyulhisar, Turkey: conditional probability, logistic regression, artificial neural networks, and support vector machine. *Environ. Earth Sci.* 61, 821–836. doi: 10.1007/s12665-009-0394-9

Youssef, A. M., Pourghasemi, H. R., Pourtaghi, Z. S., and Al-Katheeri, M. M. (2016). Landslide susceptibility mapping using random forest, boosted regression tree, classification and regression tree, and general linear models and comparison of their performance at wadi tayyah basin. Asir Region, Saudi Arabia. *Landslides.* 13, 839–856. doi: 10.1007/s10346-015-0614-1

Conflict of Interest Statement: The authors declare that the research was conducted in the absence of any commercial or financial relationships that could be construed as a potential conflict of interest.

frontiers in Earth Science

ORIGINAL RESEARCH
published: 03 September 2018
doi: 10.3389/feart.2018.00134

The Weather Radar Observations Applied to Shallow Landslides Prediction: A Case Study From North-Western Italy

Roberto Cremonini and Davide Tiranti*

Department of Natural and Environmental Risks, Regional Agency for Environmental Protection of Piemonte, Turin, Italy

In northern Italy rainfall-triggered shallow landslides are recurrent hazardous phenomena that cause casualties and extensive damages. In the last decades several early warning systems (EWSs) have been developed based on rainfall intensity–event duration (I-D) thresholds derived by long rain gages time series. However, rain gages density and their representativeness limit reliability of such EWSs. In the past decades, several studies explored successfully the usefulness of reliable quantitative precipitation estimates (QPEs) by weather radar. The availability of high spatial and temporal resolution QPEs with short latency of the data makes those observations appealing as input data to automatic EWSs. Nevertheless, weather radar based QPEs can be affected by several sources of errors and uncertainties (miscalibration, partial beam blocking, overhanging precipitation, and so on). Analyzing the heavy precipitations that hit Piemonte, north-western Italy, on November 2016, causing floods and triggering widespread shallow landslides, this work presents a fruitful case study of operational weather radar application in shallow landslides early warning system.

Keywords: slope processes, early warning system, QPE, remote sensing, heavy rainfall

OPEN ACCESS

Edited by:
Steven L. Forman,
Baylor University, United States

Reviewed by:
Stefano Luigi Gariano,
Istituto di Ricerca per la Protezione Idrogeologica (IRPI), Italy
Milad Janalipour,
K. N. Toosi University of Technology, Iran
Samuele Segoni,
Università degli Studi di Firenze, Italy

****Correspondence:***
Roberto Cremonini
r.cremonini@arpa.piemonte.it

Specialty section:
This article was submitted to Quaternary Science, Geomorphology and Paleoenvironment, a section of the journal Frontiers in Earth Science

Received: *16 March 2018*
Accepted: *17 August 2018*
Published: *03 September 2018*

Citation:
Cremonini R and Tiranti D (2018) The Weather Radar Observations Applied to Shallow Landslides Prediction: A Case Study From North-Western Italy. Front. Earth Sci. 6:134. doi: 10.3389/feart.2018.00134

INTRODUCTION

Shallow landslide early warning systems are normally implemented using rain gage network recording as input for rainfall values (Aleotti, 2004; Bosco et al., 2007; Guzzetti et al., 2007; Brunetti et al., 2010; Capparelli and Tiranti, 2010; Tiranti and Rabuffetti, 2010; Mercogliano et al., 2013; Rosi et al., 2015; Segoni et al., 2015, 2018; Devoli et al., 2018).

In the last decade, several researches focused on weather radar applications finalized to shallow landslide EWSs development (Chang et al., 2008; Chiang and Chang, 2009; Baum and Godt, 2010; Saito et al., 2010; Winter et al., 2010; Calvello et al., 2015; Jan and Chen, 2015; Nikolopoulos et al., 2015; Marra et al., 2016). In fact, the small size of the initiation catchments of debris flows, also caused by shallow landslides contribution, makes spatial resolution of observed precipitation the most relevant factor (Marra et al., 2017). Availability of high resolution observation of rainfall fields is thus mandatory in threshold-based EWSs. Especially in case of convective and localized precipitations, weather radar quantitative estimation of precipitations can overcome the poor representativeness of ground measurements, due to low density and geometry of the gage networks (Morrissey et al., 1995). Moreover, huge ground weather station networks may have longer latency of the data due to longer data transmission time. Weather radar typically scan the atmosphere close

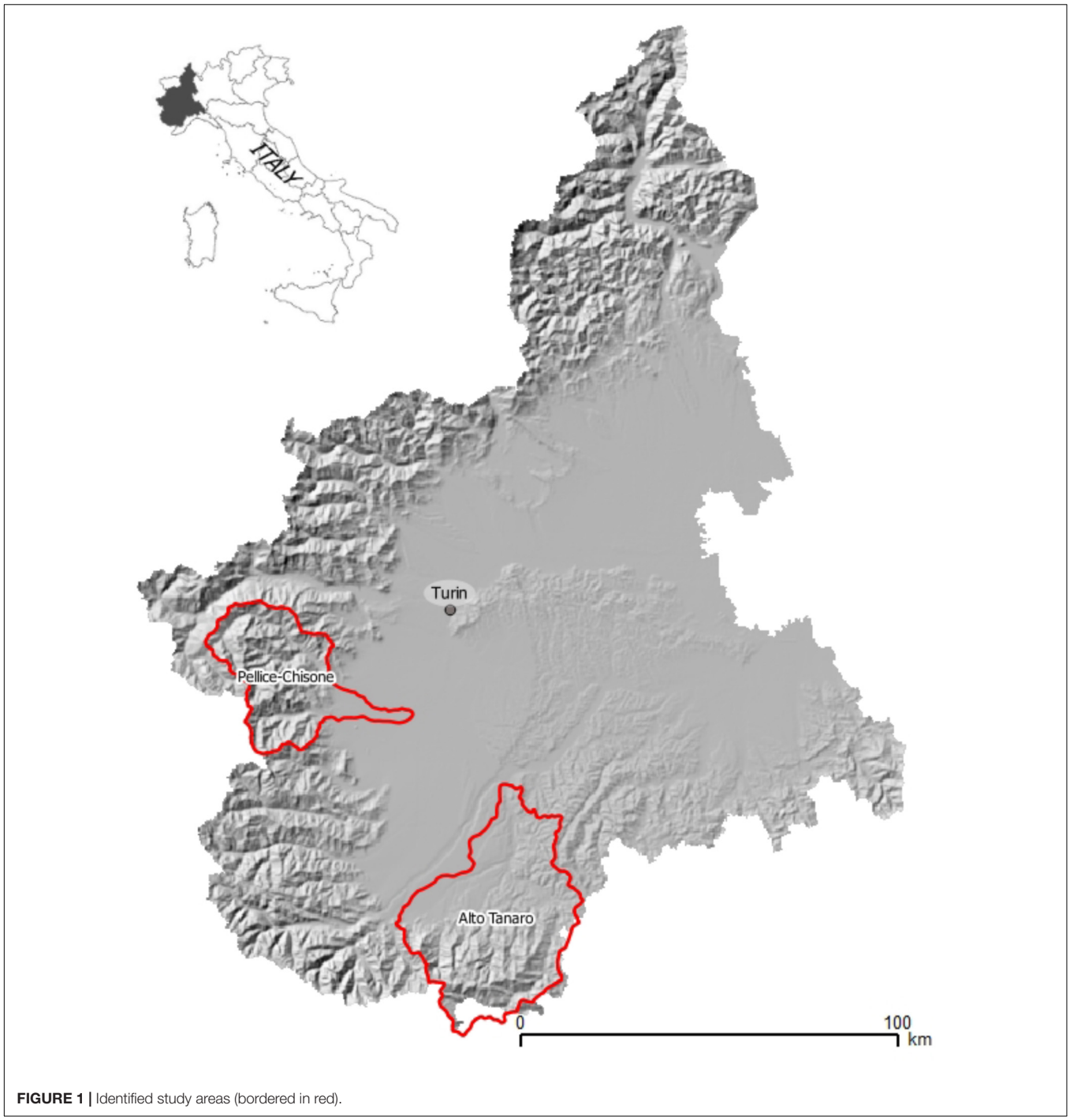

FIGURE 1 | Identified study areas (bordered in red).

to the ground up to 150 km, with 1-km resolution or less, within few minutes. Both data resolution and short delay in data availability increase effectiveness of EWSs based weather radar.

Weather radar is thus successfully used in the real-time observations of rainfall triggering values for slope phenomena caused by short-duration and intense rainfalls, such as channelized debris flows (Borga et al., 1998; Tiranti et al., 2008, 2014; Marra et al., 2014; Berenguer et al., 2015); in fact, the distinguishing features of rainstorms are easier detected and characterized by weather radar than by rain gages. However, weather radar based QPEs in complex orography are affected by several errors and uncertainties residual clutter, partial beam blocking, rain-induced attenuation, variability of drop size distribution (DSD) and wet radome. Montopoli et al. (2017) provide a comprehensive review of limiting factors in QPEs in complex orography by ground weather radar. Due to nonuniform spatial distribution of errors, reliability of weather radar based EWSs in impervious areas or data quality of long-duration

triggering rainfalls must be carefully evaluated. This paper discusses a successful operational implementation of weather radar utilization in shallow landslides EWSs in Piemonte. The areas examined in this study have good weather radar coverage and the performing weather radar data elaborating chain guarantees errors and uncertainties reduction in QPEs.

On November 2016, heavy rainfalls hit Piemonte in north-western Italy and triggered shallow landslides widely, mainly in the Alps. To estimate the rainfall parameters that triggered shallow landslides, rainfall-fields derived by weather radars observations merged with dense rain gage network data have been used. Based on higher number of shallow landslides occurred during the rainfall events, two study areas have been selected: the Pellice and Chisone Valleys and the Alto Tanaro catchments (**Figure 1**).

MATERIALS AND METHODS

The Operational Weather Radar in Piemonte

Arpa Piemonte (the Regional Agency for Environmental Protection of Piemonte) operates two polarimetric Doppler C-band weather radar, located on the hill nearby Turin (Piemonte), installed on 1998, and in the Apennines near Savona (Liguria) installed on 2000. **Table 1** summarizes the main characteristics of the weather radars.

TABLE 1 | Main characteristics of the weather radar used in this study.

	Bric della croce (piemonte)	Monte settepani (liguria)
Site coordinates (deg)	7.733E, 45.034N	8.197E, 44.246N
Altitude (m. a.s.l.)	773	1385
Polarization type	simultaneous H and V	simultaneous H and V
Antenna type	central feed	central feed
Antenna diameter (m)	4.2	4.2
Beam width (deg)	0.94	0.94
Radome type	sandwich	sandwich
Radome losses (dB)	max 0.2, one way	max 0.2, one way
Transmitter type	magnetron	magnetron
Frequency (GHz)	5.640	5.625
Peak power (kW)	250	>450
Pulse width (μs)	0.5, 1.0	0.5, 1.5, 3.0
Pulse repetition frequency (Hz)	300–1200	300–1200
Range resolution (m)	340 (4 average samples)	500 (8 average samples)

Bric della Croce and Monte Settepani radars complete polarimetric volume scans, 170 km range, every 5 min, with, respectively, 11 and 8 elevations. Given the good visibility southward, Monte Settepani operates every 5 min an additional volume scan 250 km range by single polarization, composed of two elevations. A semisupervised robust hydrometeor classification is performed on polarimetric raw volumes (Bechini and Chandrasekar, 2015) to identify clutter, anaprop, attenuation, and meteorological echoes. Finally, completely free lowest beams are used to derive the product of surface rainfall intensity (SRI), according to beam visibility. During winter season, the radar reflectivity is later corrected for vertical profile reflectivity (VPR) according to Koistinen (1991). Single radar SRIs are merged in a 800 m resolution composite considering maximum reflectivity, where more than one weather radar observation is available. Additional weather radar data are merged to Piemonte composite, including the polarimetric weather radar in Monte Lema (Swiss) operated by MeteoSwiss, and weather radar in Carpiano (Italy) operated by the National Flight Assistance Company (ENAV).

Finally, composite radar reflectivity is converted in instantaneous rainfall intensity (mm/h) according to the well-known *Z-R* relationship:

$$Z = arR^b \tag{1}$$

where Z is the linear weather radar reflectivity expressed in mm/m^3, R is rainfall intensity in mm/h and a = 300 and b = 1.5 are coefficients experimentally derived (Joss and Waldvogel, 1990). Further details on the operational weather radar operated by ARPA Piemonte can be found in Davini et al. (2011) and in Cremonini and Bechini (2010). Daily rainfall accumulations are corrected with tipping-bucket quality-controlled rain gage measurements by radar-gages assessment factors (Goudenhoofdt and Delobbe, 2009). On daily basis, the 24-h weather radar quantitative precipitation estimation (QPE) is compared with rain gages observations and for each ground weather station the following ratio is derived:

$$AF_{x,y} = 10 * log10\left(R_{x,y}/G_{x,y}\right) \tag{2}$$

where $R_{x,y}$ is the 24-h rainfall accumulation QPE co-located with the raingauge ($G_{x,y}$) placed at x,y coordinates. Only precipitation accumulations greater than 1.0 mm are considered and the outliers are also excluded and flagged as suspect ratios because they can be due to mechanical failure of raingauge or too large errors in weather radar QPE. Point assessment factors (AFs) are interpolated on the same weather radar composite grid using Ordinary Kriging method (Li and Heap, 2014) to derive the adjustment field. Finally, hourly weather radar QPEs are multiplied by assessment factor field to obtain the best unbiased hourly rainfall estimation.

Figure 2 shows the weather radar coverage in north-western Italy: stars indicate weather radar sites, circles the radar coverage and red polylines the two study basins of Pellice-Chisone and Alto Tanaro. Theoretical visibility maps, derived in standards propagation atmosphere, demonstrate that Piemonte, Lema and Carpiano weather radar have good visibility over target areas, being first completely free radar beams very close to the ground.

The Shallow Landslides EWS

On 2006, Tiranti and Rabuffetti (2010) developed a shallow landslide triggering model named "*Shallow landslides Movements Announced through Rainfall Thresholds*" (SMART) based on I-D empirical rainfall thresholds derived by statistical analysis on historical shallow landslides occurred in Piemonte from 1990

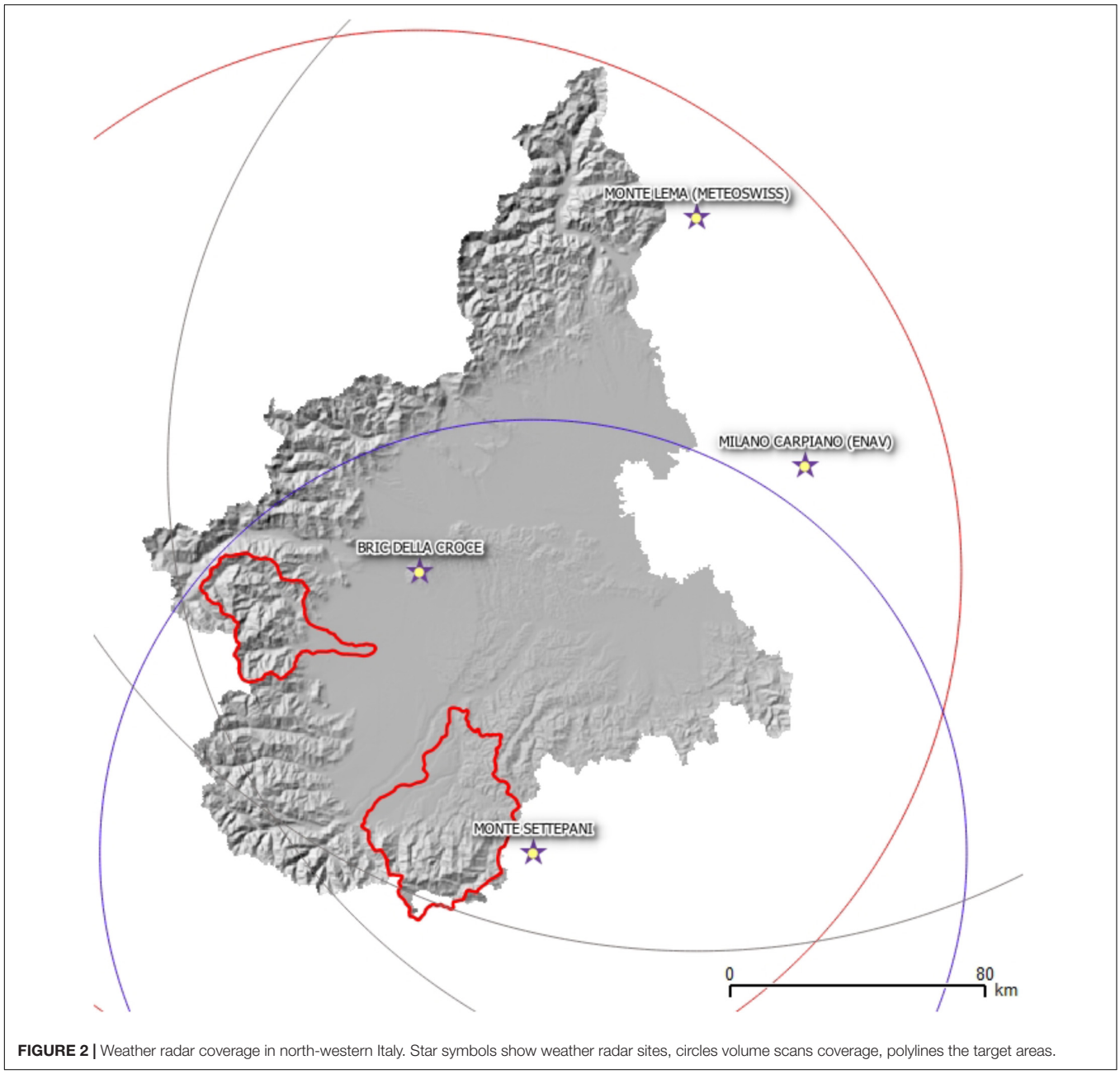

FIGURE 2 | Weather radar coverage in north-western Italy. Star symbols show weather radar sites, circles volume scans coverage, polylines the target areas.

to 2006. SMART operates since 2008 both in forecast and monitoring modes and it is part of the regional warning system for natural hazards.

For shallow landslides, SMART recognizes two homogeneous areas (**Figure 3**), characterized by two different empirical thresholds (Equations 3 and 4) for two different environments (respectively, Alpine-Appennine and hylls), and defined on rainfall accumulation longer than 12 h. For shorter durations other slope phenomena can occur like diffused and accelerated soil erosion caused by run-off or channelized debris flows in the Alpine small catchments. Based on expected landslides density three levels of scenarios have been defined: (i) isolated landslides or soil erosion due to run-off; (ii) less than ten landslides per km^2 expected; (iii) more than ten landslides per km^2 expected.

$$Area\,1\,(Alps\,and\,Apennines):\ I = 25\,D^{-0.45} \tag{3}$$

$$Area\,2\,(hills):\ I = 40\,D^{-0.65} \tag{4}$$

where l is the accumulated rainfall on D duration, the numerical coefficients are experimentally derived from statistical analysis of collected historical landslides and as exponent the Montana Coefficients (Boni and Parodi, 2001; Tiranti and Rabuffetti, 2010; Devoli et al., 2018) define rainfall effects according to the altitude.

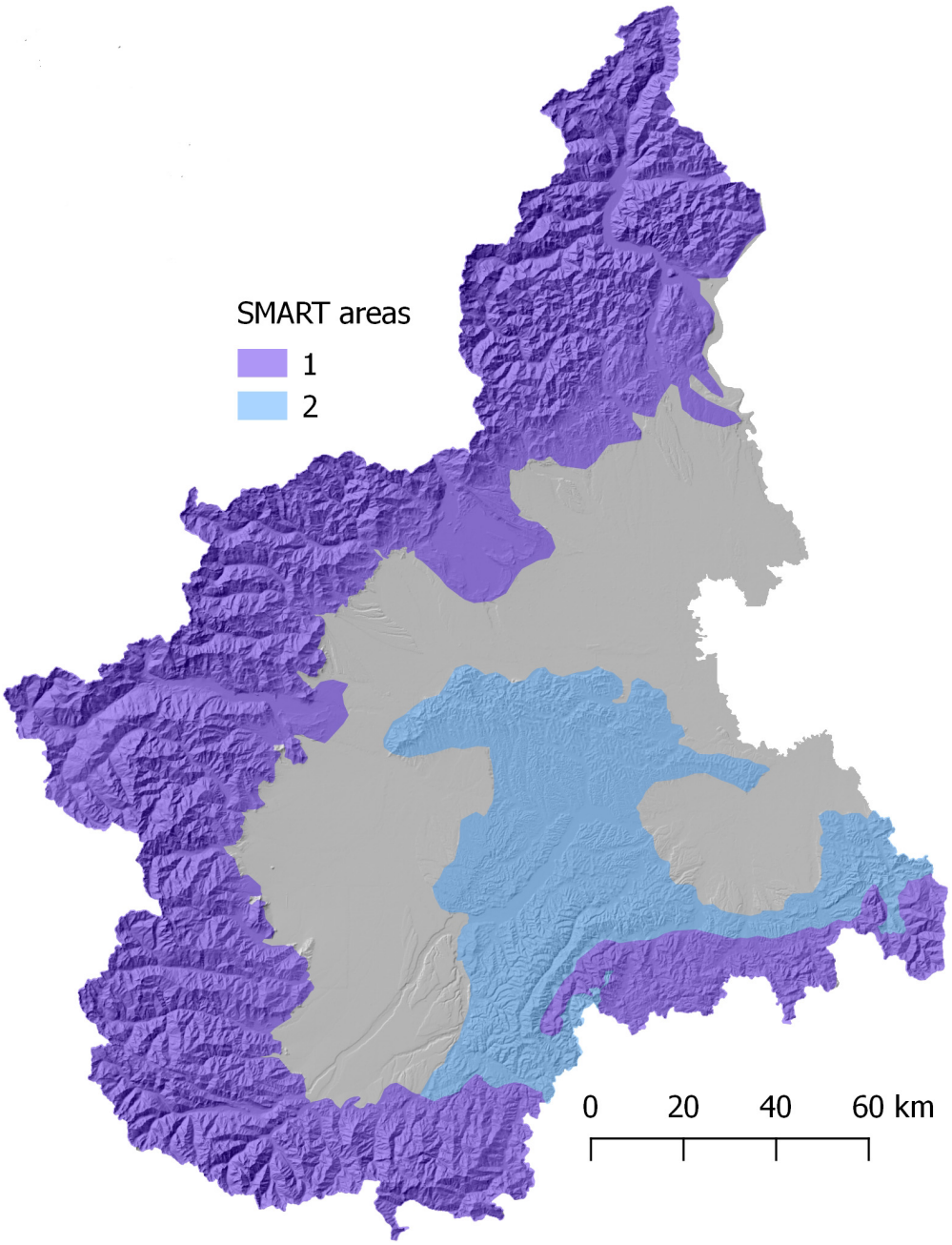

FIGURE 3 | SMART homogeneous areas. Area 1: Alpine and Apennines environments characterized by metamorphic bedrock and high rainfall values to trigger shallow landslides; Area 2: hilly environment characterized by sedimentary bedrock and moderate rainfall values to trigger shallow landslides.

The model rainfall inputs are the quantitative rainfall forecast and observed values by rain gage network, consisting in more than 400 weather stations distributed on about 10 km mesh grid for a total area of 25,402 km^2. Thresholds are linked to each raingauge with an assigned buffer range of 5 km from rain gage centroid. For this reason, shallow landslides triggered at a distance > 5 km from rain gage are characterized by major uncertainty in forecasting. Recently, the weather radar observations have been introduced as new data input of SMART to fill this gap in ground network to identify triggering rainfall.

RESULTS

Synoptic Forcing and Precipitations

From 21st to 25th November 2016, Piemonte was hit by heavy and persistent rainfalls, that have been initially localized in

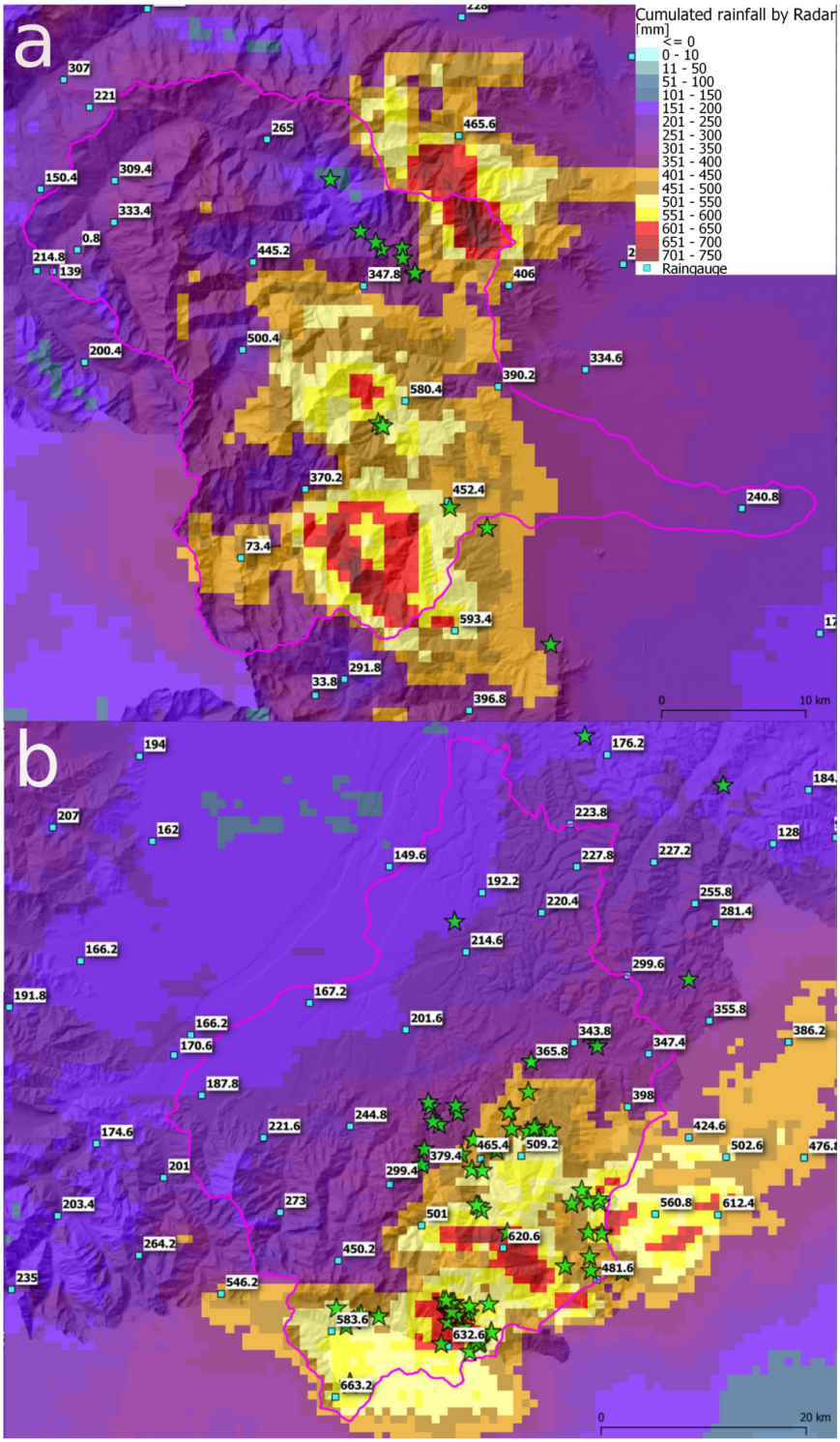

FIGURE 4 | Total rainfall accumulation, estimated by weather radar (grid) and observed by rain gages (values) from 21st to 26th November 2016 in the study areas: **(a)** Pellice-Chisone; **(b)** Alto Tanaro.

the southern areas, closed to the Ligurian Sea and then, they shifted to north-western Piemonte. On 21st November 2016 a deep trough approached western Europe, causing intense and humid south-westerly wind over the region. Low level wind convergence over Ligurian sea and diffuse atmospheric instability caused heavy localized precipitations over Apennines with more

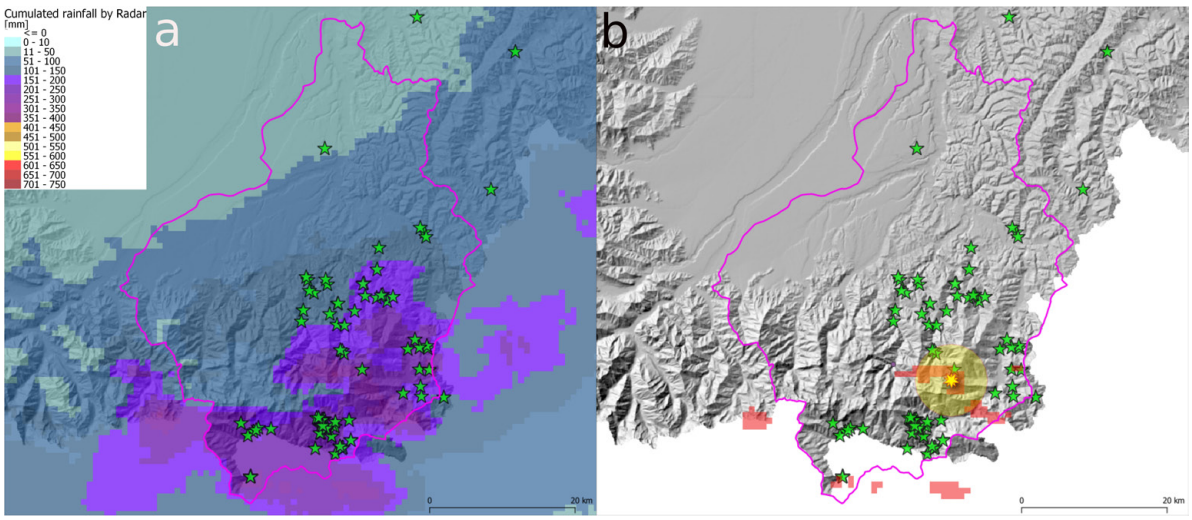

FIGURE 5 | (a) Accumulated rainfall from 23rd November at 21:00 UTC in Alto Tanaro. **(b)** In red, areas interested by precipitations that overpassed thresholds of Equation 3 (critical rainfall accumulations) and rain gages overpassing threshold (yellow asterisks) and related buffers (yellow circles); green star labels indicate occurred landslides.

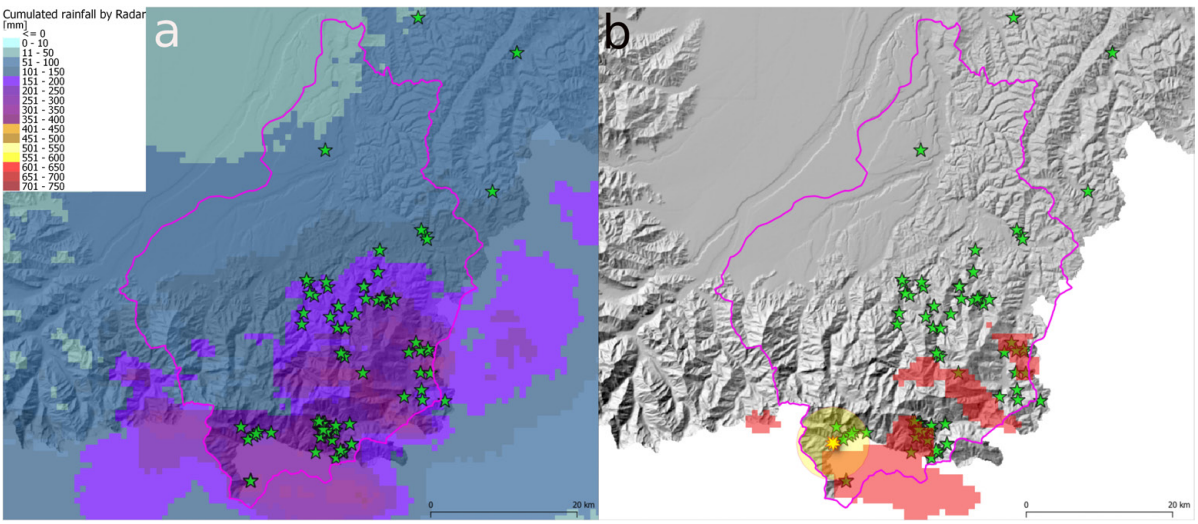

FIGURE 6 | (a) Accumulated rainfall from 24th November at 03:00 UTC in Alto Tanaro. **(b)** In red, areas interested by precipitations that overpassed thresholds of Equation 2 (critical rainfall accumulations) and rain gages overpassing threshold (yellow asterisks) and related buffers (yellow circles); green star labels indicate occurred landslides.

than 250 mm in 24 h. The following day, the low-pressure system isolated (*cut-off*), losing momentum, and becoming stationary over Iberian Peninsula. This atmospheric synoptic circulation caused intense stationary flow from Southeast over Piemonte, with heavy and diffuse precipitations. On 23rd and 24th November, low level flows turned from east, forcing heaviest rainfall in the western area of Piemonte. On 24th November rain gages recorded more than 350 mm in 24 h and, due to warm air advection, the snow level raised up to 2,000 m asl. Finally, on 25th November, the deep pressure system started to dissipate and precipitations over Piemonte progressively reduced. The largest rainfall amount recorded during 5 days was 632.6 mm; this accumulated precipitation corresponds to more than 50% mean annual rainfall in the region. The whole event was characterized by heavy convective rainfall, high spatial variability and peaks of more than 120 mm in 3 h. On 21st November, the snow level was located around 1500–1700 m asl and it increased on the following days, settling up to 1800–2000 m asl. On 24th November new cold air aloft caused a drop in the snow level up to 1400–1600 m asl, locally at lower altitude in the north-western areas of Piemonte. Rivers in the region had large increases in discharge recording maxima up to more than 50–100 years return period. About 150 shallow landslides were triggered, causing wide damages to residential

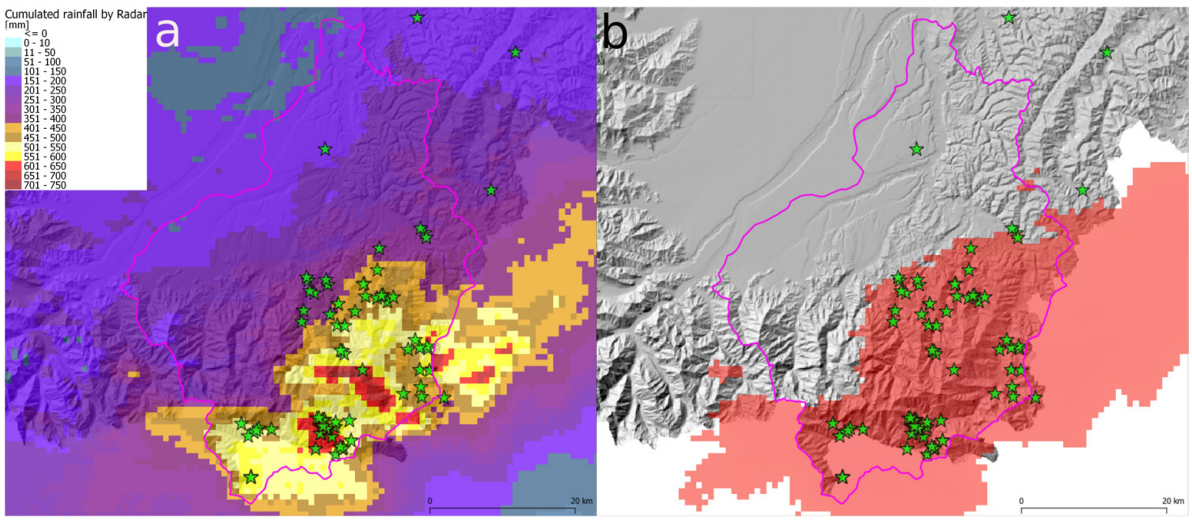

FIGURE 7 | (a) Accumulated rainfall from 24th November at 15:00 UTC in Alto Tanaro. **(b)** In red, areas interested by precipitations that overpassed thresholds of Equation 4 (critical rainfall accumulations); green star labels indicate occurred landslides.

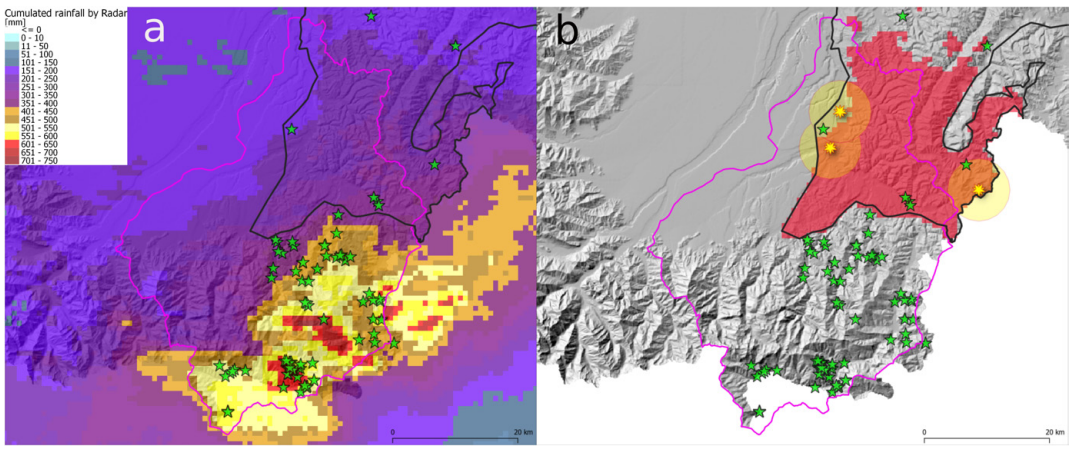

FIGURE 8 | (a) Accumulated rainfall from 25th November at 06:00 UTC over hilly areas (delimited by black contour). **(b)** In red, areas interested by precipitations that overpassed thresholds of Equation 4 (critical rainfall accumulations) and rain gages overpassing threshold (yellow asterisks) and related buffers (yellow circles); green star labels indicate occurred landslides.

buildings and infrastructures. These landslides were reported several days later after ground surveys by local authorities and Civil Protection. Their reports contain information about landslide type, location, reported damages but the triggering datetime of landslides is not available. **Figure 4** shows rainfall accumulation from 21st to 25th November 2016 derived by weather radar observations and adjusted on daily basis with rain gages of meteorological ground network managed by Arpa Piemonte.

Figure 4 demonstrates that the Piemonte raingauge network is not able to accurately describe the spatial variability of convective rainfall peaks, due to low spatial density. In Pellice-Chisone area the maximum rainfall accumulation recorded by rain gages over the whole period was 580.4 mm, meanwhile rainfall estimation by weather radar shows three peaks overpassing 700 mm.

An early warning system based trusting in rain gages observations would have probably failed where rainfall peaks are missed.

Rainfall Triggered Landslides

To evaluate the effectiveness of SMART thresholds in forecasting the triggering time of shallow landslides, the QPEs recorded during the event and derived by weather radar observations have been compared and filtered with the thresholds defined by Equation 3 in the Pellice-Chisone and Alto Tanaro mountain areas, where most landslides occurred (98 reported), and by Equation 4 for the hilly environment of Alto Tanaro (7 reported). It is possible to reconstruct the spatial-temporal evolution of phenomena, locating most prone areas to landslide triggering.

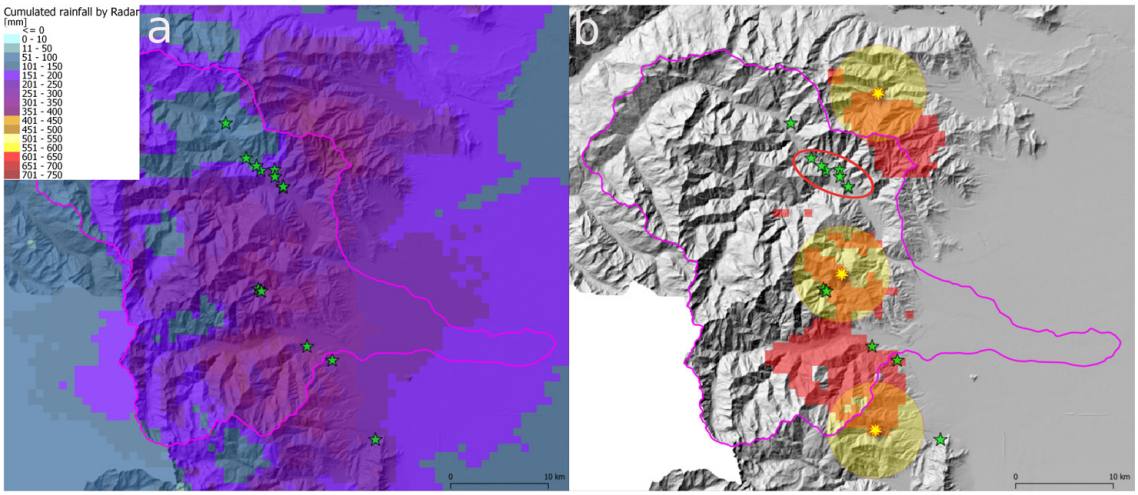

FIGURE 9 | (a) Accumulated rainfall from 24th November at 15:00 UTC in Pellice-Chisone. **(b)** In red, areas interested by precipitations that overpassed thresholds of Equation 3 (critical rainfall accumulations) and rain gages overpassing threshold (yellow asterisks) and related buffers (yellow circles); green star labels indicate occurred landslides; red circle include reported debris flows that reached the alluvial fans' areas generated from shallow landslides triggered at the basins' head and propagated along channel networks.

During night on 23rd November, in Alto Tanaro heavy rainfall started to overpass triggering thresholds. **Figures 5a,b** shows the accumulated rainfall estimated by weather radar from the beginning of event to 23rd November at 21:00 UTC, the green stars show the whole reported landslides after the rainfall event for which the triggering time is unknown. **Figure 5b** reports in red areas where thresholds were overpassed according to Equation 3. The yellow asterisk represents the raingauge that recorded an overpassing.

The critical rainfall interested wider areas in Alto Tanaro basin, causing an increase in landslides occurrence since 24th November 2016 at 03:00 UTC (**Figures 6a,b**). Only one raingauge issued a warning for threshold exceeding.

In the Alto Tanaro, where the higher number of shallow landslides has been recorded, wider area interested by overpassing has been reached on 24th November at 15:00 UTC (**Figures 7a,b**). It is interesting noting that no raingauge recorded threshold exceedance at that time.

Some shallow landslides also occurred in hilly areas of Alto Tanaro. The same approach has been followed, applying the proper equation describing the behavior of intensity according to rainfall duration (Equation 4). **Figure 8** shows that extent of rainfall critical values during the event.

The total number of landslides in this hilly area has been seven but both rain gages and weather radar catched only five of them.

Over Pellice-Chisone the first critical rainfalls were reached on 24th November at 15:00 UTC (**Figures 9a,b**), also interesting the upper part of some catchments, where channelized debris flows were triggered due to the propagation of shallow landslides into channel network and observed in alluvial fans' areas (stars in the red circle in **Figure 9b**). Three rain gages recorded threshold overpassing missing most of landslide sites.

The area of threshold exceeding reached maximum extent on 25th November 2016 at 04:00 UTC, and then rainfall intensities decreased until the end of event. **Figure 10** shows reported landslides, the area of overpassing threshold according to weather radar QPEs, the rain gages and their datetime of overpassing threshold values.

DISCUSSION

Figures 5–9 show the evolution of severe rainfall event that hit Piemonte on November 2016. All shallow landslides in Alto Tanaro's Alpine environment occurred between 400 and 1500 m asl. The four highest shallow landslides (1400–1500 m asl) have been checked with surrounding ground weather stations, assessing that no snow at ground was reported during the whole period. In Pellice-Chisone basin the seven landslides occurred between 500 and 1150 m asl, excluding a snow contribution in the phenomena triggering.

Given weather radar QPEs high spatial resolution (0.64 km^2), the warning system is more effective in landslide triggering detection than the one exclusively based on rain gages. 14 landslides were reported in Pellice-Chisone basin of which 10 have been properly detected by weather radar, while only five ones were detected by rain gages (**Figure 10a**). In Alto Tanaro's Alpine environment, 84 landslides correspond to proper detection by weather radar QPEs, while only 72 landslides were detected by rain gages, mainly due to low rain gages network density (**Figure 10b**). Nevertheless, five rain gages reported threshold exceeding corresponding to false alarms. In the hilly area, just five over seven landslides occurred were correctly detected by both radar QPEs and rain gages: this result suggests that a radar and rain gages integrated approach could have better performances in landslides triggering detection.

On 24th November 2014, temperature dropped and liquid precipitations turn to snowfall above 1200–1400 m asl in

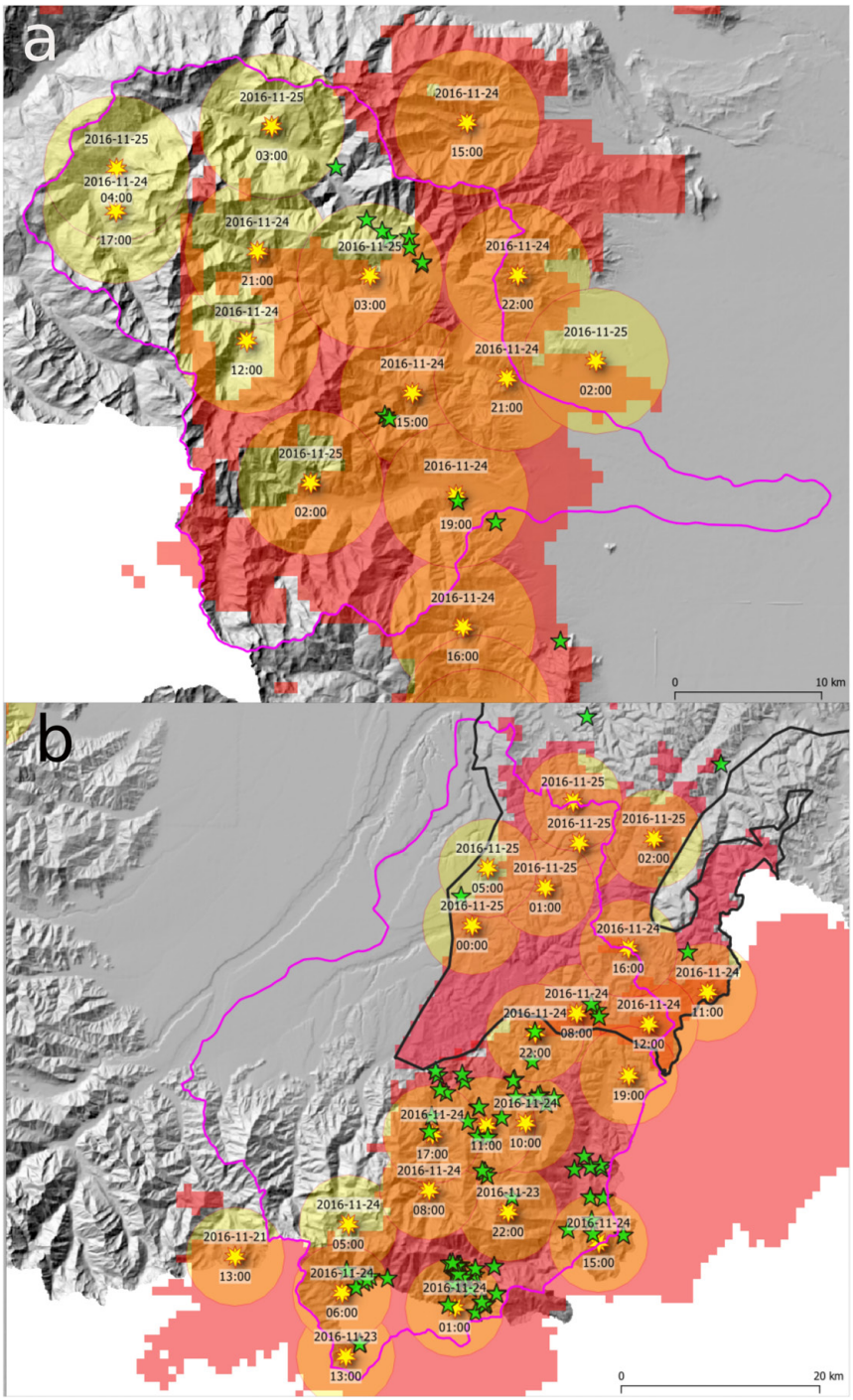

FIGURE 10 | Rainfall accumulation over Pellice-Chisone **(a)** and Alto Tanaro **(b)** basins on 25th November 2016 at 04:00 UTC. In red, areas interested by precipitations that overpassed thresholds of Equation 4 and 4 (Alto Tanaro's hilly environment delimited by black contour) from radar estimation, rain gages overpassing threshold (yellow asterisks) and related buffers (yellow circles) from the start of rainfall event to 25th November at 04:00 UTC; green star labels indicate all the reported landslides.

Pellice-Chisone basin. The following day, a sudden increase in temperature caused a new turn to liquid precipitation and melting of the snow accumulated over rain gages. Weather ground stations named Pragelato, Clot della Soma, Pra Catinat, Praly, and Massello (**Figure 11**) recorded rainfalls exceeding triggering threshold when heavy precipitation occurred but with a significant contribution due to snowmelting over the gage. These conditions determined false alarms in their surrounding

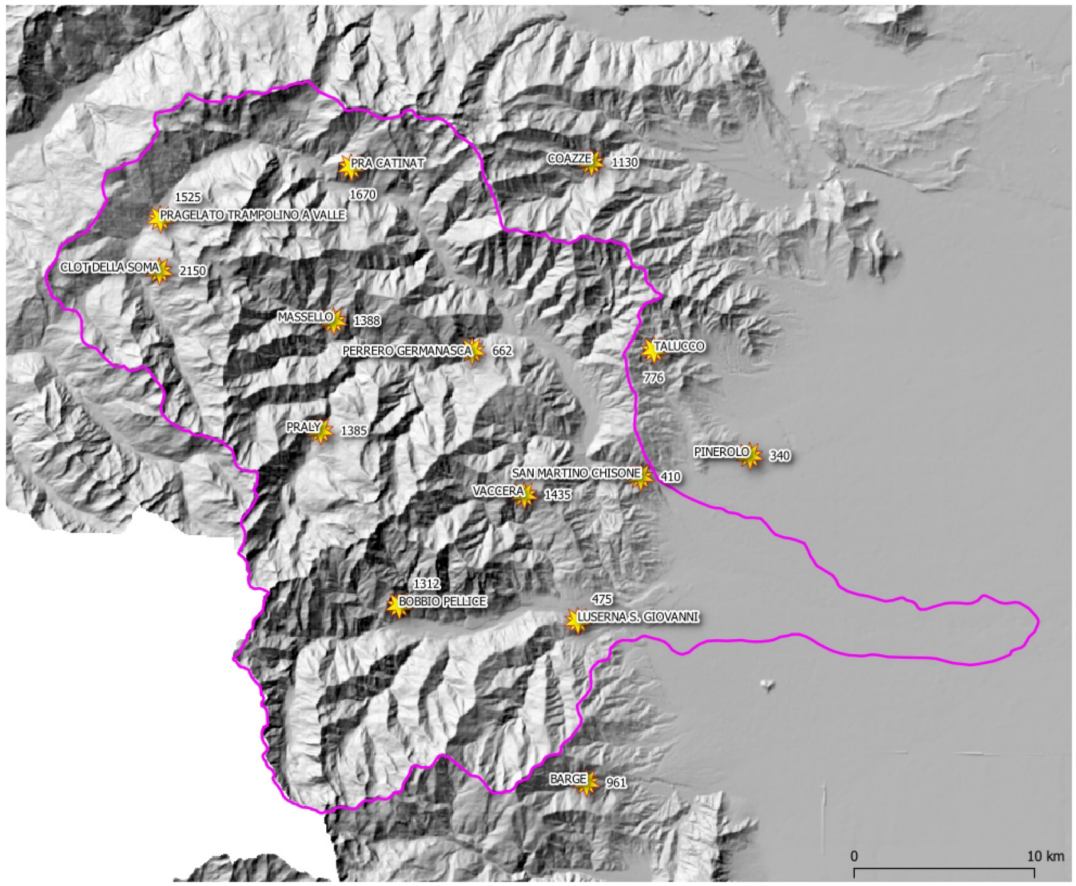

FIGURE 11 | Rain gages elevation distribution in Pellice-Chisone area.

area. It is worth noting that weather radar QPEs provided better estimations of the actual precipitation, correctly identifying that any threshold was not overpassed.

CONCLUSION

Heavy precipitation interested Piemonte (Italy) between 21st and 25th November 2016, causing floods and diffuse shallow landslides in Alto Tanaro and Pellice-Chisone basins. The illustrated case study shows that the operational use of QPEs, derived by merging weather radar observations and quality-controlled rain gages, is more reliable and effective in real-time determining a representative precipitation field responsible for triggering shallow landslides. The availability of QPEs with appropriate spatial and temporal resolution allowed characterizing the initiation of the torrential phenomena (debris flow) occurred in Pellice-Chisone basin by the observation of evolution of critical rainfalls occurred over the head of basins, where the mass transport was located. In Alto Tanaro basin weather radar based QPEs identified correctly the triggered shallow landslides distribution.

Furthermore, the widespread nature of triggers, which occurred during November 2016 heavy rainfalls, confirmed the effectiveness of the pre-announcement model of shallow landslides developed and operated by the Arpa Piemonte. The subsequent use of the distribution of critical rainfall values has finally allowed reconstructing with a good degree of reliability the timing of landslides triggering.

Given a long-time weather radar QPE dataset, a possible next development will be to derive weather radar based I-D thresholds and to compare them with gages-based ones. Although, weather radar based quantitative precipitation forecast (QPF) is not currently implemented into the Arpa Piemonte operational EWS, the real-time forecast of landslides is possible by making use of the time lag between slope failure and rainfall peak, as demonstrated during November 2016 heavy rainfall. A further development will consist in the application of weather radars QPFs to foresee the shallow landslides initiation one or 2 h ahead, improving the effectiveness of warnings.

AUTHOR CONTRIBUTIONS

RC provide weather radar data and analysis and developed algorithm for QPEs. DT developed shallow landslide early warning system.

REFERENCES

Aleotti, P. (2004). A warning system for rainfall-induced shallow failures. *Eng. Geol.* 73, 247–265. doi: 10.1016/j.enggeo.2004.01.007

Baum, R. L., and Godt, J. W. (2010). Early warning of rainfall-induced shallow landslides and debris flows in the USA. *Landslides* 7, 259–272. doi: 10.1007/s10346-009-0177-0

Bechini, R., and Chandrasekar, V. (2015). A semisupervised robust hydrometeor classification method for dual-polarization radar applications. *J. Atmos. Ocean. Technol.* 32, 22–47. doi: 10.1175/JTECH-D-14-00097.1

Berenguer, M., Sempere-Torres, D., and Hürlimann, M. (2015). Debris flow forecasting at regional scale by combining susceptibility mapping and radar rainfall. *Nat. Hazards Earth Syst. Sci.* 15, 587–602. doi: 10.5194/nhess-15-587-2015

Boni, G., and Parodi, A. (2001). Sintesi pluviometrica regionale: realizzazione di un atlante delle piogge intense sulle Alpi franco-italiane. Rapporto Finale, Progetto INTERREG II Italia-Francia. *Azione* 3, 61–80.

Borga, M., Dalla Fontana, G. D., Da Ros, D., and Marchi, L. (1998). Shallow landslide hazard assessment using a physically based model and digital elevation model. *Environ. Geol.* 35, 81–88.

Bosco, F., Campus, S., Mensio, L., Nicolò, G., and Tiranti, D. (2007). "Forecasting landslides -," in *Evaluation and Prevention of Natural Risks*, Vol. 470, eds S. Campus, S. Barbero, S. Bovo, and F. Forlati (Amsterdam: Balkema), 353–390.

Brunetti, M. T., Peruccacci, S., Rossi, M., Luciani, S., Valigi, D., and Guzzetti, F. (2010). Rainfall thresholds for the possible occurrence of landslides in Italy. *Nat. Hazards Earth Syst. Sci.* 10, 447–458. doi: 10.5194/nhess-10-447-2010

Calvello, M., d'Orsi, R. N., Piciullo, L., Paes, N., Magalhaes, M. A., and Lacerda, W. A. (2015). The Rio de Janeiro early warning system for rainfall-induced landslides: analysis of performance for the years 2010–2013. *Int. J. Disast. Risk Reduc.* 12, 3–15. doi: 10.1016/j.ijdrr.2014.10.005

Capparelli, G., and Tiranti, D. (2010). Application of the MoniFLaIR early warning system for rainfall-induced landslides in the Piedmont region (Italy). *Landslides* 7, 401–410. doi: 10.1007/s10346-009-0189-9

Chang, K. T., Chiang, S. H., and Lei, F. (2008). Analysing the relationship between typhoon-triggered landslides and critical rainfall conditions. *Earth Surf. Process. Landf.* 33, 1261–1271. doi: 10.1002/esp.1611

Chiang, S. H., and Chang, K.-T. (2009). Application of radar data to modeling rainfall-induced landslides. *Geomorphology* 103, 299–309. doi: 10.1016/j.geomorph.2008.06.012

Cremonini, R., and Bechini, R. (2010). Heavy rainfall monitoring by polarimetric c-band weather radars. *Water* 2, 838–848. doi: 10.3390/w2040838

Davini, P., Bechini, R., Cremonini, R., and Cassardo, C. (2011). Radar-based analysis of convective storms over Northwestern Italy. *Atmosphere* 3, 33–58. doi: 10.3390/atmos3010033

Devoli, G., Tiranti, D., Cremonini, R., Sund, M., and Bøje, S. (2018). Comparison of landslide forecasting services in Piemonte (Italy) and in Norway, illustrated by events in late spring 2013. *Nat. Hazards Earth Syst. Sci.* 18, 1351–1372. doi: 10.5194/nhess-18-1351-2018

Goudenhoofdt, E., and Delobbe, L. (2009). Evaluation of radar-gauge merging methods for quantitative precipitation estimates. *Hydrol. Earth Syst. Sci.* 13, 195–203. doi: 10.5194/hess-13-195-2009

Guzzetti, F., Peruccacci, S., Rossi, M., and Stark, C. P. (2007). Rainfall thresholds for the initiation of landslides in central and southern Europe. *Meteorol. Atmos. Phys.* 98, 239–267. doi: 10.1007/s00703-007-0262-7

Jan, C. D., and Chen, C. L. (2015). "Debris flows caused by Typhoon Herb in Taiwan," in *Debris Flow Hazards and Related Phenomena*, eds M. Jakob and O. Hungr (Berlin: Springer), 363–385.

Joss, J., and Waldvogel, A. (1990). "Precipitation measurement and hydrology," in *Radar in Meteorology: Battan Memorial and 40th Anniversary Radar Meteorology Conference*, ed. D. Atlas (Boston, MA: American Meteorological Society), 577–606.

Koistinen, J. (1991). "Operational correction of radar rainfall errors due to the vertical reflectivity profile," in *Proceedings 25th International Conference on Radar Meteorology*, (Providence, RI: AMS), 91–94. doi: 10.1175/2010JHM1201.1

Li, J., and Heap, A. D. (2014). Spatial interpolation methods applied in the environmental sciences: a review. *Environ. Model. Softw.* 53, 173–189. doi: 10.1016/j.envsoft.2013.12.008

Marra, F., Destro, E., Nikolopoulos, E. I., Zoccatelli, D., Dominique, J., Creutin, F. G., et al. (2017). Impact of rainfall spatial aggregation on the identification of debris flow occurrence thresholds. *Hydrol. Earth Syst. Sci.* 21, 4525–4532.

Marra, F., Nikolopoulos, E. I., Creutin, J. D., and Borga, M. (2014). Radar rainfall estimation for the identification of debris-flow occurrence thresholds. *J. Hydrol.* 519, 1607–1619. doi: 10.1016/j.jhydrol.2014.09.039

Marra, F., Nikolopoulos, E. I., Creutin, J. D., and Borga, M. (2016). Space–time organization of debris flows-triggering rainfall and its effect on the identification of the rainfall threshold relationship. *J. Hydrol.* 541, 246–255. doi: 10.1016/j.jhydrol.2015.10.010

Mercogliano, P., Segoni, S., Rossi, G., Sikorsky, B., Tofani, V., Schiano, P., et al. (2013). Brief communication "A prototype forecasting chain for rainfall induced shallow landslides". *Nat. Hazards Earth Syst. Sci.* 13, 771–777. doi: 10.5194/nhess-13-771-2013

Montopoli, M., Roberto, N., Adirosi, E., Gorgucci, E., and Baldini, L. (2017). Investigation of weather radar quantitative precipitation estimation methodologies in complex orography. *Atmosphere* 8:34.

Morrissey, M. L., Maliekal, J. A., Greene, J. S., and Wang, J. (1995). The uncertainty of simple spatial averages using rain gauge networks. *Water Resour. Res.* 31, 2011–2017. doi: 10.1029/95WR01232

Nikolopoulos, E. I., Borga, M., Creutin, J. D., and Marra, F. (2015). Estimation of debris flow triggering rainfall: influence of rain gauge density and interpolation methods. *Geomorphology* 243, 40–50. doi: 10.1016/j.geomorph.2015.04.028

Rosi, A., Lagomarsino, D., Rossi, G., Segoni, S., Battistini, A., and Casagli, N. (2015). Updating EWS rainfall thresholds for the triggering of landslides. *Nat. Hazards* 78, 297–308. doi: 10.1007/s11069-015-1717-7

Saito, H., Nakayama, D., and Matsuyama, H. (2010). Relationship between the initiation of a shallow landslide and rainfall intensity—duration thresholds in Japan. *Geomorphology* 118, 167–175. doi: 10.1016/j.geomorph.2009.12.016

Segoni, S., Battistini, A., Rossi, G., Rosi, A., Lagomarsino, D., Catani, F., et al. (2015). Technical note: an operational landslide early warning system at regional scale based ospace–time–variable rainfall thresholds. *Nat. Hazards Earth Syst. Sci.* 15, 853–861. doi: 10.5194/nhess-15-853-2015

Segoni, S., Piciullo, L., and Gariano, S. L. (2018). A review of the recent literature on rainfall thresholds for landslide occurrence. *Landslides* 15, 1483–1501. doi: 10.1007/s10346-018-0966-4

Tiranti, D., Bonetto, S., and Mandrone, G. (2008). Quantitative basin characterization to refine debris-flow triggering criteria and processes: an example from the Italian Western Alps. *Landslides* 5, 45–57. doi: 10.1007/s10346-007-0101-4

Tiranti, D., Cremonini, R., Marco, F., Gaeta, A. R., and Barbero, S. (2014). The defense (DEbris Flows triggEred by storms - Nowcasting SystEm): an early warning system for torrential processes by radar storm tracking using a Geographic Information System (GIS). *Comput. Geosci.* 70, 96–109. doi: 10.1016/j.cageo.2014.05.004

Tiranti, D., and Rabuffetti, D. (2010). Estimation of rainfall thresholds triggering shallow landslides for an operational warning system implementation. *Landslides* 7, 471–481. doi: 10.1007/s10346-010-0198-8

Winter, M. G., Dent, J., Macgregor, F., Dempsey, P., Motion, A., and Shackman, L. (2010). Debris flow, rainfall and climate change in Scotland. *Q. J. Eng. Geol. Hydrogeol.* 43, 429–446. doi: 10.1144/1470-9236/08-108

Conflict of Interest Statement: The authors declare that the research was conducted in the absence of any commercial or financial relationships that could be construed as a potential conflict of interest.

Advantages of publishing in Frontiers

OPEN ACCESS
Articles are free to read for greatest visibility and readership

FAST PUBLICATION
Around 90 days from submission to decision

HIGH QUALITY PEER-REVIEW
Rigorous, collaborative, and constructive peer-review

TRANSPARENT PEER-REVIEW
Editors and reviewers acknowledged by name on published articles

Frontiers
Avenue du Tribunal-Fédéral 34
1005 Lausanne | Switzerland

Visit us: www.frontiersin.org
Contact us: info@frontiersin.org | +41 21 510 17 00

REPRODUCIBILITY OF RESEARCH
Support open data and methods to enhance research reproducibility

DIGITAL PUBLISHING
Articles designed for optimal readership across devices

FOLLOW US
@frontiersin

IMPACT METRICS
Advanced article metrics track visibility across digital media

EXTENSIVE PROMOTION
Marketing and promotion of impactful research

LOOP RESEARCH NETWORK
Our network increases your article's readership